Microphysical properties and thermodynamic phase of Arctic low-level clouds from in-situ aircraft measurements

Dissertation zur Erlangung des Grades
"Doktor der Naturwissenschaften"

am Fachbereich Physik, Mathematik und Informatik
der Johannes Gutenberg-Universität in Mainz

Manuel Moser
geb. in Fürth
Mainz, den 19.06.2024

1. Gutachten:	Prof. Dr. Christiane Voigt
2. Gutachten:	PD Dr. Johannes Schneider

Tag der mündlichen Prüfung: 18.10.2024

Angefertigt am Deutschen Zentrum für Luft- und Raumfahrt e.V.
Institut für Physik der Atmosphäre, Oberpfaffenhofen

Abstract

The Arctic region is experiencing the most pronounced mean temperature rise of any region on Earth, causing drastic changes in the regional and global climate. Current investigations seek to elucidate the processes responsible for the intensified anthropogenic temperature change. Clouds in particular are suspected to play a crucial role in the Arctic climate feedback mechanisms. Clouds cool or warm the surface, depending on their ambient condition, microphysical properties, and thermodynamic phase. The gap in knowledge of microphysical cloud processes is particularly pronounced for mixed-phase clouds, which contain supercooled droplets with coexisting ice crystals and are frequently encountered in the lower part of the atmosphere at high latitudes. To better assess the role of clouds in the Arctic climate system, a comprehensive in-situ cloud data set of low-level Arctic clouds was measured within the scope of this thesis, using an advanced setup of airborne in-situ cloud probes.

The airborne in-situ cloud measurements were carried out over the northern Fram Strait between Greenland and Svalbard in spring 2019, summer 2020, and spring 2022. In total, 2676 min of low-level in-situ cloud observations were performed during 33 research flights above the sea ice and the open Arctic ocean with the research aircraft Polar 5 and Polar 6 of the Alfred Wegener Institute. At first, the in-situ cloud data from spring 2019 and summer 2020 are combined to investigate the distribution of particle number concentration N, effective diameter D_{eff}, and cloud water content CWC (liquid and ice) of Arctic low-level clouds, measured at latitudes between 76 °N and 83 °N. A method is developed to quantitatively derive the occurrence probability of their thermodynamic phase from the combination of microphysical cloud probe and Polar Nephelometer data. The changes in cloud microphysics and cloud thermodynamic phase are investigated related to the ambient meteorological situation in spring and summer, and the effects of surface conditions, including sea ice or open ocean, on low-level clouds are revealed. A median N from 0.2 cm^{-3} to 51.7 cm^{-3} is found, with about two orders of magnitude higher N for mainly liquid clouds in summer compared to ice and mixed-phase cloud conditions measured in spring. A southward directed air mass flow from the sea ice in cold air outbreaks dominates cloud formation processes at temperatures below -10 °C in spring. In contrast, northward directed warm air intrusions favor the formation of liquid clouds at warmer temperatures in summer. The median CWC is higher in summer (0.16 g m^{-3}) than in spring (0.06 g m^{-3}), as this is dominated by the available atmospheric water content and the temperatures at cloud formation level. Significant differences in the particle sizes in spring and summer are observed, as well as an impact of the surface conditions, which modify the heat and moisture fluxes in the boundary layer. Analyses of the cloud thermodynamic phase show that the mixed-phase state is the dominant thermodynamic cloud phase in spring, with a frequency of occurrence of 61% over the sea ice and 66% over the ocean. In summer, the cloud particles are most likely in the liquid state.
In a subsequent study on Arctic low-level mixed-phase cloud conditions, the microphysical properties suggest a distinction between classic mixed-phase clouds and mixed-phase haze. The microphysical composition of this mixed-phase haze is similar to that of classic mixed-phase clouds. However, the supercooled droplets are replaced with large ($> 2.8\,\mu\text{m}$) wet aerosol particles, and N is reduced by more than a factor of 150 in comparison to classic mixed-phase clouds. Further results show an increase of N in the atmospheric boundary layer over the sea ice compared to the open ocean, likely due to increased particle formation processes originating from the sea ice.

The results of this work enhance our understanding of the microphysical processes and thermodynamic phase composition of Arctic low-level clouds and will contribute to improve cloud parameterizations in climate and weather models. The findings will help to assess the role of low-level clouds in the Arctic radiation budget and to quantify their feedback mechanism in the region of the world with the strongest anthropogenic climate change.

Zusammenfassung

Im Vergleich zu anderen Regionen der Erde verzeichnet die Arktis den stärksten Anstieg der Durchschnittstemperatur, was zu drastischen Veränderungen des regionalen und globalen Klimas führt. Laufende Forschungsprojekte zielen darauf ab, die verantwortlichen Prozesse für den verstärkten anthropogenen Temperaturanstieg aufzuklären. Speziell die Wolken stehen im Verdacht, eine entscheidende Rolle bei den Rückkopplungsmechanismen im arktischen Klima zu spielen. In Abhängigkeit von den Umgebungsbedingungen, den mikrophysikalischen Eigenschaften von Wolken und der thermodynamischen Phase können Wolken die Oberfläche abkühlen oder erwärmen. Vor allem bei Mischphasenwolken, die sowohl aus unterkühlten Wassertropfen als auch aus Eiskristallen bestehen und häufig in hohen Breiten auftreten, ist das mikrophysikalische Verständnis der Wolkenprozesse noch unvollständig. Um die Rolle von Wolken im arktischen Klimasystem besser bewerten zu können, wurde ein umfangreicher in-situ Datensatz tiefer arktischer Wolken mit Hilfe von Flugzeugmessungen und modernen Wolkeninstrumenten erhoben.

Die Wolkenmessungen wurden über der nördlichen Framstraße zwischen Grönland und Spitzbergen im Frühjahr 2019, Sommer 2020 und Frühjahr 2022 durchgeführt. Bei 33 Forschungsflügen über dem Meereis und dem offenen Ozean wurden mit den Forschungsflugzeugen Polar 5 und Polar 6 des Alfred-Wegener-Instituts insgesamt 2676 Minuten an in-situ Wolkendaten in niedriger Höhe gemessen. Zunächst werden die Messdaten aus dem Frühjahr 2019 und dem Sommer 2020 genutzt, um die Verteilung der Partikelanzahlkonzentration N, des effektiven Durchmessers D_{eff} und des Wolkenwassergehalts CWC (enthält flüssigen und gefrorenen Anteil) von tiefen arktischen Wolken zu untersuchen. Eine Methode zur quantitativen Ableitung der Häufigkeit verschiedener thermodynamischer Wolkenphasen wird vorgestellt, welche auf einer Kombination von mikrophysikalischen Wolkeninstrumenten und einem Polarnephelometer basiert. Änderungen in der Wolkenmikrophysik und der Wolkenphase werden in Abhängigkeit von den meteorologischen Bedingungen im Frühjahr und Sommer untersucht. Zudem wird der Einfluss von Oberflächenbedingungen wie Meereis und offenem Ozean auf Wolken in niedriger Höhe herausgestellt. Der Medianwert von N liegt zwischen 0,2 cm^{-3} und 51,7 cm^{-3} und ist bei vorwiegend flüssigen Wolken im Sommer etwa zwei Größenordnungen höher als bei den Wolken im Eis- und Mischphasenzustand, die im Frühjahr dominieren. Kaltluftausbrüche mit Winden aus nördlichen Richtungen dominieren die Wolkenbildungsprozesse bei Temperaturen unter -10 °C im Frühjahr. Dagegen begünstigen Warmlufteinbrüche mit südlichen Winden die Bildung von Flüssigwolken bei wärmeren Temperaturen im Sommer. Der mediane CWC ist im Sommer höher (0,16 g m^{-3}) als im Frühjahr (0,06 g m^{-3}), was auf einen höheren verfügbaren atmosphärischen Wassergehalt und wärmere Temperaturen in der Höhe der Wolkenbildung zurückzuführen ist. Signifikante Unterschiede in der Partikelgröße im Frühling und im Sommer sowie ein Einfluss der Oberflächenbeschaffenheit auf die vorherrschenden Wolkenprozesse durch Veränderung der Wärme- und Feuchteflüsse in der Grenzschicht werden beobachtet. Die Untersuchungen der thermodynamischen Wolkenphasen zeigen, dass im Frühjahr die Mischphase dominiert. Dabei liegt die Häufigkeit des Auftretens bei 61% über dem Meereis und bei 66% über dem offenen Ozean. Im Sommer befinden sich die Wolkenpartikel am häufigsten in einem rein flüssigen Zustand.
Eine anschließende Untersuchung von Wolken in der Mischphase zeigt, dass eine Unterscheidung zwischen klassischen Mischphasenwolken und Mischphasendunst aufgrund ihrer mikrophysikalischen Eigenschaften erforderlich ist. Die mikrophysikalische Zusammensetzung des Mischphasendunstes ähnelt der von klassischen Mischphasenwolken. Anstelle der unterkühlten Tröpfchen werden hier große (> 2,8 µm) feuchte Aerosolpartikel beobachtet, und N ist im Vergleich zur klassischen Mischphasenwolke um mehr als einen Faktor 150 reduziert. Weitere Ergebnisse zeigen eine erhöhte N in der atmosphärischen Grenzschicht über dem Meereis im Vergleich zum offenen Ozean, was auf verstärkte Partikelbildungsprozesse ausgehend vom Meereis zurückzuführen ist.

Die Erkenntnisse aus dieser Arbeit erweitern unser Verständnis der mikrophysikalischen Prozesse und der thermodynamischen Phasenzusammensetzung tiefer Wolken in der Arktis und können zur Verbesserung der Wolkenparametrisierung in Klima- und Wettermodellen beitragen. Die Forschungsergebnisse werden helfen, die Auswirkungen von Wolken auf den Strahlungshaushalt in der Arktis präziser zu bewerten und die Rückkopplungsmechanismen in dieser Region, die am stärksten vom anthropogenen Klimawandel betroffen ist, genauer zu quantifizieren.

Contents

1 Introduction

1.1 Motivation

Over the past few decades, the Arctic region has drastically changed in response to global warming (Jeffries et al., 2013; IPCC, 2021). In fact, amplified warming in the Arctic, as compared to other regions on the globe, has been observed since the mid-1990s (see Fig 1). The accelerated warming, with a rate that is more than twice as fast as the global average (Overland et al., 2019), is known as a phenomenon called Arctic amplification (Serreze and Francis, 2006). The current ability to explain the causes and consequences of Arctic amplification with models is limited mainly due to the lack of knowledge of the processes and feedbacks leading to a warmer Arctic, so estimations of future trends are subjected to significant uncertainties (Smith et al., 2019). Many mechanisms behind the Arctic amplification phenomenon are widely discussed, including the reduction of albedo due to the decrease of the mean sea ice extent, the change in lapse rate, and an alteration in large scale weather patterns. The amplification is likely to be driven by a combination of multiple factors. However, clouds may play a key role in the processes underlying the intense mean temperature rise at high latitudes (Wendisch et al., 2022).

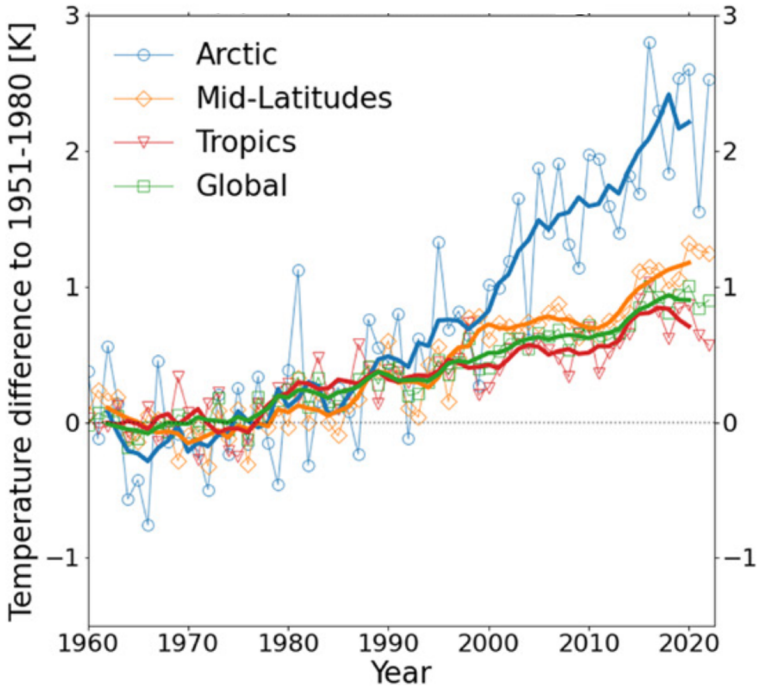

Figure 1 The annually averaged differences of the near-surface air temperature relative to the corresponding long-term mean over the period of 1951 - 1980 for the Arctic (60 °-90 °N), mid-latitudes (30 °- 60 °N), tropics (20 °S - 20 °N), and the globe. The thick lines indicate 5-year running averages. The figure and caption is from Wendisch et al. (2022).

Low-level clouds in the Arctic are often found in a mixed-phase state (Shupe et al., 2006; Morrison et al., 2011), representing a three-phase system consisting of water vapor, ice particles, and coexisting supercooled liquid water droplets. Together with stratiform liquid clouds, Arctic mixed-phase clouds are important contributors to the Arctic surface radiation budget (Shupe and Intrieri, 2004). In contrast to the absence of clouds, where the radiative energy budget is dominated by the low albedo of the dark open ocean, the abundance of clouds significantly increases the reflection of solar radiation toward space and the emission of thermal infrared radiation directed toward the surface. Such changes in the atmospheric radiative energy budget are very sensitive to the microphysical properties of Arctic clouds (Curry et al., 1996). In particular, the size, shape, and thermodynamic phase of the cloud particles influence the atmospheric energy fluxes and are often poorly represented in observations and models (Naud et al., 2014; Bodas-Salcedo et al., 2016; McCoy et al., 2016; Tan and Storelvmo, 2019; Wendisch et al., 2019; Kretzschmar et al., 2020). Observations show that the surface temperature is higher when clouds containing liquid water droplets are present compared to pure ice clouds or no clouds (Shupe and Intrieri, 2004; Shupe et al., 2022), suggesting that clouds directly impact the surface albedo, the sea ice thickness, snow depth, solar radiative energy input, and other parameters. In turn, the surface conditions have feedback effects on the cloud properties (Stapf et al., 2020). In the Arctic, the micro- and macrophysical properties of clouds are strongly affected by seasonal changes in meteorological weather situations such as atmospheric rivers, warm air intrusions, cold air outbreaks or Arctic cyclones, as well as small-scale temperature and humidity fluctuations (McFarquhar et al., 2007a; Mioche et al., 2017; Ruiz-Donoso et al., 2020; Wendisch et al., 2022). Cloud properties are affected by turbulent fluxes and moisture transport, which in turn are affected by the presence of sea ice (Lüpkes et al., 2011; Vihma et al., 2014; Wendisch et al., 2019; Elvidge et al., 2021; Schmale et al., 2021; Michaelis and Lüpkes, 2022). The total Arctic sea ice reaches its maximum extent in early March and a minimum in September (Spreen et al., 2008), which leads to a change in the overall surface properties, e.g., the surface albedo. A strong surface temperature gradient develops between the sea ice and the open ocean in spring, while in summer, the gradient is strongly reduced (Wendisch et al., 2022). This affects the structure of the atmosphere, and in particular the lowest part of the atmosphere directly influenced by the Earth's surface, called the atmospheric boundary layer (ABL), and the clouds within it. In winter, particularly low-level clouds in high latitudes have a warming effect as there is little or no solar radiation in the Arctic, and mainly terrestrial radiation dominates and is absorbed, while in summer, the clouds reflect the sunlight and induce solar cooling. However, due to the low solar zenith angles in the central Arctic, the annual mean radiative forcing of Arctic clouds at the bottom of the atmosphere is most likely positive, thus causing a surface warming (Shupe and Intrieri, 2004). In addition, different types of aerosol particles are formed and transported in the Arctic ABL and influence the cloud formation (Moschos et al., 2022).

Triggered by global warming, the mean sea ice extent declines due to the rising near surface temperature (Druckenmiller et al., 2022). In turn, the albedo decreases as the area of the darker open ocean increases. More solar radiation is absorbed, leading to radiative heating of the ocean's upper layer and to further melting of snow and sea ice (Budyko, 1969; Sellers, 1969). This amplified feedback mechanism is called the direct surface albedo feedback and is known to dominate the Arctic amplification in spring. In fall and winter, indirect mechanisms dominate, such as delayed refreezing of the sea or warming of the near surface air caused by heat stored in the ocean mixed layer (Wendisch et al., 2022). The surface albedo feedback interacts directly with the radiative and turbulent atmospheric energy fluxes, favoring an increase in water vapor in the ABL and advancing the formation of low-level clouds. As a result, the Arctic surface temperature continues to rise (Vavrus, 2004; Cronin and Tziperman, 2015; Tan and Storelvmo, 2019). Long term satellite observations have shown a systematic change in the thermodynamic phase of clouds, from the ice phase towards the liquid phase (Lelli et al., 2023). Furthermore, the prevalent surface and its changes in the mean sea ice extent significantly impact the ocean-atmosphere interaction. Increased radiative heating of the ocean leads to alterations in upper ocean processes and to emissions of trace gases and aerosol particles of marine or biogenic origin (Willis et al., 2018; Schmale et al., 2021; Wendisch et al., 2022). These aerosols trigger the cloud formation processes and change microphysical properties by facilitating the condensation of water vapor into cloud droplets and can initiate the formation of ice crystals within clouds. There is strong evidence that with ongoing Arctic amplification, large scale weather patterns will change, leading to more extreme mid-latitude weather events and enhanced mixing of mid and high latitude air masses (Francis and Vavrus, 2012; Mann et al., 2017; Coumou et al., 2018; Kretschmer et al., 2018; Heukamp et al., 2023). This can potentially bring more aerosols, trace gases, and water vapor into and out of the Arctic, influencing clouds and precipitation. However, current generations of models struggle to represent the changes in regional and large-scale atmospheric circulation (Francis and Vavrus, 2015; Pithan et al., 2018; Smith et al., 2019; Cohen et al., 2019).

The lack of knowledge in microphysical cloud processes, especially for mixed-phase clouds (Korolev et al., 2017), challenges the representation of Arctic clouds in climate and weather models so that the assessment of the absolute contribution of clouds to Arctic amplification remains highly uncertain (Morrison et al., 2011; Bock et al., 2020; IPCC, 2021; Wendisch et al., 2022). Therefore, it is essential to quantify the microphysical and thermodynamic phase of Arctic clouds. Of particular importance is to investigate the influence of local environmental conditions, such as the sea ice or the open ocean, on the microphysical cloud processes and to determine the impact of seasonal meteorological variations.

1.2 Objectives and structure of the thesis

The key objective of this dissertation is to create a comprehensive data set of low-level clouds in the Arctic using airborne in-situ cloud measurement systems. This was accomplished within the framework of three aircraft field campaigns: The Aircraft campaign observing FLUXes of energy and momentum in the cloudy boundary layer over polar sea ice and ocean (AFLUX) in spring 2019, the Multidisciplinary Drifting Observatory for the Study of Arctic Climate - Airborne observations in the Central Arctic (MOSAiC-ACA) in late summer 2020, and the Arctic Air Mass Transformations during Warm Air Intrusions and Marine Cold Air Outbreaks (HALO-$(AC)^3$) in spring 2022. For in-situ cloud observations, a set of advanced airborne instruments was selected, characterized, calibrated, and integrated into the research aircraft Polar 5 and 6 of the Alfred Wegener Institute, Helmholtz Centre for Polar and Marine Research (AWI). The research flights were planned to answer the specific scientific questions of this work and were carried out over the northern Fram Strait between Greenland and Svalbard. The collected comprehensive data set of Arctic low-level clouds is used in particular to investigate the differences in microphysical properties and thermodynamic phase of clouds in spring (maximum of the sea ice extent) and late summer (minimum of the sea ice extent). Very different meteorological conditions dominate in both seasons. In addition, the influence of the local sea ice cover on the cloud processes is investigated. Particular focus is given to the analysis of clouds in a mixed-phase state. Apart from the classic mixed-phase clouds, a mixture of ice crystals and wet sea salt particles is frequently observed at low altitudes in spring. This condition is referred to here as Arctic low-level mixed-phase haze (short: mixed-phase haze). The microphysical properties of the two conditions, mixed-phase clouds and mixed-phase haze, are examined in greater detail.
The objectives of this work can be summarized in three primary questions:

- How do the seasonal synoptic conditions affect cloud microphysical properties and thermodynamic phase of Arctic low-level clouds?
- How do surface conditions, open ocean, and sea ice impact low-level clouds?
- What are the microphysical properties of Arctic mixed-phase clouds and mixed-phase haze?

The structure of the thesis is as follows: Chapter 2 provides a brief scientific background on clouds and important microphysical cloud processes, with a particular focus on mixed-phase clouds. Chapter 3 presents the basic principles, method of operation and limitations of the airborne scattering and imaging cloud probe instruments. Particular focus is given to the characterization and calibration of the instruments and the optimization of data processing.
At the beginning of Chapter 4, the goals of the three airborne field campaigns are summarized, in which the corresponding cloud data were obtained. The environmental parameters during

the in-situ cloud observations, including the sea ice cover and the dominant weather situations, are examined. A case study shows the transformation of the microphysical cloud properties in a cold air outbreak situation. In Sect. 4.4 the distribution of microphysical cloud properties is discussed in relation to the ambient atmospheric and surface conditions (spring over sea ice, spring over the open ocean, summer over sea ice, and summer over ocean), and median and altitude resolved microphysical cloud properties are derived based on the AFLUX and MOSAiC-ACA data set. By introducing a new cloud particle classification depending on particle number concentration, size, and angular scattering properties, the microphysical properties and thermodynamic phase of low-level Arctic clouds are investigated in Sect. 4.5 and their frequency of occurrence are discussed. The same analysis on the microphysical cloud properties and the new method developed to determine the thermodynamic phase are applied to the latest spring cloud data set collected during the HALO-$(AC)^3$ campaign in Sect. 4.6. Subsequently, the microphysics and the occurrence of the thermodynamic cloud phase during two spring periods in 2019 and 2022 are compared.

Based on the cloud data from all three campaigns, the mixed-phase clouds and mixed-phase haze conditions are analyzed in greater detail in Chapter 5. The different microphysical compositions of the two cloud types are presented, and the persistence of the mixed-phase haze is explained. The cause of the increased particle number concentration above the sea ice surface is investigated using supplemental aerosol data.

Finally, the results of this thesis are summarized in the Chapter 6. Follow-up questions for future Arctic cloud research are suggested at the end.

2 Background: Clouds

2.1 Clouds in the weather and climate system

Clouds appear white as they consist of a cluster of fine condensed water and ice particles that scatter the visible wavelengths emitted by the sun. This water is part of the hydrological cycle that continuously redistributes water from one reservoir to another, driven by several physical processes, including thermodynamic phase change. The sun heats the surface of water bodies such as the ocean, and the evaporation leads to humid air above. Winds transport the humid air, and when the air parcels are adiabatically lifted or come into contact with colder surrounding air, the temperature in the air parcels decreases. This cooling causes condensation and the formation of clouds. When the water from the clouds precipitates directly into the water bodies, the cycle closes and can begin again. If the water falls on land, it can be stored in groundwater, as snow, or in glaciers, but after a while, it is released and transported back into the ocean by rivers. The hydrological cycle repeats all over again.

The whole cycle is powered by the radiation energy emitted by the sun, which interacts with the atmosphere and the surface. This incoming solar radiation is the most accurately moni-

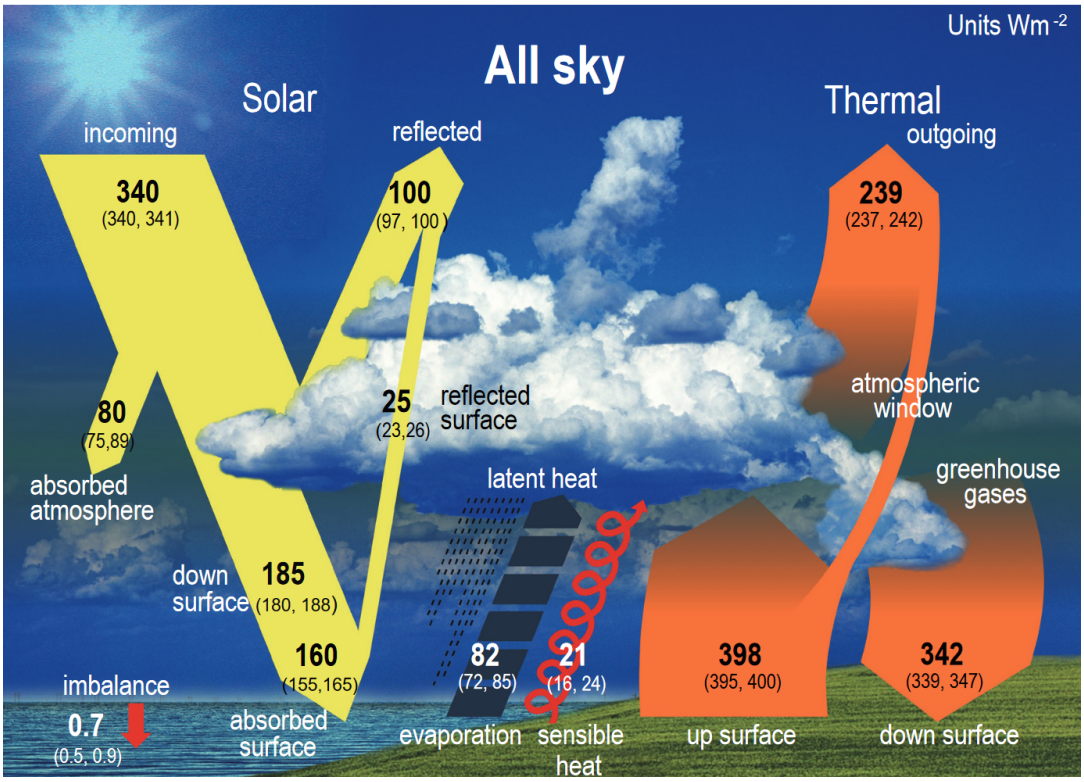

Figure 2 The global mean energy budget of the Earth representing the climate conditions at the beginning of the 21st century. Numbers give the best estimates for the averaged energy fluxes in Wm^{-2} together with their uncertainties in brackets (5-95% confidence interval). Figure from IPCC (2021).

tored flux in the global energy budget with a mean value of 340 Wm^{-2} (Lohmann et al., 2016). The processes of how the incoming radiation interacts with the Earth's atmospheric system and clouds within are illustrated in Fig. 2 from the Intergovernmental Panel on Climate Change (IPCC, 2021), which shows the energy flows relevant to the climate system of our planet. This Earth's energy budget scheme is the fundamental basis of weather and climate models. During the transit of solar light through the atmosphere (yellow arrows), the radiation interacts with the atmospheric molecules and particles and is absorbed, scattered, or transmitted. The intensity of the interaction between solar radiation and the atmosphere highly depends on the atmospheric composition, including the ambient gases, aerosols, and clouds. Approximately half of the incoming solar radiation (185 Wm^{-2}) reaches the Earth's surface and is either reflected back into the atmosphere or absorbed by the ground. The ability of a surface to diffusely reflect sunlight is described by the albedo parameter, the ratio of reflected to incident sunlight. For example, the sea ice at the poles has a much higher albedo, up to 0.95, compared to other Earth surfaces, such as the surrounding ocean, with values down to 0.05 (Stull, 2017). As the surface absorbs some of the incoming radiation from the sun, the Earth heats up and emits longer wavelength radiation into the atmosphere. For this reason, a differentiation is made between longwave for the terrestrial radiation (between 4 µm and 100 µm) and shortwave for the solar radiation (between 0.2 µm and 4 µm; Lohmann et al., 2016). The longwave radiation energy spectrum emitted from the surface corresponds approximately to that of a black body at a temperature of 15 °C or 288 K (Liou, 2002; Hobbs and Wallace, 2006). In Fig. 2, the path of the terrestrial radiation is shown as orange arrows. Again, atmospheric conditions affect the transmission, absorption, reemission, and scattering of the longwave radiation. The atmosphere is transparent for the majority range of the solar spectrum. However, this is not true for the terrestrial spectral region, where much less emitted radiation is transmitted through the atmosphere. Of the total 398 Wm^{-2} emitted from the ground by longwave radiation, about 10% is transmitted through the atmosphere, in the so-called atmospheric window between the wavelength 8 - 13 µm. The remaining radiation interacts with the clouds and atmospheric trace gases, including greenhouse gases. Such gases, like H_2O, CO_2, and O_3 absorb at specific wavelengths, hinder the thermal radiation from reaching space and keeping the global mean temperature about 33 K higher than the equilibrium temperature of an Earth system that is without an atmosphere (Liou, 2002). Hence, the absorption of terrestrial radiation in the atmosphere is essential for the habitability of the current species on the planet. During the last century, however, the global CO_2 mixing ratio in the atmosphere has been drastically increased by human activities, from ∼278 ppm in the preindustrial era (Etheridge et al., 1996) to 417 ppm in 2022 (Friedlingstein et al., 2022). The resulting higher absorption traps energy in the atmosphere, leading to more total downward radiation. The increased downward radiation causes an imbalance, compensated by anthropogenic global warming.

The net radiative energy gain at the surface in Fig. 2 is countered by latent and thermal heat transfer.

In the Earth system, clouds have a cooling effect in the shortwave regime by reflecting sunlight back into space but warm the surface in the longwave regime by absorbing and reemitting terrestrial radiation towards the surface. The radiative interaction in the short and longwave regimes with clouds depends on several parameters, including total cloud cover, cloud temperature, and cloud microphysical properties. Clouds in low altitudes cool the Earth's surface by reflecting solar radiation, while the cold, thin clouds at higher altitudes have a warming effect (Lohmann et al., 2016). The combined effect of all clouds is that the Earth's surface is colder than in a scenario where there are no clouds (IPCC, 2013; Raschke et al., 2016).

In response to global warming, the properties of clouds will change, and so will their radiative effect. The impact of these changes on the global mean surface temperature is quantified by the cloud feedback. The IPCC (2021) states with high confidence that the cloud feedback is positive, meaning that clouds accelerate global warming. Previous climate model comparisons have shown that the magnitude of cloud feedback is subject to a high degree of uncertainty when forcing global models with increased CO_2 concentrations (Stevens et al., 2016; Caldwell et al., 2016; Ceppi et al., 2017). The models showed that the cloud feedback is mainly related to cloud altitude, amount, and optical depth (Ceppi et al., 2017). The overall positive feedback of the clouds in our Earth system is dominated by the rising cloud altitude (positive longwave effect), the decrease in the frequency of low-level clouds (positive longwave effect), and the increase in the optical density of low-level clouds (a weaker negative shortwave effect; Zelinka et al., 2012). Currently, the uncertainties in the quantification of the absolute cloud feedback are mainly within the shortwave radiation range (Ceppi et al., 2017). Shortwave radiation interaction is strongly coupled to the microphysical cloud properties and the thermodynamic phase (Pruppacher and Klett, 2010). Depending on the environmental conditions, clouds can be in a pure liquid state, a pure ice state, or a mixture of both, called a mixed-phase state. In particular, low-level clouds, often observed in a liquid or mixed-phase state, strongly influence shortwave radiation. This is due to the fact that liquid particles are orders of magnitude smaller than ice crystals and therefore are more efficient at scattering sunlight per unit mass (Pruppacher and Klett, 2010).

Such low-level clouds are known to dominate at high latitudes. The IPCC (2021) reports the Arctic cloud feedback as positive and of small magnitude, but with low confidence, so the true sign and absolute value remain questionable (Tan et al., 2023). Poor representation of Arctic clouds in climate models causes this uncertainty. In particular, small-scale physical processes remain a significant challenge in climate modeling, as such processes cannot be explicitly represented by the coarse grids of the models (Morrison et al., 2011; Korolev et al., 2017). Since cloud microphysics is sensitive to small environmental changes, a better understanding of the processes is essential to make weather and climate models more robust and to quantify the absolute contribution of cloud response to global warming. This also applies to regional areas, such as the Arctic, where climate change is intensified, and potentially clouds, especially mixed-phase clouds, contribute to this accelerated temperature rise.

2.2 Microphysical cloud processes

In this section, the theory of condensation of water vapor and the subsequent formation of cloud droplets is explained, as well as the process of rapid growth of ice crystals at the expense of coexisting liquid water droplets. These fundamental processes can be explained by the Köhler equation (see Sect. 2.2.1) as well as by the Wegener-Bergeron-Findeisen process (see Sect. 2.2.2). Both concepts serve as a cornerstone in the field of cloud microphysics (Pruppacher and Klett, 2010) and will be referred to again in the further course of the microphysical cloud analysis within this thesis.

2.2.1 Particle growth by condensation

Cloud droplets do not form through homogeneous nucleation of water but always from heterogeneous nucleation, which means they originate from water condensation on aerosol particles (Hobbs and Wallace, 2006). For example, such aerosol particles consist of sodium chloride or ammonium sulfate and form a solution when environmental conditions favor the condensation process. The water vapor pressure in a droplet composed of a solution is lower than that of a droplet of the same size of pure water. That reduction in water vapor pressure due to dissolved aerosols in the droplet is described by the Raoult's law. In contrast, the Kelvin effect counteracts this favored cloud droplet activation. The Kelvin effect describes the relationship between the water vapor pressure and the curvature of a surface. Small droplets have a stronger degree of curvature, increasing the vapor pressure, resulting in faster evaporation than larger droplets with a smaller degree of curvature. The combination of Raoult's law and the Kelvin effect yields the Köhler equation, which describes the state at which a droplet is in equilibrium with its environment (Yau and Rogers, 1996):

$$S = 1 + \frac{a'}{r} - \frac{b'}{r^3} \tag{2.1}$$

where

$$a' = \frac{2\sigma}{\rho_w R_\mathrm{v} T} \qquad b' = \frac{3 i_v m_\mathrm{s} M_\mathrm{V}}{4\pi \rho_w M_\mathrm{S}}$$

with S the saturation ratio of the environment and r the droplet radius. a' represents the Kelvin effect, and b' the Raoult's law. The Köhler curve is the visual representation of the Köhler equation and is shown in Fig. 3, calculated for different solute masses of sodium chloride (NaCl). Following values are assumed for the calculation of the Köhler curves: Surface tension of water σ = 0.075 J m^{-2}, van't Hoff factor i_v = 2, gas constant for water vapor R_v = 461.5 J kg^{-1} K^{-1}, density of water ρ_w = 1000 kg m^{-3}, molar mass of the solute (NaCl) M_S = 58.44 g mol^{-1}, molar mass of water (H_2O) M_V = 18.02 g mol^{-1}, the temperature T = -15 °C and m_s the mass of solute.

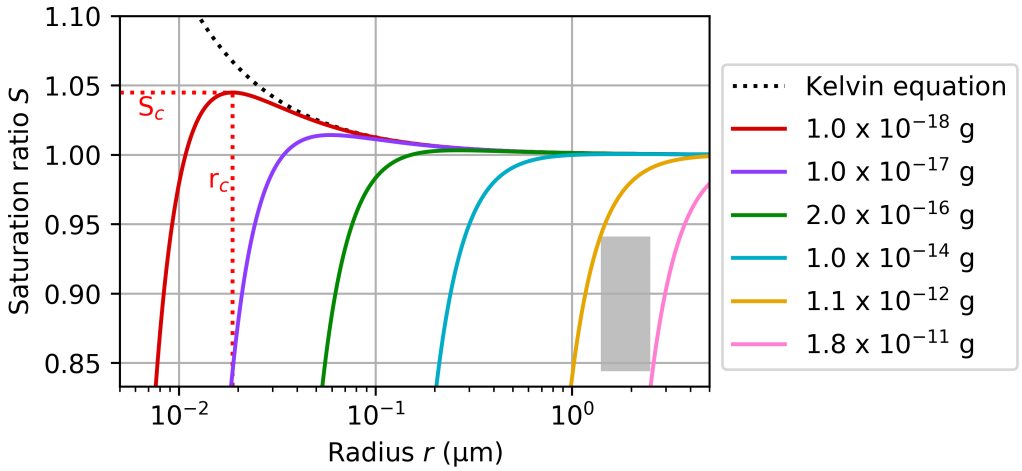

Figure 3 Köhler curves calculated for different solute masses of sodium chloride (NaCl) at a temperature of -15 °C. The Kelvin equation is given for pure water droplets. The gray rectangle shows typical conditions observed during Arctic low-level cloud measurements (results from the mixed-phase haze analysis in Chapter 5).

For a more detailed explanation of the Köhler curve, the critical radius r_c and the critical saturation ratio S_c are marked for the red curve in Fig. 3. For $r < r_c$, the relative humidity determines the size of the particle, and the droplet grows as a function of the saturation ratio. Here, the droplet is in a stable equilibrium with its environment. With further droplet growth, the critical saturation ratio S_c is reached at r_c, corresponding to the peak of the Köhler curve. When the relative humidity exceeds S_c, the droplet grows beyond r_c and is defined as "activated" (Yau and Rogers, 1996). The values $r > r_c$ on the Köhler curve are in an unstable equilibrium with the environment. Any small perturbation causes the droplet to grow or evaporate, further deviating from equilibrium. Simply put, a cloud particle is activated when r has exceeded the critical radius r_c. From this point, the particle can grow into a cloud droplet as long as the saturation ratio maintains a value above the equilibrium curve (Pruppacher and Klett, 2010). Droplets with a radius smaller than r_c are called non-activated or haze droplets (Yau and Rogers, 1996; Hobbs and Wallace, 2006). Such haze particles originating from sea salt aerosols are observed later in the analysis in Chapter 5, and their size and saturation ratio regime are marked as a gray rectangle in Fig. 3.

2.2.2 The Wegener-Bergeron-Findeisen process

When cloud droplets are cooled to temperatures below 0 °C, the crystallization temperature of a cloud droplet depends on the enclosed aerosols. In the absence of aerosols that promote ice nucleation, droplets remain liquid down to a minimum temperature of -38 °C. Below this temperature threshold, the droplets crystallize by homogeneous freezing. Between 0 °C and -38 °C, water droplets can freeze due to heterogeneous nucleation. This freezing process is

strongly dependent on the type of aerosol inducing the ice nucleation process and the ambient temperature (for more details about homogeneous and heterogeneous ice nucleation, see Kanji et al., 2017). If no ice activation occurs, droplets below 0 °C remain liquid and are referred to as supercooled liquid droplets. This implies that liquid droplets and ice particles can exist in a cloud at the same time in the temperature range between 0 °C and -38 °C. The coexistence of liquid and ice cloud particles in a narrow spatial range strongly influences the microphysical processes in a cloud in which such conditions occur. This becomes evident when looking at the saturation vapor pressure over water e_{w} and over ice e_{i}. In this thesis, the saturation vapor pressure is applied according to the definition of the World Meteorological Organization (2012):

$$e_{\mathrm{w}} = 6.112 \times \exp[17.62\,T/(243.12 + T)] \tag{2.2}$$

$$e_{\mathrm{i}} = 6.112 \times \exp[22.46\,T/(272.62 + T)] \tag{2.3}$$

with T the ambient temperature in (°C), and e_{w} and e_{i} in (hPa). This enables the relative humidity with respect to ice to be calculated as follows:

$$\mathrm{RH_{ice}} = \mathrm{RH_{w}} \times \frac{e_{\mathrm{w}}}{e_{\mathrm{i}}}. \tag{2.4}$$

The difference between e_{w} and e_{i} over the temperature is presented in Fig. 4. For a temperature at which ice crystals and water droplets can coexist, the saturation vapor pressure above water is always higher than the saturation vapor pressure above ice. For the relative humidity, it follows that $\mathrm{RH_{ice}}$ is always greater than $\mathrm{RH_{w}}$. Consequently, ice crystals and supercooled water droplets cannot coexist in equilibrium (Yau and Rogers, 1996; Pruppacher and Klett, 2010).

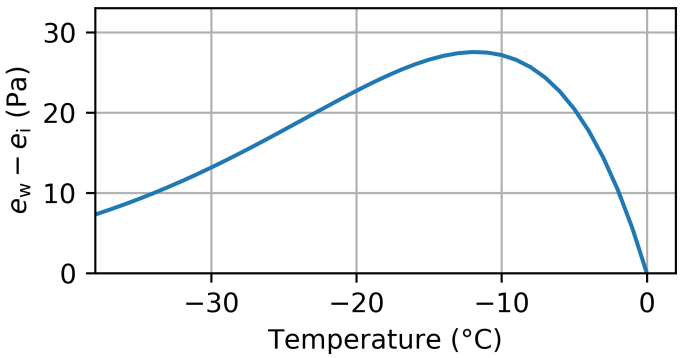

Figure 4 Difference in vapor pressure between saturated water and ice as a function of temperature.

In a mixed-phase cloud, which consists of ice crystals and supercooled liquid droplets (see Sect. 2.3), the imbalance between the vapor pressure over ice and water causes the ice crystals in the cloud to grow at the expense of the liquid particles. Figure 4 shows that the difference between the saturation vapor pressure above water and ice reaches its maximum at -12 °C. In theory, the largest ice crystal growth rate is expected at this temperature. In reality, the actual maximum shifts to a slightly lower temperature, as the local latent heat release must be compensated, and so the largest growth rate is usually found around -15 °C (Pruppacher and Klett, 2010). Once the ice crystals have reached a certain size, these cloud particles can no longer be carried by the updrafts within the cloud and fall to the ground. On their way down, the ice particles continue to grow through aggregation and rimming processes. When temperatures exceed 0 °C, the ice crystals melt and reach the Earth's surface as rain. This development of precipitation is described by the work of Wegener (1912), Bergeron (1935), and Findeisen (1938). Based on their discoveries, the process of rapidly growing ice crystals at the expense of surrounding cloud droplets was named the Wegener-Bergeron-Findeisen (WBF) process (Pruppacher and Klett, 2010; Storelvmo and Tan, 2015). Figure 5 shows an example of raw data recorded with a Cloud Imaging Probe in a mixed-phase cloud where supercooled droplets and ice crystals coexist, and the ice phase is growing at the expense of the liquid phase.

Figure 5 Example raw images of a Cloud Imaging Probe in a mixed-phase cloud where the WBF process is likely to occur. Data show coexisting supercooled liquid droplets (small dots) together with larger ice crystals. Blue arrows symbolize water mass transfer from liquid droplets to ice crystals due to the imbalance of water vapor pressure.

2.3 Arctic mixed-phase clouds

In Sect. 2.2.2 is shown how liquid droplets and ice particles can physically coexist. When such a state of mixed phases occurs within a cloud, the cloud is then called a mixed-phase cloud. There are numerous weather situations in which environmental conditions can create mixed-phase conditions, for example, in lee wave clouds, in deep frontal clouds, or in convective clouds (Korolev et al., 2017). One of the most important mixed-phase clouds, especially at high latitudes, are the so-called stratiform mixed-phase clouds, which are located in the atmospheric boundary layer (ABL). The mixed-phase state is physically unstable as the cloud converts into an ice cloud at the expense of the liquid fraction. To compensate for the mass loss of the droplets, the ambient humidity must remain above water saturation, otherwise, the mixed-phase

state crystallizes within a couple of seconds to a few minutes for Arctic low-level cloud conditions (Korolev and Isaac, 2003). However, Arctic mixed-phase boundary layer clouds persist for many days (Korolev et al., 2017). This persistence of Arctic mixed-phase clouds is caused by a balance between the loss of moisture from ice precipitation due to the WBF process and the supply of water vapor from dynamic processes in the ABL (Morrison et al., 2011). If the cloud is dynamically coupled to the energy and moisture sources on the surface, that means aerosols and gases such as water vapor from the surface can directly be mixed into the clouds through upward motion and turbulence (Shupe et al., 2013). The supercooled liquid water in the clouds can cause surface longwave radiative warming, resulting in increased fluxes of sensible heat and moisture from the ground, which in turn provide energy and moisture that maintain the liquid layer of the mixed-phase cloud. However, mixed-phase clouds can be dynamically decoupled from the surface by a stable stratification near the surface, which prevents mixing of air masses from below into the clouds. Whether clouds are coupled or decoupled to the surface is strongly dependent on the surface and the prevailing weather conditions. A warmer surface temperature relative to the lower atmosphere tends to enhance the coupling of clouds to the surface, while colder surface conditions relative to the lower atmosphere tend to enhance the decoupling (Tan et al., 2023). Even decoupled mixed-phase clouds with no water vapor supply from below show a persistent characteristic. This can be explained by a moisture inversion layer at cloud top, which is driven by large-scale advection (Solomon et al., 2011). The supercooled liquid layer in the upper part of the cloud leads to a longwave radiative cooling, which increases turbulence and, in turn, promotes the exchange of moist air that feeds the mixed-phase cloud with water vapor from above (Pinto, 1998). The characteristics of Arctic low-level mixed-phase clouds, including persistence while decoupled from the surface, the presence of a moisture inversion at the cloud top, and that the cloud can reach into the inversion layer, are in contrast to marine boundary layer clouds at lower latitudes (Morrison et al., 2011; Tan et al., 2023).
The structure of an Arctic boundary layer cloud is shown schematically in Fig. 6.

Besides dynamical processes, the ambient aerosol particles have a crucial influence on the persistence and microphysical structure of Arctic mixed-phase clouds. Aerosol particles can either act as cloud condensation nuclei (CCNs), on which liquid droplets form, or as ice nucleating particles (INPs) which act as the nucleus for the formation of ice crystals. Particle crystallization by the immersion freezing process is suggested to be most prominent in Arctic mixed-phase clouds (Westbrook and Illingworth, 2013; Boer et al., 2011), which is the process of crystallization of a supercooled water droplet by an immersed INP. Often the ice crystal number concentration is observed to be higher than the available INPs (Pasquier et al., 2022). Secondary ice production like rime splintering, collision fragmentation, splintering of the droplets during freezing, and sublimation fragmentation can increase the ice particle number concentration (Field et al., 2016). Immersion freezing on INPs and secondary ice production are the main processes that control the number concentration of ice crystals in mixed-phase clouds (Korolev

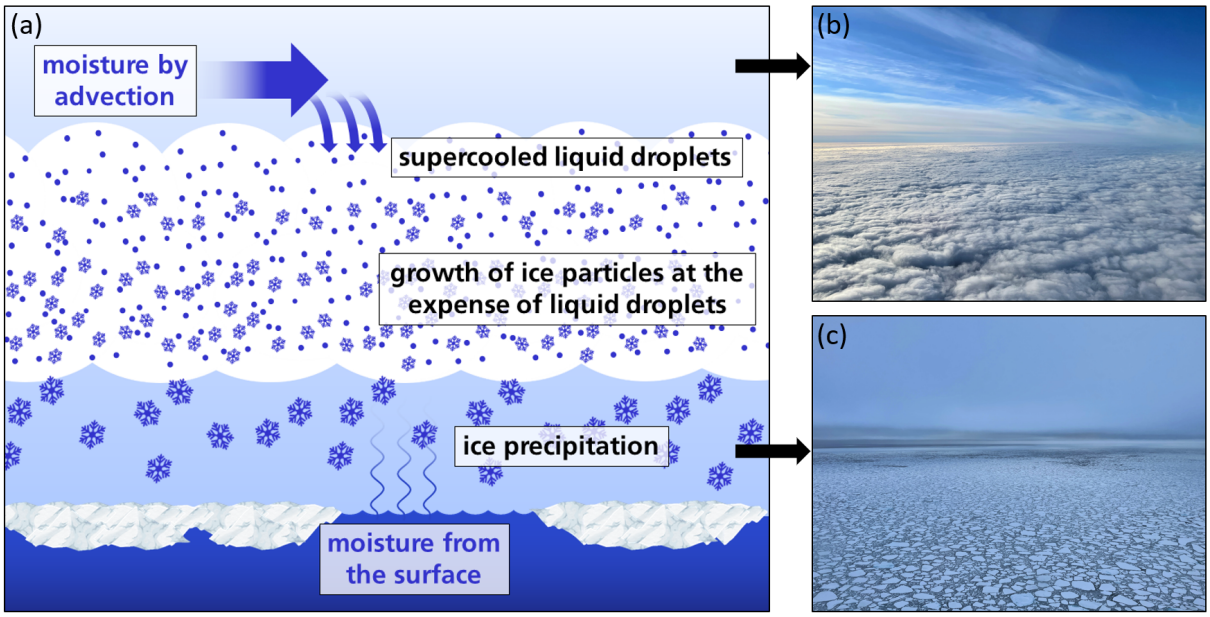

Figure 6 (a) Schematic presentation of a stratiform mixed-phase cloud in the Arctic with the characteristic structure of a liquid layer near the top of the cloud and ice within and below the liquid layer. Moisture from the surface or from above through large-scale advection compensates for water loss through ice precipitation. Images (b) and (c) show a classic Arctic mixed-phase cloud from above and below, respectively, recorded during the research flight with Polar 6 on 20 March 2022.

et al., 2017). The available CCNs can have six orders of magnitude higher concentration than INPs (Morrison et al., 2011). The extreme ratio between liquid droplets and ice crystals is a key factor for the persistence of mixed-phase clouds and an ongoing WBF process (Kanji et al., 2017; Carslaw, 2022).

The Arctic region is mainly characterized by a marine and coastal environment, where local sources from the surface, such as sea ice or the ocean, strongly influence the aerosol concentration in the ABL (Hartmann et al., 2020; Köllner et al., 2021). However, in certain periods, especially in winter, the Arctic is dominated by a high aerosol mass concentration, a phenomenon known as Arctic haze (Rahn et al., 1977; Radke et al., 1984; Willis et al., 2018; Schmale et al., 2021). These Arctic haze conditions are not to be confused with the haze particles that are being studied in the course of this thesis. Arctic haze is mainly composed of aerosols from anthropogenic emissions transported over long distances from the mid-latitudes to the Arctic and observed at all altitudes in the troposphere (Quinn et al., 2007). The haze particles studied in this thesis consist mainly of sea salt aerosols from local marine sources and are found only at low altitudes. Many studies have investigated the aerosol composition and processes in high latitudes (e.g. Kirpes et al., 2018; Willis et al., 2018; Carlsen and David, 2022; Moschos et al., 2022; Porter et al., 2022). However, models still have difficulties simulating low-level Arctic mixed-phase clouds partly stemming from the insufficient representation of CCNs and INPs

(Schmale et al., 2021). It is well known that Arctic mixed-phase clouds are an essential contributor to the surface radiation balance (Shupe and Intrieri, 2004) and contribute to the accelerated mean temperature rise in high northern latitudes compared to other regions on Earth, however, our understanding of the physical processes in mixed-phase clouds is incomplete (Korolev et al., 2017).

3 Methods: Airborne in-situ cloud measurements

3.1 Overview: In-situ cloud instrumentation

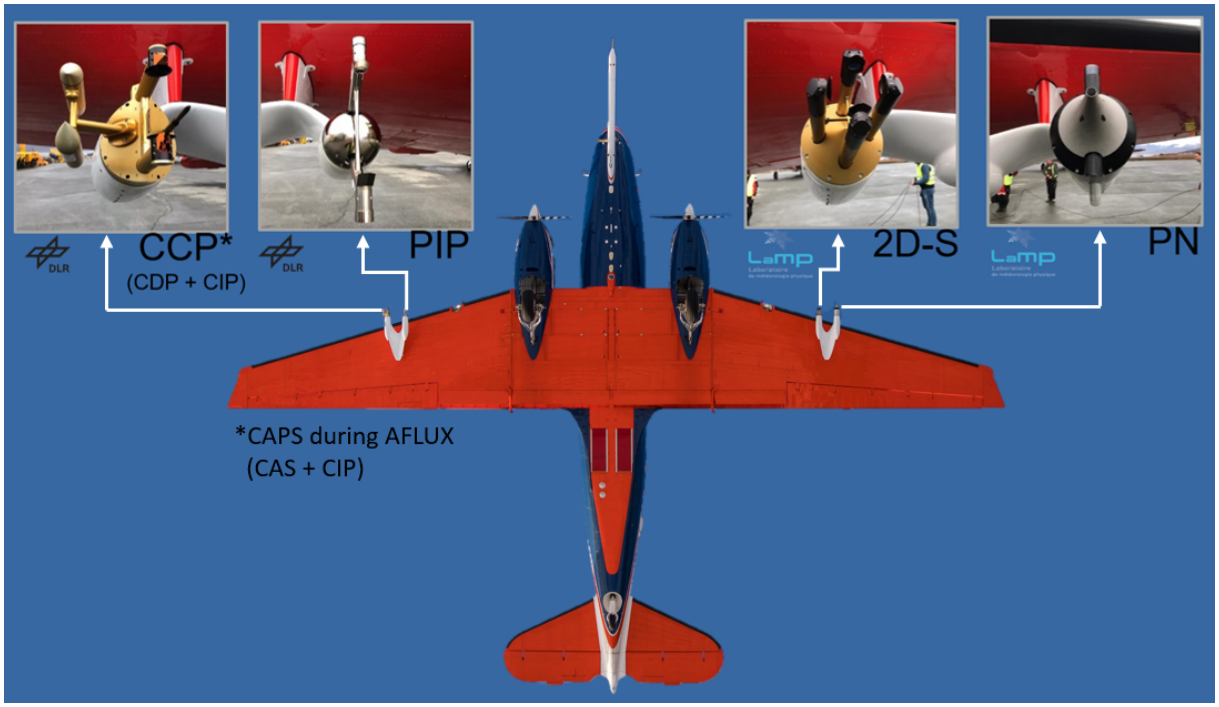

Figure 7 In-situ cloud instruments at their respective position on the research aircraft from the left to the right: Cloud Combination Probe (CCP) composed of a Cloud Droplet Probe (CDP) and Cloud Imaging Probe (CIP), Cloud Aerosol and Precipitation Spectrometer (CAPS) composed of a Cloud Aerosol Spectrometer (CAS) and a CIP, Precipitation Imaging Probe (PIP), 2D Stereo Imaging Probe (2D-S) and Polar Nephelometer (PN). Image of the research aircraft by Hanno Müller.

Many methods are available for the study of cloud microphysical properties, among which are bulk water probes, single-particle light-scattering spectrometers, and cloud-imaging probes (Wendisch and Brenguier, 2013; Baumgardner et al., 2017). The various methods offer a comprehensive insight into the small-scale structure of clouds through diverse and complementary physical approaches. To size and cover the entire cloud particle diameter range, more than one measurement technique is usually required. This work uses scattering instruments to detect cloud particles smaller than 50 µm and two-dimensional (2D) imaging techniques for larger cloud particles produced by Droplet Measurement Technologies (DMT), Longmont, CO, USA (Baumgardner et al., 2001) or by the Stratton Park Engineering Company (SPEC Inc.), Boulder, CO, USA (Lawson et al., 2006). In addition, the thermodynamic phase of the cloud can be derived from the scattering phase function measured by a polar nephelometer designed by the Laboratoire de Météorologie Physique (LaMP; Gayet et al., 1997). Figure 7 and Table 1 provide an overview of the in-situ cloud probes used during the three Arctic aircraft field cam-

paigns including the respective positions of the probes on the aircraft. All cloud probes were heated in order to avoid icing during the flights. A detailed description of each cloud instrument used in this work, including its calibration, data processing, and measurement uncertainties, is given in the following sections.

Instrument	Type	Range	Properties	Operations	Details	Manuf.	Reference
CAS, part of CAPS	Scattering instrument	0.5 - 50.0 µm	PSD, N, D_{eff}, CWC	AFLUX	See Sect. 3.2.2	DMT	Baumgardner et al. (2001)
CIP, part of CAPS	Imaging Probe	30 - 960 µm	PSD, N, D_{eff}, CWC, particle shape	AFLUX	See Sect. 3.3	DMT	Baumgardner et al. (2001)
CPD, part of CCP	Scattering instrument	2.8 - 50.0 µm	PSD, N, D_{eff}, CWC	MOSAiC-ACA, HALO-(AC)3	See Sect. 3.2.3	DMT	Lance et al. (2010)
CIP, part of CCP	Imaging Probe	30 - 960 µm	PSD, N, D_{eff}, CWC, particle shape	MOSAiC-ACA, HALO-(AC)3	See Sect. 3.3	DMT	Baumgardner et al. (2001)
PIP	Imaging Probe	200 - 6400 µm	PSD, N, D_{eff}, CWC, particle shape	AFLUX, MOSAiC-ACA, HALO-(AC)3	See Sect. 3.3	DMT	Baumgardner et al. (2001)
2D-S	Imaging Probe	20 - 1280 µm	PSD, N, D_{eff}, CWC, particle shape	AFLUX, MOSAiC-ACA, HALO-(AC)3	See Sect. 3.3	SPEC Inc.	Lawson et al. (2006)
PN	Scattering instrument	~µm to 1 mm	ASC, Ext. Coef., g	AFLUX, MOSAiC-ACA, HALO-(AC)3	See Sect. 3.2.4	LaMP	Gayet et al. (1997)

Table 1 Overview of the in-situ cloud instruments on board of research aircraft Polar 5 (for AFLUX and MOSAiC-ACA) and Polar 6 (for HALO-(AC)^3).

3.2 Scattering instruments

3.2.1 Introduction to cloud particle sizing with scattering probes

Both instruments, the Cloud Aerosol Spectrometer (CAS) and the Cloud Droplet Probe (CDP) determine the cloud particle diameter by the intensity of forward scattered laser light (e.g., Wendisch et al., 1996; Baumgardner et al., 2001; Baumgardner et al., 2011; Wendisch and Brenguier, 2013; Kleine et al., 2018; Voigt et al., 2021). The optical setup of the instruments is shown in Fig. 8. A laser with a wavelength of 658 nm is aligned perpendicular to an incoming airflow, which results from the relative speed between the aircraft and the surrounding air. If particles are present in the air, the light from the laser is scattered by the particles and captured by an optical setup in the further course of the beam. The direct beam of the laser is filtered and only the forward scattered light in an angular range from 4 ° to 12 ° is analyzed. A beam splitter distributes the scattered laser light to two photodetectors, the sizing detector which is used to derive the particle size by the intensity of the forward scattered laser light, and the qualifying detector, which is used to determine whether the incoming signal corresponds to a particle that has passed through a certain volume in the optical path of the laser or not. In contrast to the sizing detector, a pinhole aperture is set in front of the qualifying detector. The incident signals from both detectors are compared, and only data from the sizing detector is accepted if the ratio of the qualifying signal to the sizing signal exceeds a certain threshold. This is only the case when particles pass through the volume of detection. Particles that do not transit this volume, will produce a scattered signal at the qualifying detector that is too low to meet the criterion of acceptance. The volume of detection is defined by the depth of field in the direction of the optical axis (direction of the laser propagation) and by the Gaussian shape of the laser beam perpendicular to the optical axis. The projection of this volume in the direction of cloud particle incidence is called the sample area (SA). This SA is determined experimentally in the laboratory by inducing liquid water droplets or glass beads in a grid through the detection volume (Lance et al., 2010). Precise determinations of the SA have been performed in previous experimental work by Jonas Kleine[1] for the CAS and by Marcus Klingebiel[2] for the CDP. The respective areas are given in Table 2 and 4.

From the scattered laser light reaching the sizing detector of the CAS and CDP, the diameter of a liquid droplet D_{Droplets} is determined by a two-step procedure which can be summarized as follows:

$$\text{ADC}_{\text{Detector}} \xleftrightarrow[\text{Eq. 3.1}]{} \sigma_{4-12^\circ} \xleftrightarrow[\text{"Lorenz-Mie theory"}]{} D_{\text{Droplets}}.$$

[1] Conducted the laboratory work at the Institut für Physik der Atmosphäre, Deutsches Zentrum für Luft- und Raumfahrt, Wessling, Germany

[2] Conducted the laboratory work at the Institut für Physik der Atmosphäre, Johannes Gutenberg-Universität, Mainz, Germany

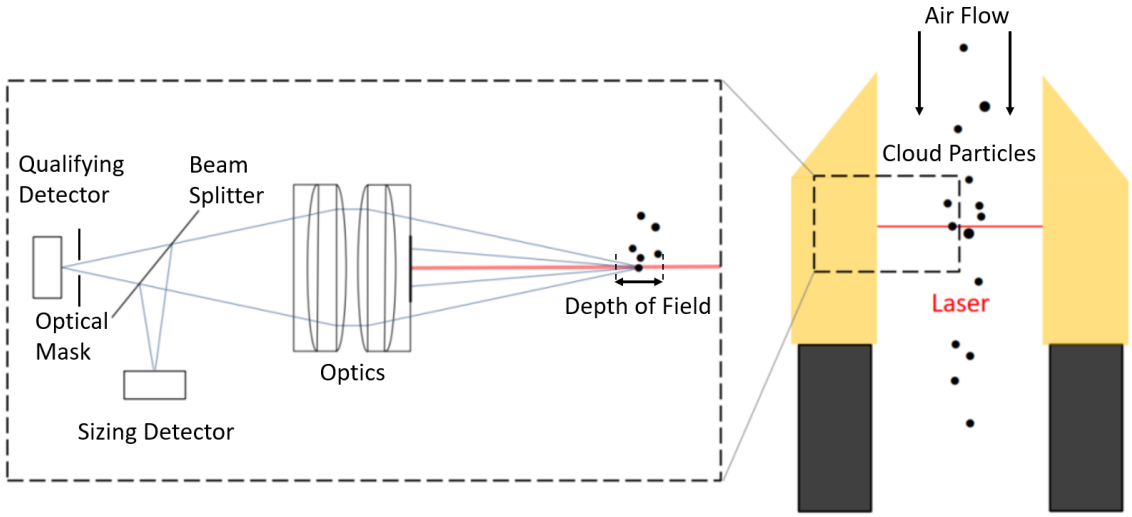

Figure 8 Theory of operation for CDP and CAS. Figure adapted from Bräuer (2022).

For each particle passing the SA, the sizing detector measures the intensity of the scattered laser light via induced photocurrent and translates these values into digital numbers by an analog-to-digital converter (ADC $\in$ 1,2,..,9216). The photocurrent is increasing linearly to the incidence of light, so the relationship between the scattering cross section integrated over the scattering angles from $4°$ to $12°$ ($\sigma_{4-12°}$) and the ADC values can be written as:

$$\sigma_{4-12°} = a \cdot \mathrm{ADC} + b. \tag{3.1}$$

Values a and b result from instrument calibrations and have to be checked on a regular basis, preferably once before, during, and after field campaigns.

The Lorenz-Mie theory provides the basis for establishing the relationship between $\sigma_{4-12°}$ and D_{Droplets}. This theory describes the scattering properties of spherical particles when the incident light, with a wavelength comparable to the particle diameters, is elastically scattered. While Rayleigh scattering applies to light scattering when the incident wavelength is significantly larger than the particle sizes ($\lambda \gg D_{\mathrm{p}}$) and geometrical optics when the wavelength is significantly smaller compared to the particle sizes ($\lambda \ll D_{\mathrm{p}}$), the Lorenz-Mie theory describes the scattering behavior in the transition region. Figure 9 shows the scattering cross sections from 4 - 12 ° for different particle diameters irradiated with monochromatic light at a wavelength $\lambda = 658$ nm. The function is calculated by assuming spherical droplets with a refractive index equal to water and no absorption (i.e. the imaginary part is zero), represented as $n = 1.333$ based on the code by Wiscombe (1980). The given function exhibits high nonlinearity, and the scattering cross section does not monotonically increase with the particle diameter. Due to the complexity of the Mie-Lorenz curve, it is non-trivial to convert the scattering signal or ADC value to a distinct particle diameter. By dedicating the particle diameters to selected size bins, these Mie-ambiguities can be avoided.

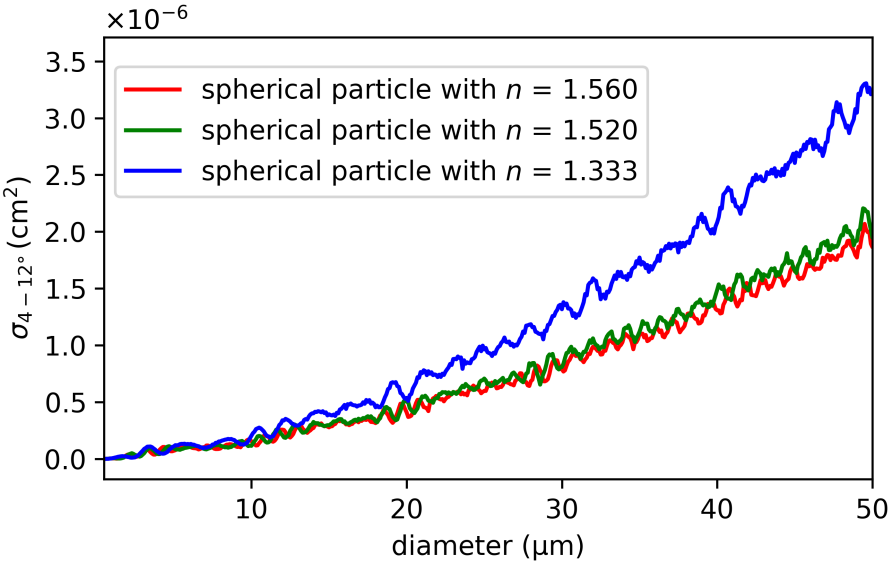

Figure 9 Theoretically calculated Lorenz-Mie curve showing the scattering cross sections for liquid water droplets ($n = 1.333$), spheres made of borosilicate glass ($n = 1.560$), and spheres made of soda-lime glass ($n = 1.520$) with parameters representing the measurement technique of the CDP and CAS. The curve is calculated using the Mie Scattering Conversion Table Generator (MieConScat) Version 1.1.8 provided by Phil Rosenberg (Rosenberg et al., 2012).

The Particle Analysis and Display System (PADS) by DMT is a LabVIEW Software that is the default interface system to communicate and store the data of the CDP (CAS). The particle by particle (PBP) file contains the exact ADC-value of each particle crossing, however only the first 256 (292) particles per second (millisecond) due to a limitation of the maximum data stream. All particles with no data loss are stored in a bulk file, where the ADC values are categorized into one of 30 size bins and stored in 1Hz frequency. The size edges of the histogram are set previously for each campaign so that Mie-ambiguities are avoided. With this method, the size of the individual particles passing through the instrument is measured. However, to determine an absolute number concentration, it is essential to know the volume in which these particles were detected. This sampling volume (SV) is composed of the sampling area mentioned above and the length that this area traverses in the direction of flight during one measurement period:

$$\mathrm{SV} = t_\mathrm{s} \times \mathrm{TAS} \times \mathrm{SA} \tag{3.2}$$

with t_s as the length of the sampling time (set to 1 s), TAS as the true airspeed, and SA as the sampling area of the scattering instrument quantified in the laboratory. By dividing the number of particles n_i detected in an arbitrary size bin i within the sampling time t_s by the sampling volume (SV), the particle number concentration N_i in the size bin i is obtained according to:

$$N_\mathrm{i} = \frac{n_\mathrm{i}(t_\mathrm{s})}{\mathrm{SV}(t_\mathrm{s})}. \tag{3.3}$$

From N_{i} several microphysical cloud properties can be derived, including the particle size distribution (PSD), the total cloud particle number concentration (N), effective diameter (D_{eff}), and other relevant properties. These calculations are discussed in Sect. 3.4.2.

Previous studies have shown that ice crystals can break up at the inlets of the in-situ cloud instruments, resulting in many individual small particles being measured instead of a single larger cloud particle. McFarquhar et al. (2007b) and Korolev et al. (2013b) have shown the significance of such shattering events on the measurement of microphysical cloud parameters in pure ice clouds. Shattering events can be detected and corrected by analyzing the inter-particle arrival time (IPT) of the cloud particles (similar as for the CIP and PIP, see *Cloud particle shattering* in Sect. 3.3.1.2). In this thesis, no cirrus clouds with high ice number concentrations are investigated, but low-level clouds in which the number concentration of small particles is dominated by droplets. Due to the relatively low number concentration of ice crystals compared to cirrus clouds, little shattering is expected here. Many cloud situations investigated here are in a mixed-phase state. Shattering correction in such clouds is not possible as the shattering mode in the IPT analysis is dominated by the liquid droplets (Field et al., 2006; Korolev et al., 2017). However, the inlets of all cloud instruments are designed to minimize shattering (Korolev et al., 2013a). In the Appendix A, IPT analyses measured by the CAS and CDP in different cloud situations are discussed. It is shown that no shattering correction is required for the particles measured with the scattering probes in Arctic low-level clouds.

The two instruments, CAS and CDP, differ in shape and data processing of the detector signals. For both instruments, a separate size binning must be defined before every operation during a field campaign, and the relationship between detector signal and particle sizes is calibrated to ensure high data quality. The instrument calibration, size binning, and data processing for the respective measurement campaigns will be discussed individually in the following.

3.2.2 Characterization of the Cloud Aerosol Spectrometer

The Cloud Aerosol Spectrometer (CAS) was used to measure cloud particles with diameters smaller than 50 µm during the AFLUX field campaign. The CAS is part of a larger instrument, the Cloud Aerosol Precipitation Spectrometer (CAPS; Baumgardner et al., 2001) manufactured by Droplet Measurement Technologies (DMT). The instrument is owned by the British Antarctic Survey (BAS) and was operated on loan by the Deutsches Zentrum für Luft- und Raumfahrt (DLR) from 2016 to 2019. The optical setup is similar to Fig. 8, but with the difference that the air does not flow through two arms but is directed through a single tube (see the tube inlet of the CAS in Fig. 10). Furthermore, the CAS consists of a second optical setup, measuring the scattered light in backward direction from 168 ° to 176 °. The backward scattered light contains information that could be used to analyze the shape and phase of the measured particles

(Baumgardner et al., 2014; Costa et al., 2017). However, to reduce the currently large uncertainties, this method requires more research. In this thesis, the backscattered signal recorded by the CAPS is not considered in the data analysis and is not mentioned further.

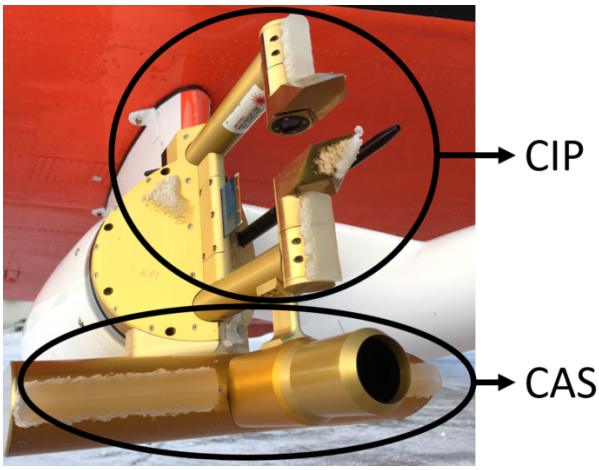

Figure 10 The CAPS and its sub-instruments CAS and CIP mounted on the Polar 5 aircraft. Picture taken after research flight RF03 (AFLUX, 21 March 2019).

Sampling area	Size binning for AFLUX
0.30 mm^2	See Table 11 in Appendix B. For processing the 1 Hz file is used.

Table 2 Parameterization for the processing of the CAS data from AFLUX. Sampling area from Kleine (2019).

An additional difference from the CDP is, that the CAS is designed to have not one, but three amplification stages, that amplify the detector signal output, with the highest amplification for small particles and the lowest amplification for large particles. Therefore, the values a and b in Eq. 3.1 must be determined for each of the three size ranges: The high gain stage (HGS), the mid gain stage (MGS) and the low gain stage (LGS), which are given in Table 3. These linear regression values are provided by a precise characterization and calibration of the CAS by Kleine (2019).

Both the laser and the detectors of the probe are components with a limited lifetime. It can be assumed that the light intensity and detector efficiency will continuously deteriorate during the lifetime of the probe as well as misaligned of the laser beam might result from transportation and vibrations during operations. In order to prevent erroneous size determination and to ensure optimal functioning of the instrument, it is necessary to check the constants a and b on a regular basis. During AFLUX, this calibration was performed in Longyearbyen right after

Gain stage	a (cm^2)	b (cm^2)	
HGS	$4.572 \cdot 10^{-12}$	$-4.305 \cdot 10^{-10}$	ADC $\in \{191, 192, ..., 3072\}$
MGS	$4.571 \cdot 10^{-11}$	$-1.331 \cdot 10^{-7}$	ADC $\in \{3210, 3211, ..., 6144\}$
LGS	$1.205 \cdot 10^{-9}$	$-7.37 \cdot 10^{-6}$	ADC $\in \{6239, 6240, ..., 9216\}$

Table 3 Calibration values a and b for the three gain stages of the CAS. Values from Kleine (2019).

the integration of the instruments on the research aircraft Polar 5 (20 March 2019), once at mid-campaign (31 March 2019), and after the last research flight (12 April 2019). The standard calibration method by Rosenberg et al. (2012) is applied, using mono-disperse glass beads made out of borosilicate glass for particle sizes smaller 25 µm, and soda-lime glass beads simulating larger particles. The resulting ADC values for the respective size calibration are determined by a Gaussian fit to the ADC values given in the CAS PBP file and the corresponding scattering cross section for the particle size is converted by the Lorenz-Mie curve (see Lorenz-Mie curves in Fig. 9).

The calibration line of the MGS and LGS including all calibration points collected during AFLUX are shown in Fig. 11. The HGS is not shown here, as no calibration has been conducted in this size regime, as well in further analyses only particles from the mid gain and high gain stages are considered. The majority of the calibration points hardly deviate from the regression line, which is why the settings of Kleine (2019) are used.
Once the linear relationship between the ADC values and σ_{4-12° is established, the diameter of particles is determined based on the Mie curve of liquid water droplets. To obtain the data with the highest statistical properties, for further data evaluation the bulk file with the original ADC binning (given by the manufacturer) is used. The Mie water curve together with the CAS binning is shown in Fig. 12. Due to the shape of the Mie curve, the conversion from σ_{4-12° to D_{Droplets} is not unique and a final binning is selected by combining certain bins in order to avoid the given ambiguities. The blue dots in Fig. 12 indicate the positions where the gain stages overlap. To prevent double counting of particles, this bin must be omitted for further calculations. The final binning and the exact position of the gain stage overlaps are given in Table 11 in Appendix B.

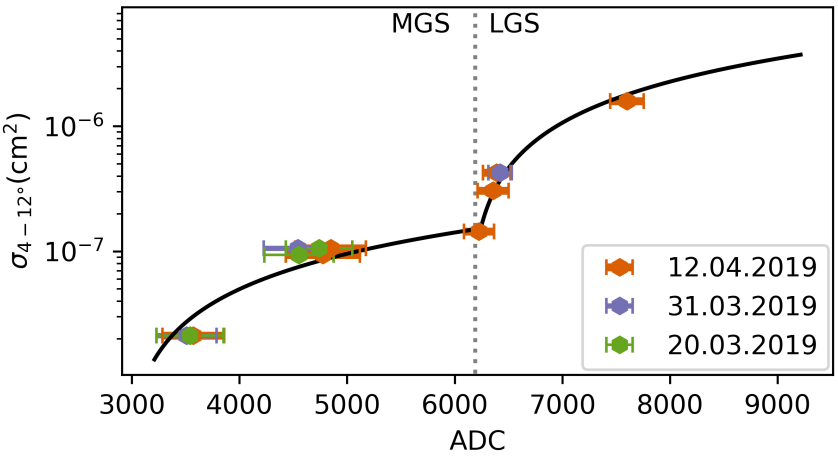

Figure 11 The calculated scattering cross sections for the calibration glass beads plotted against the experimentally determined ADC values of the corresponding mean of the peak. The colors indicate the different days of calibration. The error bars result from the width of the Gaussian distribution fitted to the ADC peaks. Black lines show the linear relationship for the gain stages (MGS, LGS) with the values from Table 3.

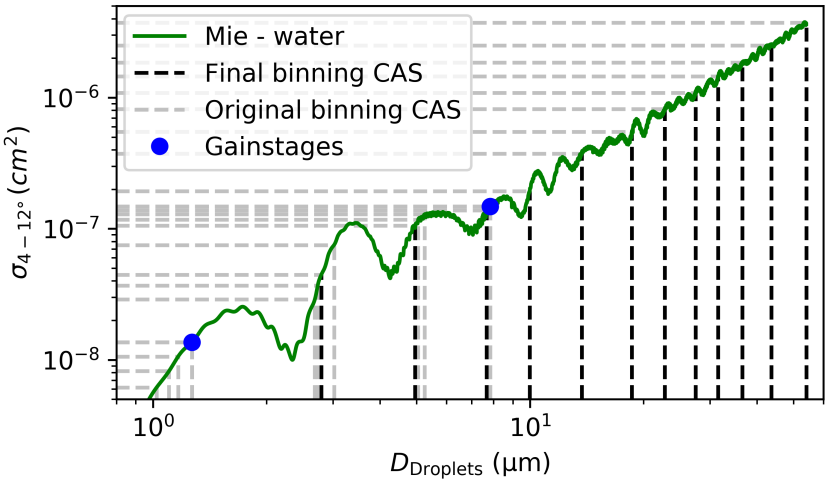

Figure 12 Mie scattering cross sections $\sigma_{4-12°}$ calculated for water (green) including CAS original bin settings (gray) and gain stage overlaps (blue). Black lines indicate the binning used for further data analyses.

3.2.3 Characterization of the Cloud Droplet Probe

For cloud particle sizing of particles smaller 50 µm, the CDP was used during the MOSAiC-ACA and HALO-(AC)^3 campaign. The CDP is a sub-instrument of the CCP shown in Fig. 13. During both campaigns, the settings of the size bin edges varied slightly. The variations and the applied size binning are explained in more detail in the following for both campaigns separately.

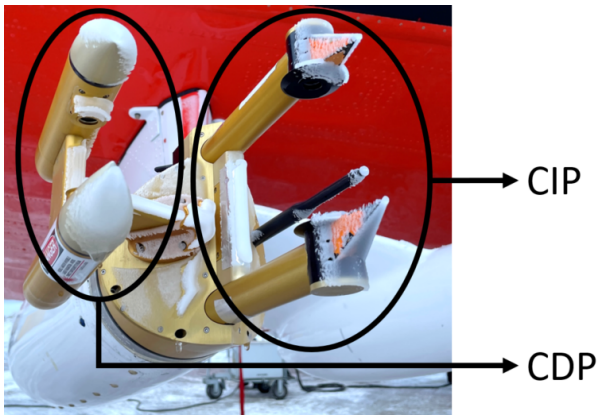

Figure 13 The Cloud Combination Probe (CCP) and its sub-instruments Cloud Droplet Probe (CDP) and Cloud Imaging Probe (CIP) mounted on the Polar 6 aircraft. Picture taken after research flight on 20 March 2022 during HALO-(AC)^3. Some icing occurred before landing.

Sampling area	Size binning for MOSAiC-ACA	Size binning for HALO-(AC)^3
0.27 mm^2	See Table 12 in Appendix B. For processing a hybrid version of the 1 Hz file and the PBP file is used	See Table 13 in Appendix B. For processing the 1 Hz file is used

Table 4 Parameterization for the processing of the CDP data for MOSAiC-ACA and HALO-(AC)^3. The sampling area is from Klingebiel et al. (2015).

The Cloud Droplet Probe during MOSAiC-ACA: During MOSAiC-ACA the bulk data were recorded with an original binning given by the manufacturer. However from laboratory work by Lucke (2024) a new binning assuming liquid droplets was suggested for the MOSAiC-ACA data processing. These proposed CDP settings were checked using the calibration data collected before the campaign in Bremen (14 February 2020), at the beginning (29 August 2020), and at the end of the campaign (14 September 2020) in Longyearbyen. Figure 14 shows all calibration points in combination with the CDP settings used for further data processing.

The same calibration procedure using glass beads as described in Sect. 3.2.2 is applied. The data in Fig. 14 indicate that the settings used for data processing match the calibration data well, so no further corrections are needed. Since the binning, set during the campaign, is different from what is used for further processing, the bulk file cannot only be used. Droplets smaller than 30 µm are sized by the use of the PBP file, and for statistical reasons droplets larger than 30 µm are extracted from the bulk file. This is done as the PBP file only counts a limited amount of particles per second (256) and for larger particles, the statistic might not be high enough to recalculate the total counts in the corresponding size bins. The binning used for CDP data evaluation for the MOSAiC-ACA campaign is given in Table 12 in Appendix B.

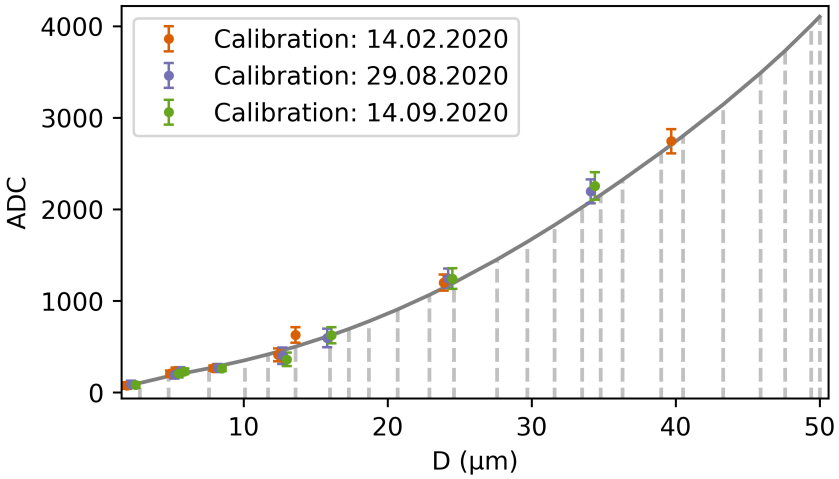

Figure 14 The binning used for particle sizing with the CDP during the MOSAiC-ACA campaign (gray). The calibrations performed with glass beads confirm the binning taken with the CAS.

The Cloud Droplet Probe during HALO-(AC)^3: For the measurements with the CDP during the HALO-(AC)^3 field campaign, a binning adapted to liquid droplets has been set previous to the campaign. The full binning is given in Table 13 in the Appendix. This binning was confirmed by a glass bead calibration (see Sect. 3.2.2) in the cloud laboratory in Oberpfaffenhofen (07 December 2021), as well as during the campaign in Longyearbyen (07 April 2022). Figure 15 shows the calibration data together with the predefined binning of the CDP. A favorable agreement is observed, and the bulk file is used for subsequent data analysis.

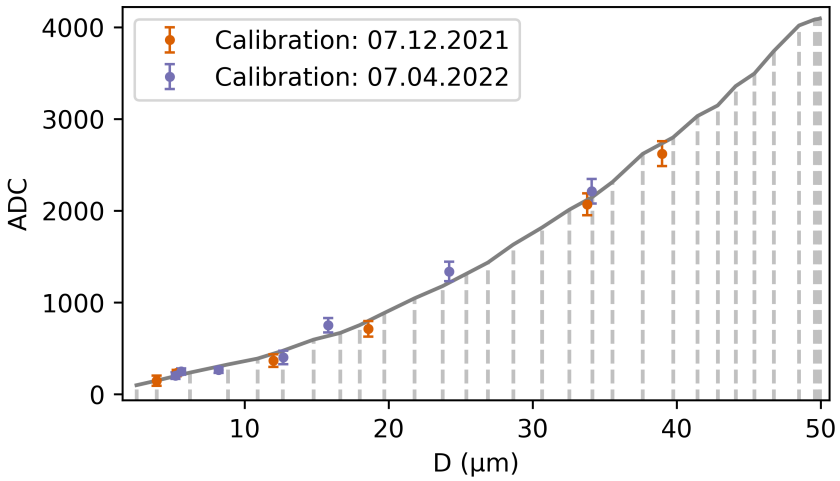

Figure 15 The binning used for particle sizing with the CDP during the HALO-(AC)^3 campaign (gray). The glass bead calibrations confirm the setting of the CDP.

3.2.4 The Polar Nephelometer

Parts of this subsection are published on page 7262 in Moser et al. (2023).
The Polar Nephelometer is designed by Laboratoire de Météorologie Physique (LaMP), France (Gayet et al., 1997). The instrument provides a direct measurement of the non-normalized scattering phase function (i.e. angular scattering coefficient, ASC) of a volume of cloud particles crossing a collimated laser beam with a wavelength of 0.8 µm near the focal point of a parabolic mirror. The light scattered by water droplets, ice crystals, or a mixture of both is recorded by a circular array of photodiodes (channels). Hence, the angular scattering pattern of cloud particles with a diameter from a few micrometers to one millimeter can be obtained for scattering angles ranging from ±15 to ±162° and with an angular resolution of 3.5°. Measurement errors are between 3 to 5% for scattering angles ranging from 15 to 155° with a maximum of 20% at 162° (Shcherbakov et al., 2006). Averaged values of the calibrated ASCs were computed at a 1 Hz frequency and synchronized with the data recorded on the aircraft system. Electronic offsets of each channel were estimated and subtracted, based on the signal measured during clear air sequences. Extinction coefficient (Ext. Coef.) and asymmetry parameter g can be derived from the ASC measurements (Gerber et al., 2000; Gayet et al., 2002, 2012) with uncertainties of ~25% and ±0.04, respectively. Jourdan et al. (2003, 2010) showed that the combination of these parameters can be used to discriminate spherical from non-spherical cloud particles, as well as the dominant cloud thermodynamic phase. Section 4.5 demonstrates the utilization of PN data for thermodynamic phase discrimination of Arctic clouds. The PN data used for further analyses is processed and provided by LaMP.

3.3 Optical Array Probes

Optical Array Probes (OAPs), which are imaging probes introduced by Knollenberg (1970), have been used for airborne in-situ measurements of cloud and precipitating particles over the past few decades. The basic measurement of a OAP is shadowgraphy of water and ice particles. The main advantage of OAPs in comparison to scattering probes is that in addition to measuring the size and concentration of cloud particles, OAPs take two dimensional images of each particle passing through the sampling area. Therefore, a more precise evaluation of atmospheric cloud particles is possible which is essential for a better understanding of cloud microphysical processes. The general optical setup for all OAPs is similar, a laser aligned between two arms through which cloud particles pass. However, there are differences in resolution and sampling volume between different OAPs depending on their experimental purpose.

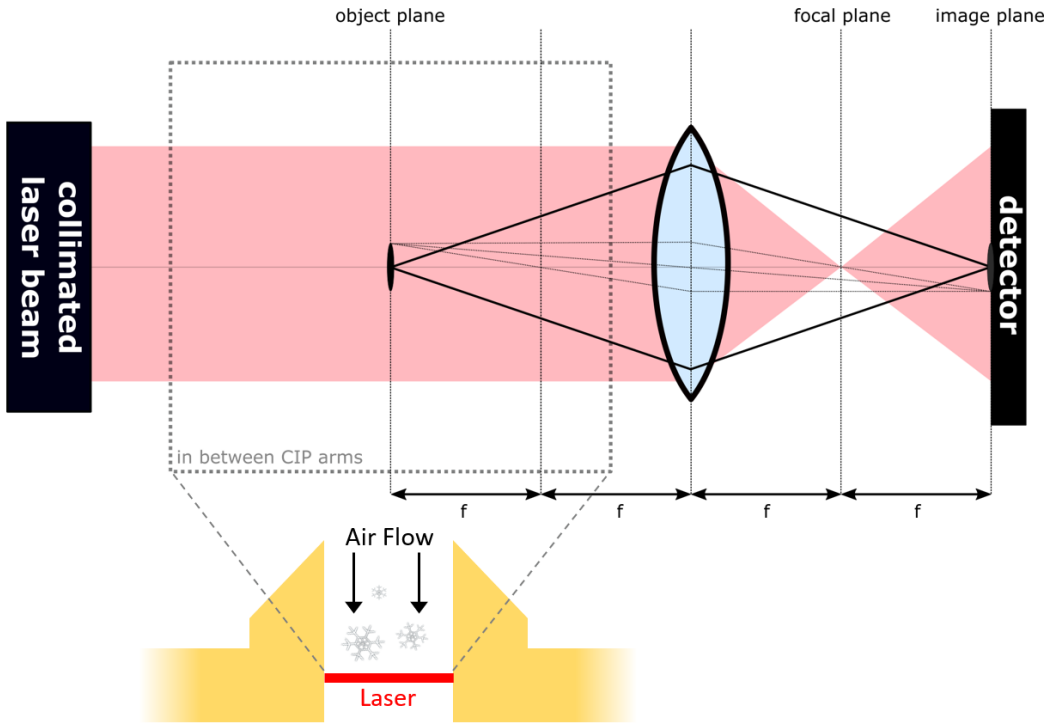

Figure 16 The optical setup of an OAP. Figure taken from Moser (2018).

The optical setup is shown in Fig. 16. A collimated laser beam is guided through a window in one arm to the sampling zone between the arms and re-enters the instrument through a window in the second arm. Particles passing through the laser beam create a shadow. A lens behind the second window focuses the collimated light beam onto the focal plane at a distance f behind the lens and a detector is placed at a distance of $2 \times f$. This arrangement creates an object plane between the arms and the shadows that are produced by particles passing near this plane are projected onto the image plane at the detector. Between the lens and the detector, a setup for optical magnification is installed. The detector itself is a line of PIN (positive-intrinsic-negative)

photodiodes aligned perpendicular to the projected airflow. As a particle passes near the object plane, its image is reconstructed from a series of adjacent slices. Each slice contains the state of the detected light intensities recorded by the photodiode array at a given moment in time. A slice must be stored each time when the particle passes through the laser beam at a distance equal to the resolution of the instrument. In simple terms, this method is similar to a scanner that produces images of the particle's shadow. The sampling frequency f_s at which the slices must be read is calculated as

$$f_\mathrm{s} = \frac{\mathrm{TAS}}{\alpha'} \tag{3.4}$$

with TAS the true air speed (in Fig. 16 the speed of the air flow) and α' the resolution of the OAP. An example of 2D cloud particle shadow images captured in this way is shown in Fig. 17.

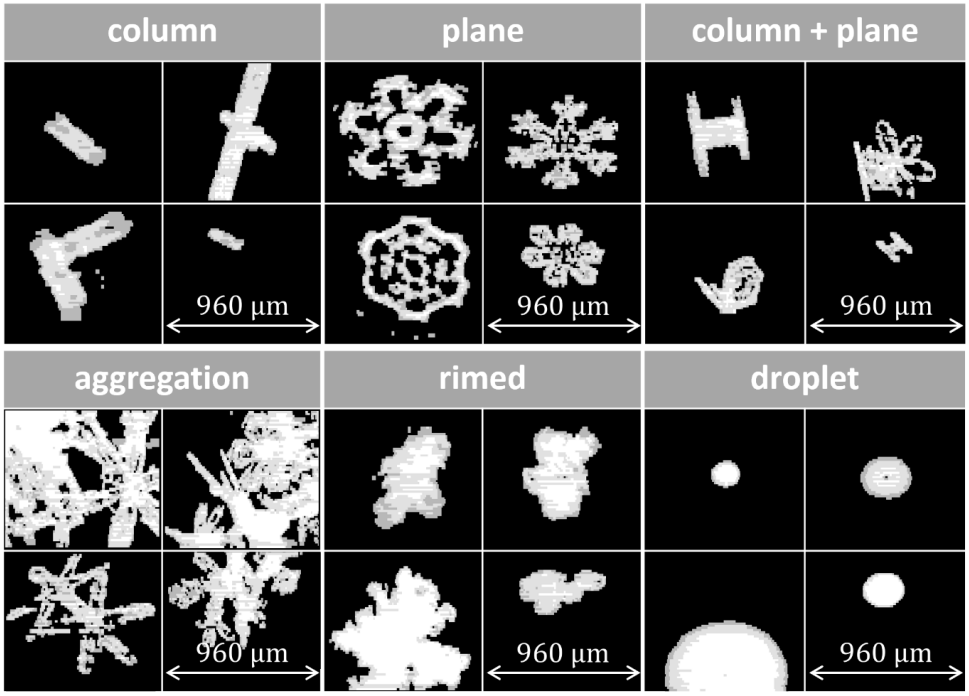

Figure 17 Example of 2D shadow images recorded by the CIP during the Arctic field campaigns. Grayscale is inverted, white indicates full shading and black no shading. Snow and ice crystal classification followed by Kikuchi et al. (2013) including the groups *column crystals*, *plane crystals*, *combination of column and plane crystals*, *aggregation of snow crystals* and *rimed snow crystals*. Additionally example images of *droplets* are shown.

The incoming laser light must be shaded above a certain threshold for a photodiode to give a signal and thus detect a shadow. Commonly OAPs are set to 50% of shading. However, some imaging probes can detect and store three different values at the same time. Such probes are called grayscale imaging probes. The further away from the object plane a particle passes the arms, the more blurred the image of the shadow on the detector becomes. At a certain distance from the object plane, the shadow of such a particle will no longer exceed the shadow threshold and will not be detected. How blurry the shadow image becomes away from the object plane

depends strongly on the size of the particles. Therefore, a depth of field (DOF) must be calculated for each particle size to determine the sample volume and particle concentration. In the following chapter, the handling of OAP data is described in more detail, as well as other aspects to consider when processing microphysical cloud properties. Subsequently, the OAP used for the analyses of the low-level clouds during the Arctic field campaigns is further characterized.

3.3.1 Processing of Optical Array Probe data

During the three Arctic aircraft field campaigns, OAPs from two different manufacturers were installed under the wings of the research aircraft (see the cloud instrumentation overview in Fig. 7). The CIP and PIP from DMT and the 2D-S from SPEC Inc.. The optical setup as described in the previous section is similar for both manufacturers, however the recording and processing of the cloud data differs. The 2D-S belongs to the French Institute Laboratoire de Météorologie Physique (LaMP) that was responsible for its operation and data processing. For further information about the 2D-S, the method for 2D-S data analysis, and the code used to process the data please refer to Lawson et al. (2006), Leroy et al. (2017), and Mech et al. (2022). The 2D-S data used in this thesis are accessible via the Open Access library PANGAEA (Dupuy et al., 2022a; Dupuy et al., 2022b).

How the data of the CIP and PIP from DMT is recorded and processed is illustrated in Fig. 18. Data from the instruments is transmitted via two RS422 data streams to a computer inside the cabin. For the one-dimensional (1D) sizing data an internal processor monitors the transition of particles and uses the maximum width in the direction of the array to determine the size of the particle. The processor stores the cumulative number of particles, the number of particles counted within each respective size bin, and the number of particles rejected due to touching the edge of the photodiode array within a sampling period, usually set to one second. This data is then decoded and displayed live by DMT's LabVIEW-based Particle Analysis and Display System (PADS) software. PADS is also used to communicate with the probe to change the settings if necessary. The second data stream contains the 2D image data, which are the raw shadow images recorded by the OAP. This data also includes the exact time when a particle enters the sampling volume and a particle counter that is incremented with each new particle detected. Whenever the data fills a 4096-byte buffer, it is sent to the computer, and PADS stores the entire data to disk while displaying selected 2D images live. In the PADS system, a sampling frequency is set that corresponds to a TAS of $120\,\mathrm{m\,s^{-1}}$, which is a speed that the aircraft never exceeds when sampling in low-level clouds. As a result, the 2D images are stretched in length in flight direction. This has the advantage that the details of the particle shapes are not lost compared to the compression that would occur when the TAS is set below the speed of the aircraft. An alternative method could be to use a pitot tube integrated into the instrument as a real-time TAS reference. However, this runs the risk of the tube icing up and the applied TAS

dropping to zero, resulting in data loss. Using a constant value above the actual speed of the aircraft ensures continuous data recording without any loss of information. The stretched image data have to be corrected later.

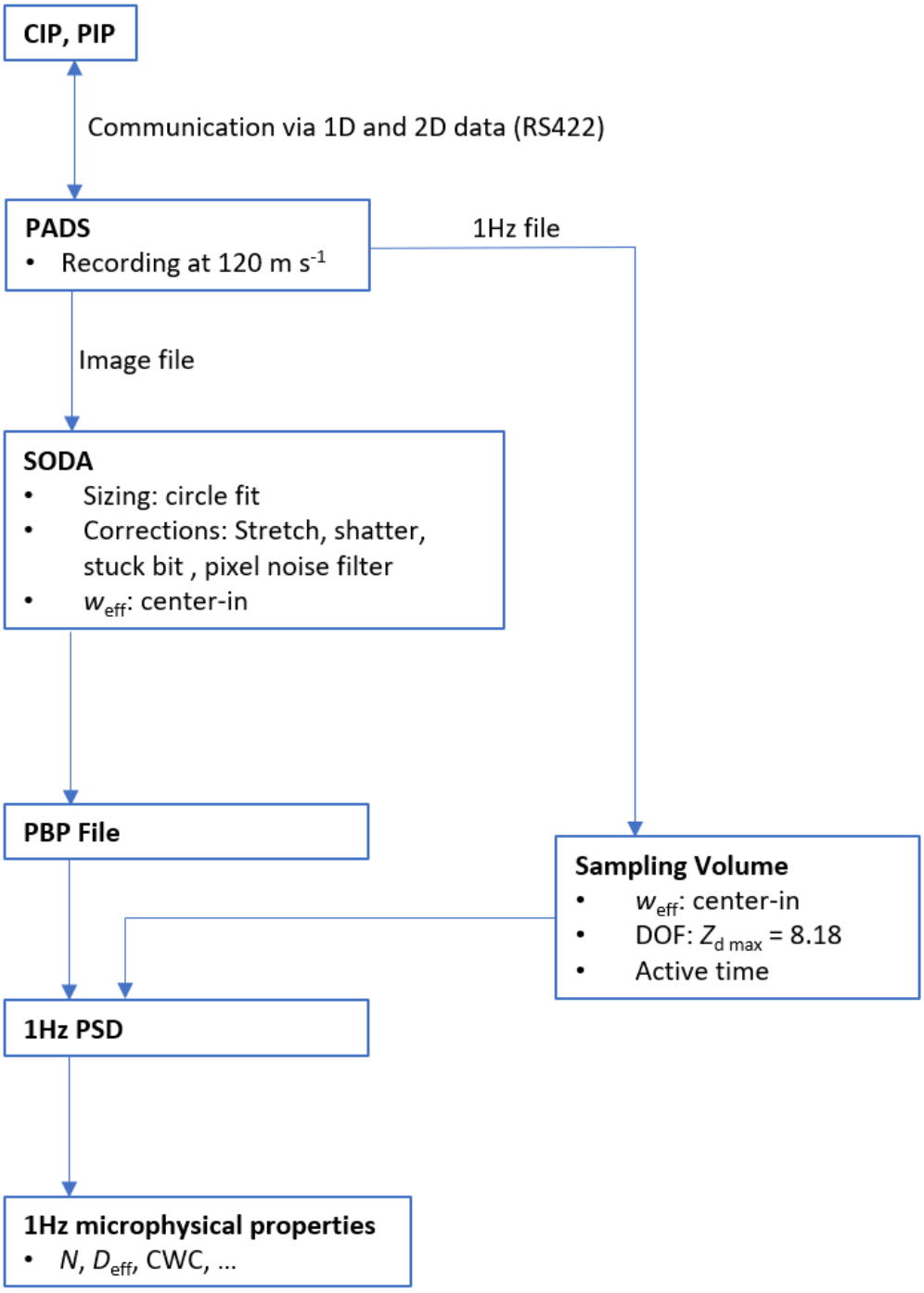

Figure 18 Overview: Processing of OAP data.

PADS generates a 1 Hz file including the information from the 1D data stream, and an image file containing the raw data from the 2D shadow images. This image file is used for further data processing with SODA (Software for OAP Data Analysis; Bansemer, 2023). In SODA, the particle images are compressed in flight direction according to the difference between 120 m s^{-1} and the actual aircraft speed with respect to the surrounding air, which is measured by the nose boom. The size of the particles is calculated using the so-called circle-fit method, which is the diameter of the smallest enclosing circle of the projected 2D image (see Fig. 24). In addition, further corrections are applied, such as the shatter correction to filter burst particles, the stuck bit correction and pixel noise filters to remove artifacts from faulty pixels. In the SODA data processing the method "center-in" is used for the effective array width. This means only particles whose center is within the generated 2D image are considered and, if required, reconstructed for only partially cloud particles captured by the photodiode array. In this way, each particle is assigned a diameter size, together with a flag if rejected or accepted by the given processing criteria. The obtained data including the size and a rejection flag is stored for the individual particles in the so-called "particle-by-particle" file.

In order to derive the microphysical cloud properties from this file, SODA could be further used. However, SODA is limited to the settings and advanced corrections that need to be applied here to ensure a high level of quality in the cloud data. In some cloud situations, the SODA processing may even fail completely. Consequently, a separate Phython script was developed within the scope of this thesis for further data processing using the "particle-by-particle" file.
In the next step, a script assigns the particles to their respective size bin and integrates the number of counts in one size bin over the sample time. The number of bins results from the number of pixels, in the case of DMT probes 64, and the particle size assigned to the corresponding bin depends on the resolution of the instrument (CIP: 15 µm, PIP: 100 µm). To calculate the particle concentration for the respective size bins, the particles counted in the certain size bin during a given sample time have to be divided by the sampling volume of the size bin (SV_i):

$$N_\mathrm{i} = \frac{n_\mathrm{i}(t_\mathrm{s})}{\mathrm{SV_i}(t_\mathrm{s})}. \tag{3.5}$$

Unlike the concentration calculation for the scattering probes (see Eq. 3.3), here the SV depends on the size of the particles. For the sake of simplicity, the index i is omitted from SV_i in the following. The volume, to be calculated for every size bin individually is defined as:

$$\mathrm{SV} = w_\mathrm{eff} \times \mathrm{DOF} \times (\mathrm{TAS} \times t_\mathrm{a}) \tag{3.6}$$

with the effective array width w_eff defining the SV in the direction of the photodiode array, DOF in the direction of the laser beam, and TAS $\times$ t_a in flight direction. The t_a is the corrected sampling time during which the instrument is active to detect cloud particles. The sampling volume is schematically depicted in Fig. 19.

With the retrieved particle size distribution in 1Hz resolution by combining the particle counts and the respective SV further microphysical cloud properties such as the total cloud particle number concentration (N), effective diameter (D_{eff}), or the cloud water content (CWC) are derived. More details on the calculation of these cloud parameters are described in Sect. 3.4.2.
The following sections 3.3.1.1 and 3.3.1.2 describe in more detail the processing methods mentioned, including the effective array width, depth of field, and particle sizing, as well as the correction methods mentioned, such as cloud particle shattering and active time correction.

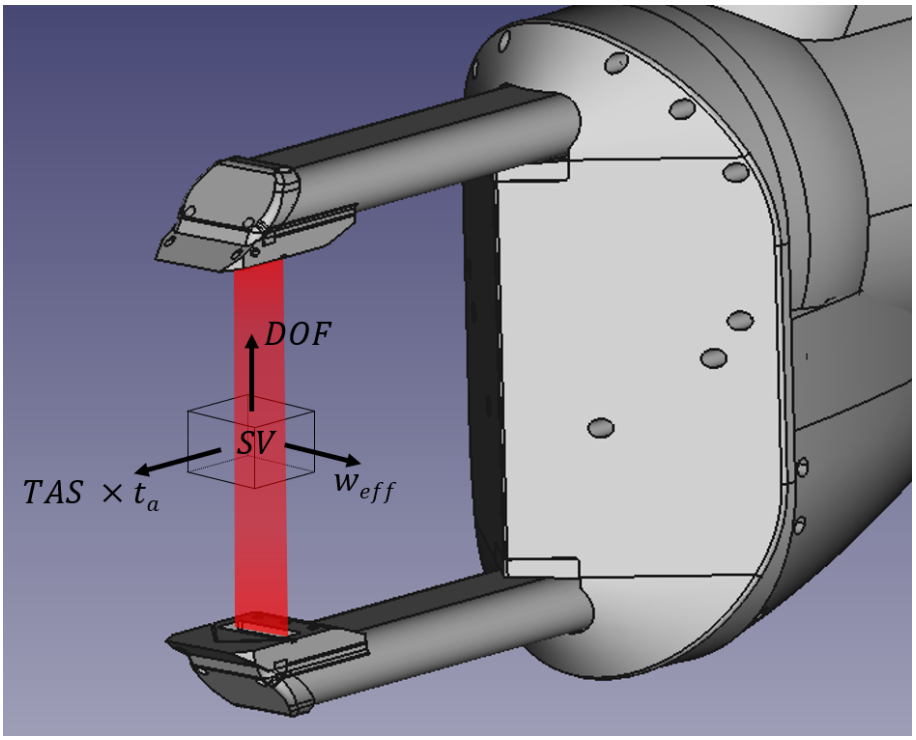

Figure 19 Schematic diagram of the sampling volume SV of an OAP. Three-dimensional model of a High Volume Precipitation Spectrometer (HVPS) provided by SPEC Inc..

3.3.1.1 Methods of processing

Effective array width: One of the three dimensions defining the SV in Eq. 3.6 is given by w_{eff}, which is pointing in the direction the photodiode array is oriented (see Fig. 19). The simplest method is the "all-in" method, which takes into account only particles that have flown entirely within the width of the photodiode array, i.e., not shadowing any edge diodes. With this "all-in" method, the w_{eff} depends on the size of the particle and becomes smaller for larger particles:

$$w_{\text{eff}} = \alpha' \times (k-1) - D_{\text{y}} \tag{3.7}$$

where k is the number of detector elements and D_{y} is the particle diameter measured in the direction of the array width. However, this method has a significant disadvantage for larger particles, as they are inherently less abundant than smaller ones, and the sample volume is reduced due to the reduction in w_{eff}. Thus, there is a limitation in the ability to statistically detect particle sizes approaching the diameter of the array width.

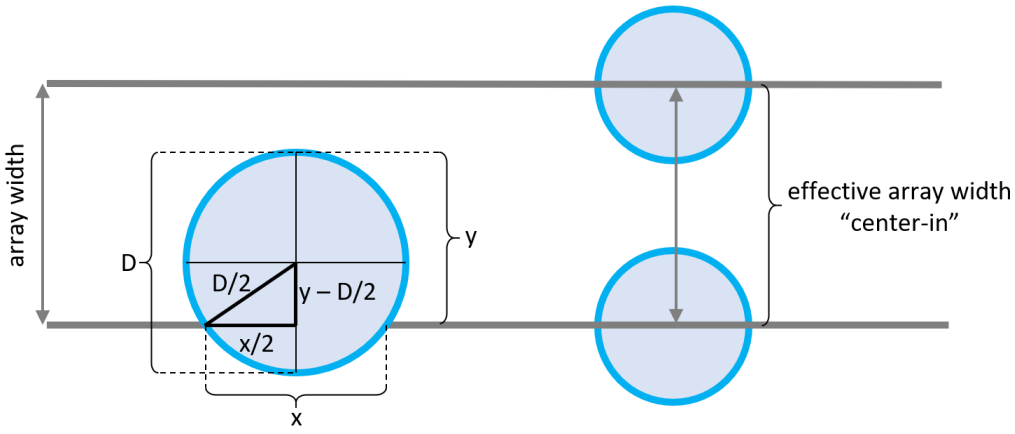

Figure 20 Method used to reconstruct the size of a partially captured cloud particle (left). By reconstructing the cloud particles, the "center-in" method for the effective array width can be applied (right).

A method in which the w_{eff} remains independent of the particle's diameter is the "center-in" method introduced by Heymsfield and Parrish (1978). Here, all particles are considered for further processing if their center is within the array width (see Fig. 20). The following condition must be met: $x < 2y$, with y the detected particle size in the array direction and x the length of the obscured end diode in flight direction. With the Pythagorean theorem, the following relationship applies:

$$\left(\frac{D}{2}\right)^2 = \left(y - \frac{D}{2}\right)^2 + \left(\frac{x}{2}\right)^2. \tag{3.8}$$

The particle diameter is then given by:

$$D = \frac{\left(\frac{x}{2}\right)^2 + y^2}{y} \tag{3.9}$$

with the reconstruction of the particles whose center is within the width of the array, the w_{eff} is now calculated:

$$w_{\text{eff}} = \alpha' \times k. \tag{3.10}$$

This effective array width method including the reconstruction of partially imaged particles may fail for asymmetric cloud particles such as needles or long columns. However, for particles observed predominantly in low-level Arctic clouds, such as raindrops, rimed particles, plates, and dendrites, this method performs reliably (Heymsfield and Parrish, 1978).

The depth of field: The depth of field (DOF) defines the extension of the SV in the direction of the laser beam (see Fig. 19), and is limited by how far away from the object plane individual particles can be detected. Only the shadow of particles that pass exactly through the object plane (see the optical setup in Fig. 16) are perfectly imaged by the OAPs. The larger the distance between the trajectory of the particle and the object plane, the more the shadow image becomes blurred. As well, the size of a particle has an influence on how blurred the image gets when not passing the object plane. From the Fresnel–Kirchhoff theory of diffraction, a dimensionless variable Z_{d} can be derived which represents the diffraction images of an opaque disk, that produces the same shadow as a spherical particle, described by Korolev et al. (1998):

$$Z_{\text{d}} = \frac{\lambda \times \mid Z \mid}{R^2} \tag{3.11}$$

where λ is the wavelength of the laser, $\mid Z \mid$ is the absolute distance to the object plane, and R is the radius of the particle. From this equation, it follows, that two droplets with different diameters will give the same diffraction image if $\mid Z_1 \mid / \mid Z_2 \mid = R_1^2/R_2^2$. The diffraction image is also independent of the sign of Z, i.e. the diffraction image of a droplet at the same distance will be the same on opposite sides of the object plane. An example of such diffraction images is shown in Fig. 21. The more blurred an image becomes with increasing Z, the higher the value of the minimum light intensity in the image. The intensity level is defined as the ratio I/I_0 where I is the light intensity level at a certain point in the shadow image and I_0 the intensity of the incident laser light (i.e. a level of 100% is unshadowed and 0% is completely dark). Figure 22 shows the theoretical minimum light intensity that can be found within particle shadow image at a certain maximum distance from the object plane, here given in the dimensionless variable $Z_{\text{d max}}$. OAP instruments are typically set to an intensity threshold of 50%, which means that data is only recorded and processed when a photodiode is shaded by at least half of the laser light intensity. From Fig. 22 results, theoretically only particles with diffraction values $Z_{\text{d}} \leq 8.18$ can be detected by the instruments.

The first experimental determination of the $Z_{\text{d max}}$ value has been done by Knollenberg (1970), where he found that the size measurements using a 50% threshold level are accurate to within $\pm 10\%$ for a $Z_{\text{d max}}$ value of 3.0. This value used to be standard for the processing of cloud data

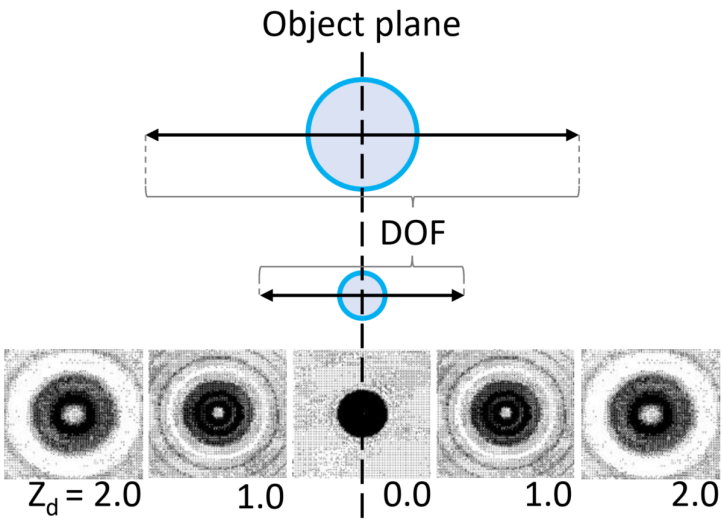

Figure 21 Larger particles have a wider DOF compared to smaller particles. Example of diffraction images shown for different Z_{d} values. Diffraction images taken from Korolev et al. (1998).

over the past decades, however, recent studies suggest this value might not be appropriate for today's OAPs anymore. In the course of my master thesis (Moser, 2018), the DOF of OAPs was extensively investigated in laboratory work, and the empirical value of $Z_{\mathrm{d\,max}} = 8.18$ was proposed for future cloud data processing. An independent laboratory study by Gurganus and Lawson (2018) confirmed a similar value at the same time. With Eq. 3.11 and $Z_{\mathrm{d\,max}} = 8.18$, the DOF in this thesis is calculated as follows:

$$\mathrm{DOF} = \pm Z_{\mathrm{d\,max}} \times \frac{R^2}{\lambda}. \tag{3.12}$$

The DOF increases with the size of the particles but is mechanically limited by the distance between the probe arms. Figure 23 shows the DOF over the particle diameter calculated for the PIP, the CIP from the CCP, and the CIP from the CAPS respectively.

The laboratory measurements and theoretical calculations of the DOF are based on spherical particles. Non-spherical ice particles might have a slightly modified $Z_{\mathrm{d\,max}}$ (Guélis et al., 2019; O'Shea et al., 2021). A deviation in the DOF would be particularly noticeable in the SV calculation of the particles sized with the smallest size bins of the OAPs. In the evaluation of this thesis, however, a combination of several cloud instruments is used. Thus, the smallest size bins of the CIP are mostly covered by the scattering instruments, and the smallest bins of the PIP are covered by larger bins of the CIP. The method of how the individual sizing instruments are combined is explained in Sect. 3.4.1.

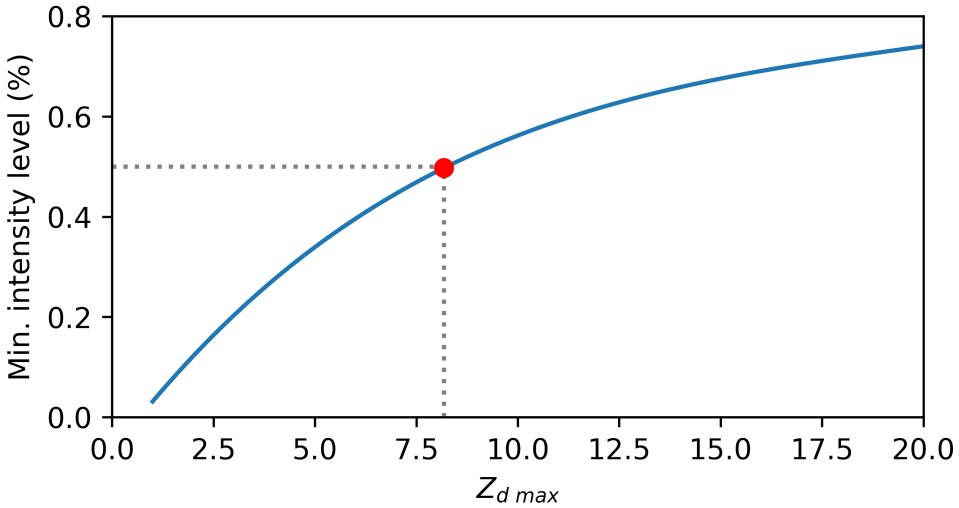

Figure 22 Dependence of intensity level on the maximum distance from the object plane $Z_{\mathrm{d\,max}}$ where this level still exists. Plot is taken from Korolev et al. (1998). The red marker shows the OAP's 50% threshold settings.

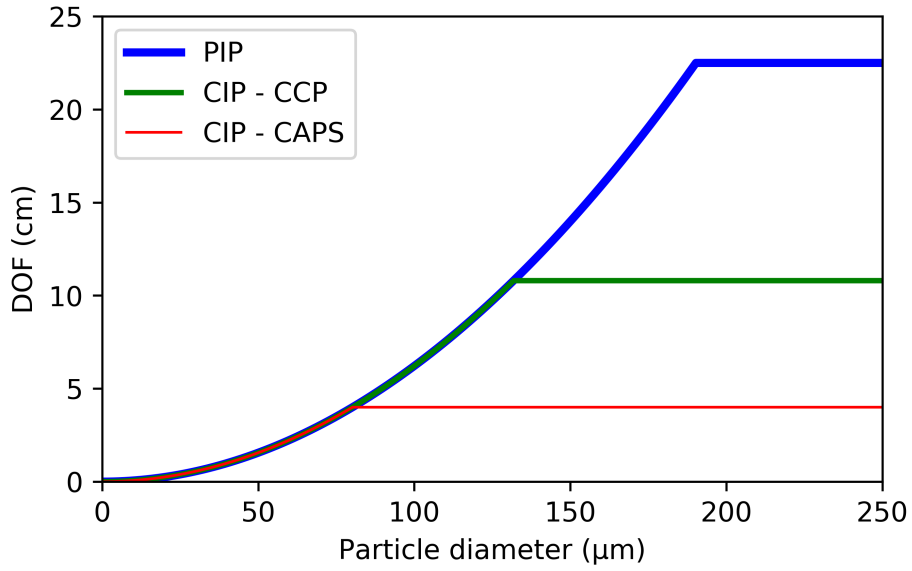

Figure 23 DOF with $Z_{\mathrm{d\,max}} = 8.18$ calculated for the PIP, the CIP from the CCP, and the CIP from the CAPS.

Cloud particle sizing: There is no standardized procedure or clear definition for assigning unique sizes to cloud particles. One possibility is to determine the maximum diameter D_{max} of a cloud particle as the maximum length of the 2D shadow in the direction of flight (x-direction) or in the direction in which the photodiode array is aligned (y-direction). For sizing in the direction of flight, it is important to ensure that the sampling frequency is well synchronized with the flight speed, or that the 2D images have been properly squeezed or stretched afterwards. Sizing in the direction of the photodiode array is used, for example, to calibrate the OAPs (see Sect. 3.3.2), but the sizing in x- or y-directions is not recommended for any cloud in-situ measurements. For example, McFarquhar and Heymsfield (1996) used the maximum value of x and y to define the size of a cloud particle, while Brown and Francis (1995) used an average value between x and y. Wu and McFarquhar (2016) recommend the diameter of the smallest enclosing circle as the optimal definition of D_{max} as an invariant measure concerning the orientation of the particles in the imaging plane for 2D imaging probes. This method is most commonly used to determine the maximum dimension of cloud particles, and many other microphysical calculations such as IWC or D_{eff} are based on this definition (Hogan et al., 2012). It should be noted that in the case of spherical particles (e.g. liquid particles), each of these definitions results in a similar value. For ice particles with one or two dimensional growth, such as needles or plates, the calculation of D_{max} does not represent the volume of the particle well and significantly overestimates it. However, in-situ cloud measurements are often compared with other methods where the spatial extent of cloud particles physically dominates, such as models with radiative transfer calculations or cloud lidar measurements. Therefore, D_{max}, derived from the circle fit, is a good method to describe the size of ice particles. For radar measurements, the mass of the cloud particles has a major influence on the observation. Thus, when comparing in-situ cloud data with cloud microphysics from radar measurements, a mutual measurable particle size must be determined. For example, in Blanke et al. (2023) this was solved by estimating a melted equivalent droplet size for bulk particles using the mass-dimension relationship.
A schematic representation of how D_{max}, the diameter of the smallest enclosing circle, is defined in this work is shown in Fig. 24. For grayscale imaging probes as in Fig. 24 (a), the definition of D_{max} refers to the 50% shadow threshold.

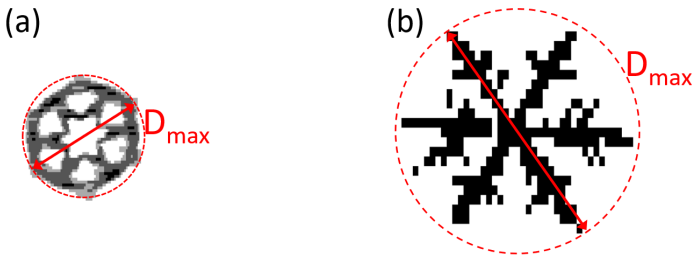

Figure 24 Size definition of a cloud particle as the diameter of the smallest enclosing circle (D_{max}). (a) 2D image of a plate, recorded with the CIP, where light gray, gray, and black represent 25%, 50%, and 75% shadow intensity. (b) 2D snowflake image recorded by the PIP.

3.3.1.2 Methods of correction

Cloud particle shattering: Shattering occurs when large cloud particles hit the arms of the instrument and break into numerous individual pieces, causing the total particle number concentration to be overestimated. By looking at the frequency distribution of the inter-particle arrival time (IPT), i.e. the time between the detection of two particles, over a certain period, one can distinguish shattered particles from non-shattered particles. The interarrival time of natural cloud particles is assumed to be Poisson distributed. In situations where shattering occurs, the distribution of natural cloud particles is overlapped with an additional distribution. Shattered particles have a much shorter IPT, allowing them to be easily distinguished from normal cloud particles by setting an IPT threshold. The second distribution, which is located at much shorter interarrival times, is assigned to shattered particles. Such a bimodal distribution is shown as an example in Fig. 25. The red line indicates the threshold that divides shattered pieces from natural particles. This threshold is usually in the region of about 10^{-5} s for OAPs. Here, the shattering correction is automatically applied during the data processing with SODA and follows the method of Field et al. (2006). However, it must be emphasized that such shattering situations are rather rare in thin Arctic low-level clouds since these effects only become relevant at higher particle number concentrations. In addition, the arms of the OAPs are specially designed to minimize cloud particle fragments passing through the laser beam (Korolev et al., 2013a).

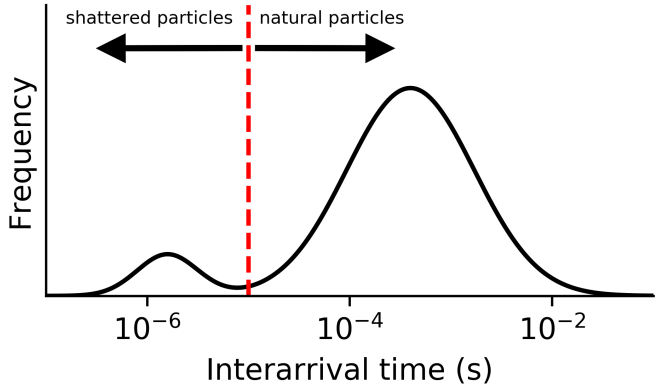

Figure 25 Example of an inter-particle arrival time distribution of a natural cloud including shattered particles.

Active time correction: The dimension of the sampling volume perpendicular to the w_{eff} and DOF is dependent on the distance the OAP cuts through the air within a given time. This time is also called sampling time t_{s}, which is usually fixed to one second. The speed at which the air mass passes through the instrument is referred to as the TAS. Theoretically, the length TAS $\times$ t_{s} can be used for the calculation of the SV, however, Gurganus and Lawson (2018) have shown that OAPs do not measure continuously and a fraction of data gets lost while recording. Therefore, a specific active time must be estimated for each second of measurement and applied to the calculation of the sampling volume.

During in-situ cloud measurements, when the concentration of particles is high, OAPs have to process a large amount of 2D image data. If the data rate exceeds the throughput capacity of the digital electronics, the data acquisition stops for a short time and the probe goes into the so-called "overload" condition. During this short period, no 2D image data can be recorded and so-called "dead time" (t_{d}) is produced. The two manufacturers of the probes used here during the Arctic aircraft campaigns (CIP and PIP by DMT, 2D-S by SPEC Inc.) handle this dead time differently. The 2D-S evaluated by the LaMP team can determine the dead time with great accuracy, as an additional independent data stream beside the particles is recorded, which measures the exact times of the passing particles. This allows a determination of the dead time within 50 ns for the 2D-S. With DMT's CIP and PIP, however, there is no such additional time stamp. Here, in addition to the 2D data stream, a particle counter is provided that increments by one every time when at least one photodiode is shadowed. If the instrument records perfectly without going into overload, the particle counter will count the same number of particles as the number of images captured in the 2D data stream. However, if the counter is higher than the number of image particles, the instrument has temporarily gone into overload and cannot record 2D image data during this dead time. It is assumed that the particle counter is fast enough to cover all particle crossings. By comparing the number of particles in the image file with the number of particles in the counter, the dead time within a given time interval can be estimated (McFarquhar et al., 2017). As described in Sect. 3.3.1, the SODA software is used for cloud data processing, and the generated PBP file is used for further calculations. In SODA a dead time correction is implemented, so the PBP file additionally lists the missed particles calculated by comparing the particle counter of the probe between two consecutive particles in the image file. A threshold is set to $t_{\text{d}} / t_{\text{s}} > 0.9$ which means when the dead time of the probe is above 90% of the sample time, the measurement period is discarded. Assuming the SODA processing as the truth, in more than 90% of the cloud measurements, conducted with the CIP during the AFLUX field campaign, the dead time exceeds a threshold of rejection.

The high rejection rate results from an unnaturally high amount of counts in the particle counter. Several laboratory studies with the DMT cloud probes were performed to trace the origin of

the high number of particles in the particle counter of the CIP data [3]. We identified that the particle counter does not react to a 50% grayscale threshold, which is usually taken for OAP data processing, but to 25%. From the perspective of the instrument manufacturer, this setting is justifiable, as the particle counter should keep track of all particles that the instrument is sensitive to. Accordingly, under natural cloud conditions, constantly too many particles are recorded in the particle counter, as only images with a 50% threshold are evaluated during processing, but those with a 25% shadow intensity threshold are counted. However, in most cases, the difference between the particle counter of the CIP and the number of particles in the 2D image data is so significant that it cannot be explained by this threshold difference alone. Most of the counts in the particle counter are caused by a stuck bit that exceeds the 25% threshold, but not the 50% threshold. This is shown by an analysis of the raw images. Aaron Bansemer, the inventor of SODA, also suspects a falsely triggered particle counter for the DMT probes, as we discovered in the laboratory (personal communication). However, since the algorithm and settings behind the particle counter remain hidden in the instrument's electronics, the dead time correction for DMT imaging probes is therefore no longer supported by SODA. Changing the order of data processing in SODA could potentially correct the stuck bit at the 25% threshold level and thus improve the implemented dead time correction.
Another open question is whether the threshold of the particle counter is set to the threshold setting of the probe, or whether they are independent of each other. To answer this question, one would have to change the lowest threshold level during a cloud measurement in which stuck bits occur. If both settings are coupled, the miscounting could be solved by reducing the sensitivity of the lowest threshold to 50%. However, this would reduce the information in the grayscale images.
In selected measurement sections during AFLUX, a very high particle counter is also observed with the PIP. Since the PIP can only detect a grayscale level of 50%, this cannot be explained by the previous hypothesis. In order to process the image data independently of the particle counter, a new method is developed for the DMT's imaging probes to reasonably correct the measured data with respect to the dead time. The following algorithm is feasible as the instruments manufactured by DMT produce an independent second 1D data stream including cloud particle counting only (see Sect. 3.3.1 for more detail).

For the development of the active time correction method, the data of the 2D-S are used as a reference. Since the 2D-S dead time can be determined more accurately due to the additional recorded time stamp, the processed number concentration can be taken as truth here. This assumption is supported by previous studies, which have shown that in general OAPs by the manufacturer SPEC Inc. show negligible dead time while recording cloud particles (e.g. Gurganus and Lawson, 2018). Own analyses (Blanke et al., 2023) on OAP data from SPEC

[3] Laboratory work on tracing the origin of the overestimated particle counter was carried out in a joint project with Elena De La Torre Castro, Institut für Physik der Atmosphäre, Deutsches Zentrum für Luft- und Raumfahrt, Wessling, Germany

Inc. instruments (2D-S, High Volume Precipitation Spectrometer (HVPS)) recorded during the OLYMPEX field campaign (Houze et al., 2017) have confirmed these findings.

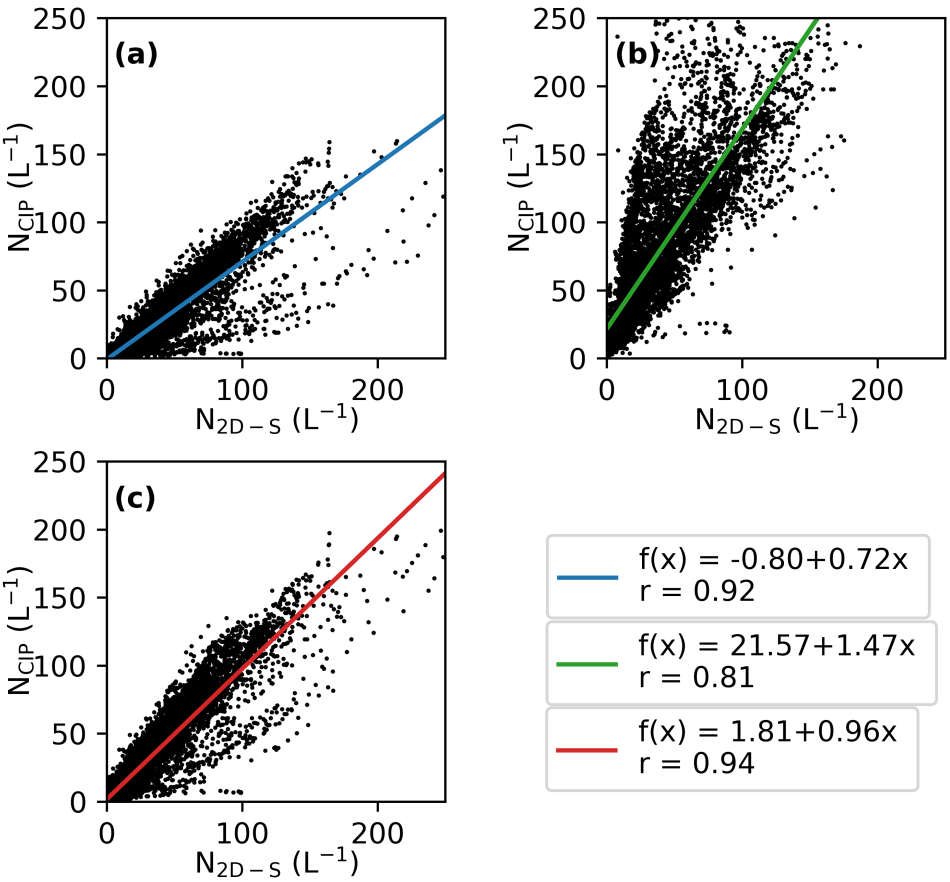

Figure 26 Correlation of N for particles between 100 - 500 µm measured by the 2D-S and the CIP. In a) no dead time is assumed for the CIP, b) CIP's active time is corrected following Gurganus and Lawson (2018), and c) a new hybrid version of (a) and (b) with γ - correction followed by Eq. 3.14 is applied to the CIP's active time (here $\gamma = 0.6$).

Figure 26 (a)-(c) correlates the cloud particle number concentration measured during AFLUX with the CIP and 2D-S in the size range 100 - 500 µm with different dead time corrections applied on the CIP data. Only straight flight legs at constant altitude (vertical speed < 1.1 m s^{-1} and roll < 8 °) are considered. The upper and lower particle size limits for the comparison were chosen since both instruments take measurements with the highest accuracy in this range. In Fig. 26 (a) no correction is applied to the CIP data, i.e. the active time is left constant at 1 Hz. Correlating the two instruments, the Pearson correlation coefficient of r = 0.92 indicates a strong correlation, however, the slope of the linear fit function shows a 28% reduction in the number concentration of particles detected by the CIP missed due to dead time. Gurganus and Lawson (2018) have proposed a method for estimating the active time t_a of DMT probes:

$$t_{\mathrm{a}} = t_{\mathrm{s}} - t_{\mathrm{d}} = t_{\mathrm{s}} - \left[t_{\mathrm{s}} \times \left(1 - \frac{N_{\mathrm{image}}}{N_{\mathrm{all}}} \right) \right] \tag{3.13}$$

with N_{image} the number of images recorded by the image file and N_{all} the number of particles counted by the 1D component (1 Hz - file) of the probe. Similar to SODA, a threshold of $t_d/t_s > 0.9$ is set to discard time series where the probe dead time is too high. Following this method, half of the data set is lost due to the supposed high overload. The slope of the linear regression in Fig. 26 (b) also indicates that the number concentration by the CIP is overestimated following the dead time correction method by Gurganus and Lawson (2018). In order not to underestimate the active time and not to discard most of the measurements due to the threshold ($t_d/t_s > 0.9$ or $t_a < 0.1$), but still to resolve the variability of the active time within the cloud measurements, a new method for active time correction is introduced:

$$t_{\mathrm{a},\gamma} = \begin{cases} t_{\mathrm{a}}^{(1-\gamma)}, & \text{if } t_{\mathrm{a}} \geq 0.1 \\ 0.1^{(1-\gamma)}, & \text{if } t_{\mathrm{a}} < 0.1 \end{cases} \tag{3.14}$$

with t_{a} calculated according to Eq. 3.13 and a γ-correction value. With this new method, the active time t_a is now adjusted to larger values, and no measurements are discarded anymore. The optimal value for γ is chosen such that the correlation factor between the 2D-S and the CIP data, corrected corresponding to Eq. 3.14, is maximized (see Fig. 27 (a)). This occurs at $\gamma = 0.6$, with a Pearson correlation coefficient of 0.94. The resulting slope of the linear regression is 0.96 (see Fig. 27 (b)). The correlation between 2D-S and the corrected CIP data via γ-optimization is shown in Fig. 26 (c). With the newly introduced γ-method, no data is discarded anymore, the slope of the correlation line has been brought closer to 1 compared to the method by Gurganus and Lawson (2018), and the Pearson correlation factor has been improved. Based on these results, all CIP data recorded during the AFLUX campaign were processed according to Eq. 3.14 with $\gamma = 0.6$.

The recording of CIP data during AFLUX differs from the data recorded during MOSAiC-ACA and HALO-(AC)^3 by the fact that the shading threshold for the 1 Hz file was set to 25% in the PADS settings during AFLUX. As a result, the particle counts in the 1 Hz CIP data during AFLUX are slightly overestimated compared to the particle counts in the image file resulting in an overestimation of t_{a}. To compensate for the different settings, a γ-value of 0.5 is assumed for the CIP data recorded during MOSAiC and HALO-(AC)^3. Please note, during the time of CIP data processing for the AFLUX, MOSAiC-ACA, and HALO-(AC)^3 campaign, only validated 2D-S data from the AFLUX field campaign were available. For that reason, all active time corrections applied to all three campaigns are based on the AFLUX data set only. In the meantime, the 2D-S data of the MOSAiC-ACA campaign were made available as well. A correlation of CIP and 2D-S data collected during MOSAiC-ACA with respect to the probe's active time is discussed in Appendix C.

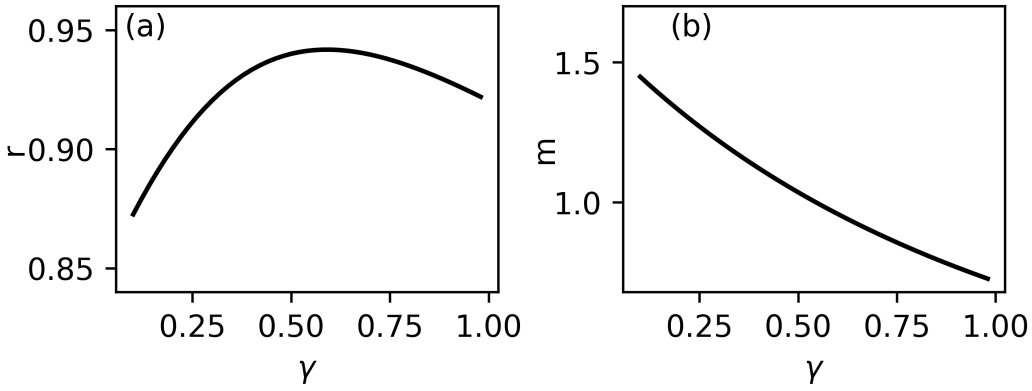

Figure 27 Optimization of the γ value for the new active time correction: (a) gives the Pearson correlation coefficient r for the correlation between 2D-S data and the new active time corrected CIP data with different γ values, and (b) gives the slope m of a linear fit of this correlation.

A direct correlation between 2D-S data and PIP data is impossible as the overlap size regime is not sufficient. The PIP uses the same processing electronics as the CIP, except that only the 50% threshold level is recorded (mono-scale imaging probe). Therefore, the PIP data for all campaigns have been active time corrected according to Eq. 3.14 with $\gamma = 0.5$.

3.3.2 Characterization of the Cloud Imaging Probe

The operating principle of the CIP is described in Sect. 3.3. Two different CIPs were used in this work. During AFLUX the CIP is a part of the larger instrument CAPS (see Figure 10) and during MOSAiC-ACA and HALO-(AC)^3 the CIP is a part of the CCP (see Fig. 13). The difference between the two CIPs is their mechanical design including the width of the arms, which results in slight differences in the sampling volume of the two instruments. The resolution of one photo element is specified by the manufacturer for both instruments as 15 µm. Due to rough transport or vibrations during flight operation, the optical path of the laser might be affected, including the optical magnification. For this reason, it is important to have regular instrument calibration and resolution checks. To do so, a spinning disk by DMT is used. The spinning disk consists of a glass disk with opaque dots of different sizes. When the disk is placed inside the sampling volume in the center of the OAP, the dots simulate shadows of spherical droplets with the same diameter as the opaque dots (Droplet Measurement Technologies, 2017a). Six dots with different sizes are repeated in the following order: 50 µm, 125 µm, 250 µm, 500 µm, 1000 µm, 2000 µm. An example of raw 2D-image data from a CIP calibration is shown in Figure 28.

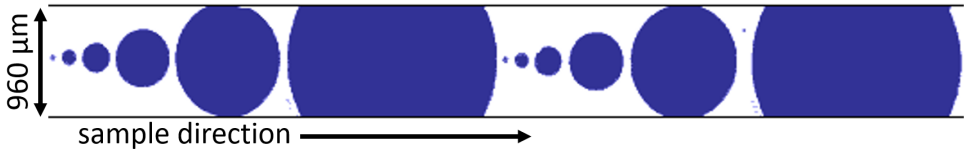

Figure 28 Raw CIP images during spinning disk calibration.

Calibration on 13 March 2019 at the end of the AFLUX campaign revealed a resolution of 14.9 µm for the CIP-CAPS. This value was determined as follows: The sizes of all detected particles (here from 09:38:30 - 09:39:30 UTC) are plotted in a histogram in Fig. 29, where the size of a bin depends on the resolution of the CIP. A Gaussian function is fitted over each peak in the histogram, and its mean position gives the respective size of the simulated calibration droplet in bin units. This allows each peak in the histogram to be assigned a real size corresponding to the diameters of the known opaque dots on the spinning disk. This correlation is shown in Fig. 30. A linear regression allows the determination of the actual resolution of the CIP.

In the histogram in Fig. 29 some noise is visible, especially for small particles. This is caused by the fact that the spinning disk could not be completely cleaned before the measurement, due to the harsh working conditions in the Arctic. Additionally, the calibration was performed under slight freezing drizzle conditions. As the peak of the smallest simulated droplet is discarded and the noise is significantly reduced for bins > 6, no degradation in the quality of the results is expected. The high number of counts in the largest bins is because the analysis for this

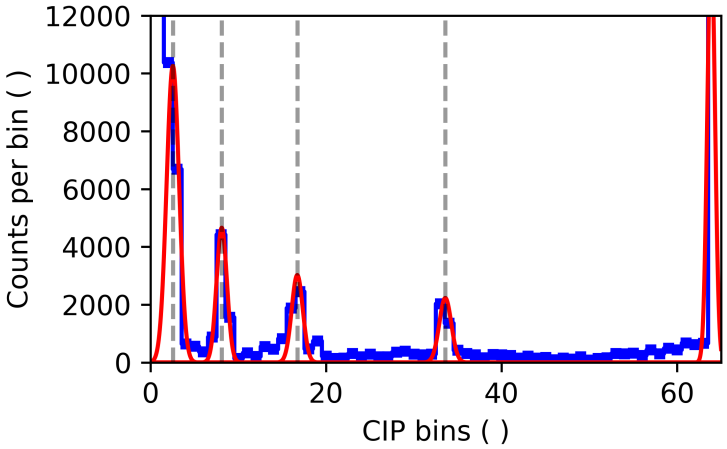

Figure 29 Count distribution from the calibration of the CIP using the spinning disk. Date of calibration: 13 April 2019, 09:38:30 - 09:39:30 UTC.

calibration also processes particles larger than the maximum width of the array. Thus, the two largest simulated drops on the spinning disk (1000 µm and 2000 µm) are assigned bin number 64. In Fig. 30, only the simulated droplets with sizes 125 µm, 250 µm and 500 µm are used to determine the resolution. The manufacturer specifies the resolution of the CIP probe as 15 µm. Laboratory work before the AFLUX campaign revealed similar values. For simplicity, a value of 15 µm is assumed for the processing of the CIP-CAPS data.

The same procedure is applied to the CIP-CCP. Here, the resolution of 15 µm was confirmed during several calibrations: (15.0 $\pm$ 0.1) µm on the 29 August 2020, (15.0 $\pm$ 0.1) µm on the 14 September 2020 and (15.2 $\pm$ 0.1) µm on the 7 April 2022.

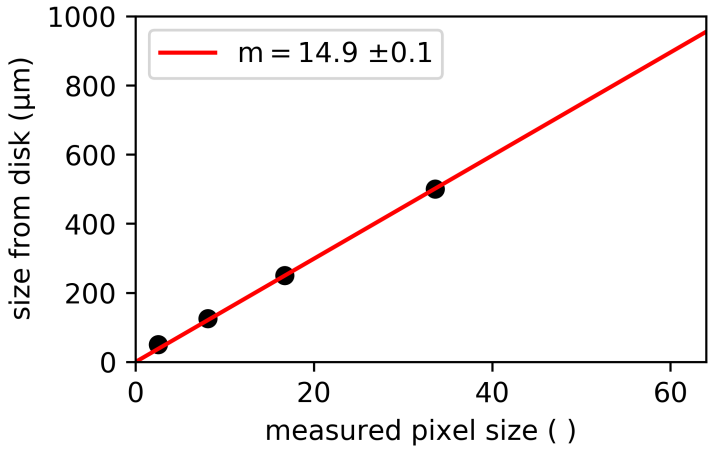

Figure 30 Linear fit to determine the resolution of the CIP. Due to noise in the first bins, the smallest point is not included in the linear fit.

For the active time correction, a new method is presented in Sect. 3.3.1, where a γ correction value is introduced. For the CIP-CAPS, this value is characterized as 0.6. To correct the active time of the CIP-CCP as well, γ was estimated to be 0.5. A review of this γ-value for the CIP-CAPS is discussed in Appendix C.

The depth of field constant $Z_{\mathrm{d\,max}}$ for the grayscale threshold of 50% was determined empirically in laboratory work for the DMT imagers. For more detail, refer to Sect. 3.3.1. Both CIPs are grayscale OAPs, which means that in addition to the 50% shadow threshold, the 25% and 75% thresholds are included in the raw data. The advantage is that 2D images have higher contrast and individual particles are easier to classify in terms of cloud particle classification as presented in Fig. 17. However, the general processing of microphysics is based on the 50% threshold (sizing and sampling volume), and therefore only this value is used for further evaluation. This ensures the highest quality of the processed data as most algorithms and technical characterizations are based on this threshold. All characteristic parameters required for processing the CIP data are given in Table 5.

	Number of diodes	Arm width	Resolution	Grayscale levels	γ	$Z_{\mathrm{d\,max}}$
CIP - CAPS	64	4.0 cm	15.0 µm	50% (25/75%)	0.6	8.18
CIP - CCP	64	10.8 cm	15.0 µm	50% (25/75%)	0.5	8.18

Table 5 Values used for the data processing of the two CIPs.

3.3.3 Characterization of the Precipitation Imaging Probe

For all three Arctic field campaigns, the same PIP from the DLR (shown in Fig. 31) was used in this thesis and is described in the following. The PIP is designed to detect larger cloud particles compared to the CIP. This is achieved by a smaller magnification factor in the optics, which results in a different resolution. As the PIP is a monoscale imager, shadows are only captured at one grayscale level. This level is set to a threshold of 50%. By nature, larger particles are less likely to be present than smaller ones. For this reason, it is important to increase the sampling volume for the measurement of large particles, which is achieved by a larger arm and array width of the PIP compared to the two CIPs. All characteristic parameters required for processing the PIP data are given in Table 6.

	Number of diodes	Arm width	Resolution	Grayscale levels	γ	$Z_{\mathrm{d\,max}}$
PIP	64	22.5 cm	103.0 µm	50%	0.5	8.18

Table 6 Values used for PIP data processing.

To determine the PIP's resolution, the same calibration method used for CIP is applied (see Sect. 3.3.2). A different spinning disk with opaque dots is used to simulate spherical particles with diameters of 250 µm, 500 µm, 1000 µm, 3000 µm, and 5000 µm. For the final calibration, however, only the sizes 500 µm, 1000 µm, and 3000 µm are used, as these are best captured by the PIP. The calibrations yielded a resolution of (102.8 ± 0.8) µm on 7 April 2019, (103.4 ± 1.5) µm on 14 September 2020 and (102.7 ± 1.0) µm on 7 April 2022, respectively. A constant deviation of approximately 3 µm relative to the value of 100 µm specified by the manufacturer is found (Droplet Measurement Technologies, 2017b). Hence, a value of 103 µm is assumed for the processing of the PIP data.

The theoretically calculated constant for the characterization of the CIP's DOF matched the empirically measured value exactly (see Sect. 3.3.1). Since theory and measurement agree well, these results can be transferred to similar measurement systems with the same laser wavelength. Therefore, a Z_d value of 8.18 is applicable here as well.

The γ value of 0.5 is based on assumptions derived from the results of the characterization of the active time of the CIP-CAPS in Sect. 3.3.1. This is a reasonable assumption since the same hardware is installed in all imagers produced by DMT. An evaluation as performed for the CIP, where the data were directly compared to the 2D-S, is challenging here due to the small overlap in the size distribution. However, the computed combined PSDs indicate that this value was appropriately chosen (see Sect. 3.4.1).

Figure 31 PIP mounted under the wing of Polar 6 during the HALO-(AC)^3 campaign.

3.4 Processing a combined in-situ cloud data set

3.4.1 Combining in-situ cloud particle sizing techniques

In Sect. 3.2 and 3.3 different measurement techniques for measuring the size of cloud particles are introduced. By combining the sizing instruments CAS/CDP, CIP, and PIP, cloud particles from diameters 2.8 µm up to 6.4 mm can be measured. This size range includes the immediate size of cloud particles after their formation as well as grown cloud water droplets, pure ice crystals, aggregates, pristine ice crystals, and large precipitation particles such as rain or snow. The advantage of three different measuring systems is, that each system is designed for a different size range and the respective size ranges overlap. To obtain a continuous size distribution, size limits in which each instrument contributes to the particle size determination are defined. Additionally, transition regions are defined in which an average value is calculated between the two measuring devices. These transition regions are set from 36 µm to 48 µm for CAS/CDP - CIP and from 300 µm to 450 µm for CIP - PIP. These limits are placed such that each size range is covered optimally by the respective instrument. Particularly the first two size bins of OAPs are known to be the most uncertain due to the challenges defining their sampling volume (see DOF in Sect. 3.3.1). By the combination, these size bins are covered by the instrument which is sensible to the respective smaller particles.
For the calculation of the mean value in the transition region, the measured particle size distributions of both instruments are scaled down to a new binning with 1 µm resolution to directly compare the total particle number concentration measured by both instruments. After a mean value is determined in this transition region, the bin resolution has to be scaled back into the original binning which boundaries are given by the individual instruments. As the transition region is not exactly in line with the original binning of the instruments, a fraction of the next higher and lower bins of the respective instruments are added to the transition region. This results in a transition bin, with boundaries fitting into the original binning of the instruments. For the individual campaigns, the final boundaries for the transition bin result to 33 - 53 µm and 294 - 464 µm for AFLUX, and 34 - 53 µm and 294 - 464 µm for MOSAiC-ACA and HALO-(AC)^3. Technically, the transition region could be larger, since the OAPs cover a broader size range than is applied here. However, the first bins of OAPs are subjected to large uncertainties. For this reason, CIP and PIP data are used from the 3rd bin onwards only. CIP data larger than 450 µm is also discarded, as the PIP has significantly better statistics than the CIP due to its larger sampling volume. These size boundaries ensure that particles are detected in the optimal size range of the respective instruments, which leads to a minimization of uncertainties and an optimization of the sampling volume. The size ranges of the scattering probes CIP and PIP including their transition regions are shown schematically in Fig. 32.

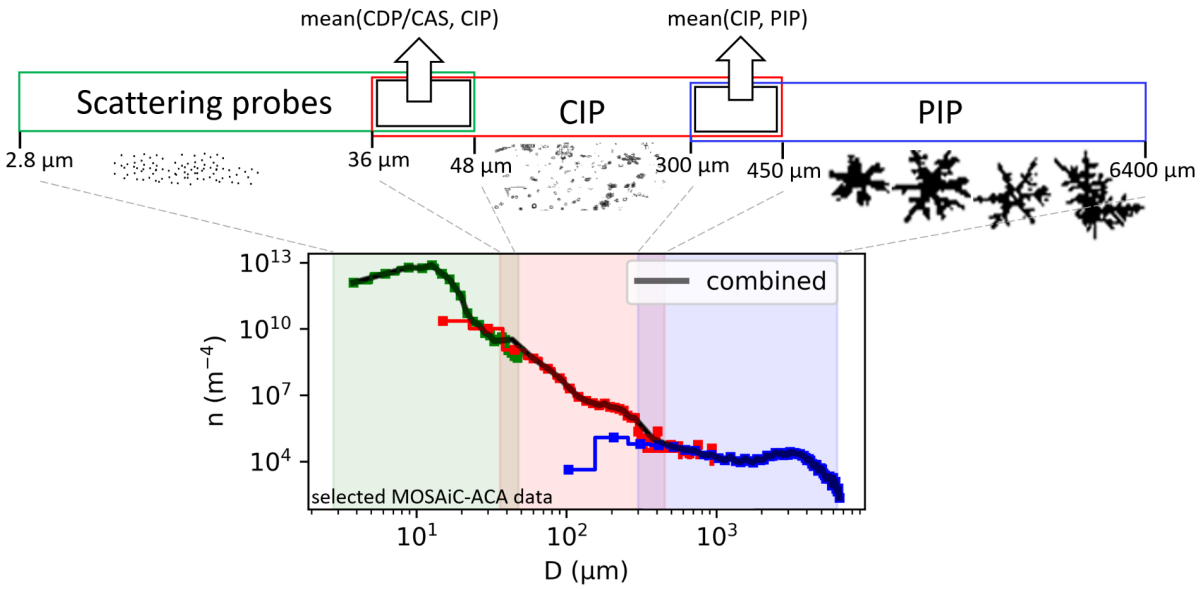

Figure 32 Colors show the different particle size ranges, where the in-situ instruments are sensitive and how the instruments are combined to obtain a continuous particle size distribution.

Cloud particle data from the research flight on 6 April 2019 are used, in order to check whether the measured mean value in the transition regions was calculated appropriately. Figure 33 displays how often a certain particle number concentration in the size range from 36 µm to 48 µm (a) and from 300 µm to 450 µm (b) is detected by the respective sizing instrument. There are two distributions in both size ranges, one for each instrument. They overlap by more than 1.5 orders of magnitude in (a) and (b). Additionally, the distribution in gray gives the mean values of both instruments. The fact, that the respective instrument suitable for measuring larger particles detects more frequently fewer number concentration values, can be attributed to the sampling volume. A larger sampling volume allows for the measurement of a lower particle number concentration, which is no longer detectable by the instrument designed for smaller particles. However high concentrations of smaller particles are better resolved by the instrument which is suitable for smaller particles. Using an average value within the transition overlap region provides a reliable approach to reducing the variation in the data by effectively balancing the results of both instruments. The correlation coefficient calculated over an average of 15 s is 0.85 in (a) and 0.75 in (b). Overall, the mean value seems to represent the measurements of both instruments very well in both overlap regions.

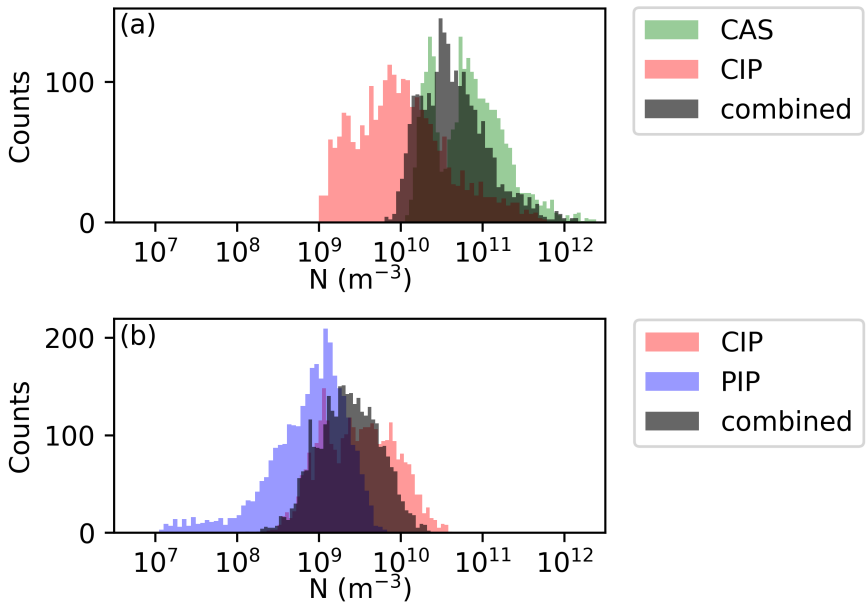

Figure 33 Frequency of the particle number concentration measured by different instruments in the size regime from 36 µm to 48 µm (a) and from 300 µm to 450 µm (b). Additionally, the mean values between the respective two instruments are shown ("combined").

3.4.2 Deriving microphysical cloud properties

Section 3.4.1 describes how a continuous particle size distribution is obtained from 2.8 µm to 6.4 mm by combining the sizing measurements that were used during the Arctic field campaigns. This combined particle size distribution serves as a basis to derive further microphysical cloud properties of Arctic low-level clouds. The following equations do not have to be applied exclusively to the combined spectrum. They can be flexibly applied to different sub size ranges, for example, only to the CAS/CDP data or CIP data, depending on the specific requirements of the analysis.

The total cloud particle number concentration N is the sum of all particle concentrations of the considered size bins:

$$N = \sum_{\mathrm{i}} N_{\mathrm{i}} \tag{3.15}$$

with N_{i} the particle number concentration in size bin i. To calculate the effective diameter (D_{eff}), several definitions are available in the literature, some examples are given by McFarquhar and Heymsfield (1998). Here the following definition by Parol et al. (1991) is used to calculate the effective diameter of the given particle size distribution:

$$D_{\mathrm{eff}} = \frac{\sum_{\mathrm{i}} D_{\mathrm{i}}^3 N_{\mathrm{i}}}{\sum_{\mathrm{i}} D_{\mathrm{i}}^2 N_{\mathrm{i}}} \tag{3.16}$$

with D_i the mean diameter of the respective size bin. It is important to emphasize, that there is no standardized calculation for D_{eff}. Therefore, when comparing the given D_{eff} to other

methods, like data from modeling or remote sensing instruments, the definitions of both effective sizes must match. As well the definition of the particle's diameter influences the D_{eff}. Here for the 2D probes, the diameter of the smallest circle enclosing the particle is used (see Sect. 3.3.1.1). This method for measuring the diameter of a cloud particle is recommended as the optimal definition to measure the maximum diameter of a cloud particle (Wu and McFarquhar, 2016).

The liquid water content (LWC) results from the sum of all water droplets in the sampling volume. Here, the cloud particles are considered as spheres:

$$\text{LWC} = \sum_{\text{i}} \text{LWC}_{\text{i}} = \sum_{\text{i}} N_{\text{i}} \times \rho_{\text{w}} \times \frac{4}{3}\pi \left(\frac{D_{\text{i}}}{2}\right)^3 \tag{3.17}$$

where LWC_i is the liquid water content in the respective size bin and $\rho_{\text{w}} = 1\,\text{g}\,\text{cm}^{-3}$ is the density of water.

Compared to the calculation of liquid water content, the determination of ice water content (IWC) is more challenging because the volume of a frozen cloud particle cannot be directly determined from the measured diameter due to the complex shape of ice crystals. The estimation of the IWC from in-situ cloud probes is based on in-situ cloud data sets by which a mass-dimension relationship was derived empirically. Many such published data sets exist, the best known and most widely mass-dimension relationship used in the in-situ community is by Brown and Francis (1995). However, the method by Brown and Francis (1995) was shown to underestimate the ice water content in clouds (Heymsfield et al., 2010). In this work, the parameters ($\alpha = 0.00528\,\text{g}\,\text{cm}^{-b}$ and $\beta = 2.1$) proposed by Heymsfield et al. (2010, 2023) are used which are appropriate for in-situ cloud measurements under Arctic conditions. The IWC is obtained by:

$$\text{IWC} = \sum_{\text{i}} \text{IWC}_{\text{i}} = \sum_{\text{i}} N_{\text{i}} \times m_{\text{i}} = \sum_{\text{i}} N_{\text{i}} \times \alpha \times D_{\text{i}}^{\beta} \tag{3.18}$$

with IWC_{i} the ice water content and m_{i} the ice mass in the respective size bin.

The derived water or ice water content is based on the assumption that the particles in the selected size range are in a thermodynamic liquid or ice phase. A direct phase differentiation with the sizing instruments is not possible. In this work, however, low-level Arctic clouds are analyzed, which are most likely in a mixed-phase state. McFarquhar et al. (2007a) and Korolev et al. (2017) have shown that in low-level Arctic mixed-phase clouds small particles are in a liquid state and the large particles correspond to the ice phase. Thus, a reasonable assumption is made that all particles smaller than 50 µm are considered to be liquid for the cloud water content (CWC) calculation and ice for diameters starting at 50 µm. The CWC, which is the sum of LWC and IWC, is then calculated as:

$$\text{CWC} = \sum_{\text{i}:D_{\text{i}}<50\mu\text{m}} \text{LWC}_{\text{i}} + \sum_{\text{i}:D_{\text{i}}\geq 50\mu\text{m}} \text{IWC}_{\text{i}} = \text{LWC} + \text{IWC}. \tag{3.19}$$

3.4.3 Discussion of uncertainties in the microphysical cloud properties

In Chapter 4 in-situ cloud data of Arctic low-level clouds is investigated and microphysical cloud parameters in different thermodynamic cloud phases are analyzed. The uncertainties of the acquired microphysical cloud properties strongly depend on the thermodynamic cloud phase. This is due to the fact that a different cloud phase results in a different cloud particle size distribution. The sizing instruments used in this work are sensitive to different size ranges and have their respective uncertainties. This implies that N has a measurement uncertainty range of 10-30% in liquid and mixed phase clouds, since N is predominantly derived from the scattering probes (Baumgardner et al., 2017). In ice clouds, the larger ice crystals are counted for N by the OAPs with an uncertainty of approximately 50% (Baumgardner et al., 2017; McFarquhar et al., 2017). Sizes of droplets in liquid clouds are in the size regime in which the scattering probes are sensitive, ranging from 10-50% uncertainty (Baumgardner et al., 2017). In ice and mixed-phase clouds the particle sizing is dominated by data from the OAPs which have an uncertainty of 20% (Baumgardner et al., 2017; Gurganus and Lawson, 2018). For the calculation of the CWC, the LWC values in liquid clouds have an uncertainty of 20% (Faber et al., 2018). For the IWC, an uncertainty of 50% is assumed for the calculation in ice clouds (Heymsfield et al., 2010; Hogan et al., 2012). In mixed-phase clouds, the uncertainty of CWC is estimated to be in between LWC and IWC uncertainty calculation, hence 20-50%. A summary of the uncertainties is given in Table 7. The uncertainties given here, caused by the OAPs, agree with the laboratory results given in Moser (2018). It should be noted that in certain cloud situations, the reported uncertainties may be slightly higher due to optimistic estimates.

	Counting	Sizing	Water content
liquid phase	10-30% Baumgardner et al. (2017)	10-50% Baumgardner et al. (2017)	20% Faber et al. (2018)
mixed-phase	10-30% Baumgardner et al. (2017)	20% Baumgardner et al. (2017) Gurganus and Lawson (2018)	20-50%
ice phase	50% Baumgardner et al. (2017) McFarquhar et al. (2017)	20% Baumgardner et al. (2017) Gurganus and Lawson (2018)	50% Heymsfield et al. (2010) Hogan et al. (2012)

Table 7 Uncertainties of the particle counting, particle sizing, and calculation of the water content in the cloud using a combination of the sizing instruments CAS/CDP, CIP, and PIP. The uncertainties differ depending on the thermodynamic phase of the cloud.

3.4.4 Deriving cloud data sets for microphysical and thermodynamic phase analyses

In Sect. 4.4 and 4.5, low-level clouds in the Arctic are analyzed from a microphysical and thermodynamic phase perspective. Slightly different methods are applied for the two analyses. The analysis of the cloud microphysics is based on a cloud data set (see a in Fig. 34), while a particle data set is used for the thermodynamic phase analysis of the particles (see b in Fig. 34). The 1 Hz combined particle size distribution from Sect. 3.4.1 is used as the basis for both analyses, from which the microphysical properties such as N, D_{eff}, and CWC are derived. In the Arctic, cloud particles can have a relatively low number concentration, so it is of great importance to measure these particles using high statistics. When conducting in-situ cloud measurements while changing altitude, such as the sawtooth pattern in Fig. 38, the air masses are not measured long enough to collect robust data. In addition, the ascent and descent may affect the incident flow of the instruments and could impact the measurements. For this reason, only data recorded at a constant flight altitude without turns, in most cases obtained from the racetrack or staircase patterns (see Fig. 38), are used.

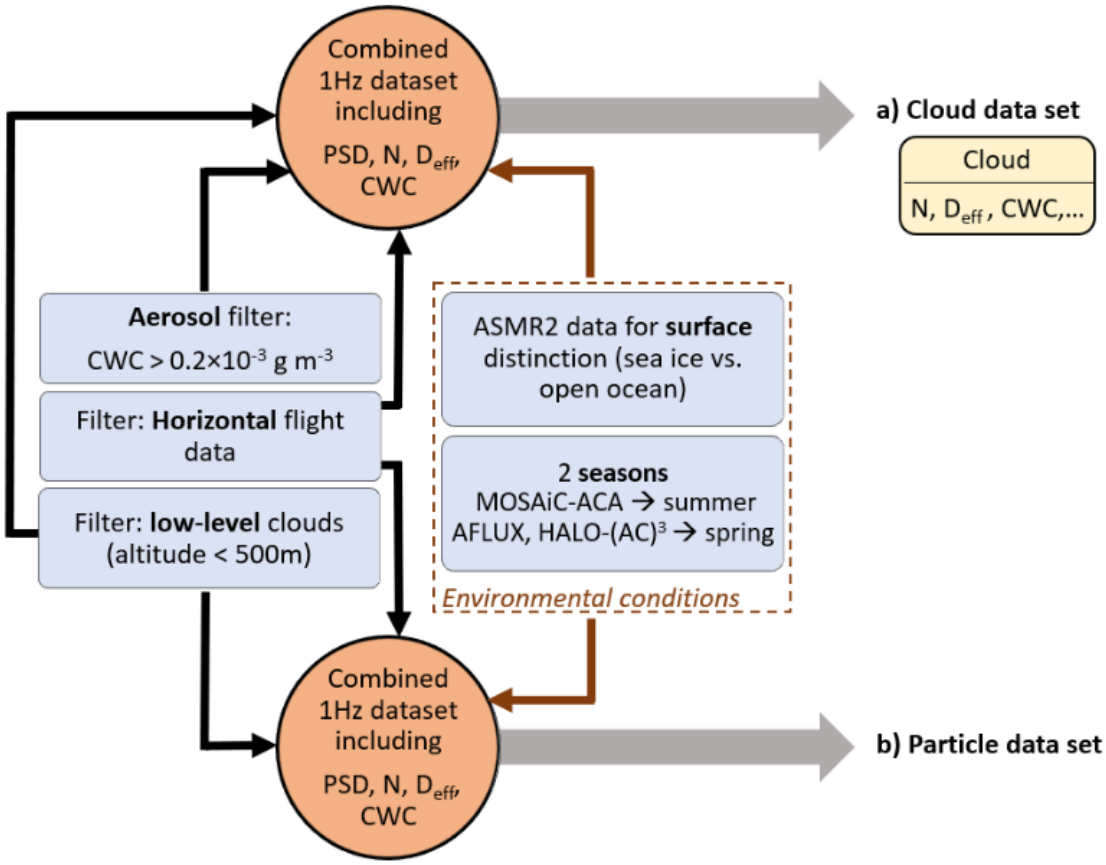

Figure 34 Filters and segmentations (blue boxes), applied to the 1 Hz data set (orange circles), to derive a) a cloud data set for microphysical analyses of Arctic low-level clouds and b) a particle data set for the thermodynamic phase analyses.

In order to perform cloud analyses exclusively on low-level clouds, an altitude threshold is defined. As will be shown later in Sect. 4.4, almost all low-level cloud measurements during AFLUX and MOSAiC-ACA were below 500 m, so this value is used as the upper limit for low-level cloud measurements for these two campaigns. Later in Sect. 4.6 the additional cloud data set from the HALO-(AC)^3 campaign is introduced. Here, the low-level cloud measurements reach up to 1000 m. If not otherwise stated, an altitude threshold of 500 m is used for low-level clouds during AFLUX and MOSAiC-ACA and a threshold of 1000 m for the HALO-(AC)^3 campaign.

Both data sets are segmented in terms of environmental conditions. The classification of the surface with the AMSR2 satellite is explained in Sect. 3.5, and the seasonal classification is made according to the season in which the respective campaign took place.

The particle data set includes all particles detected by the particle measurement system. These data are analyzed in terms of the thermodynamic phase and used for particle classification into liquid, ice, mixed-phase, and aerosol particles. With the cloud data set, absolute microphysical properties of Arctic low-level clouds are determined, which is why a filter must be defined to exclude non cloud particles, like aerosols. Kirschler et al. (2022) defines a cloud period where the CWC and N exceeds 0.02 g m^{-3} and 20 cm^{-3}, respectively. Only one threshold is used in the Arctic cloud study by Young et al. (2016), here in-cloud and out-of-cloud observations are distinguished using a threshold of 0.01 g m^{-3}. Figure 35 shows how a certain CWC threshold can filter the individual cloud phases, which are defined in Sect. 4.5. The threshold by Young et al. (2016) appears to be good in representing liquid clouds, however, filtering a significant amount of mixed-phase and ice clouds. To take non-pure liquid clouds with relatively low CWC values into account, but to exclude measurements of aerosols, the CWC threshold for cloud measurements is set to 2×10^{-4} g m^{-3}. This value is very efficient in leaving Arctic cloud particles including light precipitation or thin ice clouds untouched and filtering 98% of all measurements corresponding to aerosol particles only.

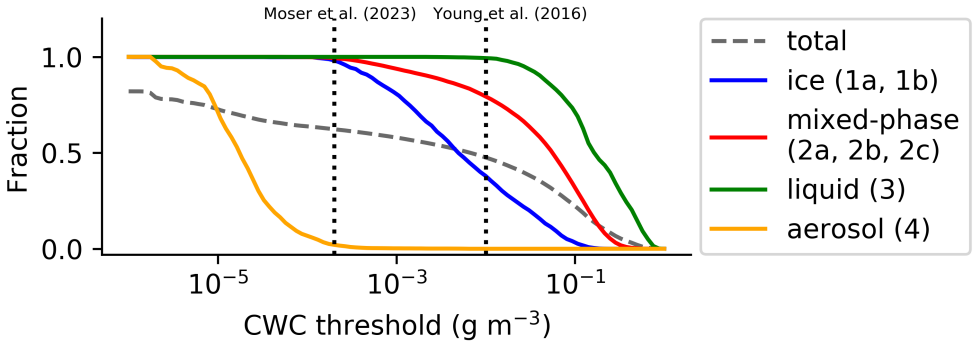

Figure 35 The fraction of measurements taken into account depending on the setting of a CWC threshold. The definitions of ice (regime 1a and 1b), mixed-phase (regime 2a, 2b and 2c), liquid (regime 3), aerosol (regime 4), and total measurements (no regime filter, all data) are given in Sect. 4.5.

In the course of this thesis, distributions of measured microphysical cloud parameters are compared. Given that the distributions of microphysical cloud data often exhibit a degree of asymmetry, the median offers a more robust and meaningful representation of this data than, for example, the arithmetic mean. The median is a statistical measure that divides the data into two equal halves and is relatively unaffected by outliers.

3.5 Complementary data

Navigation system and nose boom: Internal navigation systems (INS) installed on Polar 5 and Polar 6 provide longitude, latitude, ground speed, and angular rates to determine the position and heading of the aircraft in the Earth's coordinate system (Ehrlich et al., 2019). A five-hole probe measuring at high frequency is installed in the tip of the nose boom deriving a three-dimensional wind vector and turbulent fluxes of momentum. Additional sensors next to the five-hole probe provide further meteorological data, including the static pressure, air temperature, and humidity. More information about the accuracy and calibration methods is given by Mech et al. (2022).

Sea ice concentration: In order to classify the ocean surface, remote sensing data from the Global Change Observation Mission-Water (GCOM-W1) satellite is used. By the Advanced Microwave Scanning Radiometer 2 (AMSR2) instrument on board the satellite, the fraction of sea ice concentration (SIC) is recorded at a 3.125 km grid space resolution for the Arctic and Antarctic (Spreen et al., 2008). The SIC is provided on a daily base by the University of Bremen (https://data.seaice.uni-bremen.de/amsr2/asi_daygrid_swath/n3125/, last access: 13 June 2024). In combination with the INS, a data set including the SIC below the flight path is derived. This is later used to classify the surface below the in-situ cloud measurements into either ocean or sea ice conditions.

Air mass history modeling: To assess the daily meteorological situations and to classify the air mass origin the Hybrid Single Particle Lagrangian Integrated Trajectory model (HYSPLIT) is used (Stein et al., 2015; Rolph et al., 2017). The Global Data Assimilation System (GDAS) with 0.5 ° horizontal resolution served as a meteorological input during the AFLUX field campaign. Since July 2019 Global Forecast System (GFS), with 0.25 ° horizontal resolution is implemented in HYSPLIT, which is used for MOSAiC-ACA and HALO-(AC)^3. With the backward trajectories over the last 24 h, the air masses sampled with the aircraft get classified with an air mass origin from the ocean or the sea ice depending on the dominant surface condition below the air mass pathways.
Additionally, with a backward calculation of up to 100 h, the air masses can be assigned on a

larger scale, with a classification of air mass origin from the Central Arctic, Siberia, Greenland, or the South.

3.6 The research aircraft Polar 5 and Polar 6

The two aircraft used to collect in-situ cloud data in the scope of this work are two identical Basler BT-67 from the AWI, specifically modified for flying under extreme polar conditions (Wesche et al., 2016). During all three aircraft field campaigns, flight operations were carried out by Kenn Borek Air Ltd. Canada. Both aircraft, the Polar 5 and Polar 6 are modern versions of the Douglas DC-3 built in 1942 (Polar 5) and 1943 (Polar 6), equipped with up-to-date avionics and turbo-prob engines. Optional ski-wheel gear can be attached, which allows landing on snow. The extended nose boom serves as a platform for meteorological data acquisition, such as wind vectors, temperature, pressure, and humidity. The fuselage and the wings provide space for a variety of scientific instruments, which can be mounted as required for scientific missions. An overview of the installed instruments for the in-situ cloud measurements for the respective field campaigns is given in Sect. 3.1. Both aircraft are unpressurized, have an endurance of 5 to 6 h, and can fly at low altitudes down to 200 ft and at low speed, which is around 60 m s^{-1} during low-level in-situ cloud measurements.

Figure 36 Photo of the AWI research aircraft Polar 5 during preparation for a test flight at the airport of Longyearbyen during the AFLUX campaign.

4 Characterization of Arctic low-level clouds

4.1 The airborne field campaigns AFLUX, MOSAiC-ACA, and HALO-(AC)^3

In this work, three aircraft field campaigns were conducted in the Fram Strait, the area between Svalbard and Greenland. The airport of Longyearbyen (LYR; 78 °N, 015 °E) served as the base. All field campaigns were conducted within the framework of the "ArctiC Amplification: Climate Relevant Atmospheric and SurfaCe Processes, and Feedback Mechanisms (AC)^3" project (Wendisch et al., 2022).

The first campaign called the "Aircraft campaign observing FLUXes of energy and momentum in the cloudy boundary layer over polar sea ice and ocean" (AFLUX) took place in March and April 2019 (Mech et al., 2022). The second campaign complemented the local atmospheric measurements on board the German icebreaker research vessel Polarstern during the "Multidisciplinary Drifting Observatory for the Study of Arctic Climate" (MOSAiC) expedition (Knust, 2017; Shupe et al., 2022). These research flights "MOSAiC - Airborne observations in the Central Arctic" (MOSAiC-ACA) were performed in September 2020 (Herber et al., 2021). In both campaigns, AFLUX and MOSAiC-ACA, the flight strategy was to provide both in-situ and remote sensing measurements over the sea ice and the open ocean with Polar 5 research aircraft serving as a platform. A detailed description of the data collected during the two campaigns is described by Mech et al. (2022). The third field campaign "Arctic Air Mass Transformations during Warm Air Intrusions and Marine Cold Air Outbreaks" (HALO-(AC)^3) took place in March and April 2022 (Walbröl et al., 2023). Three aircraft were deployed to perform large-scale and collocated atmospheric measurements. The High Altitude and Long Range Research Aircraft (HALO; Krautstrunk and Giez, 2012) and Polar 5 were equipped with remote sensing instruments, while the Polar 6 airplane carried out in-situ measurements only. In addition to the cloud particle measurement systems, in-situ instruments for analyzing aerosol and trace gases were also operated on board. AFLUX and HALO-(AC)^3 took place in spring when the sea ice extent reaches its maximum, while the MOSAiC-ACA campaign took place in late summer when the sea ice extent has its minimum. The respective flight paths are displayed in Fig. 37 together with the fraction of sea ice concentration at a representative time for each campaign. The scientific target, the time of in-situ cloud measurement, the temperature within the clouds, and the origin of the sampled air masses are listed for every scientific flight in the Tables 14, 15, and 16 in the Appendix D. The meteorological situations during the campaigns and a classification of the air mass origin of the sampled air are described in more detail in Sect. 4.2. During all three campaigns, the same types of flight patterns were applied as shown in Fig. 38. The so-called racetrack pattern, sawtooth, and staircase pattern for collecting in-situ cloud data are described in detail by Mech et al. (2022).

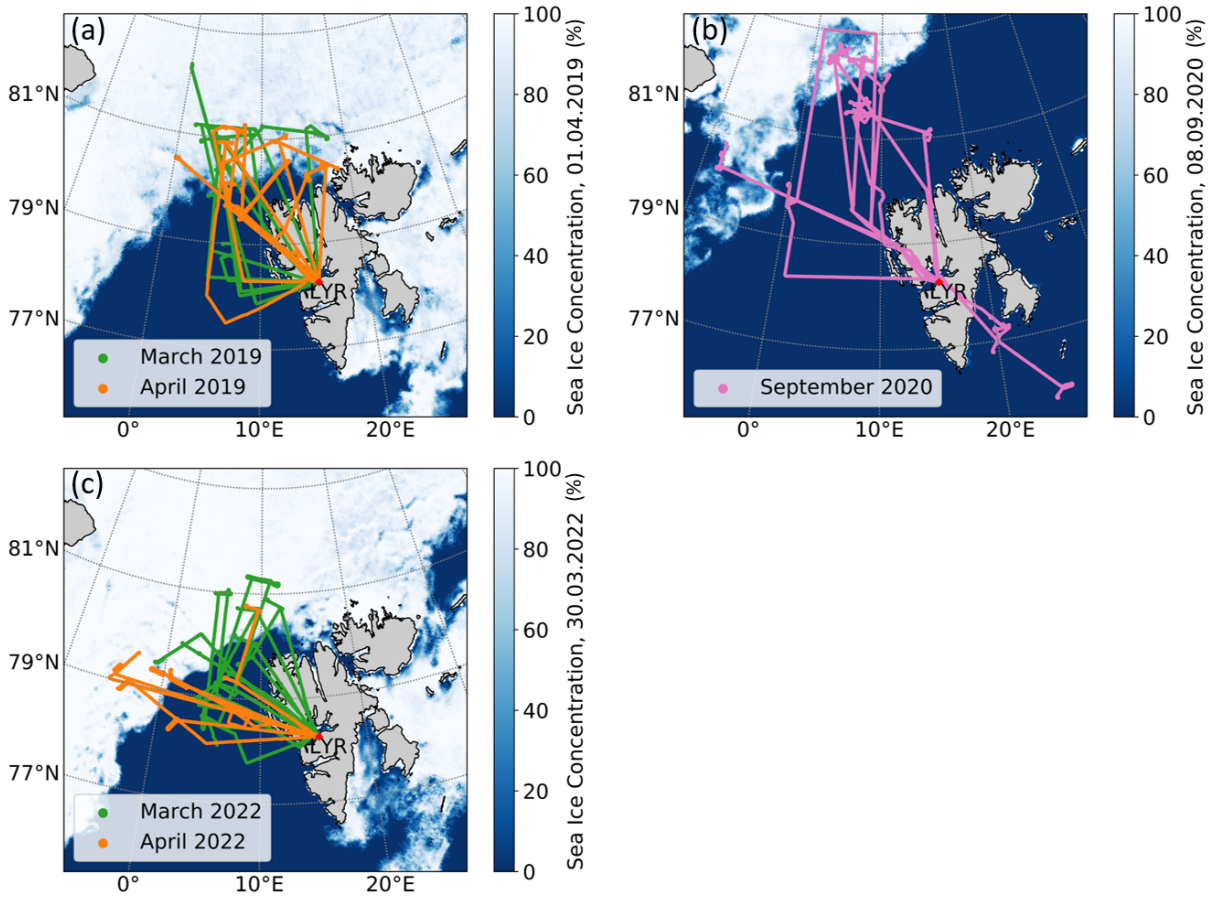

Figure 37 Map of the flights conducted (a) during AFLUX, (b) MOSAiC-ACA, and (c) HALO-(AC)^3 in the vicinity of Svalbard, Longyearbyen (LYR). Background shows the sea ice concentration at halftime of the respective campaign detected by the AMSR2.

All flights were planned in such a way that, within the limited campaign time available (between 3 and 4 weeks), a research flight was flown on every possible day, as far as this was technically possible, and the meteorological conditions at Longyearbyen airport were safe for flying. Weather forecast models and satellite images were used to actively search for clouds, and the flight plan was set the day before. Despite occasional weather changes on the day of the flight, the flight plan was not significantly modified during the flight. Since all 33 research flights were planned and carried out according to an almost similar pattern, a major bias due to the flight strategy can be excluded. Therefore, the statistical analyses, e.g. on the frequency of occurrence of the cloud phases and aerosols in Sections 4.5 and 4.6, can be considered representative for the respective surface condition and season where cloudy conditions are expected.

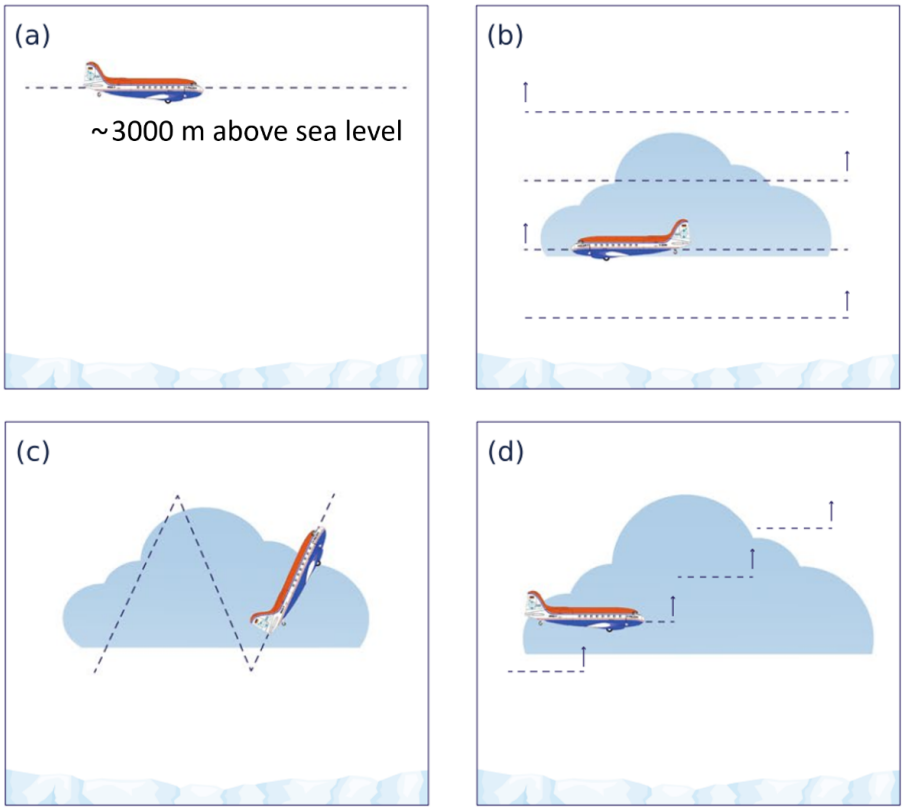

Figure 38 Different types of flight patterns flown during the campaigns: (a) remote sensing leg and (b) racetrack, (c) saw tooth, and (d) staircase pattern. Figure taken from Mech et al. (2022).

4.2 Meteorological and surface conditions

Parts of this section are published in Moser et al. (2023). In order to make the data representing the environmental conditions of the respective three campaigns comparable, a different altitude threshold for low-level clouds is used in this section compared to the altitude threshold set in Moser et al. (2023), which only included AFLUX and MOSAiC-ACA cloud data. In this section an altitude threshold of 1000 m is set because higher low-level clouds were observed during HALO-(AC)^3 and to ensure comparability of the different campaign data. Therefore the absolute values presented in this section may differ slightly from those given by Moser et al. (2023).

The conditions in the two seasons of the three campaigns were significantly different. Colder temperatures in spring compared to summer and differences in the Arctic sea ice extent have a major influence on the atmospheric temperature structure. Large-scale weather systems favor southward directed air mass transport in the Fram Strait in spring, e.g. cold air outbreaks (CAO), and northward directed transport during summer, e.g. warm air intrusions (WAI) and atmospheric rivers. As clouds form within a couple of hours inside the atmospheric boundary

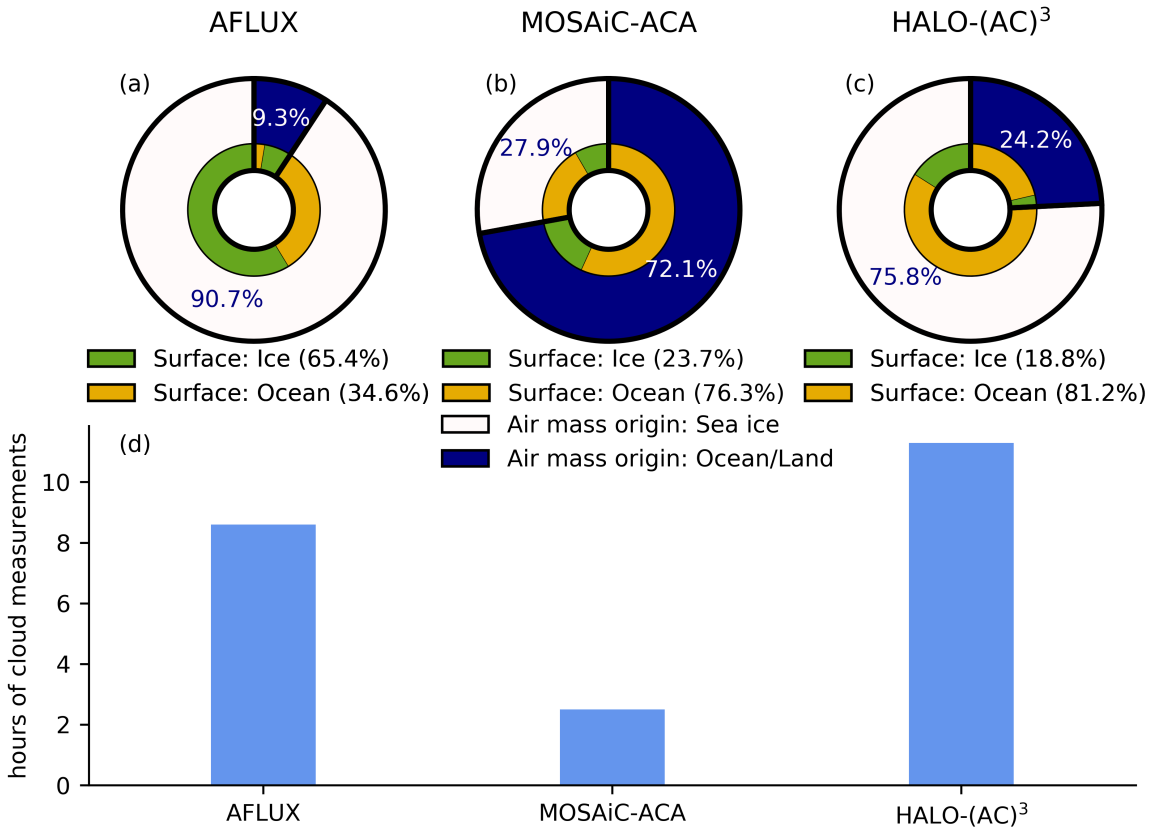

Figure 39 Percentage of time with measurements inside low-level clouds (< 1000 m) partitioned by air mass, classified as originating from the ocean or sea ice, and the surface condition below the cloud measurement for the AFLUX (a), the MOSAiC-ACA (b), and the HALO-(AC)^3. Total time within clouds over the sea ice or open ocean for each campaign is shown in (d).

layer (ABL), the sampled air masses with the low-level clouds were primarily under the influence of the sea ice during CAOs and primarily under the influence of the ocean during WAIs. Also, studies have shown that aerosol particle number concentration and chemical composition inside the Arctic ABL strongly depend on regional processes (Hartmann et al., 2020; Köllner et al., 2021). In order to determine the origin of the probed air masses during the field campaigns, backward trajectories using HYSPLIT (see Sect. 3.5) were calculated for each day with flights inside the ABL. With trajectories ending at 100 m, 300 m, and 500 m altitude at a position representative of the low-level in-situ cloud measurements (80.27 °N, 007.20 °E). In combination with the AMSR2 sea ice coverage (see Sect. 3.5), the cloud data for each flight day were classified with an air mass origin from the ocean or from the sea ice depending on the dominant surface condition below the air mass pathways over the last 24 h. The fraction of air masses in the clouds originating from the sea ice or from the open ocean is shown for every campaign in Fig. 39 (a - c) in white and blue colors. In total, 8.6 h of clouds were measured during spring 2019 (AFLUX), 2.5 h during summer 2020 (MOASiC-ACA), and 11.3 h during spring 2022

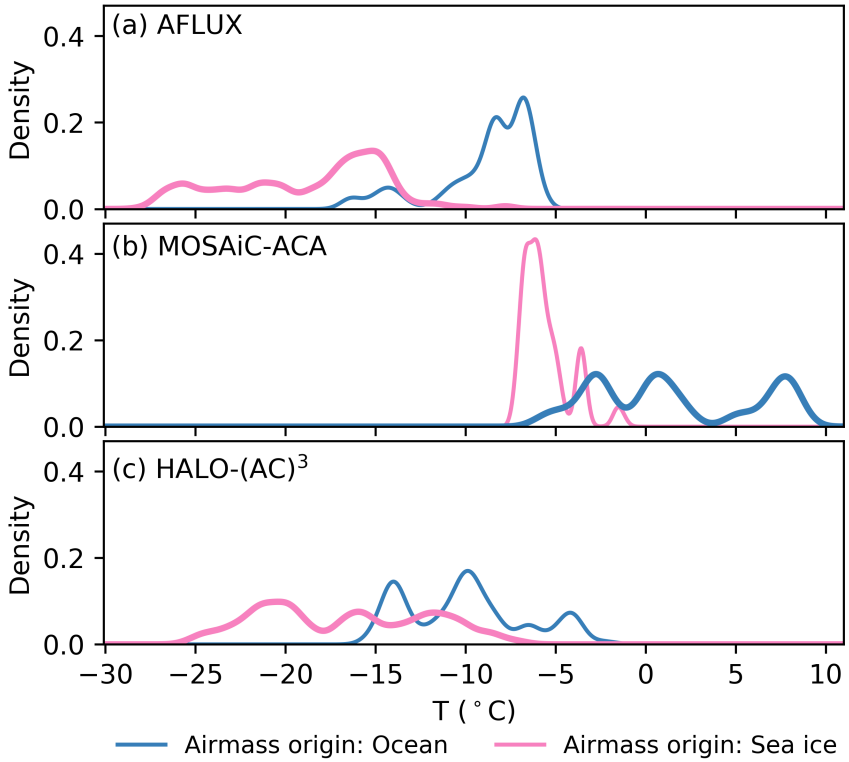

Figure 40 Normalized frequency distribution of cloud temperatures during all three campaigns. The cloud temperatures in air masses originating from the sea ice and the open ocean are shown separately with different colors. Thicker lines indicate the dominant air mass origin of the respective campaign.

(HALO-(AC)^3). Only cloud measurements either over the sea ice (SIC > 80%) or open ocean (SIC < 20%) and at altitudes below 1000 m are considered here. Clouds in the marginal sea ice zone (MIZ; 20% < SIC < 80%) are excluded. All flights during AFLUX and MOSAiC-ACA were planned to avoid any influence of Svalbard, thus the clouds sampled in these air masses are completely unaffected by land surface for the last 24 h. Due to the coordinated flight strategy with other aircraft during the HALO-(AC)^3 campaign, it was taken into account that some of the sampled air masses were influenced by the land masses of the Svalbard archipelago. These specific days are given in Table 16 in Appendix D.

The general wind direction during both spring campaigns (Fig. 39 (a, c)) was dominated by off-ice direction (wind from the north) while on-ice flow (wind from the south) prevailed during summer (Fig. 39 (b)). Air masses classified as originating from the sea ice often are associated with CAOs. Here typically strong winds transport air masses over longer distances from the north through the Fram Strait within 24 h. In contrast, air masses originating from the ocean are mostly of regional origin, with the lowest observed latitude over the last 24 h being 77 °N. Also, cloud temperature is strongly linked to the air mass origin, with colder temperatures during off-ice flow compared to on-ice flow. The temperature range for the low-level cloud measurements

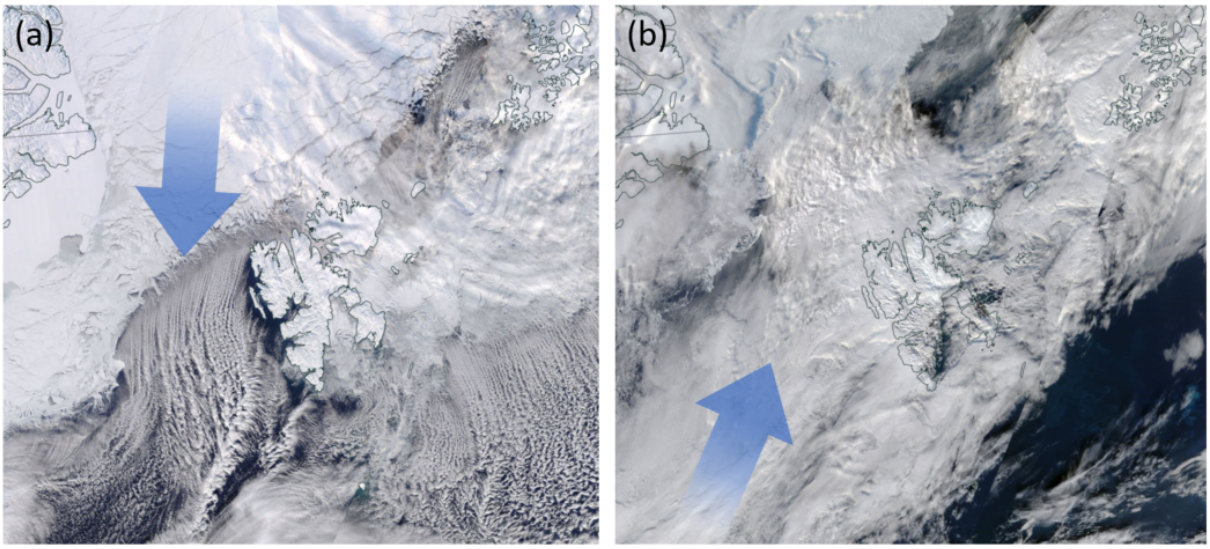

Figure 41 Satellite images by a Terra/MODIS composite from NASA worldview https://worldview.earthdata.nasa.gov (last access: 14 June 2024) showing the two weather situations dominating in the Fram Strait. (a) shows a CAO on 25 March 2022 and (b) a WAI on 4 September 2020. The blue arrow indicates the direction of the air mass transportation.

during the respective field campaigns is shown in Fig. 40, separated according to their air mass origin. Climatological studies on air mass flow direction in the Fram Strait by Dahlke et al. (2022) are in line with the meteorological analyses for the seasons spring 2019, 2022, and summer 2020, supporting the hypothesis that the measured clouds can represent spring and summer conditions in the Arctic near Svalbard. Satellite images from the two dominating weather situations in the Fram Strait are shown as an example in Fig. 41. Strong off-ice flow is usually observed during CAOs (Fig. 41 (a)), inducing cloud formation at the sea ice edge, favoring the alignment into cloud streets due to dynamical processes (Murray-Watson et al., 2023). On ice flow induced by WAIs (Fig. 41 (b)) usually transports warmer and humid air from lower latitudes onto the sea ice, leading to complex cloud structures. While CAOs and WAIs dominated the weather situation during all three campaigns, during HALO-(AC)^3 clouds have also been sampled in the vicinity of a convergence line and polar low leading to higher cloud tops.

Additionally to the air mass origins, the pie charts in Fig. 39 indicate the ratio of the surface conditions below the in-situ cloud measurements, classified as sea ice or open ocean, shown in orange and green colors. The highest fraction of clouds above sea ice was observed during the AFLUX campaign with 65.4%, while during MOSAiC-ACA and HALO-(AC)^3 the ratio was much smaller with 23.7% and 18.8%, respectively. The large difference between the two spring campaigns with respect to cloud formation over the sea ice was further investigated by studying the long range air mass transport. It was suspected that the air mass origins could be significantly different for AFLUX and HALO-(AC)^3, which was proven to be wrong by the analyses of air mass trajectories. Air masses were traced back up to 100 h using HYSPLIT and

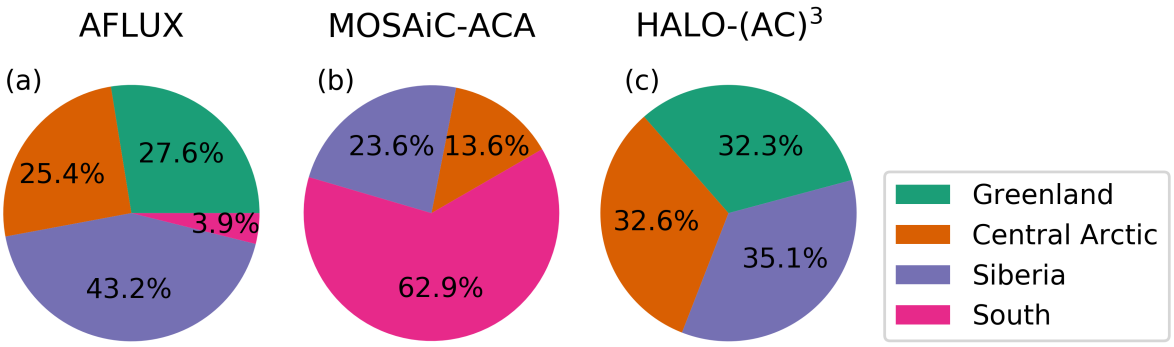

Figure 42 Long range air mass origin of the sampled clouds in the ABL for the three campaigns based on 100 h backward trajectory analyses.

classified into four categories: Greenland, Central Arctic, Siberia, and South. The respective fractions of the long range air mass origin are shown for each campaign in Fig. 42. The analysis shows that there is a significant difference between the two seasons spring and summer, as air mass transport from the south is dominating during summer. The air masses during the two spring campaigns AFLUX and HALO-(AC)^3 show comparable origins. Thus, long range transport can be excluded as a reason for the increased cloud formation observed over the sea ice during AFLUX. Subsequently, the increased cloud fraction over the sea ice during the time of the AFLUX campaign was confirmed by Schirmacher et al. (2023), as well as the fact that the reason for the increased cloud formation over the sea ice during AFLUX compared to HALO-(AC)^3 is presumably independent of the air mass origin.

Other environmental characteristics have to be considered as possible reasons for the higher cloud fraction over the sea ice during spring 2019. For example, Fig. 40 shows that colder clouds were observed in spring 2019 compared to spring 2022. In addition, leads, i.e. open areas caused by cracks in the sea ice, could contribute to an increased cloud formation process during AFLUX. However, the detection of such leads with the AMSR2 satellite data is challenging due to a resolution which is not high enough to detect leads. For future studies, data from the onboard fish eye camera could taken into account for a high-resolution sea ice concentration and to detect leads below the in-situ cloud measurements (Mech et al., 2022). Increased cloud formation may also be attributed to generally more moist air masses entering the region above the sea ice during AFLUX. The discussed environmental condition could explain the observed increased cloud formation during AFLUX compared to HALO-(AC)^3. However, further investigations are needed to confirm these hypotheses. The air mass origin, classified over the last 24 h as well as the origin from long range transport and the cloud temperatures for the respective research flights are listed in the Tables 14, 15, and 16 in Appendix D.

4.3 Transformation of microphysical cloud properties during cold air outbreaks

During most AFLUX research flights, the meteorological situation was dominated by CAOs. Here, air masses can be clearly assessed to be originated from the sea ice blowing southwards to the open ocean. The large surface temperature gradient, humidity, and aerosol intrusion change the atmospheric boundary layer (ABL) and hence the microphysical cloud composition. In Sect. 4.3.1, at first a case study of data recorded during a CAO in springtime is discussed. Further all CAO - spring cases observed during AFLUX are selected in order to analyze the microphysical change of clouds when air masses get transformed at the sea ice edge (Sect. 4.3.2).

4.3.1 Analysis of a case study

The following case study was done by Manuel Moser and parts of this study are published in Mech et al. (2022).

On 6 April 2019, the weather situation in the Fram Strait was dominated by a cold air outbreak with wind in the ABL from the north, accompanied by low- and mid-level clouds. The flight strategy aimed to sample the low-level clouds with a racetrack pattern over the covered sea ice, followed by a racetrack pattern over the marginal sea ice zone (MIZ), and a racetrack pattern over the open ocean. The flight altitude over time for the three racetrack patterns are shown in Fig. 43 (b). Corresponding 1 Hz particle size measurements combined by CAS, CIP, and PIP are shown color coded in (a). For each racetrack pattern, the mean particle size distributions of each horizontal leg are shown, in (c) for cloud measurements over the sea ice cover, (d) during measurements over the MIZ, and (e) over the open ocean. Additionally, the normalized angular scattering coefficient (ASC) and the derived asymmetry parameter g are given for every flight leg. Values with $g < 0.80$ indicate a cloud in a pure ice phase, $g > 0.83$ a liquid cloud, and values in between correspond to a mixed-phase cloud. Particle size distributions differ depending on the surface conditions, however show similarity at different altitudes. Exceptions are found for particle size distributions close and above the boundary layer where more particles smaller than 10 µm to 30 µm are observed. The boundary layer top is determined as the temperature-inversion base at 210 m for case (c) and (d), and at 300 m over the open ocean for case (e). The offset to a higher number concentration in the smaller size regime, compared to measurements below the boundary layer height, corresponds to supercooled liquid droplets. Supercooled droplets are observed also slightly below the boundary layer height, above the MIZ during the measuring flight leg at 188 m. The maximum diameter of the part of the PSD corresponding to the supercooled droplets is approximately 10 µm over the ocean and 30 µm over the sea ice. The increased number concentration in the smallest bin, observed in all cases, is associated with aerosol particles (shown in Sect. 4.5). The remaining part of the particle size distribution is attributed to ice

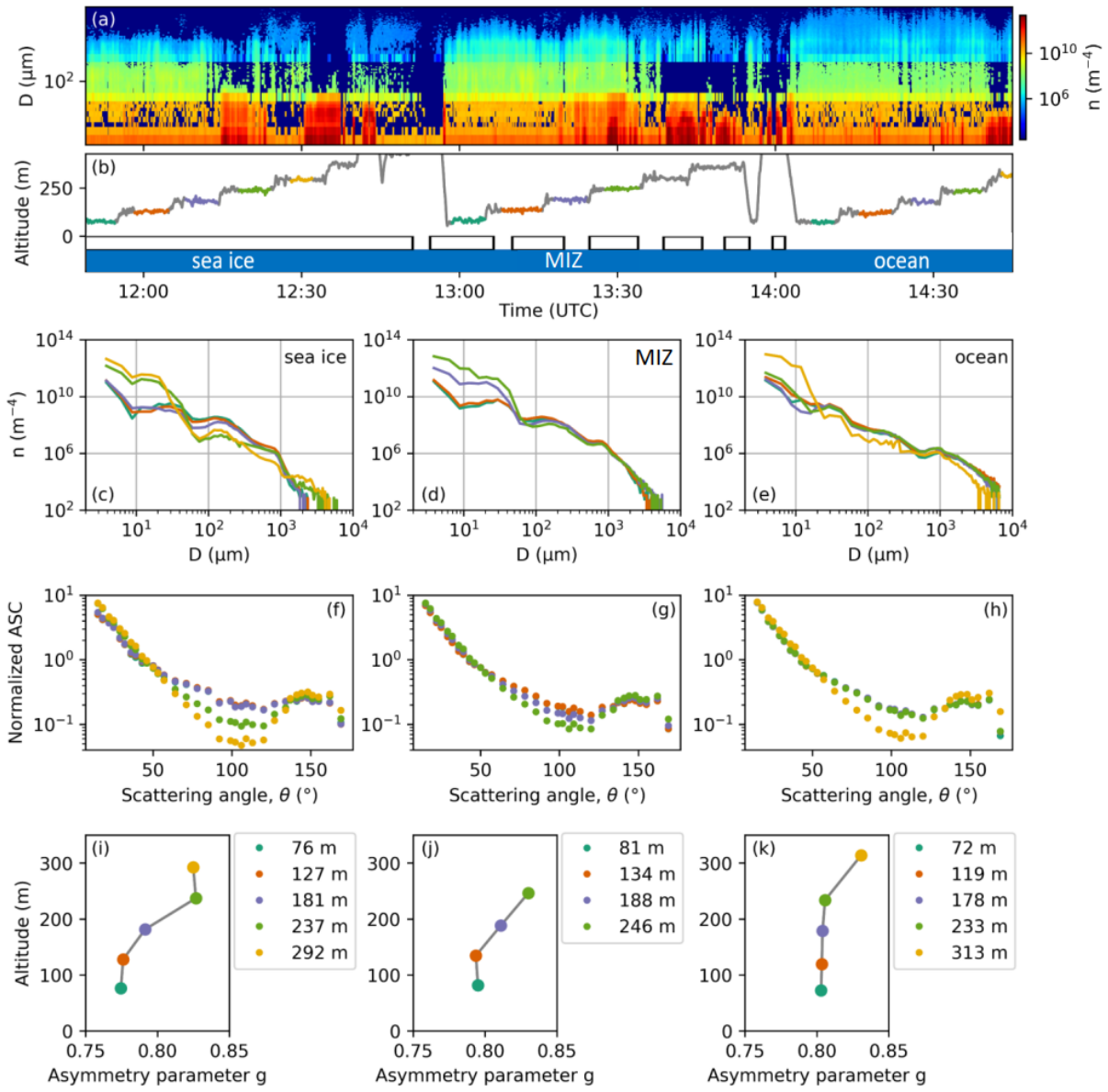

Figure 43 Case study: Cloud in-situ measurements during a racetrack pattern (b) over the sea ice, over the MIZ, and over the open ocean in the Fram Strait on 6 April 2019. (a) shows the particle size distribution from the CAS, CIP, and PIP combination color coded over the time. (c-e) give the mean particle size distribution for the horizontal flight legs for the respective surface conditions. Corresponding normalized angular scattering coefficient (ASC; f-h) and asymmetry parameter g (i-k) measured by the PN are given for each horizontal flight leg. The upper two horizontal flight legs above the MIZ had to be discarded due to an error in the CIP data.

crystals. Ice crystal size distribution hardly changes with altitude, especially over open ocean, where the boundary layer is well mixed, which is typically for low-level mixed-phase clouds in the central Arctic (Mioche et al., 2017). Multiple distinct size modes are observed in the size distribution over the sea ice, in contrast to the ocean where the modes are smoothed. An increase of turbulence is expected in the boundary layer with a decrease of sea ice, which leads

to an enhanced growth of particles by aggregation and riming processes (Benmoshe and Khain, 2014). This broadens the size modes and smoothes the size distribution. In addition, a higher particle number concentrations of large particles (> 1000 µm) is measured over the ocean as ice crystals grow faster due to enhanced humidity and turbulence over the open water. The influence of the surface conditions on the microphysical cloud properties are in line with the findings from Young et al. (2016). The results from Fig. 43 support the conclusion from Young et al. (2016) that the cloud droplet sizes increase over the MIZ. In both studies, larger ice crystals are observed over the ocean, favored by increase aggregation and riming processes. However, the decrease of the liquid droplet number concentration further downstream over the ocean together with an increase in droplet sizes triggered by collision-coalescence, is not directly observed during the case study on 6 April 2019. Reasons for such deviations in both case studies could be slightly different meteorological conditions, such as the intensity of the CAO, temperature, and humidity, which are influenced by the long range air mass origin, among other factors.

4.3.2 Statistical cloud data of several outbreak situations

In this section, all low-level cloud data (< 500 m) from horizontal flight legs obtained in CAO weather situations during AFLUX are investigated. In total, on 5 flight days, CAOs occurred, namely on 24 March 2019, 25 March 2019, 31 March 2019, 06 April 2019, and 11 April 2019. 51 flight legs in clouds were measured over the sea ice, 31 over the MIZ, and 26 over the open ocean. Despite the atmospheric structure depends on the distance to the sea ice edge (Schirmacher et al., 2023; Murray-Watson et al., 2023), only the differences between the three surface types are examined here. The median particle size distribution for each of the three surface types ocean, marginal sea ice zone and sea ice are shown in Fig. 44 including the 10 and 90% percentiles. Above 25 µm, the particle size distributions of the respective surface properties are well-defined, since the percentiles hardly deviate from the median. The wide range of number concentrations for particles smaller than 25 µm originate from the liquid droplets at the cloud top. As shown in the case study, the vertical structure of Arctic boundary layer mixed-phase clouds mainly varies in the number concentration of super-cooled droplets. The low variability of the ice crystal distribution in Arctic mixed-phase clouds was previously observed by Mioche et al. (2017). The particle size distribution varies with surface properties: Over the sea ice, up to 10 times more particles in the size range between 60 µm and 300 µm is observed. This is opposed to particles larger than 1000 µm, where more particles are predominant over the ocean. Particle size distributions in the MIZ are in a superposition of measurements over the ocean and over the sea ice. An exception are particles larger than 3 mm which are hardly observed here. The particular size modes in measurements over the ice and the growth of large snow crystals over the ocean are both consistent with the case study shown in section 4.3.1. As particle size distributions from Fig. 43 match with the median size distribution from all CAO

events during AFLUX, the case study represents well the microphysical properties of low-level boundary layer clouds during CAO situations during springtime in the central Arctic.

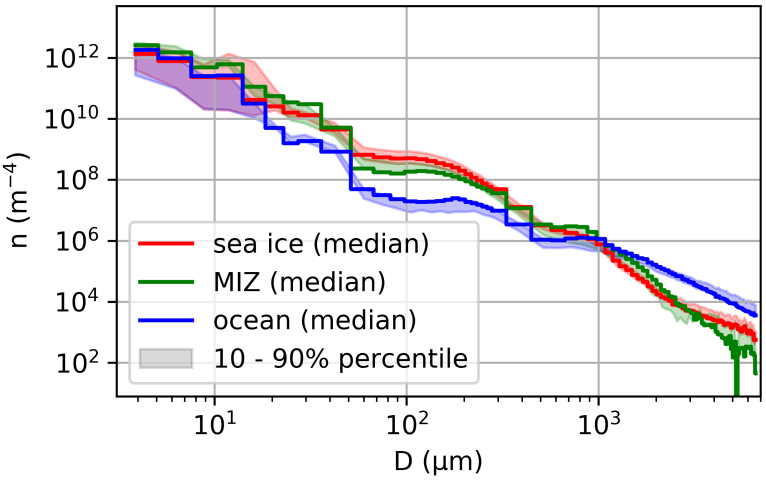

Figure 44 Median particle size distribution derived from all low-level flight legs in clouds during cold air outbreak situations in spring 2019. Size distributions are divided into measurements over the sea ice (red), the marginal sea ice zone (MIZ; green), and the open ocean (blue). The 10 - 90 % percentile is indicated by the colored area around the median particle size distribution.

4.4 Microphysical properties of Arctic low-level clouds at different ambient meteorological and surface conditions

The following section is published in Moser et al. (2023).

In the following, the measured microphysical low-level cloud (< 500 m) properties collected over sea ice and the open ocean during spring and summer are analyzed and distinguished in terms of seasons and surface conditions. A summary plot in Fig. 45 shows the variability of the CWC measured during both campaigns, AFLUX representing clouds in spring (c), and MOSAiC-ACA representing clouds in summer (d), as a function of altitude. Additionally, the median temperature for the two seasons is shown in (e). Each circle in (c) and (d) represents a mean of a cloud measurement along one horizontal flight leg in clouds where successive 1 Hz datapoints fulfill CWC > 2×10^{-4} g m^{-3}. This threshold removes more than 98% of all measurements disturbed by aerosol particles, leaving, for example, the data of thick clouds, thin ice clouds, and the measurement of light precipitation untouched. For more details about the aerosol threshold see Sect. 3.4.4. The diameter of the datapoints indicates the mean N and the color transparency shows the duration of each continuous cloud measurement. Red datapoints correspond to clouds where surface conditions are classified as sea ice and blue correspond to datapoints over open ocean. Box plots in (a) and (b) show the CWC data from (c)

and (d) respectively, weighted by the measurement time within the cloud. The boxes represent the median, the upper and lower quartile, and the whiskers give the 97.5th and 2.5th percentile. Large differences between summer and spring clouds and clouds over sea ice and ocean are revealed.

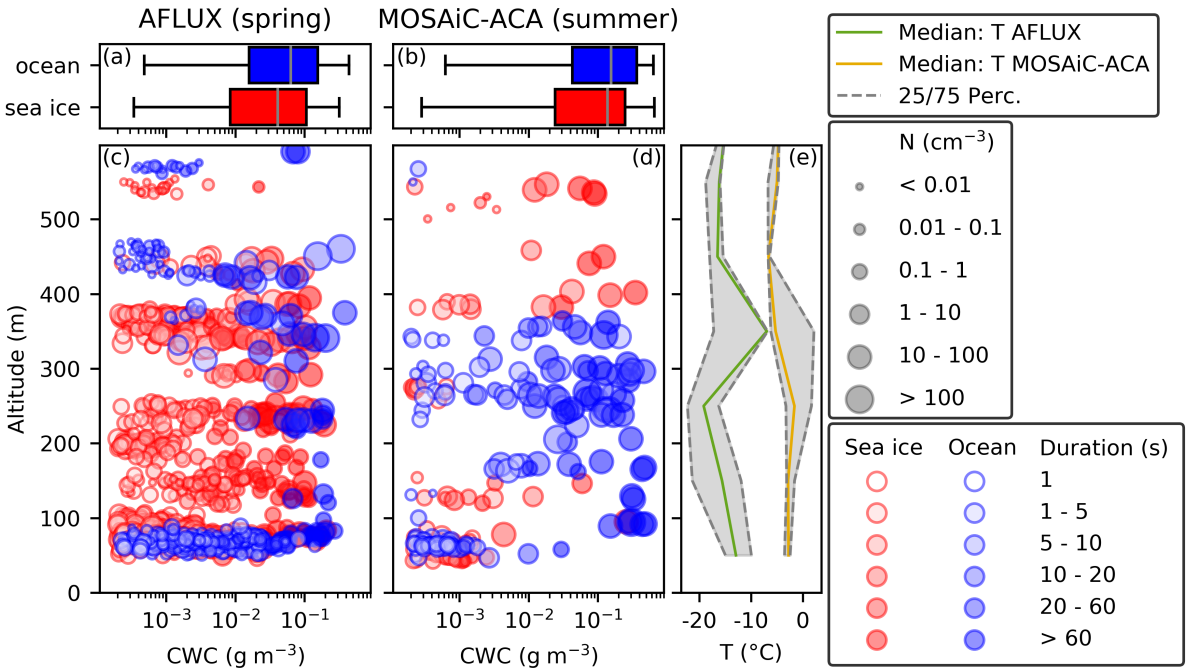

Figure 45 Overview of the in-situ measured low-level clouds during spring represented by AFLUX data set (a, c) and summer represented by the MOSAiC-ACA data set (b, d), depending on surface condition. Panels (a) and (b) show all CWC measurements below 500 m in boxplots. Panels (c) and (d) present the respective CWC values in altitude including information about N and the duration of each cloud measurement. The median temperature for both seasons is shown in (e).

The median and percentiles of the measured low-level microphysical cloud properties in Fig. 45 over the sea ice and the ocean during AFLUX and MOSAiC-ACA field campaign are given in Table 8. In addition to the microphysical cloud properties based on particles in the size range from 2.8 µm to 6.4 mm, the microphysical cloud properties for liquid particles (based on particles < 50 µm) and ice particles (based on particles > 50 µm) only are presented. The threshold of 50 µm to distinguish between ice and liquid particles is discussed in Sect. 3.4.2. In order to determine whether two values within a single column in Table 8 are statistically different, a T-tests for the mean values and Wilcoxon tests for the medians is conducted. The significance level was set at 5% to decide whether the prevalent environmental conditions influence the properties of the clouds. The following combinations are examined for each property value within a row: Between the surface condition sea ice (i) and ocean (o) in spring (a) and in summer (m) (ia-oa, im-om), between spring and summer for the two surface conditions (ia-im, oa-om), as well as

	AFLUX (spring)		MOSAiC-ACA (summer)	
	sea ice	ocean	sea ice	ocean
$\tilde{N}$ (cm^{-3})*	0.70 [0.30 / 1.88]	0.21 [0.07 / 0.57]	51.72 [7.26 / 66.93]	37.42 [13.94 / 65.80]
$\tilde{D}_{\text{eff}}$ (µm)	403 [161 / 924]	1442 [807 / 2508]	27 [19 / 32]	33 [23 / 50]
$\widetilde{\text{CWC}}$ ($g\,m^{-3}$)	0.04 [0.01 / 0.11]	0.06 [0.02 / 0.16]	0.14 [0.02 / 0.25]	0.16 [0.04 / 0.37]
$\overline{d_{\text{cloud}}}$ (m)***	1207	1313	1210	2670
$\tilde{N}_{<50\mu m}$ (cm^{-3})*	0.65 [0.27 / 1.74]	0.20 [0.06 / 0.56]	51.68 [6.97 / 66.54]	37.12 [13.66 / 65.22]
$\tilde{D}_{\text{eff}<50\mu m}$ (µm)*	17 [6 / 34]	10 [4 / 30]	21 [15 / 25]	22 [13 / 28]
$\widetilde{\text{CWC}}_{<50\mu m}$ ($g\,m^{-3}$)	(1.74 [0.04 / 10.01])$\times 10^{-3}$	(0.14 [0.004 / 2.07])$\times 10^{-3}$	0.12 [0.02 / 0.20]	0.13 [0.02 / 0.26]
$\tilde{N}_{>50\mu m}$ (cm^{-3})*	(6.0 [0.1 / 56.4])$\times 10^{-3}$	(2.5 [0.2 / 7.3])$\times 10^{-3}$	0.14 [0.01 / 0.36]	0.11 [0.002 / 0.60]
$\tilde{D}_{\text{eff}>50\mu m}$ (µm)	627 [367 / 1340]	1651 [979 / 2706]	69 [66 / 83]	72 [67 / 506]
$\widetilde{\text{CWC}}_{>50\mu m}$ ($g\,m^{-3}$)	0.02 [0.003 / 0.09]	0.06 [0.01 / 0.15]	0.02 [0.002 / 0.05]	0.04 [0.01 / 0.09]

Table 8 Properties of Arctic low-level clouds (< 500 m) during AFLUX and MOSAiC-ACA for surface condition sea ice or ocean: Median number concentration $\tilde{N}$, median effective diameter $\tilde{D}_{\text{eff}}$, median cloud water content $\widetilde{\text{CWC}}$ and mean horizontal cloud extent $\overline{d_{\text{cloud}}}$ (calculated using the duration in cloud and mean aircraft speed, $V = 60\,\text{m s}^{-1}$). The values in the square brackets give the 25th and 75th percentile respectively. The microphysical properties are calculated from all detected cloud particles as well as for particles smaller than 50 µm (assumed to be liquid) and for particles larger than 50 µm (assumed to be ice). An asterisk indicates that a combination of two values within this column is not significantly different. These combinations are as follows: $\tilde{N}$: im-om, $\overline{d_{\text{cloud}}}$: ia-oa, ia-im, i-o, $\tilde{N}_{<50\mu m}$: im-om, $\tilde{D}_{\text{eff}<50\mu m}$: ia-im, $\tilde{N}_{>50\mu m}$: i-o.

between the cloud data for each season (a-m) and surface condition (i-o). In case there is a combination for which the difference is not statistically significant, it is marked with an asterisk in Table 8, and the corresponding combination is indicated in the caption. For example, the asterisk in the first row indicates that there is no significant difference in the data between the median number concentration ($\tilde{N}$) for clouds observed over sea ice compared to clouds over the ocean during the summer campaign.

The largest differences of cloud properties are associated with the different seasons. Especially the medians of the D_{eff} during summer are significantly reduced compared to spring, with values of 27 µm over the sea ice and 33 µm over the ocean in summer, compared to values of 403 µm over sea ice and 1442 µm over the ocean in spring. The main reason for this reduction is the ambient cloud temperatures in the respective seasons. As shown in Sect. 4.2 cloud temperatures during summer campaign period are warmer compared to spring, with temperatures between -6.8 °C and +13.6 °C during MOSAiC-ACA and between -28.3 °C and -1.8 °C during AFLUX. In microphysical cloud analysis, it is important to consider the impact of seasonal temperature variations. During the spring months, temperatures favor the growth of ice crystals, while temperatures above the freezing point during summer only allow for the existence of liquid cloud particles. As a result, the D_{eff} during spring correspond to ice crystals, while in summer, these values result from smaller liquid cloud particles. During summer at warmer temperatures,

the median CWC is increased with a value of 0.16 g m^{-3} over the ocean and 0.14 g m^{-3} over the sea ice compared to colder conditions in spring, where the median CWC over the ocean is 0.06 g m^{-3} and over the sea ice 0.04 g m^{-3}. Also higher median N are found in summer, 51.7 cm^{-3} over the sea ice and 37.4 cm^{-3} over the ocean. In spring these values are reduced, 0.7 cm^{-3} measured over the sea ice and 0.2 cm^{-3} over the ocean. Similar to D_{eff}, these changes in CWC and N can be traced back to the different temperature ranges and meteorological situations during both seasons. Greater CWC during MOSAiC-ACA is related to higher humidity and higher temperatures compared to cloud measurements during AFLUX. In spring, cold air outbreaks with strong winds from the sea ice bring dry air with a low aerosol load. In contrast, in summer, the weather situations favor the transport of moist air masses from the open ocean toward the sea ice. These different synoptic situations impact cloud condensation nuclei and ice nuclei concentration, and thus influence N by cloud particle formation processes (Mech et al., 2020; Kirschler et al., 2022). The findings are supported by the microphysical cloud properties calculated for particles < 50 µm and > 50 µm in Table 8. Ice crystals dominate the D_{eff} in spring and droplets dominate the D_{eff} in summer. While droplets are the main contributor to the total CWC in summer, ice particles contribute most to the CWC in spring. The horizontal cloud extension is represented by the duration of a cloud measurement (mean aircraft speed at low-level cloud measurements at 60 m s^{-1}) in Fig. 45. Mean low-level cloud length in summer over ocean is 2670 m (44.6 s) and over the sea ice less than half 1210 m (20.0 s). In spring horizontal cloud lengths are similar, 1313 m (21.8 s) over the ocean and 1207 m (20.3 s) over the sea ice. As a result of the ambient atmospheric conditions in spring, clouds are more patchy compared to summer. This may be due to strong winds, common in the Arctic spring, which may favor the formation of cumulus clouds in cold air outbreak weather situations. Warm air intrusions and frontal systems lead to larger cloud lengths in summer. The influence of different surface conditions on the horizontal cloud extension does not appear to be significant in the in-situ cloud data set. In Fig. 45 a more homogeneous cloud distribution with altitude is observed during the time of the spring campaign compared to summer. In spring, clouds are more equally distributed up to 450 m, with slightly smaller median CWC over sea ice compared to ocean. In summer, the CWC distribution with respect to altitude is more patchy and the measured cloud heights depend on the surface conditions. Over the ocean, most of the clouds were measured in altitudes between 220-380 m with CWC reaching 0.5 g m^{-3}. The cloud layer in summer above the sea ice reaches to higher altitudes compared to the clouds above the ocean. However, hardly any clouds are observed between 150-350 m. The more homogeneous vertical cloud distribution in spring and the more clustered and multilayered cloud structure in summer are in line with the visual observations made onboard the research aircraft. During AFLUX, one homogeneous cloud layer in the low-level altitude regime was regularly observed while most of the time during summer, a complex and patchy cloud structure with multiple individual layers was present. This can be associated to a stronger coupling of the ABL in spring time which leads to a well-mixed boundary layer. In summer, warm and moist air advection from the south leads

to a stronger temperature inversion and favors multilayer clouds (Eirund et al., 2020). Besides the seasons, the prevalent surface conditions below the clouds show an impact on the microphysical cloud properties. A slightly greater CWC over the ocean is related to higher humidity and higher temperatures compared to cloud measurements over the sea ice. Over the warmer ocean compared to the sea ice, increased heat fluxes are induced and lead to a warmer and more turbulent ABL. Hence, an increased adiabatic liquid water content and the enhanced moisture transport into the ABL cause an increase of the cloud water content, allow cloud particles to grow faster and lead to a deepening of the cloud layer. This also has an impact on particle growth rate. Due to the warmer and more turbulent ABL over the ocean, larger D_{eff} are a result of a higher efficient collision-coalescence and subsequent growth via sustained supersaturation as explained by Young et al. (2016). This process could also explain the reduction of N over the ocean, which is significantly observed in spring. However, analyses in Sect. 4.5 show, that the differences of N measured over the sea ice and the open ocean might result from different aerosol sources.

Consistent with Fig. 45 and Table 8 similar trends in altitude resolved cloud properties in Fig. 46 are observed. The altitude resolved profiles show lower N, larger D_{eff} and lower CWC in spring compared to summer clouds. In Arctic spring clouds N increases with altitude to a maximum near 300 m and decreases near the top of the boundary layer. The large amount of particles, but relatively small D_{eff} at 300 m can be related to supercooled water droplets. Below, N decreases and D_{eff} increases, which is due to ice crystals growing at the expense of supercooled water droplets and then precipitate. Lower CWC values at the upper cloud part can be explained by turbulent mixing and entrainment of dry air. Also during summer when clouds are most likely in a liquid state a decrease of D_{eff} with altitude is observed. The larger median values of D_{eff} at 300 m in summer can be addressed to the presence of ice crystals. Multilayer cloud structure and lower statistics in summer hampers the interpretation of altitude resolved summer clouds especially for N and CWC. Nevertheless, altitude resolved microphysical cloud parameters derived in spring is in line with the study of Lawson and Zuidema (2009) and Mioche et al. (2017) where the in-situ data were collected in vertical profiles.

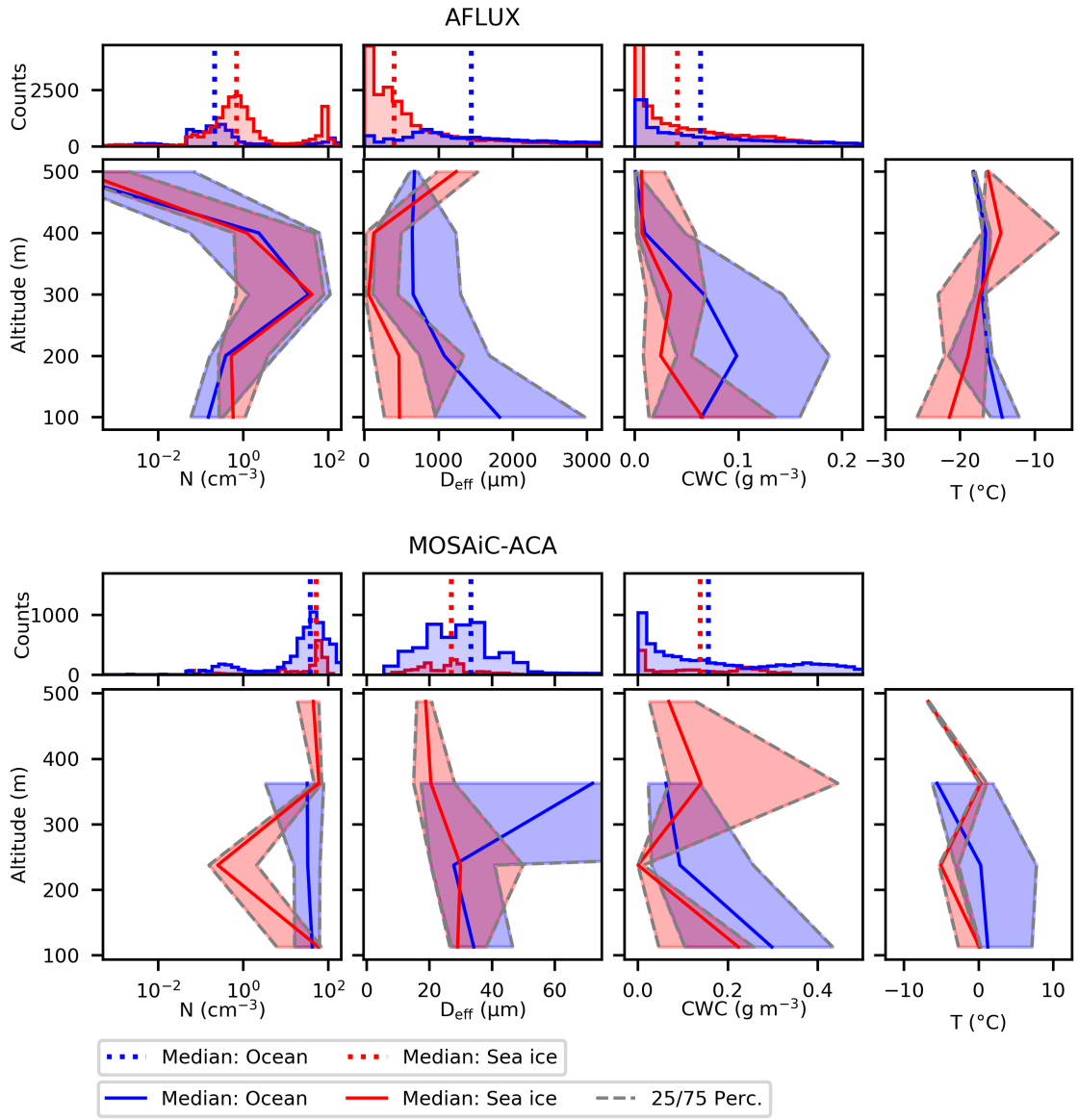

Figure 46 Height resolved microphysical cloud properties including N, D_{eff} and CWC for condition spring (AFLUX), summer (MOSAiC-ACA), over sea ice and over the ocean.

4.5 Thermodynamic phase analyses of Arctic low-level clouds with respect to different ambient meteorological and surface conditions

The following section is published in Moser et al. (2023).

In the following changes in microphysical cloud properties are discussed, including cloud particle size, concentration and thermodynamic phase, depending on surface structure and seasonal meteorological variations. All 1 Hz particle bulk measurements over the sea ice and the open ocean below 500 m for both campaigns are displayed in Fig. 47 in D_{eff} versus N space. The color displays the number of 1 Hz particle measurements at the indicated D_{eff} and N values. Peaks, which are areas with a higher probability of occurrence, are enclosed by rectangles, and in total 7 regimes are identified. The boundary values for each regime are bounded to include 80% of all data in one peak (D_{eff} and N values between 10th to 90th percentile). Each peak of higher occurrence is separated by the minimum value to the neighboring peak. According to the prevailing thermodynamic phase, particle measurements in these regimes are classified as ice (1: 1a, 1b), mixed-phase (2: 2a, 2b, 2c), liquid (3) and aerosol particles (4).

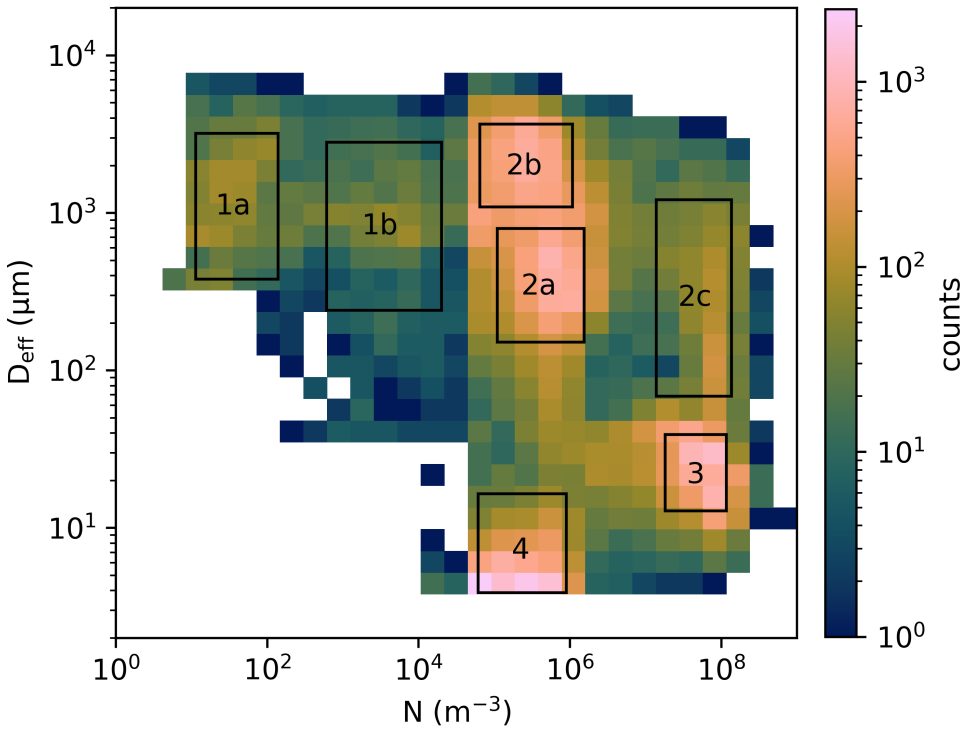

Figure 47 N versus D_{eff} for 1 Hz low-level particle data (< 500 m) over sea ice and the open ocean from the AFLUX and MOSAiC-ACA campaign combined, color coded by their occurrence. Regimes with increased occurrence frequency are marked with a rectangle. Associated cloud particles: 1 - ice, 2 - mixed-phase, 3 - liquid, 4 - aerosol particles.

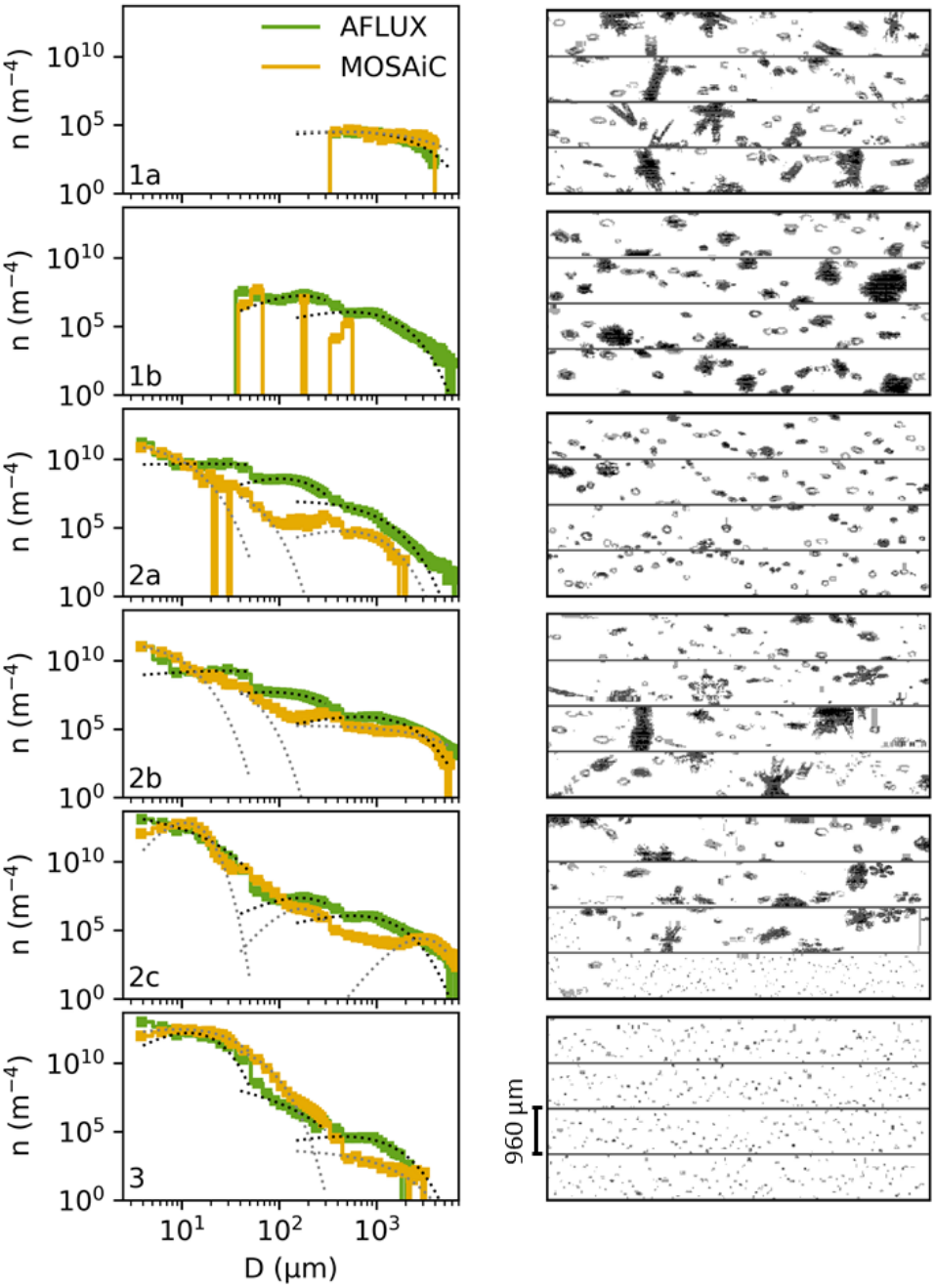

Figure 48 Particle size distribution and associated representative 2D images from CIP, for each rectangle cloud regime given by the Fig. 47.

This classification is supported by particle size distributions from the combined particle measurement systems and by particle images by the CIP (Fig. 48) as well as by the asymmetry parameter and extinction coefficient measured with the PN (Fig. 49). In addition to the particle size distributions in Fig. 48, gamma functions are fitted over the sensitive size range of the respective instrument. Cloud particle size distribution usually follows gamma type functions of the form:

$$N(D) = N_0 D^{\mu} e^{-\lambda' D}. \tag{4.1}$$

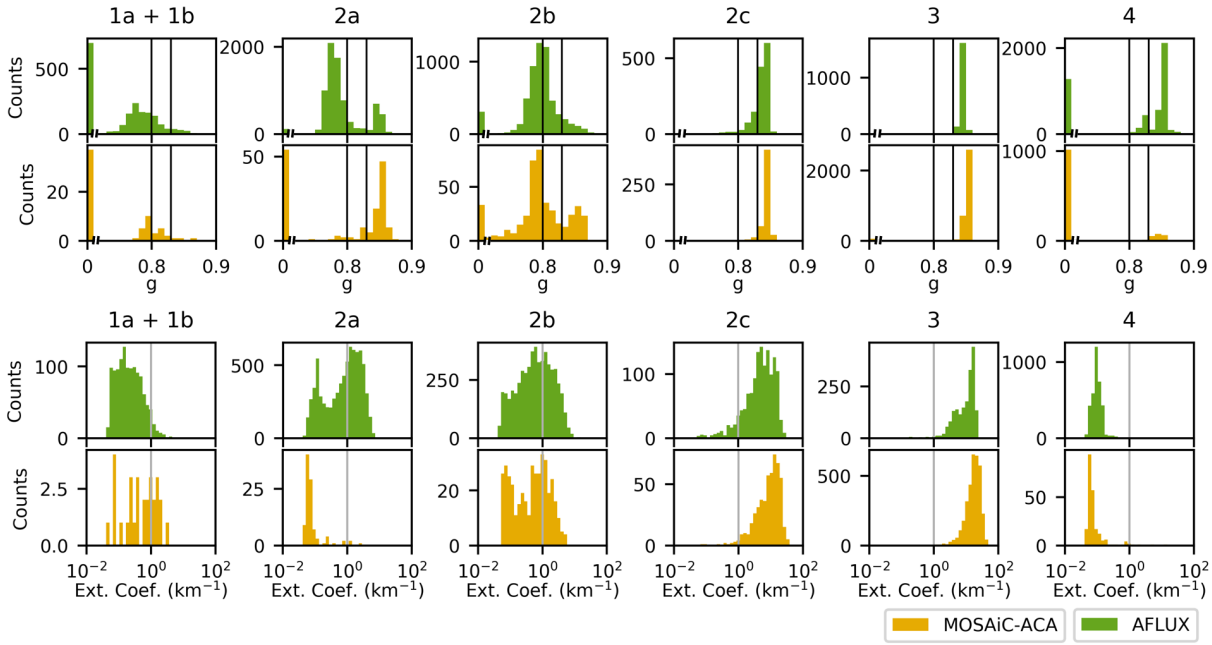

Figure 49 Frequency distribution of the asymmetry parameter and the extinction coefficient measured by the PN in each particle regime. Data is separated into measurements during AFLUX and MOSAiC-ACA.

The fitted values for the dispersion μ, the slope λ' and the intercept N_0 are given in Table 21 in the Appendix E. Ice particles in the regimes 1a and 1b have low N and larger sizes. Regime 1a shows N between 11-140 m^{-3} with D_{eff} between 0.4-3.2 mm, and regime 1b shows higher N between 620-(2×10^4) m^{-3} with diameters between 0.24-2.8 mm. Images from the CIP indicate that pristine ice crystals dominate for 1a, whereas graupel particles prevail in 1b (see Fig. 48). Regime 1 measurements are precipitating ice particles from cloud layers above while a high fraction of 1b particles could have been in contact with a cloud layer where supercooled droplets were present facilitating the formation of graupel. Phase determination with the PN data remains challenging due to the very low N and large diameters of these ice crystals, often the PN does not detect any particles (extinction coefficient < 0.05 km^{-1}). Nevertheless, the remaining data show a clear trend towards ice phase, with $g < 0.8$ and extinction coefficient values between 0.1-1 km^{-1}.

Regime 2 indicated the presence of a mixed-phase state. In total three sub-divisions are addressed to regime 2: 2a (1.1×10^5 m^{-3} < N < 1.5×10^6 m^{-3} and 0.15 mm < D_{eff} < 0.80 mm), 2b (6.5×10^4 m^{-3} < N < 1.1×10^6 m^{-3} and 1.1 mm < D_{eff} < 3.6 mm) and 2c (1.4×10^7 m^{-3} < N < 1.4×10^8 m^{-3} and 0.07 mm < D_{eff} < 1.2 mm). The N in these regimes are dominated by particles smaller than 40 µm and the D_{eff} by the larger ice crystals. Data from the PN measurements reveal a mixed-phase state as g values cannot be clearly assigned to either liquid (g > 0.83) or ice phase (g < 0.8). Extinction coefficient ranges between 0.05 and 33 km^{-1}, intermediate values are typically observed for ice and liquid water. The individual regimes 2a and 2b dif-

fer slightly by the size of the ice crystals and the N of liquid droplets. Later in this section it is shown, that 2a mixed-phase particles are frequently measured during AFLUX over the sea ice and 2b during AFLUX over the ocean. Thus, Arctic clouds in a mixed-phase state over the ocean tend to have a slightly smaller N of liquid droplets and larger sizes of ice crystals compared to clouds over the sea ice in the same season. The air temperature, vertical wind velocities, humidity and aerosol particle concentrations impact the microphysical processes in the Arctic low-level mixed-phase clouds. The mixed-phase regimes were measured at a mean temperature at -17.9 °C which is close to -15 °C, where the maximum difference between water vapor partial pressure over ice and water is located. Such temperatures favor an enhanced ice crystal growth rate in mixed-phase clouds. The larger temperature gradient between open ocean and the atmosphere enhances vertical velocities and humidity transport which might induce a faster ice crystal growth rate. Similar to the slight increase of the total N in clouds (see Sect. 4.4) over the sea ice compared to the open ocean, the higher number of liquid droplets in mixed-phase conditions over the sea ice could be explained by an increased cloud condensation nuclei concentration. Smaller ice crystals with higher N can be related to enhanced ice nucleating particle concentrations, which has been observed in other studies in the central Arctic before (Hartmann et al., 2020; Porter et al., 2022). Regime 2c, mixed-phase cloud measurements, is dominated by supercooled liquid cloud droplets with coexisting ice crystals, which have a higher N than 2a and 2b, as well as larger diameters compared to 2b. In number 2 regimes the Wegener-Bergeron-Findeisen process (WBF; Wegener, 1912; Bergeron, 1935; Findeisen, 1938) is very likely, with different ice crystal and water droplet growth and evaporation rates.

Cloud data with $1.8\times10^7\,\mathrm{m^{-3}} < N < 1.2\times10^8\,\mathrm{m^{-3}}$, and $13\,\mu\mathrm{m} < D_{\mathrm{eff}} < 40\,\mu\mathrm{m}$ are addressed to regime 3, cloud particles in liquid state. 2D images from the CIP show spherical particles while the extinction coefficient and asymmetry parameter from the PN support the assumption of the liquid phase (mean values: $g = 0.84$ and extinction coefficient = $16\,\mathrm{km^{-1}}$). Very rarely larger ice crystals may be present at the same time with liquid droplets. These particles are visible in the PSD, however negligible in the total particle concentration with > 5 orders of magnitude lower concentration than the liquid droplets.

Particle measurements with very small D_{eff} ($< 16\,\mu\mathrm{m}$) and $6.2\times10^4\,\mathrm{m^{-3}} < N < 9.0\times10^5\,\mathrm{m^{-3}}$ are attributed to regime 4. These particles are too small to be resolved by the CIP and are exclusively recorded by the CAS and CDP. The PN data recorded here in this regime can not be addressed to any distinct cloud phase. Videos from onboard cameras show no visible clouds during regime 4 particle observations. These particles are addressed to large aerosol particles (lower detection limit of the particle measurement system: 2.8 µm) originated by the ocean and the sea ice.

The frequency of occurrence of each particle regime with respect to the four conditions (spring-ice, spring-ocean, summer-ice and summer-ocean) is given in Fig. 50. In spring Arctic low-

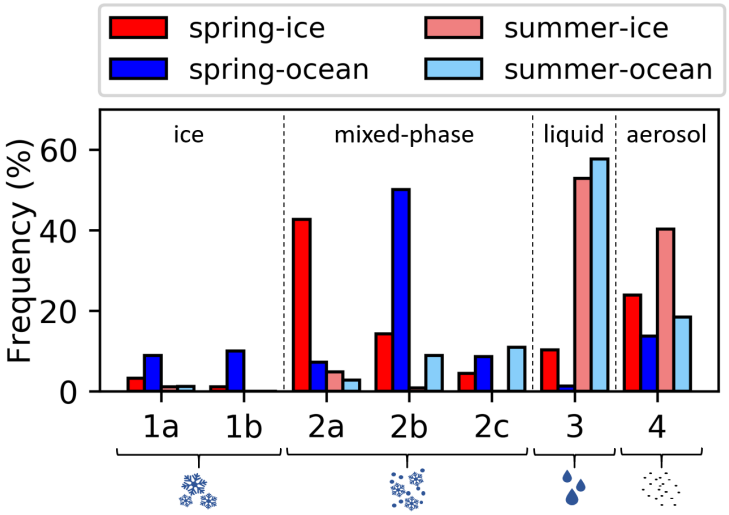

Figure 50 Frequency of occurrence for each particle regime (1a, 1b: Ice particles; 2a, 2b, 2c: Mixed-phase particles; 3: liquid particles; 4: Aerosol particles), separated by season and surface conditions. The values are normalized by the respective environmental conditions.

level clouds are most likely in a mixed-phase state (regimes 2a, 2b or 2c). The microphysics of mixed-phase regimes is slightly different depending on surface conditions as the 2a cloud regime is measured with a higher frequency over the sea ice and 2b cloud regime dominates over the open ocean. Mixed-phase clouds with microphysics corresponding to 2c are observed with very low probability and are not found in summertime over the sea ice. In general the mixed-phase state in clouds is suppressed in summertime as temperatures are too warm to favor ice formation and the WBF process. Pure liquid phase (regime 3) is the prevailing cloud type in summertime, regardless of the surface. Temperatures close to 0 °C during the MOSAiC-ACA campaign (see Fig. 40) are warmer compared to spring and do suppress ice crystal formation or lead to melting of precipitating particles from above. So pristine ice clouds (1a and 1b) are mainly detected in spring, here with a higher probability over the ocean. Aerosols without liquid or ice phase particles (regime 4) are frequently measured during both seasons with a higher frequency over the sea ice for both cases. An elevated N of small particles over the sea ice was already observed in previous studies, e.g. in a case study by Young et al. (2016). Here the enhanced N is explained by swollen aerosol particles associated with a haze layer over the sea ice. As this increase is observed systematically in summer and spring where air mass origin differs strongly, a local source is assumed. Such sources could be driven by biological processes in the sea ice (Dall´Osto et al., 2017; Hartmann et al., 2020), however the presence of cracks, open leads and polynyas[4] in the sea ice have to be assumed. A more likely assumption is aerosols consisting of sea salt as the aerosol particles exceed diameters larger than 2.8 µm (Kirpes et al., 2018) (minimum size to be detected by the CDP). Over the ocean sea spray aerosols are emitted into the atmosphere via wave breaking mechanism (Blanchard, 1989).

[4] Polynyas are large areas of open water surrounded by sea ice.

Over snow and ice-covered areas sea salt aerosols might be brought into the atmosphere by mechanisms related to blowing snow or frost flowers (Yang et al., 2008; Seguin et al., 2014; Xu et al., 2016; Huang and Jaeglé, 2017). But the mechanism of these processes is still under discussion (Willis et al., 2018). In this respect, the data of AFLUX and MOSAiC-ACA propose that sea salt emitting processes over the sea ice are more efficient than over the open ocean. Sea salt aerosols can act as cloud condensation nuclei. Therefore, the higher number of sea salt aerosol particles over the sea ice could explain the enhanced N observed in Sect. 4.4 and the distribution of occurrence of 2a and 2b over the sea ice and the open ocean. Please note, the difference of $\tilde{N}$ between the surface ocean and sea ice in Table 8 does not pass a statistical significance test for the MOSAiC-ACA campaign. However calculating $\tilde{N}$ for the dominant phase in summer, reveals a higher number of liquid particles over the sea ice during summer (see Table 19 in Appendix E).

End of the part published in Moser et al. (2023).

An overview of the thermodynamic phase distribution, separated for all flights, is presented in Fig. 67 for AFLUX and Fig. 68 for MOSAiC-ACA in Appendix D. Based on the presented thermodynamic phase separation, the microphysical properties for the ice (see Fig. 70 and Table 17), mixed-phase (see Fig. 71 and Table 18), liquid (see Fig. 72 and Table 19), and aerosol (see Table 20) regimes are given separately in the Appendix E.

Visual presentation of the cloud regimes

A starboard facing camera was installed on Polar 5 during the AFLUX field campaign. Figure 51 shows various cloud situations, which can be assigned to a specific regime at the time of capture. Regimes 2c and 3 contain images that were not taken directly during the phase detection but show the respective cloud situations from above. The captured images of the cloud situations are consistent with the in-situ measurement and thermodynamic phase classifications. During the ice phase measurements (1a, 1b), either precipitation from an upper cloud layer or haze, which corresponds to a pure ice cloud, is observed. Similar thin clouds as in the case of ice clouds are observed in the mixed-phase regimes (2a, 2b). Clouds with a higher optical thickness are observed in the mixed-phase state 2c compared to 2a and 2b. In all mixed-phase regimes, optical phenomena such as parhelia, halos, rainbows, and glories can be observed, some of which occur in combination. Rainbows and glories indicate liquid particles in the atmosphere, while optical phenomena such as parhelia and halos are caused by ice crystals. A cloud structure with similar optical thickness as in regime 2c is observed for liquid clouds (3). Also here, glories are frequently observed, which confirms the liquid phase. In regime 4 measurements which correspond to aerosols, no clouds are visible at the current flight altitude. In some cases, situations with very clear visibility and cloud free skies are observed.

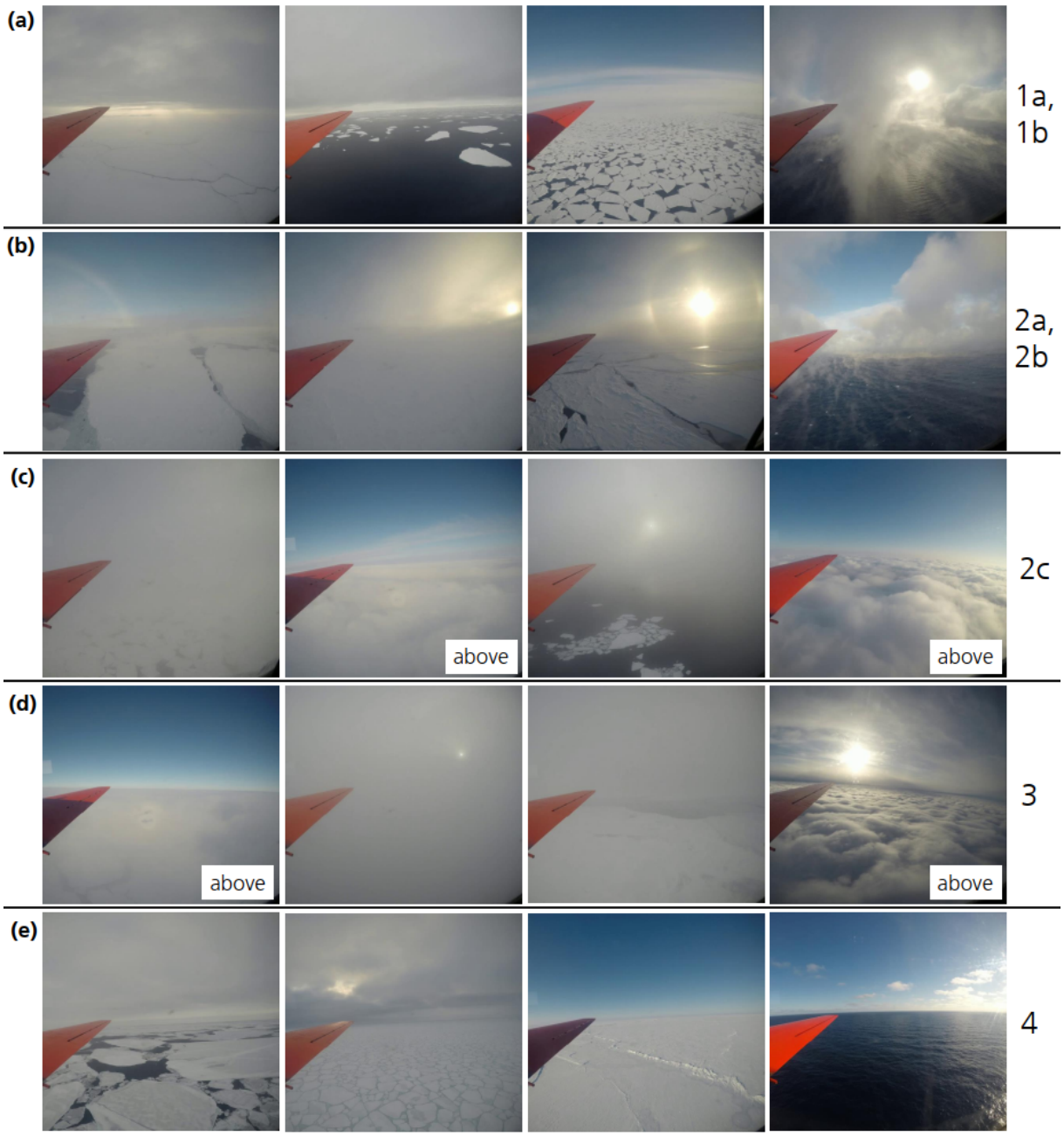

Figure 51 Images were taken by an on-board camera and show situations in which different thermodynamic phases were detected by the in-situ cloud instruments: Ice phase in (a), mixed-phase in (b) and (c), liquid phase in (d), and aerosols in (e). The label "above" in some images indicates that the cloud below the aircraft corresponds to the assigned phase. This categorization was assigned during an ascent or descent shortly before or after the image was taken.

4.6 Cloud properties in spring 2022 during HALO-(AC)^3

In Sect. 4.4 and 4.5, the microphysical properties and thermodynamic phases of low-level Arctic clouds were analyzed based on the two campaigns AFLUX and MOSAiC-ACA. In 2022, an additional data set of Arctic low-level clouds was collected during a third campaign within the scope of this thesis. The HALO-(AC)^3 campaign took place at the same time of year as the 2019 AFLUX campaign and in the same region near Svalbard. For more details on the campaigns, see Sect. 4.1.

Here, the in-situ cloud data are analyzed using the same methods as applied in Sect. 4.4 and 4.5 to determine the properties of low-level Arctic clouds in early spring 2022. Subsequently, these results are compared to the 2019 spring data from the AFLUX campaign, questioning whether the two spring campaigns yield similar results and whether the data set collected is generally representative for spring in the Fram Strait.

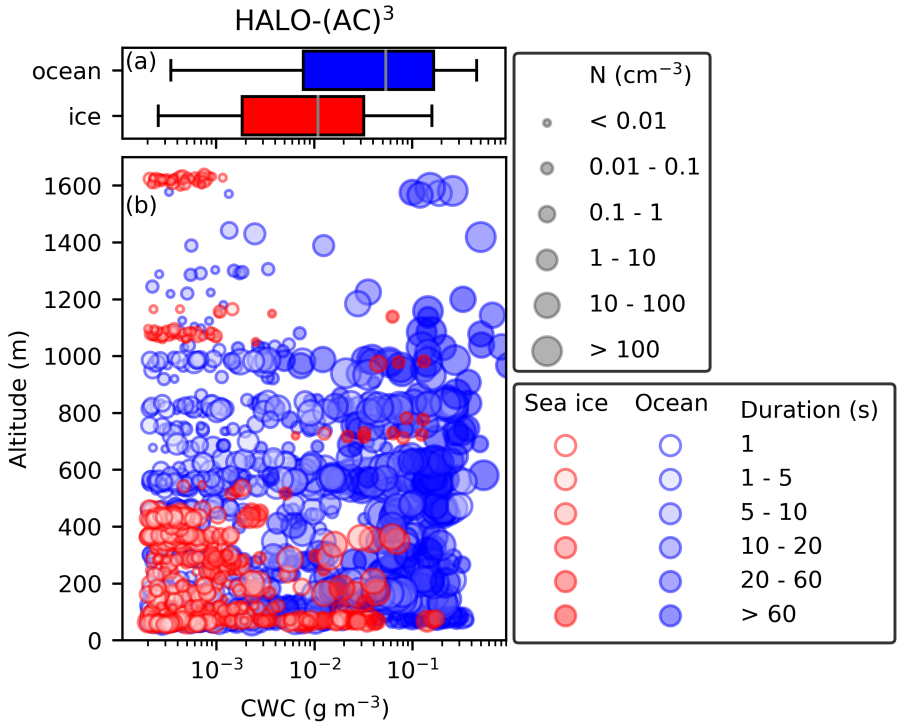

Figure 52 Overview of the in-situ measured low-level clouds during the HALO-(AC)^3 campaign, divided into the surface conditions ocean and sea ice. Panel (a) shows all CWC measurements below 1000 m in boxplots. Panel (b) presents the respective CWC values in altitude, including information about N and the duration of each cloud measurement.

An overview of all in-situ cloud measurements during the HALO-(AC)^3 campaign is shown in Fig. 52. The presentation of this overview is based on Fig. 45, which compares the AFLUX and MOSAiC-ACA measurements. Each circle in (b) represents a mean of a cloud measurement along one horizontal flight leg in clouds where successive 1 Hz data points satisfy CWC $> 2\times10^{-4}$ g m^{-3}. The diameter of the data points indicates the mean N and the color

	HALO-(AC)^3	
	Sea ice	Ocean
$\tilde{N}$ (cm^{-3})	0.07 [0.003 / 0.21]	0.18 [0.06 / 32.96]
$\tilde{D}_{\text{eff}}$ (µm)	480.08 [272.53 / 795.17]	693.65 [207.97 / 1392.24]
$\widetilde{\text{CWC}}$ (g m^{-3})	0.01 [0.002 / 0.03]	0.05 [0.008 / 0.17]
$\overline{d_{\text{cloud}}}$ (m)	798	1390
$\tilde{N}_{<50\mu\text{m}}$ (cm^{-3})	0.12 [0.06 / 0.30]	0.24 [0.07 / 58.34]
$\tilde{D}_{\text{eff}<50\mu\text{m}}$ (µm)	10.72 [3.90 / 30.16]	10.48 [6.20 / 18.65]
$\widetilde{\text{CWC}}_{<50\mu\text{m}}$ (g m^{-3})	(0.003 [0.0 / 0.34])$\times 10^{-3}$	(0.03 [0.002 / 12.33])$\times 10^{-3}$
$\tilde{N}_{>50\mu\text{m}}$ (cm^{-3})	(1.31 [0.27 / 6.94])$\times 10^{-3}$	(3.09 [0.32 / 11.32])$\times 10^{-3}$
$\tilde{D}_{\text{eff}>50\mu\text{m}}$ (µm)	550.89 [325.39 / 823.58]	1019.06 [553.36 / 1635.55]
$\widetilde{\text{CWC}}_{>50\mu\text{m}}$ (g m^{-3})	(9.82 [1.53 / 30.31])$\times 10^{-3}$	(26.47 [3.92 / 116.68])$\times 10^{-3}$

Table 9 Properties of Arctic low-level clouds (< 1000 m) during HALO-(AC)^3 for surface condition sea ice or ocean: Median number concentration $\tilde{N}$, median effective diameter $\tilde{D}_{\text{eff}}$, median cloud water content $\widetilde{\text{CWC}}$ and mean horizontal cloud extent $\overline{d_{\text{cloud}}}$ (calculated using the duration in cloud and mean aircraft speed, $V = 60\,\text{m s}^{-1}$). The values in the square brackets give the 25th and 75th percentiles, respectively. The microphysical properties are calculated from all detected cloud particles as well as for particles smaller than 50 µm (assumed to be liquid) and for particles larger than 50 µm (assumed to be ice). Similar to Table 8, the data was checked using significance tests. All combinations show that the values within a column are significantly different.

transparency indicates the duration of each continuous cloud measurement. Red data points correspond to clouds where surface conditions below are classified as sea ice, and blue corresponds to data points over open ocean. The boxplots in (a) contain the 1 Hz data of all cloud measurements below 1000 m. The boxes represent the median, the upper and lower quartiles, and the whiskers give the 97.5th and 2.5th percentiles.

Similar to Table 8, which shows the cloud microphysical properties during the AFLUX and MOSAiC-ACA campaigns in spring 2019 and summer 2020, Table 9 presents the median and percentiles of the cloud microphysical properties from Fig. 52 over sea ice and the open ocean during the HALO-(AC)^3 campaign. In addition to the microphysical cloud properties based on particles in the size range from 2.8 µm to 6.4 mm, the microphysical cloud properties for liquid particles (based on particles < 50 µm) and ice particles (based on particles > 50 µm) are presented separately. As was done with the AFLUX and MOSAiC-ACA data, a statistical significance test was performed here to check whether the clouds over sea ice and the open ocean were significantly different. All combinations within one row in Table 9 resulted in significant differences.

The AFLUX and the HALO-(AC)^3 campaign took place in spring, but the first campaign in 2019 and the second in 2022. The differences and similarities in the cloud microphysics of the

two spring campaigns are elaborated in the following, as well as how the summer 2020 campaign differs from the spring campaigns.
Comparing the height distributions of the clouds in Fig. 45 and Fig. 52, it is noticeable that low-level clouds were observed at higher altitudes during HALO-(AC)^3. While over the sea ice, almost all low-level clouds are measured below 500 m, low-level clouds over the ocean are measured up to 1000 m height during HALO-(AC)^3. For this reason, an altitude threshold of 1000 m is used for the HALO-(AC)^3 cloud data in Table 9. Weather conditions are likely to be the reason for clouds with higher altitudes over the ocean in 2022 compared to 2019. While during AFLUX, there were only two dominant weather situations, CAO and WAI, during the HALO-(AC)^3 campaign, additional cloud structures originating from a convergence line and a polar low were measured. For comparison of the cloud microphysics between the three campaigns, the microphysical cloud values from Table 8 of the AFLUX and MOSAiC-ACA campaigns and the microphysical cloud values from Table 9 of the HALO-(AC)^3 campaign are displayed in Fig. 53. The red and blue colors distinguish the cloud measurements over the sea ice and the open ocean, respectively. Dark colors represent cloud measurements during spring of 2019 (AFLUX) and 2022 (HALO-(AC)^3), while bright colors represent cloud measurements during the summer 2020 (MOSAiC-ACA). The first column (N, D_{eff}, CWC) shows the cloud microphysics calculated from the entire particle size range from 2.8 µm to 6.4 mm. Columns two ($N_{<50\mu m}$, $D_{\text{eff}<50\mu m}$, $\text{CWC}_{<50\mu m}$) and three ($N_{>50\mu m}$, $D_{\text{eff}>50\mu m}$, $\text{CWC}_{>50\mu m}$), respectively, represent only particles smaller than 50 µm, considered here as liquid particles, and particles larger than 50 µm, considered as ice particles.

In order to compare the distributions of the microphysical cloud properties between the three campaigns, the Wasserstein metric W is applied in the following. The Wasserstein distance measures the similarity between two distributions. The distance is calculated from the minimum cost required to redistribute the data from one distribution to match the other (Ramdas et al., 2015). The cost is the product of the amount of data to be redistributed and the distance over which it is moved. A small value of the Wasserstein distance indicates that the distributions are similar, while a large value indicates differences. The Wasserstein distance can be calculated from the cumulative distribution functions and is equal to the area between both cumulative distribution functions. The unit of the Wasserstein distance is the same as the unit of the distance measurement in the respective data space. In Table 10, the Wasserstein distance of the microphysical cloud data between the three campaigns are calculated. The AFLUX data set is used as the reference. In addition, the data is separated between measurements over the sea ice and measurements over the ocean. The corresponding entries in the matrices in Table 10 can be represented mathematically as follows:

$$a_{\text{ij}} = W(A_{\text{i}}, B_{\text{j}}) = \int_{-\infty}^{+\infty} \left| F_{A_i}(x) - F_{B_j}(x) \right| \, dx \tag{4.2}$$

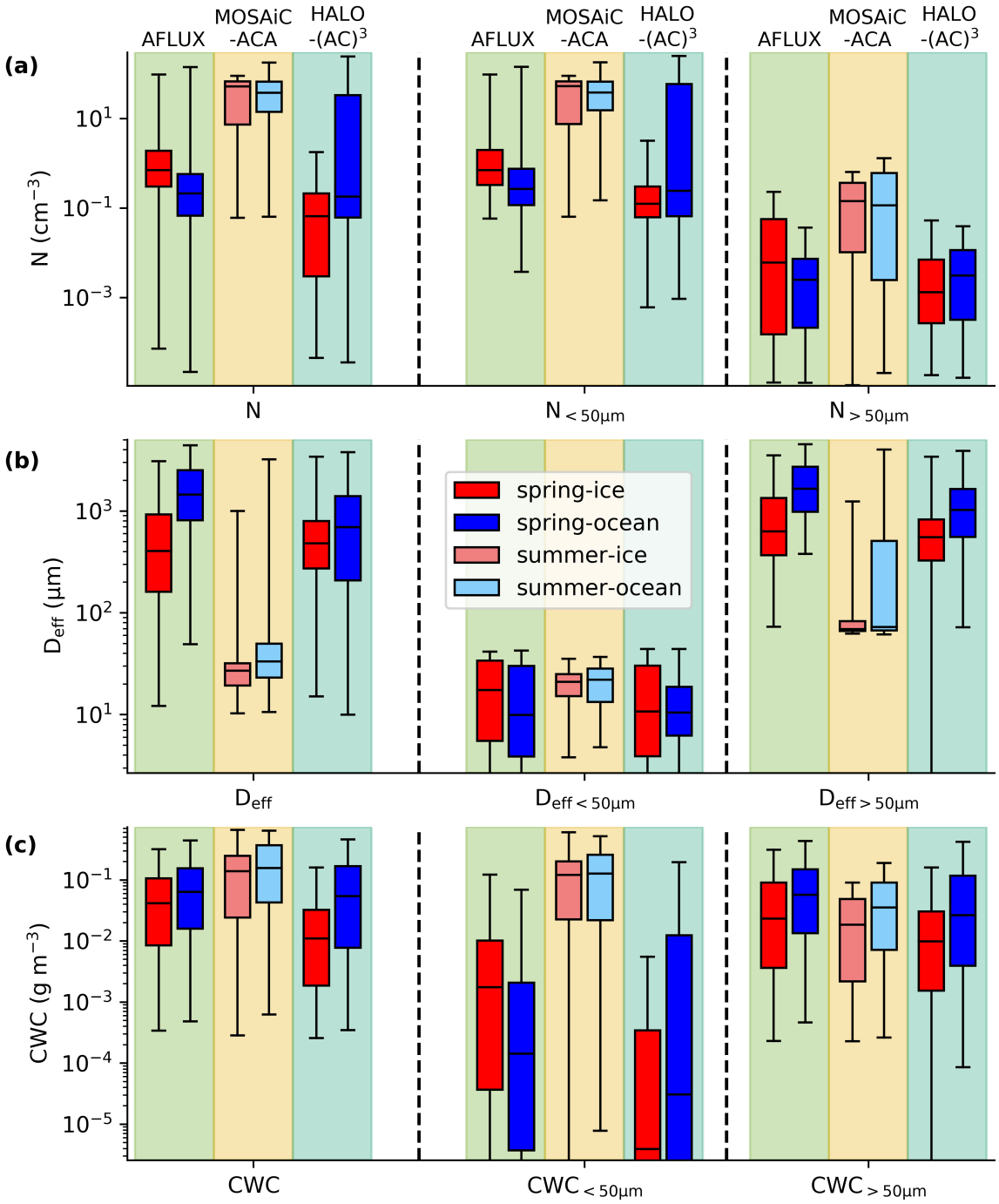

Figure 53 Overview of the microphysical cloud values from Table 8 and 9. The boxplots include the median, upper, and lower quartiles, and the whiskers give the 2.5th and 97.5th percentile. Data is classified in clouds measured above the sea ice (red) and the open ocean (blue). Boxplots, including the microphysical properties from all detected cloud particles, are given in the first column, microphysical properties from particles smaller than 50 µm (assumed to be liquid) in the second column, and the microphysical properties from particles larger than 50 µm (assumed to be ice) in the third column.

where A and B are the set of 1 Hz data of a microphysical quantity, e.g. N, D_{eff} or CWC of a given campaign. F represents the cumulative distribution functions of the respective data set. The subscripts i and j divide the measurements into cloud data above the sea ice or the open ocean.

To test the significance of the calculated Wasserstein distances, a bootstrapping procedure (Efron and Tibshirani, 1994) with 1000 iterations is applied. In this process, the two data sets are combined, and data points are randomly selected with replacement from the combined data set in order to generate two new samples, each with the size of the original respective data sets. The Wasserstein distance is calculated for each of the newly generated 1000 sample pairs. From this, a p-value is calculated that quantifies how frequently the bootstrapped distances are greater than or equal to the observed distance. The significance level is set at 1%. The calculated Wasserstein distances in Table 10 all have $p < 1\%$, indicating that all given values are statistically significant. In the following, only the same surface types are compared, so only the entries along the diagonal in the matrices in Table 10 are mentioned.

(a)

	$B_1 = N_{\text{MOSAiC-ACA, ice}}$ $B_2 = N_{\text{MOSAiC-ACA, ocean}}$	$B_1 = N_{\text{HALO-(AC)}^3\text{, ice}}$ $B_2 = N_{\text{HALO-(AC)}^3\text{, ocean}}$
$A_1 = N_{\text{AFLUX, ice}}$ $A_2 = N_{\text{AFLUX, ocean}}$	$a_{ij} = \begin{bmatrix} \mathbf{29.60\,cm^{-3}} & 35.54\,\text{cm}^{-3} \\ 35.86\,\text{cm}^{-3} & \mathbf{37.07\,cm^{-3}} \end{bmatrix}$	$a_{ij} = \begin{bmatrix} \mathbf{12.03\,cm^{-3}} & 22.05\,\text{cm}^{-3} \\ 10.53\,\text{cm}^{-3} & \mathbf{23.13\,cm^{-3}} \end{bmatrix}$

(b)

	$B_1 = D_{\text{eff MOSAiC-ACA, ice}}$ $B_2 = D_{\text{eff MOSAiC-ACA, ocean}}$	$B_1 = D_{\text{eff HALO-(AC)}^3\text{, ice}}$ $B_2 = D_{\text{eff HALO-(AC)}^3\text{, ocean}}$
$A_1 = D_{\text{eff AFLUX, ice}}$ $A_2 = D_{\text{eff AFLUX, ocean}}$	$a_{ij} = \begin{bmatrix} \mathbf{601\,\mu m} & 379\,\mu\text{m} \\ 1630\,\mu\text{m} & \mathbf{1385\,\mu m} \end{bmatrix}$	$a_{ij} = \begin{bmatrix} \mathbf{169\,\mu m} & 286\,\mu\text{m} \\ 1063\,\mu\text{m} & \mathbf{744\,\mu m} \end{bmatrix}$

(c)

	$B_1 = \text{CWC}_{\text{MOSAiC-ACA, ice}}$ $B_2 = \text{CWC}_{\text{MOSAiC-ACA, ocean}}$	$B_1 = \text{CWC}_{\text{HALO-(AC)}^3\text{, ice}}$ $B_2 = \text{CWC}_{\text{HALO-(AC)}^3\text{, ocean}}$
$A_1 = \text{CWC}_{\text{AFLUX, ice}}$ $A_2 = \text{CWC}_{\text{AFLUX, ocean}}$	$a_{ij} = \begin{bmatrix} \mathbf{0.10\,g\,cm^{-3}} & 0.14\,\text{g cm}^{-3} \\ 0.06\,\text{g cm}^{-3} & \mathbf{0.10\,g\,cm^{-3}} \end{bmatrix}$	$a_{ij} = \begin{bmatrix} \mathbf{0.04\,g\,cm^{-3}} & 0.04\,\text{g cm}^{-3} \\ 0.08\,\text{g cm}^{-3} & \mathbf{0.01\,g\,cm^{-3}} \end{bmatrix}$

Table 10 Matrices calculated according to Eq. 4.2. The entries inside a matrix give the Wasserstein distance between the distributions of the respective data sets. The values provide a measure of how similar two distributions are. A higher value of the Wasserstein distance indicates a larger dissimilarity between the distributions, while a lower value indicates a larger similarity. Measurements above the same surface type are shown on the diagonal. The matrices are calculated from the 1 Hz microphysical data set of N (a), D_{eff} (b) and CWC (c). All values were tested for significance using a bootstrap procedure with 1000 iterations and were found to be significant with $p < 0.01$.

Figure 53 suggests that the overall number concentration of cloud particles is dominated by water droplets ($N < 50\,\mu m$). Also, it is observed that the total number concentration of cloud particles has a broader distribution during the HALO-(AC)^3 campaign compared to AFLUX. Although the distribution of N in HALO-(AC)^3 is quite broad, the Wasserstein distances between the AFLUX data and HALO-(AC)^3 data are more than two times smaller than the Wasserstein distances between the AFLUX and MOSAiC-ACA campaigns. These smaller Wasserstein distances (with 12.03 cm^{-3} over the sea ice and 23.13 cm^{-3} over the ocean) indicate a much more similar data distribution of N between AFLUX and HALO-(AC)^3 than between AFLUX and MOSAiC-ACA, where the Wasserstein distances are about twice as high (29.60 cm^{-3} over the sea ice and 37.07 cm^{-3} over the ocean). For the HALO-(AC)^3, no increase in cloud particle number concentration over sea ice is observed, which is in contrast to the other two campaigns. The effective diameter is driven by ice particles ($> 50\,\mu m$) in both spring campaigns and by liquid droplets ($< 50\,\mu m$) in summer. For all three campaigns, the effective diameter is increased over the ocean. Also here, the Wasserstein distance indicates that the data distribution of D_{eff} during the two spring campaigns (AFLUX and HALO-(AC)^3) is significantly more similar than the comparison between spring and summer (AFLUX and MOSAiC-ACA). Based on the Wasserstein metric, the data distributions of D_{eff} over the sea ice between the two spring campaigns are very similar, since the Wasserstein distance is 3.6 times smaller than compared to the D_{eff} distributions between spring and summer. Over the ocean, the difference is a factor of 1.9.
Similar to the effective diameter, the CWC is primarily composed by the ice particles during AFLUX and HALO-(AC)^3. During MOSAiC-ACA, liquid particles comprise the largest proportion of the total CWC. The CWC is increased over the ocean for all three campaigns. However, the measurements during HALO-(AC)^3 show slightly smaller values compared to AFLUX. The Wasserstein distances between the CWC distributions of both spring campaigns (AFLUX and HALO-(AC)^3) are smaller than between AFLUX and MOSAiC over the sea ice and ocean. The small Wasserstein distance of 0.01 g cm^{-3} indicates that the CWC distributions above the ocean are almost identical in the two spring campaigns.

In terms of microphysics, there are apparent differences between the summer campaign and the two spring campaigns. The two spring campaigns have very similar distribution of their microphysical cloud properties but show slightly different median values in some cases, such as $\tilde{N}$ being increased over the ocean during HALO-(AC)^3, which is not seen for AFLUX. The discrepancies in absolute median cloud values and small variations in the distributions of microphysical values in the two spring campaigns can be attributed to slightly different weather situations, flight strategies, air mass origin, and temperature differences.

In the following, the thermodynamic phase properties of cloud measurements during the HALO-(AC)^3 campaign are analyzed and discussed with respect to the results from the AFLUX and MOSAiC-ACA evaluation. Figure 54 shows the 1 Hz particle bulk measurements over the

sea ice and the open ocean below 1000 m for the cloud data set collected in spring 2022. As shown earlier in Sect. 4.5, certain regimes in the phase diagram show a higher probability of occurrence. These regimes were assigned to thermodynamic phases based on the asymmetry parameter and the extinction coefficient measured by the PN. Determining the boundary values for the individual regimes followed the same procedure as in Sect. 4.5 and resulted in slightly adapted values: 1a corresponds to cloud data with $10\,\mathrm{m^{-3}} < N < 196\,\mathrm{m^{-3}}$ and $0.4\,\mathrm{mm} < D_{\mathrm{eff}} < 2.7\,\mathrm{mm}$, 1b corresponds to $513\,\mathrm{m^{-3}} < N < 1.9\times10^{4}\,\mathrm{m^{-3}}$ and $0.34\,\mathrm{mm} < D_{\mathrm{eff}} < 2.4\,\mathrm{mm}$, 2a to $6.1\times10^{4}\,\mathrm{m^{-3}} < N < 7.1\times10^{5}\,\mathrm{m^{-3}}$ and $0.15\,\mathrm{mm} < D_{\mathrm{eff}} < 0.82\,\mathrm{mm}$, 2b to $6.0\times10^{4}\,\mathrm{m^{-3}} < N < 4.3\times10^{5}\,\mathrm{m^{-3}}$ and $1.1\,\mathrm{mm} < D_{\mathrm{eff}} < 3.6\,\mathrm{mm}$, 2c to $1.8\times10^{7}\,\mathrm{m^{-3}} < N < 2.1\times10^{8}\,\mathrm{m^{-3}}$ and $0.07\,\mathrm{mm} < D_{\mathrm{eff}} < 0.99\,\mathrm{mm}$, 3 to $2.4\times10^{7}\,\mathrm{m^{-3}} < N < 2.5\times10^{8}\,\mathrm{m^{-3}}$ and $9\,\mu\mathrm{m} < D_{\mathrm{eff}} < 38\,\mu\mathrm{m}$, and 4 to $6.0\times10^{4}\,\mathrm{m^{-3}} < N < 4.0\times10^{5}\,\mathrm{m^{-3}}$ and $D_{\mathrm{eff}} < 10\,\mu\mathrm{m}$.

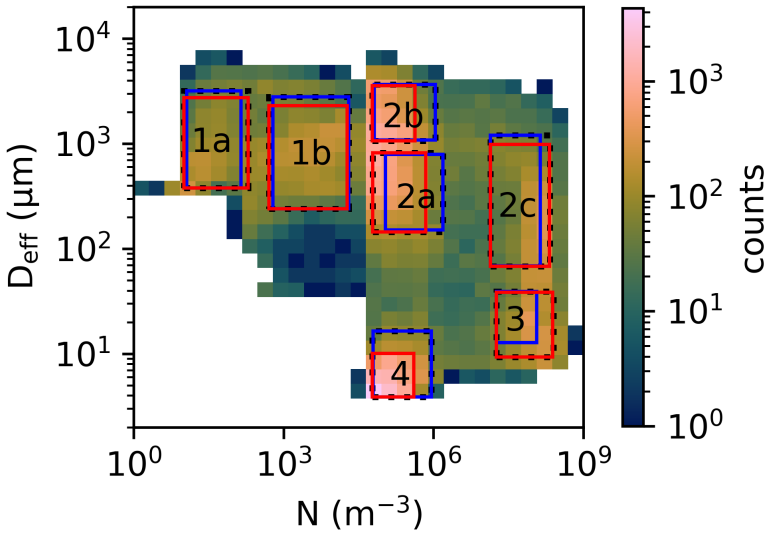

Figure 54 N versus D_{eff} for 1Hz low-level particle data (< 1000 m) over sea ice and the open ocean from the HALO-(AC)^3 campaign, color coded by their occurrence. Regimes with increased occurrence frequency are marked with a red rectangle. The blue rectangle shows the regimes determined by the AFLUX and MOSAiC-ACA cloud data from Sect 4.5. Associated cloud particles: 1 - ice, 2 - mixed-phase, 3 - liquid, 4 - aerosol particles. The dotted black rectangle represents the smallest rectangle enclosing the blue and red rectangles.

In Fig. 54, these new regimes for the HALO-(AC)^3 data set are shown in red, and the regimes previously defined by the AFLUX and MOSAiC-ACA data are shown in blue. A cross-check of how many data points from the regime definition of AFLUX and MOSAiC-ACA lie in the new regime definition shows that regimes 1a, 1b, 2b, and 4 agree very well with more than 80% overlap. Larger deviations are observed for 2a, 2c and 3 with respectively 62%, 71% and 50% overlap. On the one hand, these discrepancies may result from natural cloud variations. On the other hand, in particular, for 2c and 3, the different measurement techniques come into account.

Different instruments and methods for data processing were used in all three campaigns. Thus, slightly varying sensitivities for N, especially in areas with high particle number concentration, can result from a different definition of the size binning and also from the hardware of the different types of scattering probes (see Sect. 3.2 for more details about the scattering probes). Since all regimes overlap quite well in the N - D_{eff} space, no additional thermodynamic phase validation with the data from the PN is needed. The thermodynamic phase definition from Sect. 4.5 is applied where regime 1a and 1b are assigned to pure ice phase, 2a, 2b, and 2c correspond to a mixed-phase state, regime 3 are liquid clouds, and regime 4 represents large aerosols.

The frequency of occurrence of each particle regime over the ocean and sea ice during the HALO-(AC)^3 campaign is shown in Fig. 55. One can see that in spring 2022, the mixed-phase regime dominates over both surfaces, the sea ice and the open ocean. Here, the surface influences the mixed-phase microphysics, as regime 2a is measured most frequently over the sea ice and regime 2b most frequently over the open ocean. The mixed-phase regime 2c and pure liquid clouds are observed exclusively over the ocean. Ice clouds (1a and 1b) occur at almost the same frequency over both surfaces. Aerosols are regularly observed over the sea ice and the ocean, but with a frequency that is more than twice as high over the sea ice as over the ocean.
Comparing these thermodynamic phase distribution results with the AFLUX and MOSAiC-ACA results in Fig. 50, it is noticeable how well the thermodynamic phase distribution of HALO-(AC)^3 agrees with the AFLUX campaign. For a second time, it can be observed that the mixed-phase regime 2a dominates over the sea ice, and the mixed-phase regime 2b dominates over the open ocean. Particularly significant are the larger effective diameters (resulting from the regime 2b) over the open ocean, due to the higher availability of water. The microphysical properties of these two regimes are studied in more detail in Chapter 5. The two spring campaigns also agree well on the frequency distribution of aerosols. Minor discrepancies are found for pure ice and liquid clouds. While ice clouds are seen almost exclusively over the ocean during AFLUX, they are measured almost equally over both surfaces during HALO-(AC)^3. The AFLUX data show that liquid clouds formed exclusively over the sea ice, while during HALO-(AC)^3 they are only observed over the ocean. Overall, one can conclude that the spring campaigns of 2019 and 2022 are very similar in thermodynamic phase distribution and that the spring cloud data are in clear contrast to the summer campaign.

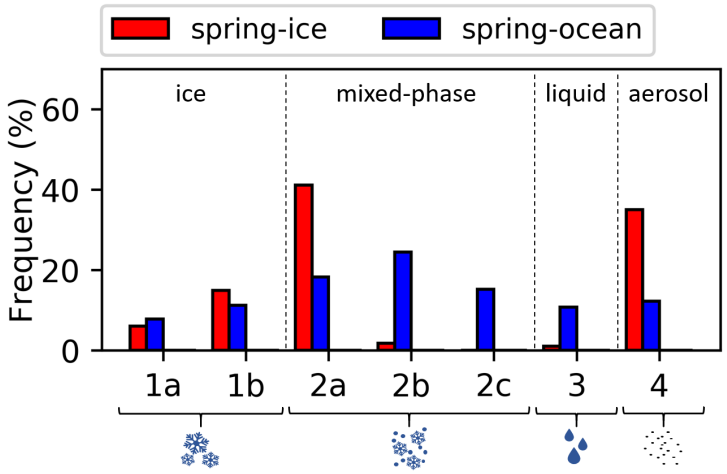

Figure 55 Frequency of occurrence for each particle regime (1a, 1b: Ice particles; 2a, 2b, 2c: Mixed-phase particles; 3: Liquid particles; 4: Aerosol particles), separated by surface conditions for the HALO-(AC)^3 low-level cloud data (< 1000 m). The values are normalized by the respective surface condition.

An overview of the thermodynamic phase distribution, separated for each flight during HALO-(AC)^3, is presented in Fig. 69 in Appendix D.

5 Investigation of Arctic low-level clouds and mixed-phase haze

5.1 Mixed-phase clouds and mixed-phase haze

In the following, a deeper analysis of the mixed-phase cloud regimes is carried out, with a particular focus on the microphysical properties. Here it is shown that the mixed-phase states, as they occur in regimes 2a and 2b, differ significantly from the mixed-phase regime 2c, and that the term *Arctic low-level mixed-phase haze* or *mixed-phase haze* (MPH) adequately describes the regime 2a and 2b.

In Sect. 4.5, the regimes 2a, 2b, and 2c were introduced and defined as mixed-phase cloud regime supported by the data from the Polar Nephelometer. All three regimes show optical properties typical for a classic mixed-phase cloud. Microphysically, however, the two regimes 2a and 2b differ significantly from the regime 2c (absolute values of the microphysical properties are given in Table 22 in Appendix G). The PSD of the 2c regime (see Fig. 48) correspond to that of a mixed-phase cloud typically described in literature (see Sect. 2.3; McFarquhar et al., 2007a; Korolev et al., 2017) and now will be referred to *classic mixed-phase cloud* (MPC). The liquid particles can be easily recognized by the mode in the PSD at approximately 15 µm, while the larger particles correspond to ice crystals. Such a mode of liquid particles is not observed in the mixed-phase haze clouds (2a and 2b) in Fig. 48. In particular, the two smallest size bins, < 5 µm, show a maximum in the PSD in these two regimes. While in the classic mixed-phase clouds (2c), the local maximum in the PSD is caused by liquid particles, in the mixed-phase haze regimes (2a and 2b), the maximum is composed of haze droplets, in which sea salt aerosols (SSA) are dissolved. Consequently, the mixed-phase haze regimes 2a and 2b consist of a mixture of small (< 5 µm) wet SSA and larger ice crystals. Compared to the median number concentration of droplets in classic mixed-phase cloud conditions ($\tilde{N}_{<50\mu m} = 84.4\,cm^{-3}$), a lower median number concentration of wet SSA ($\tilde{N}_{<50\mu m} = 0.4\,cm^{-3}$) is observed in mixed-phase haze. The difference in microphysical composition, droplets vs. haze droplets, is related to the environmental conditions that prevail to form the respective cloud regimes. The meteorological parameters T, RH_w and RH_{ice}, which were measured in the mixed-phase cloud and mixed-phase haze conditions, are shown in Fig. 56. The data in this figure only contain measurements from the AFLUX and MOSAiC-ACA campaigns, as the humidity data during HALO-$(AC)^3$ are subject to large uncertainties.

For the classic mixed-phase clouds, the relative humidity is observed to be above $RH_w = 98\%$ in 97.7% of all cases. Here, the limit of $RH_w = 98\%$ is assumed for water vapor saturation, as the measurement accuracy for the humidity sensor is $\pm 2\%$ according to Mech et al. (2022). Since mixed-phase clouds only exist at temperatures below 0 °C, all mixed-phase cloud measurements show supersaturation with respect to ice. These results are in line with expectations, as classic stratiform mixed-phase clouds consist of ice particles and water droplets, with the ice crystals

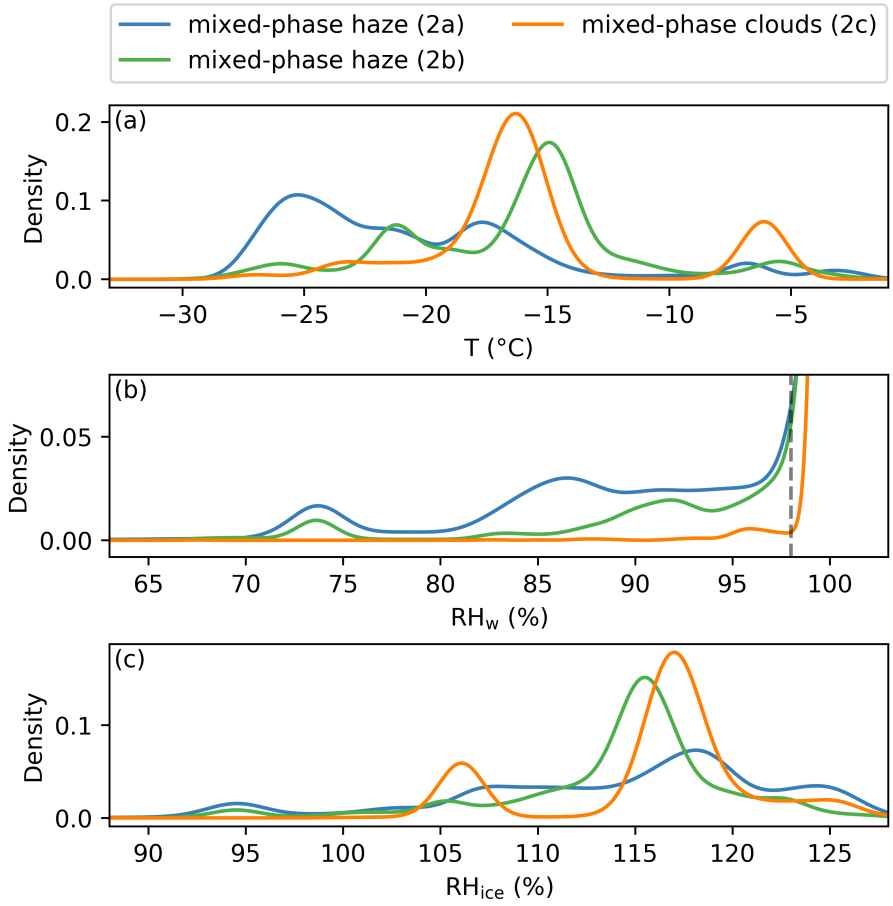

Figure 56 Environmental conditions during mixed-phase haze and mixed-phase clouds conditions. Data are based only on the AFLUX and MOSAiC-ACA data and for measurements below 500 m and at temperatures below freezing. Density plots for the three regimes are shown over the temperature in (a), over the relative humidity with respect to water in (b), and over the relative humidity with respect to ice in (c).

growing at the expense of the liquid droplets due to water vapor deposition (see WBF process in Sect. 2.2.2). By a constant supply of moisture provided by convection and advection, the mixed-phase structure is maintained (Morrison et al., 2011). A persistent WBF process in the mixed-phase clouds implies saturation with respect to water in order to compensate the water mass transfer from the liquid droplets to the ice crystals. Consequently, a mixed-phase is unexpected to be measured at a humidity far below saturation with respect to water, because of the short relaxation time (only a few seconds) of liquid droplets (Korolev et al., 2017). Previous studies, such as Korolev and Isaac (2006), have confirmed that the water vapor in mixed-phase clouds is close to saturation over water. This suggests that the mixed-phase regime 2c corresponds to a classic mixed-phase state with a continuous ongoing WBF process (Costa et al., 2017). The small fraction of subsaturated values with respect to water at $RH_w \approx 96\%$ measured in mixed-phase clouds can be explained by cloud holes created by dry air intrusion into the clouds and by measurements close to the cloud edges due to the spatial resolution of humidity sensors

and the PMS instruments (Gerber et al., 2005; Korolev and Isaac, 2006; Pruppacher and Klett, 2010; Klingebiel et al., 2015). In the mixed-phase haze conditions, the ambient meteorological conditions are significantly different. Here, 38.8% of the measurements are observed below saturation with respect to water. Due to the low temperatures, the relative humidity with respect to ice is frequently above saturation, which favors the growth and persistence of ice crystals. However, a small fraction of the mixed-phase haze is observed at $RH_{ice} < 100\%$. This is not unusual, as ice crystals are frequently measured in non-equilibrium conditions (Korolev and Isaac, 2006; Voigt et al., 2017; De La Torre Castro et al., 2023; Dekoutsidis et al., 2023). Frequent measurements of mixed-phase haze in subsaturated conditions with respect to water indicate that the fraction of small particles cannot be cloud droplets. While ice crystals can persist in subsaturated air masses due to a prolonged phase relaxation time, which is comparable to the lifetime of an entire ice cloud (Krämer et al., 2009; Rollins et al., 2016; Korolev et al., 2017), small water droplets would evaporate immediately when exposed to subsaturated air. However, the mixed-phase haze condition is the most prevalent cloud type measured in both spring campaigns, which implies that a stable condition must be present. A thermodynamically stable condition of these persistent cloud conditions in subsaturated humidity with respect to water can be explained by haze droplets consisting of water and dissolved SSA. It is known that sodium chloride (NaCl) is one of the main aerosol types emitted locally in marine Arctic areas (Kirpes et al., 2018). These NaCl aerosols attract moisture from the environment and swell into small droplets of a saline solution. The growth rate must be high enough to reach a diameter that can be detected by the in-situ cloud instrumentation with a lower size limit of 2.8 µm. This so-called hygroscopic growth of the salt aerosols depends on the ambient humidity and can be derived from the Köhler theory (see Sect. 2.2.1). This relationship between the hygroscopic growth factor g_e and RH_w is shown in Fig. 57.

In the size range between 2.8 - 5 µm, in which the haze droplets are measured with the scattering cloud probes and $RH_w < 100\%$, the shape of the Köhler curves no longer changes, as the Kelvin effect becomes negligible (see size range of the gray rectangle in Fig. 3). This allows one to calculate a hygroscopic growth factor $g_e = r/r_0$ independent of the mass of dissolved NaCl in the droplet, where r is the haze droplet radius and r_0 is the dry radius of the dissolved salt particle. The Köhler equation reaches its limitations at low humidity, as deliquescence and efflorescence need to be considered. Deliquescence describes the process of becoming liquid due to absorbing moisture from the ambient air, while efflorescence is the crystallization of a liquid droplet. Both transitions take place at different relative humidity, resulting in a hysteresis. Thus, there is a range from $RH_w = 74\%$ (Zieger et al., 2017) to $RH_w = 48\%$ (Tang et al., 1997) where solid crystals and liquid droplets coexist, depending on the particle's moisture history. In Fig. 57, the 25th, 50th, and 75th percentiles of the RH_w values measured in subsaturated mixed-phase haze regimes are shown in red. The median hygroscopic growth factor of the sea salt particles results in 2.33 (25th percentile = 2.04 / 75th percentile = 2.82). This results to a median refractive

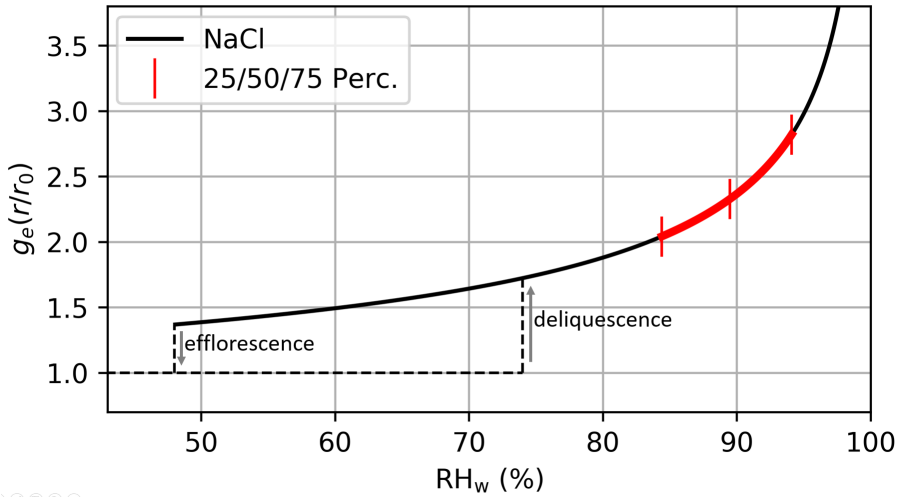

Figure 57 Hygroscopic growth factor versus relative humidity, calculated for a NaCl particle. The RH_w measurement range, measured in subsaturated mixed-phase haze conditions, are shown in red.

index of 1.35 (1.34 / 1.36) when a NaCl-H_2O mixture is considered. Compared to the refractive index of pure water, the Lorenz-Mie curve used for the scattering instrument calibration (see Sect. 3.2.1) changes insignificantly in the size regime of the lower size limit of 2.8 µm. Therefore, it can be assumed that the slight change in the refractive index and its influence on the measured total particle number concentration detected by the scattering cloud instruments can be neglected. By assuming that the measured haze droplets have a diameter between 2.8 µm and 5 µm, the derived hygroscopic growth factor for NaCl results in a possible size range of the dry aerosol diameter between 1.0 - 2.5 µm, or expressed in mass, 1.1×10^{-12} g to 1.8×10^{-11} g. Previous studies, e.g. Willis et al. (2018), have shown that the particles in this diameter range are dominated by marine sea salt particles. This is also supported by preliminary analyses[5] of the measurements by the Aircraft-based Laser ABlation Aerosol MAss spectrometer (ALABAMA; Brands et al., 2011; Köllner et al., 2017), which was also on board the Polar 6 aircraft during the HALO-(AC)^3 campaign (Eppers et al., 2023b).

For further investigation of the mixed-phase haze, the relationships between the different cloud regimes are analyzed using a network plot in Fig. 58. The individual regimes are shown as circles, where the size of one circle represents how often the respective regime is detected again in the subsequent 1 Hz measurement. The lines and relative distances between the circles are calculated according to the Fruchterman-Reingold algorithm (Fruchterman and Reingold, 1991). The connections between the circles in this network plot represent transitions between the microphysical regimes. The thickness of the lines indicates how often a transition between the corresponding regimes is observed within one second. The thicker the line, the closer the

[5] Preliminary analysis of the particle composition in the ABL was carried out by Oliver Eppers, Particle Chemistry Department, Max-Planck-Institut für Chemie (MPIC), Mainz, Germany.

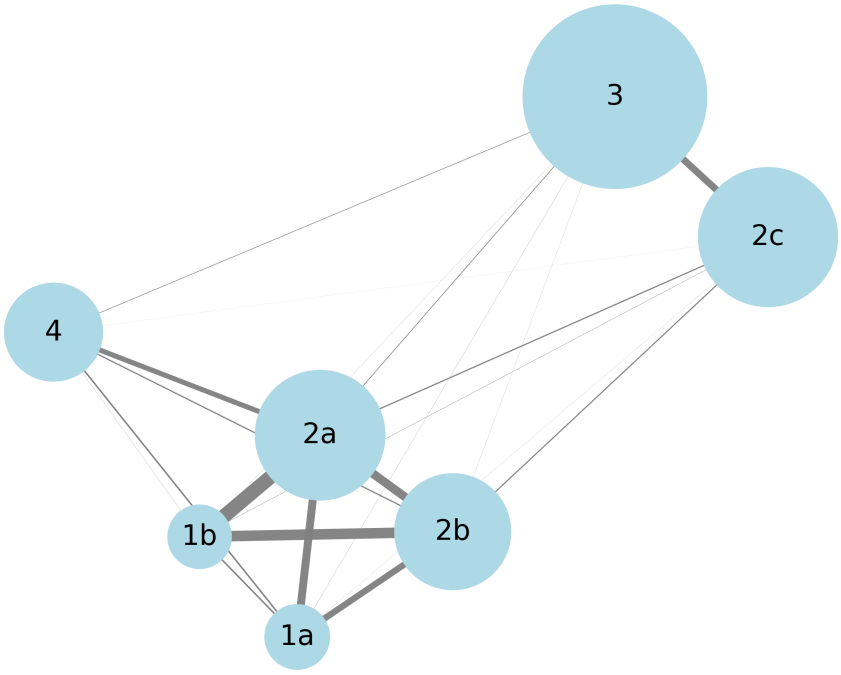

Figure 58 Network plot based on the algorithm by Fruchterman and Reingold (1991), representing the transitions between the different microphysical regimes within the 1 Hz cloud data set. All cloud data below 1000 m altitude are taken into account. 1a, 1b: Ice phase; 2a, 2b: Mixed-phase haze; 2c: Classic mixed-phase cloud; 3: Liquid phase; 4: Aerosols.

two regimes are placed in the network plot and the more frequent this transition is registered. The figure illustrates how cloud regimes are spatially correlated and, therefore, preferentially coexist. Regime 3, corresponding to liquid clouds, is shown as the circle with the largest diameter, indicating that this is a thermodynamic state stable on a large spatial scale. Together with classic mixed-phase clouds (2c), these two regimes are shown to be the furthest from all other regimes. The strong connection between classic mixed-phase and the liquid phase is as expected since stratiform mixed-phase clouds originate from supercooled liquid cloud layers. Another cluster is formed by the regimes 1a, 1b, 2a, and 2b, which correspond to pure ice clouds and mixed-phase haze. Between these regimes, a strong spatial correlation is observed. The correlation is most likely caused by the environmental conditions in which ice clouds and mixed-phase haze occur. The fraction of ice in both regimes is equally sensitive to the relative humidity with respect to ice, while the fraction of haze droplets in the mixed-phase haze is in thermodynamic equilibrium with the environment over an extensive range of relative humidity. The aerosol regime (4) detected with the in-situ cloud instrumentation is presumably wet SSA, similar to the haze droplets in the mixed-phase haze but without the ice component. There are several possible explanations for the formation of the mixed-phase haze clouds. One possibility is mixing of two different air masses. An air mass that includes wet SSA and an air mass containing pure ice crystals (mixture of regimes 1 and 4). Figure 58 supports this mixing process

as the aerosols (4) are located near the cluster containing the ice and mixed-phase haze regimes (1a, 1b, 2a, 2c). Another possibility is the dry-out process of a classic mixed-phase cloud (2c) through environmental changes. When no more moisture is introduced into the cloud, the WBF process stops and the water droplets evaporate. However, they evaporate only up to a stable size described by the Köhler curve ($r < r_c$). The ice crystals evaporate as the humidity decreases further and only the wet aerosol particles remain. This hypothesis is supported by the fact that 21.4% of the aerosol measurements in subsaturated air are below $RH_w = 74\%$ with respect to water. Those measurements are in the upper part of the hysteresis in Fig. 57, implying that those haze droplets were previously in moister air. The dry out of a mixed-phase cloud into a state of ice crystals and aerosol particles was also proposed by Costa et al. (2017). The study describes that in a mixed-phase cloud with $RH_w < 100\%$ and $RH_{ice} > 100\%$, the liquid droplets evaporate and only ice crystals and aerosols remain. The mixed-phase haze could also develop from a mixture of CCNs and INPs. Haze droplets can grow on CCNs and ice crystals can grow on the INPs when environmental conditions of cold temperature and high relative humidity with respect to ice are present. Thus, some of the so called diamond dust events (Intrieri and Shupe, 2004; Hobbs and Wallace, 2006) could also be attributed to mixed-phase haze conditions.
Further analysis is needed to confirm the hypothesis that mixed-phase haze conditions originate from dried-out classic mixed-phase clouds. Such analyses must be conducted with instruments that are able to cover the complete size distribution of the marine aerosol particles in the ABL.

5.2 Influence of surface conditions on the particle formation in mixed-phase haze

The sections 4.5 and 4.6 show that the mixed-phase haze conditions 2a and 2b are the most frequently measured cloud types in spring. A remarkable result is that the mixed-phase haze type 2a dominates over sea ice surfaces, while the mixed-phase haze type 2b dominates over the open ocean. Microphysically, these two regimes differ, with the 2a cloud type showing a smaller D_{eff} and higher N. The main contribution to the total particle number concentration in the mixed-phase haze is particles formed from a water - sea salt solute, which are stable in a subsaturated environment. In a natural particle size distribution, SSA belong to the coarse mode and are usually found in a size range between 0.5 µm to 10 µm (Lohmann et al., 2016). Such coarse modes are illustrated by distribution functions in Fig. 59. In the in-situ cloud particle measurement setup, the scattering instruments are responsible for the detection of the smallest particles. These instruments have the lower threshold for particle size detection at $D_{lt} = 2.8$ µm. Due to this threshold, the in-situ cloud instruments cannot detect the complete coarse mode. Only particles larger than D_{lt} are measured, indicated by the dark colored area below the distribution functions.

Two possible explanations are discussed for an increased concentration of small particles observed by the in-situ cloud instruments. An increased N could result either from an overall

higher number of particles in the coarse mode, as illustrated in case (a) in Fig. 59, or from a general shift of the coarse mode towards larger particles, as illustrated in case (b). Case (a) represents the scenario of an enhanced cloud particle formation process over the sea ice. However, due to the lower detection limit, a shift in the coarse mode in case (b) can falsely result in an increased total particle number concentration value as well. Apart from the aerosol chemical composition, the shift of the coarse mode to larger diameters is mainly determined by the relative humidity. According to Köhler's theory, a higher humidity results in a larger wet radius at which a haze droplet is in thermodynamic equilibrium. To identify which of the two hypotheses from Fig. 59 is more likely, the number concentration measured in the mixed-phase haze conditions is correlated with the relative humidity. The particle number concentration measured during the AFLUX and MOSAiC-ACA campaign below 500 m altitude above the ambient relative humidity is shown in Fig. 60. Cloud data from the HALO-(AC)^3 campaign are not included in this correlation as no validated humidity measurements are available up to this point. The correlation shows that the highest median particle number concentrations ($\tilde{N}$) in mixed-phase haze conditions are found at relative humidity values below 80%. The higher the relative humidity, the lower the median particle number concentration in mixed-phase haze conditions is observed. This anti-correlation between $\tilde{N}$ and RH_w contrasts the hypothesis that the increased number concentrations is due to a shift of the coarse mode.

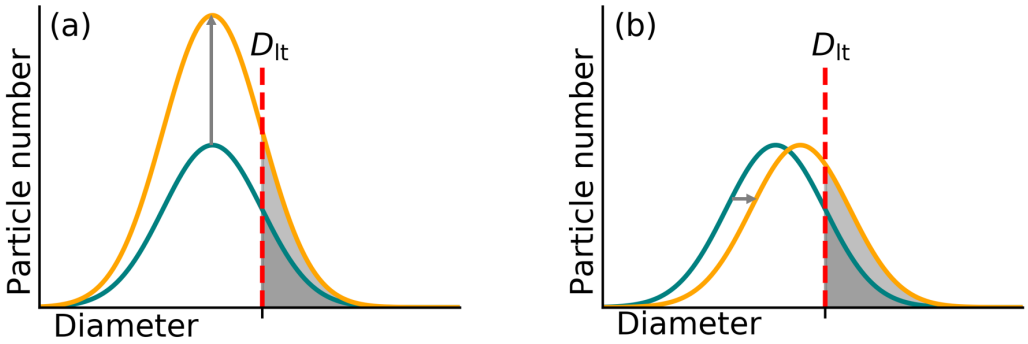

Figure 59 Schematic representation of the two hypotheses on how the in-situ cloud probes detect an increased N in the mixed-phase haze regime. The blue and yellow distributions represent size distributions of coarse mode aerosols. While in (a), the absolute particle number in the coarse mode is increased, in (b), the coarse mode is shifted to a larger particle diameter. D_{lt} represents the lower size detection threshold of the scattering probes.

Additionally to the in-situ cloud probes, the Polar 6 was equipped with advanced aerosol instruments during HALO-(AC)^3, similar to the previous Arctic airborne field campaign ACLOUD (Ehrlich et al., 2019). The aerosol measuring systems include an optical particle counter (Grimm Sky-OPC; Walser et al., 2017) operated and processed by the Max Planck Institute for Chemistry, Mainz (Eppers et al., 2023a). Figure 61 shows boxplots of N data and D_{eff} data recorded by the OPC for particles in the size range between 500 nm and 4 µm, separated by measurements over the sea ice and the open ocean. In addition, the data only contain measure-

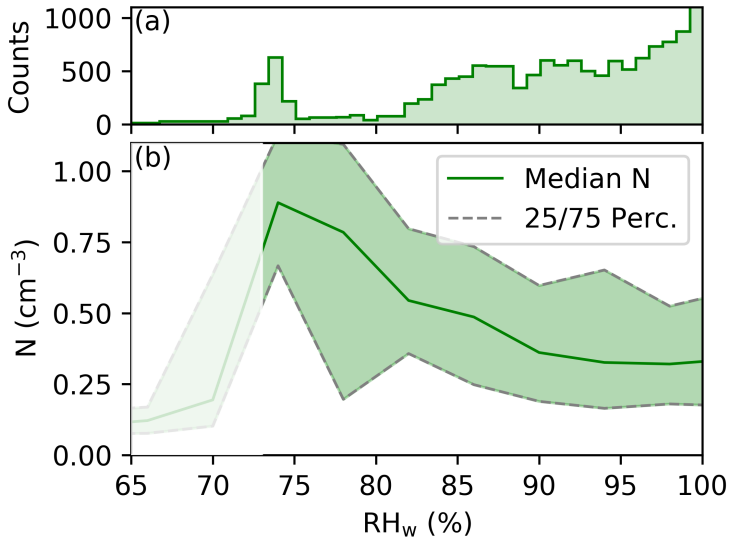

Figure 60 (a) shows the distribution of humidity measurements and (b) the $\tilde{N}$ versus relative humidity in the mixed-phase haze regimes 2a and 2b. Median and percentile values of N are calculated in 4% intervals of RH_w. Data includes flight segments from AFLUX and MOSAiC-ACA only at flight levels below 500 m. Insufficient data due to low statistics is grayed out.

ments at flight altitudes below 300 m, time series where the cloud probes detect mixed-phase haze or aerosol regimes, and flight segments in which the aerosol instruments are not set to cloud sampling, i.e., the counterflow virtual impactor (CVI) is switched off (Mertes and Wetzel, 2023). This ensures that only SSA within the ABL are captured here. A total sampling time of 9272 s was achieved in the ABL over the open ocean and 10715 s in the ABL over the sea ice. Similar to the studies with the in-situ cloud instrumentation in the mixed-phase haze conditions, an increase in aerosol number concentration is observed in the coarse mode over the sea ice compared to the measurements over the ocean. Since the relative humidity is not available during HALO-(AC)^3, the effective diameter over both surfaces is investigated in Fig. 61 (b). Here, a reduction in the $\tilde{D}_{\text{eff}}$ of the haze droplets is observed over the sea ice, while the median number concentration of particles in (a) increases. This observation is in clear contrast to hypothesis (b) in Fig. 59, as an increase in $\tilde{D}_{\text{eff}}$ would be expected in that case. Based on the anti-correlation of RH_w and $\tilde{N}$ in the cloud probe data in Fig. 60 and the increase in particle concentration over ice in the coarse mode, measured with the OPC in Fig. 61, it is very likely that more SSA enter the ABL over the sea ice compared to the surface condition of the open ocean. The absolute increase in $\tilde{N}$ from the open ocean to the sea ice is a factor of 2.3 (from 0.17 cm^{-3} to 0.38 cm^{-3}) for the measurements conducted with the in-situ cloud probes and 1.4 (from 1.34 cm^{-3} to 1.89 cm^{-3}) for the measurements with the OPC. Measurements of N with the OPC are pressure-corrected to standard temperature and pressure (STP). Given that the increase fraction in the OPC measurements is slightly below the increase fraction measured with

the cloud probes, a certain contribution caused by a higher RH_w above the sea ice (hypothesis (b) in Fig. 59) or a change in the coarse mode shape cannot be excluded.

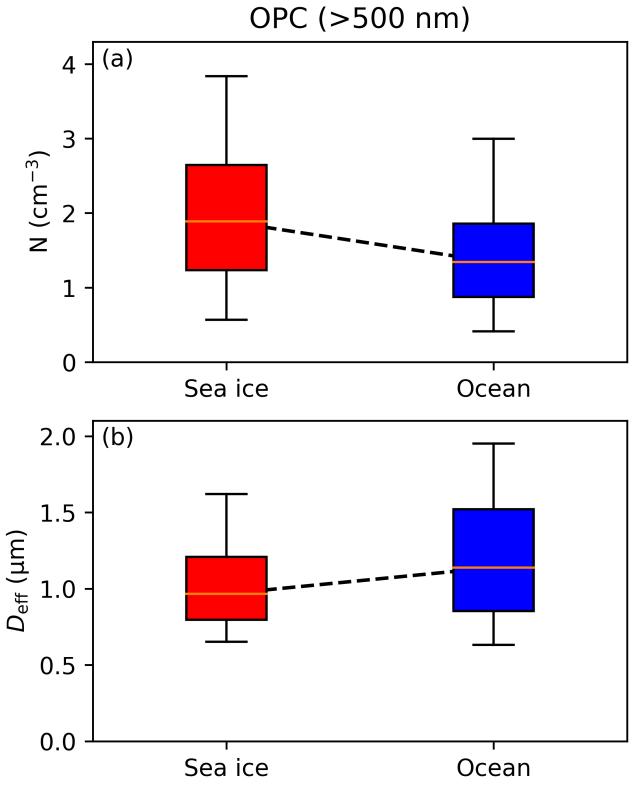

Figure 61 Boxplot of N data (a) and boxplot of D_{eff} data (b) derived from the OPC during HALO-(AC)^3. Only particle with diameters larger 500 nm inside the ABL and during aerosol or mixed-phase haze conditions are considered. The boxplots include the median, upper, and lower quartiles, and the whiskers give the 5th and 95th percentile.

After it has been shown that the aerosol concentration of sea salt causing the haze droplets is increased in the ABL above the sea ice compared to the open ocean, the question arises of where these particles originate. It is known from previous studies that over the ocean, sea salt is emitted into the atmosphere by wave breaking mechanisms (Blanchard, 1989), while processes such as blowing snow or frost flowers are considered over the sea ice (Yang et al., 2008; Seguin et al., 2014; Xu et al., 2016; Huang and Jaeglé, 2017; Willis et al., 2018). All discussed processes emitting sea salt into the atmosphere are wind-driven. Previous studies have shown that the mass of marine SSA over the ocean increases exponentially with the horizontal wind speed. Ovadnevaite et al. (2012) and Klingebiel et al. (2019) observed this exponential increase starting at a windspeed of 4 m s^{-1}, and Lewandowska and Falkowska (2013) starting at 3 m s^{-1}. This increase at a given wind speed can be explained by the formation of whitecaps from ocean waves, leading to processes emitting SSA into the atmosphere (Deike et al., 2022).

Figure 62 shows the median values of N and the 25th and 75th percentiles at rising horizontal wind speeds, separated between mixed-phase haze conditions (2a and 2b) over the sea ice

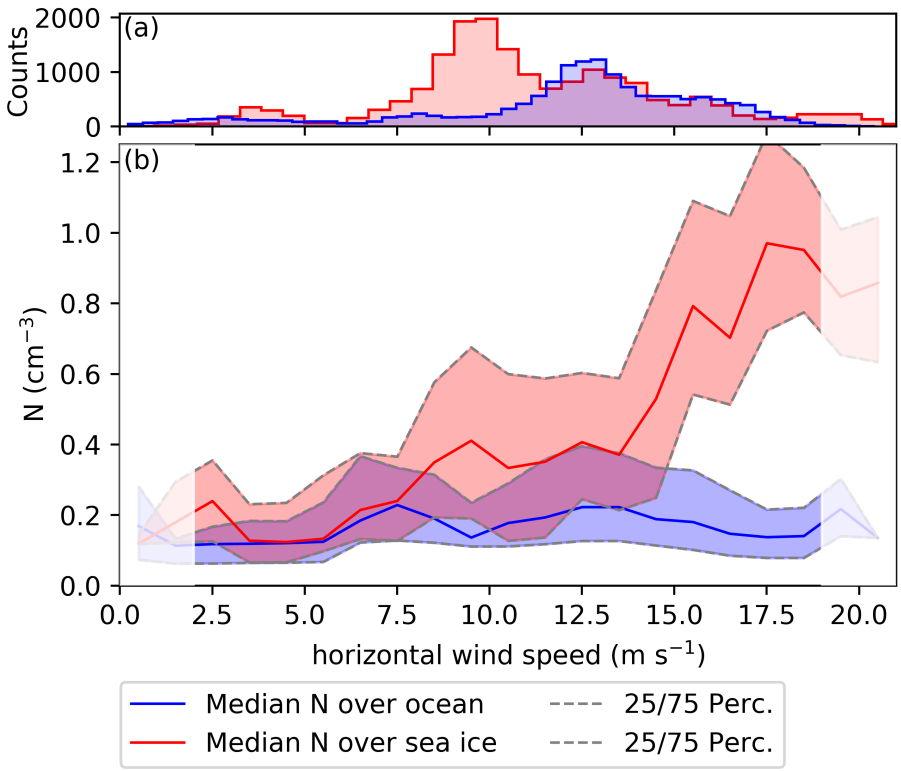

Figure 62 Horizontal wind speed distribution shown in (a). In (b): $\tilde{N}$ over the measured horizontal wind speed for the mixed-phase haze regimes 2a and 2b, separated into measurements above the sea ice (red) and above the ocean (blue). Median and percentile values of N are calculated in 1 m s^{-1} intervals of the horizontal wind speed. All horizontal cloud data collected during AFLUX, MOSAiC-ACA and HALO-(AC)^3 at altitudes below 500 m are considered.

and over the open ocean.[6] Over the ocean, $\tilde{N}$ starts to increase at a horizontal wind speed of 5.0 m s^{-1} but does not increase exponentially as observed in previous studies. Instead, $\tilde{N}$ remains at a constant level. The measurements above the sea ice show a different response to the horizontal wind. An increase of $\tilde{N}$ is observed with increasing wind speeds between 5.0 m s^{-1} and 9.5 m s^{-1}. A further increase is observed from 13.5 m s^{-1} to 17.5 m s^{-1} where the median N reaches a maximum of 1.0 cm^{-3}. Over the entire wind speed spectrum, the median N values from the measurement over the sea ice are above the median N values detected over the ocean. Why an exponential increase of marine aerosols is not observed over the ocean with rising wind speed, as observed in other studies, remains an open question. Unlike the previous studies using instruments that are sensitive to aerosols only, particles larger than 2.8 µm are considered in Fig. 62. Besides, high wind speeds are often associated with CAOs, which favor cloud formation over the ocean. This cloud formation can reduce the number concentration of SSA due to wet deposition. During this process, liquid or classic mixed-phase clouds could form from the mixed-phase haze, removing the aerosols from the ABL by precipitation. Since a

[6] Due to icing on the nose boom during the research flights on 24 March 2022, 26 March 2022, 28 March 2022, 4 April 2022, and 10 April 2022, no horizontal wind speed data are available on these days.

strong correlation between $\tilde{N}$ and horizontal wind speed is observed over the sea ice in Fig. 62, these particles are likely caused by processes, such as frost flowers or blowing snow. Additionally, these sources of the sea ice emitting SSA into the atmosphere are likely to be enhanced compared to wave breaking mechanisms of the open ocean.

6 Summary

The Arctic is warming due to climate change at a rate that far exceeds the average global temperature rise. There are a number of mechanisms involved in this phenomenon, and clouds appear to play a crucial role. Yet our understanding of clouds at these high latitudes is limited, so the influence of Arctic clouds can only be determined with low confidence.
This thesis focuses on the experimental investigation of low-level Arctic clouds, considering their microphysical properties and thermodynamic phase. A comprehensive cloud data set from a combination of advanced in-situ cloud particle measurement systems was collected and analyzed. A total of 33 research flights carried out over the northern Fram Strait between Greenland and Svalbard during the three aircraft field campaigns AFLUX (spring 2019), MOSAiC-ACA (summer 2020), and HALO-(AC)^3 (spring 2022). An algorithm based on the cloud's microphysical properties is developed in this thesis to classify the particle measurements into ice clouds, liquid clouds, mixed-phase clouds, and aerosol particles. The extensive amount of in-situ cloud data, with measurements in the vicinity of the sea ice edge during two different seasons, enables statistical analysis and identification of the effect of different environmental conditions on the microphysical cloud properties. The presented microphysical cloud properties and their influence by the ambient environmental conditions help to improve the quantification of the role of clouds in Arctic amplification. The first two research questions of this thesis address the influence of seasonal variations and surface conditions on low-level clouds:

- How do the seasonal synoptic conditions affect cloud microphysical properties and thermodynamic phase of Arctic low-level clouds?

- How do surface conditions, open ocean, and sea ice impact low-level clouds?

Data from the spring 2019 and summer 2020 campaigns are used to answer these questions. An overview of the results is visualized in Fig. 63 (a). The data show a significant contrast between spring and summer clouds and that the seasonal meteorological variation is the main driver for the different microphysical cloud properties (outer box in Fig. 63 a). While clouds in summer are dominated by the liquid phase, the most frequently observed cloud thermodynamic state in spring is mixed-phase. The environmental conditions favor an increased median particle number concentration $\tilde{N}$ by up to two orders of magnitude in summer and an increased median cloud water content $\widetilde{\mathrm{CWC}}$ of 0.16 g m^{-3} compared to 0.06 g m^{-3} in spring. The median effective diameter $\tilde{D}_{\mathrm{eff}}$ is significantly reduced in summer due to the predominance of the liquid phase. These strong seasonal differences in the microphysical properties of Arctic low-level clouds are caused by strong variations in seasonal meteorological conditions, which are quantified by the aircraft's meteorological sensors and backward trajectory modeling. In summer, the Fram Strait is dominated by a northward directed wind that transports warm air from lower to higher latitudes and exposes air masses in the atmospheric boundary layer (ABL) to the ocean prior to the

cloud in-situ measurement. In the spring, the air mass flow is reversed, with strong southward directed winds due to cold air outbreaks (CAOs), and cold air from the sea ice is blown over the sea ice edge to more southerly latitudes.
Besides the seasonal dependence of low-level cloud properties in the Arctic, surface conditions below the clouds modify cloud microphysical properties (inner box in Fig. 63 a). Over the ocean, the clouds have a higher $\widetilde{\mathrm{CWC}}$ and larger $\tilde{D}_{\mathrm{eff}}$ compared to clouds over the sea ice, which is due to a more turbulent ABL and increased heat fluxes. A slightly increased $\tilde{N}$ above the sea ice is repeatedly observed in the clouds in a mixed-phase state, in the liquid clouds, and in the aerosol measurements. The cause of this phenomenon results from surface processes and is analyzed in more detail within the scope of the third research question.
A comparison of the microphysical cloud properties and thermodynamic phase distribution between the spring 2019 and 2022 campaigns shows very similar results, supporting the assumption that the presented cloud values are generally representative of the selected seasons.

An in-depth investigation of the microphysics of the clouds which are in a mixed-phase state shows that a distinction using the terms *Arctic mixed-phase cloud* and *Arctic low-level mixed-phase haze* (short: *mixed-phase haze*) is appropriate. Therefore, the third research question is as follows:

- What are the microphysical properties of Arctic mixed-phase clouds and mixed-phase haze?

The microphysical composition of the two cloud types is schematically shown in Fig. 63 (b) and (c). Arctic mixed-phase clouds correspond to classic stratiform boundary layer mixed-phase clouds in which liquid droplets and ice crystals coexist. The impact of the coexistence of both thermodynamic phases is described by the Wegener–Bergeron–Findeisen process, and the relative humidity is at saturation with respect to water. In contrast, the mixed-phase haze is stable in a subsaturated environment with respect to water and is the most frequently measured cloud type in the ABL in spring, with a fraction of 66% of all collected in-situ cloud measurements below 500 m. Such a physically stable cloud is explained by haze droplets, which are solutions of water and sea salt aerosols, mixed with ice crystals. Compared to the classic mixed-phase clouds, the median N of mixed-phase haze is two orders of magnitude smaller, indicating that the number concentration of haze droplets in mixed-phase haze is less than liquid droplets in mixed-phase clouds. The measured D_{eff}, is more than twice as large in mixed-phase haze compared to mixed-phase clouds, suggesting larger ice crystals in mixed-phase haze conditions, as the D_{eff} calculation is dominated by the ice crystals. Again, in the case of the mixed-phase haze, a slightly higher number concentration of haze droplets is observed over the sea ice compared to the ocean. Different aerosol sources cause this difference in N for the two surface conditions. Over the ocean, cloud condensation nuclei (CCNs) are introduced into the ABL by wave

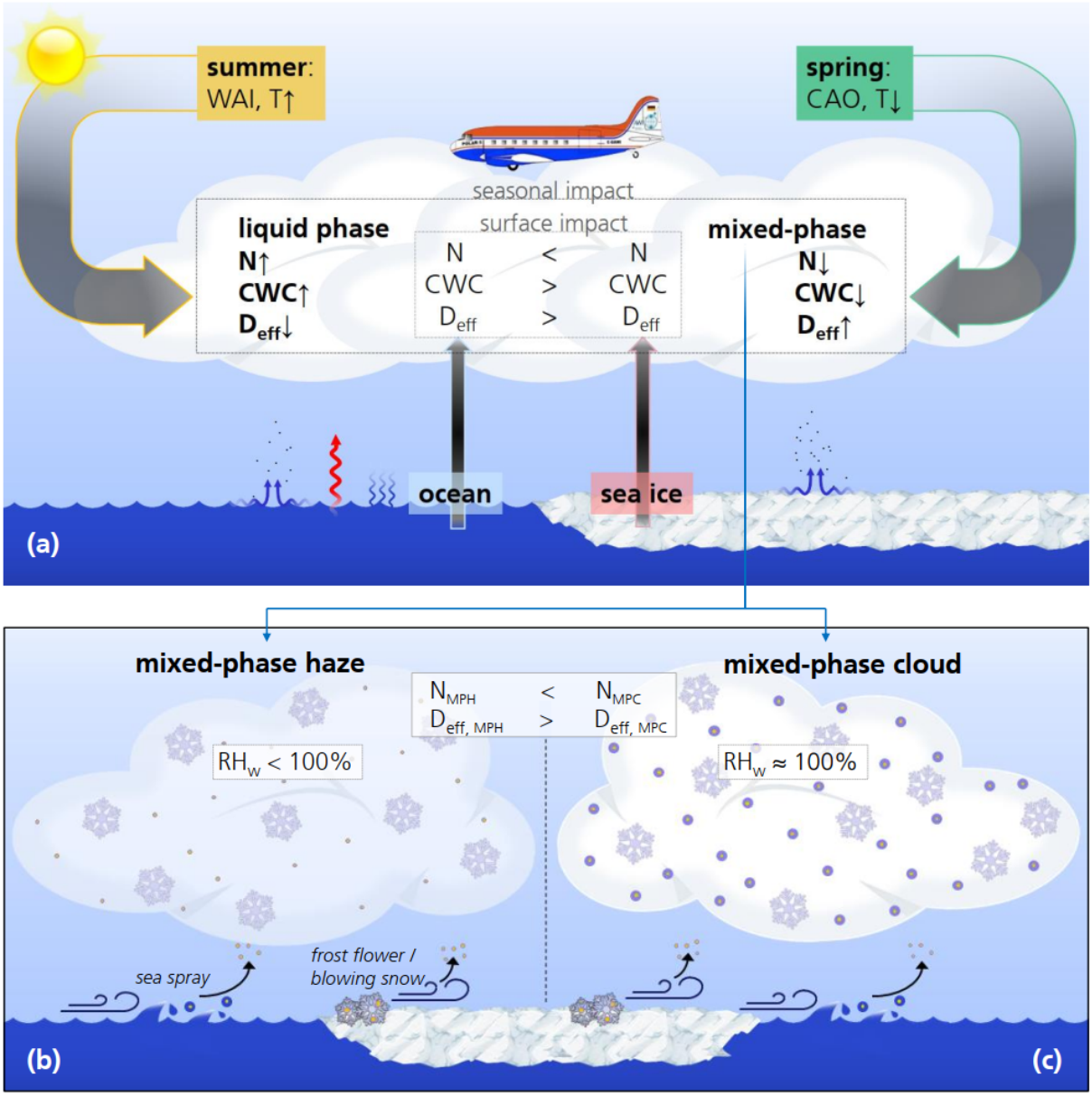

Figure 63 Schematic representation of the results of the first two research questions in Fig. (a): Black arrows symbolize the influence on the microphysical properties of Arctic low-level clouds, which is most pronounced during different seasons. In both seasons, the prevailing surface conditions modify the microphysical cloud properties due to regional atmospheric–surface processes. Abbreviations: WAI – *warm air intrusion*, CAO – *cold air outbreak*. Schematic representation of the results of the third research question: (b) illustrates the microphysical properties of mixed-phase haze and (c) the microphysical properties of a classic mixed-phase cloud. Fig. (a) and corresponding caption from Moser et al. (2023).

breaking mechanisms and over the sea ice by frost flowers and blowing snow. The processes by which CCNs are introduced into the ABL appear to be enhanced over the sea ice.

The investigation on microphysical cloud properties and thermodynamic phases contribute to an improved understanding of the variability of Arctic low-level clouds as a function of the ambient conditions. This study can help to evaluate and improve remote sensing retrievals of Arctic clouds by providing insights into microphysical cloud processes and directly measured microphysical cloud properties with highest accuracy due to in-situ observations. The presented cloud data are also ideally suited for developing and evaluating parameterizations of Arctic low-level clouds in process models to investigate the influence of different meteorological and surface conditions on clouds in more detail. Therefore the results of this thesis can contribute to the improved representation of microphysical cloud properties and their radiative impact in global climate models and further elucidate the role of clouds in Arctic amplification.

7 Outlook

The results of this work suggest new approaches for future research activities. In the following, an outlook will be given towards new questions and ideas for further methods in the field of cloud physics. The following ideas can be applied to existing in-situ data sets and future research flight campaign plans.

Assessing cloud contributions to Arctic amplification

In this thesis, in-situ cloud measurements are presented to improve the knowledge of the microphysical processes and the thermodynamic phase of clouds in the Arctic. One goal of current research is to assess the role of clouds in Arctic amplification and to quantify feedback mechanisms for individual cloud processes. To answer these questions, climate models have to be used. However, future model-based projections of Arctic climate change are highly uncertain (Smith et al., 2019; Cohen et al., 2019; Linke et al., 2023) because of the challenges in modeling the effects and evolution of clouds and the interaction of the environment with clouds (Pithan et al., 2013; Wendisch et al., 2019; Huang et al., 2019). The cloud data presented here are based on airborne in-situ measurements. No other measuring technique can derive more accurate microphysical properties of natural clouds than in-situ measurements. A limitation for airborne in-situ observations, however, is that the measurements are only recorded along a 1D trajectory, and research flights are limited to a few hours per day. Resolving microphysical cloud processes in 2D or 3D at a given time is only possible to a limited extent, for instance, through specific flight strategies. Therefore, model simulations are required to understand the role of clouds in the Arctic climate system. Good results can be achieved when models are supplied with large-scale and long-term measurements of cloud parameters. For this purpose, measurements from remote sensing instruments are the most suitable. It should be noted, however, that such measurements cannot detect small-scale cloud processes as precisely as in-situ cloud probes. Additionally, cloud parameters are often indirectly measured and based on retrievals, which are associated with significant uncertainties. For this reason, validating and improving the cloud microphysical retrievals of active remote sensing instruments such as radar, lidar, or passive remote instruments with in-situ data is essential. This will lead to more accurate representations of cloud microphysics in large-scale remote sensing data from ground base, airborne, or space borne observations and, in turn, to improved cloud parameterization in climate models. With future climate models that include such optimized cloud parameterizations, it will be possible to link specific feedback mechanisms (e.g. cloud albedo feedback, cloud phase feedback, surface feedbacks, ...) to individual cloud processes with less uncertainty, which will help quantify the role of clouds in the Arctic climate system.

Unraveling Arctic mixed-phase haze conditions

The data collected in this work show that the cloud type mixed-phase haze, which is a mixture of haze droplets and ice crystals, is frequently present in spring. In addition, large aerosol particles are observed in many cloud-free regions. These particles have similar microphysical properties compared to the haze droplets in mixed-phase haze conditions. Based on these findings, further questions arise regarding the haze droplets and the Arctic low-level mixed-phase haze.

The first question is how the mixed-phase haze clouds form. This cannot be clarified with the presented cloud data only. The mixed-phase haze conditions can either be a mixture of the ice crystals and aerosols with no physical relation, or these regimes could have originated from a dried-out mixed-phase cloud, which is also suggested by Costa et al. (2017). To answer this question, subsequent analyses of the aerosols are required. For this purpose, future studies on mixed-phase haze conditions should consider all available particle and trace gas measurements from the HALO-(AC)^3 campaign. In case a significant fraction of swollen sea salt particles is observed with the aerosol instrumentation at $RH_w < 74\%$, these aerosol particles could be associated with a dried out mixed-phase cloud when found in the upper part of the hysteresis of the hygroscopic growth factor. Process studies with models and satellite data could help to test the hypothesis of the development from a mixed-phase cloud to a mixed-phase haze condition.

To understand the mixed-phase haze in more detail, it is essential to address questions about microphysical processes in future studies. Are ice crystals and the swollen sea salt particles spatially close enough to affect each other? Do the wet aerosols grow at the expense of the ice content or vice versa? Theoretical analysis similar to the glaciation time calculations for classic mixed-phase clouds (Korolev et al., 2017, and references therein), but modified for wet sea salt aerosols instead of droplets, can help to answer previous questions. High resolution aerosol and cloud measurements e.g. with a holographic instrument (Fugal et al., 2004), a high speed imager (Esposito et al., 2019), or a cloud particle imager (Lawson et al., 2001) could deliver new results here.

A further question related to the mixed-phase haze is the increased concentration of small particles above the sea ice compared to the open ocean. The results suggest that this is caused by an increased aerosol source originating from the sea ice. Work from other parts of polar research could help to investigate these sources further. Many studies deal with the interaction between the cryosphere and the atmosphere. A particular focus is on investigating bromine explosion events (Barrie et al., 1988; Jones et al., 2009; Frieß et al., 2023), in which high bromine values are observed in the polar troposphere during spring. One possible explanation for such events is the formation of bromine from saline snow. The bromine is released into the atmosphere via a photochemical reaction on saline surfaces, leading to ozone depletion. Such an increase of bromine and a simultaneous ozone decrease in the ABL is often associated with blowing snow events. Several studies have been carried out to integrate the chemical processes responsible for the formation of bromine explosion events into chemical models (e.g., p-TOMCAT or GEOS-

Model; Huang and Jaeglé, 2017; Yang et al., 2019; Yang et al., 2020). Such models could relate blowing snow events with the in-situ cloud measurements, enabling further options to investigate the correlation between blowing snow and the observed increased particle number concentration above the sea ice. In addition to the chemical models, the trace gas measurements from the HALO-$(AC)^3$ campaign could potentially deliver additional information on the mixed-phase haze processes.

The recent study by Gong et al. (2023) has shown that sea salt aerosols from blowing snow affect cloud formation and increase the long-wave emissivity of clouds, leading to increased surface warming under cloudy conditions. This indirect effect of SSA from blowing snow is estimated to increase the downward longwave radiation by about 2.30 $\mathrm{W\,m^{-2}}$ under cloudy skies from November to April north of 70 °N. Future studies should include the direct radiative effect based on the presented microphysical properties of mixed-phase haze and pure haze conditions. The lower optical thickness of the mixed-phase haze conditions and their decreased particle number concentrations suggest that their radiative effect on the atmospheric energy budget is smaller than classic mixed-phase clouds. However, it should be emphasized that this work shows that the occurrence of mixed-phase haze and pure haze droplets is significantly higher than the occurrence of classic cloud conditions. Considering the prevalence of mixed-phase haze and haze droplets, these conditions could potentially significantly impact the radiative energy budget of the Arctic atmosphere. Therefore, this thesis strongly recommends to quantify this effect using e.g. a radiative transfer model, while considering the frequency of occurrence, since atmospheric conditions with haze droplets could potentially contribute to Arctic amplification.

As the Arctic continues to warm, the surface will undergo further changes. The fraction of multiyear sea ice will decrease significantly, increasing the proportion of thin sea ice with higher saline load (Xu et al., 2016). This may affect the aerosol concentration in the future Arctic ABL and thus further increase cloud and haze formation over the sea ice. However, the total sea ice extent will decline drastically (IPCC, 2021).

Improvements in in-situ data processing

Although the analysis and processing of the in-situ data in this study was performed with a high degree of accuracy, there may still be potential for further processing optimization. In this thesis, the ice particles are separated from the liquid droplets by applying a size threshold. Particles smaller than 50 µm are considered as liquid, and anything above is considered as ice, which is a reasonable assumption for stratiform mixed-phase clouds and validated with the Polar Nephelometer. For further microphysical cloud analysis, applying more advanced phase separation is suggested. Some algorithms have already been developed for this purpose, as described by Korolev et al. (2017) or D'Alessandro et al. (2019). In future algorithms for cloud in-situ data processing, neural networks have great potential (Jaffeux et al., 2022). Such networks could be trained to distinguish between water droplets and ice crystals, allowing the

liquid and ice phases to be treated separately for further analysis. Neural networks can also help classify ice crystals as shown in Fig. 17, which would lead to a deeper insight into the microphysical processes of the clouds, such as differentiating between pristine ice crystals, aggregation, and riming.

A particular challenge is to match in-situ cloud measurements, remote sensing of clouds, and clouds in models for subsequent applications like evaluations, validations, or for developing retrieval algorithms. Microphysical parameters such as N or CWC are often well defined, while there are multiple definitions for D_{eff} depending on the method. For instance, while the in-situ measured D_{eff} is based on the maximum size of the individual ice crystals, models, such as atmospheric radiative transfer models, represent the size of the ice crystals based on their physical properties. Consequently, in-situ data can significantly overestimate the D_{eff} of ice crystals compared to atmospheric models. To derive a D'_{eff} measured with in-situ cloud probes, suitable to compare with models, the following equation could be used (derived from an equation used in Meerkötter et al. (1999) and Wang et al. (2019)):

$$D'_{\text{eff}} = \frac{3 \cdot Q_{\text{e}} \cdot \text{IWC}(z)}{2 \cdot \rho_{\text{ice}} \cdot \text{Ext. Coef.}} \tag{7.1}$$

with ρ_{ice} the density of ice and Q_{e} the extinction efficiency. D'_{eff} is thus a function of in-situ measured IWC and Ext. Coef.. This formula can only be applied when both IWC and Ext. Coef. are measured simultaneously on board of a research aircraft. However, instruments that can provide the Ext. Coef. such as the Polar Nephelometer are not always on board during aircraft field campaigns. Data sets, including OAP image data and simultaneous measured Ext. Coef. values could be the basis for developing a relationship to estimate the Ext. Coef. or D'_{eff} from parameters derived from 2D raw images. Similar to the mass-dimension relationship, which empirically estimates a relationship between the size of an ice crystal and its mass (see IWC calculation in Sect. 3.4.2).

Further scientific potential of the collected data set

This thesis mainly analyzes microphysical cloud data on horizontal flight segments flown at constant altitudes. This approach ensures high data quality, as the instrument angle of attack is ideal and the environmental conditions such as pressure, temperature, and humidity remain stable, resulting in reliable statistics. Although measurement accuracy may decrease during ascents and descents, vertical investigations with data from such flight legs enable further valuable insight into the vertical distribution of microphysical properties of Arctic clouds. Such a study has been previously done by Mioche et al. (2017), where microphysical cloud properties are presented in a normalized cloud altitude. Normalization was based on the altitude of the cloud liquid water content. The presented microphysical cloud data sets from the AFLUX, MOSAiC-ACA, and HALO-(AC)^3 campaigns also contain numerous ascents and descents through boundary layer clouds, which enable statistical vertical cloud analysis. However, it is recommended not to normalize the height according to the liquid water content, but according to the height

of the boundary layer, which can be derived from meteorological data such as the height of the temperature inversion (Dong et al., 2015). This approach enables cloud microphysics to be analyzed with respect to atmospheric stratification. This includes, for example, the influence of a coupled or decoupled atmosphere to the surface and the presence and depth of a moisture inversion layer above the ABL. Such factors that control Arctic low-level clouds are yet not well understood (Tan et al., 2023).
Another potential use of the collected data set is the investigation of secondary ice production in Arctic low-level clouds (Field et al., 2016; Li et al., 2021; Pasquier et al., 2022). In particular, the in-situ cloud data collected during the HALO-(AC)^3 campaign is of great value, as in-situ measurements of ice nucleating particles were carried out at the same time with the cloud particle in-situ measurements on board the research aircraft Polar 6. This allows for the determination of the amount of secondary ice with high accuracy while also considering all relevant environmental parameters and cloud microphysical properties. This enables a comprehensive analysis of the relevant secondary ice production processes and provides an assessment of the importance of secondary ice production in Arctic low-level clouds.

Scientific questions for planned aircraft field campaigns

To a certain extent, the environmental conditions in the Antarctic are similar to those found in the Arctic. Particularly in the Antarctic marginal sea ice zone, conditions similar to those in the northern hemisphere occur. Both regions have similar local aerosol sources and similar atmospheric stratification characterized by low surface temperatures (Carslaw, 2022). This raises the question of whether the microphysical properties and thermodynamic phases of low-level clouds in Antarctica's marginal sea ice zone are similar to those in the northern hemisphere. Questions of this kind can potentially be investigated in future flight missions, such as the planned HALO-South campaign in 2025.
All presented results are based on airborne in-situ cloud measurements taken during the daytime only. Are the microphysical properties and thermodynamic cloud phases shown here representative of night conditions, too? Potential differences in cloud processes during the polar night can be identified within the field campaign Contrasting Polar Night and Day (CONIDA). This mission is planned for 2028 in similar locations as HALO-(AC)^3 but with research flights planned at night.

List of Publications

Moser, M., Voigt, C., Jurkat-Witschas, T., Hahn, V., Mioche, G., Jourdan, O., Dupuy, R., Gourbeyre, C., Schwarzenboeck, A., Lucke, J., Boose, Y., Mech, M., Borrmann, S., Ehrlich, A., Herber, A., Lüpkes, C., and Wendisch, M. (2023). "Microphysical and thermodynamic phase analyses of Arctic low-level clouds measured above the sea ice and the open ocean in spring and summer". In: *Atmospheric Chemistry and Physics* 23.13, pp. 7257–7280. DOI: 10.5194/acp-23-7257-2023.

Blanke, A., Heymsfield, A. J., **Moser, M.**, and Trömel, S. (2023). "Evaluation of polarimetric ice microphysical retrievals with OLYMPEX campaign data". In: *Atmospheric Measurement Techniques* 16.8, pp. 2089–2106. DOI: 10.5194/amt-16-2089-2023.

Maherndl, N., **Moser, M.**, Lucke, J., Mech, M., Risse, N., Schirmacher, I., and Maahn, M. (2024). "Quantifying riming from airborne data during the HALO-(AC)^3 campaign". In: Atmospheric Measurement Techniques 17.5, pp. 1475–1495. ISSN: 1867-8548. DOI: 10.5194/amt-17-1475-2024.

Mech, M., Ehrlich, A., Herber, A., Lüpkes, C., Wendisch, M., Becker, S., Boose, Y., Chechin, D., Crewell, S., Dupuy, R., Gourbeyre, C., Hartmann, J., Jäkel, E., Jourdan, O., Kliesch, L.-L., Klingebiel, M., Kulla, B. S., Mioche, G., **Moser, M.**, Risse, N., Ruiz-Donoso, E., Schäfer, M., Stapf, J., and Voigt, C. (2022). "MOSAiC-ACA and AFLUX - Arctic airborne campaigns characterizing the exit area of MOSAiC". In: *Scientific Data* 9.1. DOI: 10.1038/s41597-022-01900-7.

Lucke, J., Jurkat-Witschas, T., Heller, R., Hahn, V., Hamman, M., Breitfuss, W., Bora, V. R., **Moser, M.**, and Voigt, C. (2022). "Icing wind tunnel measurements of supercooled large droplets using the 12 mm total water content cone of the Nevzorov probe". In: *Atmospheric Measurement Techniques* 15.24, pp. 7375–7394. DOI: 10.5194/amt-15-7375-2022.

Hahn, V., Meerkötter, R., Voigt, C., Gisinger, S., Sauer, D., Catoire, V., Dreiling, V., Coe, H., Flamant, C., Kaufmann, S., Kleine, J., Knippertz, P., **Moser, M.**, Rosenberg, P., Schlager, H., Schwarzenboeck, A., and Taylor, J. (2023). "Pollution slightly enhances atmospheric cooling by low-level clouds in tropical West Africa". In: *Atmospheric Chemistry and Physics* 23.15, pp. 8515–8530. DOI: 10.5194/acp-23-8515-2023.

Lucke, J. R., Jurkat, T., Baumgardner, D., Kalinka, F., **Moser, M.**, Castro, E. D. L. T., and Voigt, C. (2023). "Characterization of Atmospheric Icing Conditions during the HALO-(AC)^3 Campaign with the Nevzorov Probe and the Backscatter Cloud Probe with Polarization Detection". In: *SAE Technical Paper Series.* SAE International. DOI: 10.4271/2023-01-1485.

Klingebiel, M., Ehrlich, A., Ruiz-Donoso, E., Risse, N., Schirmacher, I., Jäkel, E., Schäfer, M., Wolf, K., Mech, M., **Moser, M.**, Voigt, C., and Wendisch, M. (2023). "Variability and properties of liquid-dominated clouds over the ice-free and sea-ice-covered Arctic Ocean". In: *Atmospheric Chemistry and Physics* 23.24, pp. 15289–15304. DOI: 10.5194/acp- 23-15289-2023.

Kirbus, B., Schirmacher, I., Klingebiel, M., Schäfer, M., Ehrlich, A., Slättberg, N., Lucke, J., **Moser, M.**, Müller, H., and Wendisch, M. (2024). "Thermodynamic and cloud evolution in a cold-air outbreak during HALO-(AC)^3: quasi-Lagrangian observations compared to the ERA5 and CARRA reanalyses". In: Atmospheric Chemistry and Physics 24.6, pp. 3883–3904. ISSN: 1680-7324. DOI: 10.5194/acp-24-3883-2024.

Shupe, M. D., Rex, M., Blomquist, B., Persson, P. O. G., Schmale, J., Uttal, T., Althausen, D., Angot, H., Archer, S., Bariteau, L., Beck, I., Bilberry, J., Bucci, S., Buck, C., Boyer, M., Brasseur, Z., Brooks, I. M., Calmer, R., Cassano, J., Castro, V., Chu, D., Costa, D., Cox, C. J., Creamean, J., Crewell, S., Dahlke, S., Damm, E., Boer, G. de, Deckelmann, H., Dethloff, K., Dütsch, M., Ebell, K., Ehrlich, A., Ellis, J., Engelmann, R., Fong, A. A., Frey, M. M., Gallagher, M. R., Ganzeveld, L., Gradinger, R., Graeser, J., Greenamyer, V., Griesche, H., Griffiths, S., Hamilton, J., Heinemann, G., Helmig, D., Herber, A., Heuzé, C., Hofer, J., Houchens, T., Howard, D., Inoue, J., Jacobi, H.-W., Jaiser, R., Jokinen, T., Jourdan, O., Jozef, G., King, W., Kirchgaessner, A., Klingebiel, M., Krassovski, M., Krumpen, T., Lampert, A., Landing, W., Laurila, T., Lawrence, D., Lonardi, M., Loose, B., Lüpkes, C., Maahn, M., Macke, A., Maslowski, W., Marsay, C., Maturilli, M., Mech, M., Morris, S., **Moser, M.**, Nicolaus, M., Ortega, P., Osborn, J., Pätzold, F., Perovich, D. K., Petäjä, T., Pilz, C., Pirazzini, R., Posman, K., Powers, H., Pratt, K. A., Preußer, A., Quéléver, L., Radenz, M., Rabe, B., Rinke, A., Sachs, T., Schulz, A., Siebert, H., Silva, T., Solomon, A., Sommerfeld, A., Spreen, G., Stephens, M., Stohl, A., Svensson, G., Uin, J., Viegas, J., Voigt, C., Gathen, P. von der, Wehner, B., Welker, J. M., Wendisch, M., Werner, M., Xie, Z., and Yue, F. (2022). "Overview of the MOSAiC expedition—Atmosphere". In: *Elementa: Science of the Anthropocene* 10.1. DOI: 10.1525/elementa.2021.00060.

Wendisch, M., Brückner, M., Crewell, S., Ehrlich, A., Notholt, J., Lüpkes, C., Macke, A., Burrows, J. P., Rinke, A., Quaas, J., Maturilli, M., Schemann, V., Shupe, M. D., Akansu, E. F., Barrientos-Velasco, C., Bärfuss, K., Blechschmidt, A.-M., Block, K., Bougoudis, I., Bozem, H., Böckmann, C., Bracher, A., Bresson, H., Bretschneider, L., Buschmann, M., Chechin, D. G., Chylik, J., Dahlke, S., Deneke, H., Dethloff, K., Donth, T., Dorn, W., Dupuy, R., Ebell, K., Egerer, U., Engelmann, R., Eppers, O., Gerdes, R., Gierens, R., Gorodetskaya, I. V., Gottschalk, M., Griesche, H., Gryanik, V. M., Handorf, D., Harm-Altstädter, B., Hartmann, J., Hartmann, M., Heinold, B., Herber, A., Herrmann, H., Heygster, G., Höschel, I., Hofmann, Z., Hölemann, J., Hünerbein, A., Jafariserajehlou, S., Jäkel, E., Jacobi, C., Janout, M., Jansen, F., Jourdan, O.,

Jurányi, Z., Kalesse-Los, H., Kanzow, T., Käthner, R., Kliesch, L. L., Klingebiel, M., Knudsen, E. M., Kovács, T., Körtke, W., Krampe, D., Kretzschmar, J., Kreyling, D., Kulla, B., Kunkel, D., Lampert, A., Lauer, M., Lelli, L., Lerber, A. von, Linke, O., Löhnert, U., Lonardi, M., Losa, S. N., Losch, M., Maahn, M., Mech, M., Mei, L., Mertes, S., Metzner, E., Mewes, D., Michaelis, J., Mioche, G., **Moser, M.**, Nakoudi, K., Neggers, R., Neuber, R., Nomokonova, T., Oelker, J., Papakonstantinou-Presvelou, I., Pätzold, F., Pefanis, V., Pohl, C., Pinxteren, M. van, Radovan, A., Rhein, M., Rex, M., Richter, A., Risse, N., Ritter, C., Rostosky, P., Rozanov, V. V., Donoso, E. R., Saavedra Garfias, P., Salzmann, M., Schacht, J., Schäfer, M., Schneider, J., Schnierstein, N., Seifert, P., Seo, S., Siebert, H., Soppa, M. A., Spreen, G., Stachlewska, I. S., Stapf, J., Stratmann, F., Tegen, I., Viceto, C., Voigt, C., Vountas, M., Walbröl, A., Walter, M., Wehner, B., Wex, H., Willmes, S., Zanatta, M., and Zeppenfeld, S. (2022). "Atmospheric and Surface Processes, and Feedback Mechanisms Determining Arctic Amplification: A Review of First Results and Prospects of the $(AC)^3$ Project". In: *Bulletin of the American Meteorological Society.* DOI: 10.1175/bams-d-21-0218.1.

Trömel, S., Simmer, C., Blahak, U., Blanke, A., Doktorowski, S., Ewald, F., Frech, M., Gergely, M., Hagen, M., Janjic, T., Kalesse-Los, H., Kneifel, S., Knote, C., Mendrok, J., **Moser, M.**, Köcher, G., Mühlbauer, K., Myagkov, A., Pejcic, V., Seifert, P., Shrestha, P., Teisseire, A., Terzi, L. von, Tetoni, E., Vogl, T., Voigt, C., Zeng, Y., Zinner, T., and Quaas, J. (2021). "Overview: Fusion of radar polarimetry and numerical atmospheric modelling towards an improved understanding of cloud and precipitation processes". In: *Atmospheric Chemistry and Physics* 21.23, pp. 17291–17314. DOI: 10.5194/acp-21-17291-2021.

Abbreviations

$(AC)^3$	ArctiC Amplification: Climate Relevant Atmospheric and SurfaCe Processes, and Feedback Mechanisms
1D	one-dimensional
2D	two-dimensional
2D-S	2D Stereo Imaging Probe
ABL	atmospheric boundary layer
ACLOUD	Arctic CLoud Observations Using airborne measurements during polar Day
ADC	analog-to-digital converter
AFLUX	Aircraft campaign observing FLUXes of energy and momentum in the cloudy boundary layer over polar sea ice and ocean
ALABAMA	Aircraft-based Laser ABlation Aerosol MAss spectrometer
AMSR2	Advanced Microwave Scanning Radiometer 2
AWI	Alfred Wegener Institute
BAS	British Antarctic Survey
CAO	cold air outbreak
CAPS	Cloud Aerosol and Precipitation Spectrometer
CAS	Cloud Aerosol Spectrometer
CCN	cloud condensation nuclei
CCP	Cloud Combination Probe
CDP	Cloud Droplet Probe
CIP	Cloud Imaging Probe
CONIDA	Contrasting Polar Night and Day
CVI	counterflow virtual impactor
DLR	Deutsches Zentrum für Luft- und Raumfahrt
DMT	Droplet Measurement Technologies
GCOM-W1	Global Change Observation Mission-Water
GDAS	Global Data Assimilation System
GEOS	Goddard Earth Observing System
GFS	Global Forecast System
HALO	High Altitude and Long Range Research Aircraft
HALO-$(AC)^3$	Arctic Air Mass Transformations during Warm Air Intrusions and Marine Cold Air Outbreaks
HGS	high gain stage
HVPS	High Volume Precipitation Spectrometer
HYSPLIT	Hybrid Single Particle Lagrangian Integrated Trajectory model
INP	ice nucleating particle
INS	Internal navigation system
IPCC	Intergovernmental Panel on Climate Change

LabVIEW	Laboratory Virtual Instrument Engineering Workbench
LaMP	Laboratoire de Météorologie Physique
LGS	low gain stage
lidar	light detection and ranging
LYR	IATA-Code for the Longyearbyen airport
MGS	mid gain stage
MIZ	marginal sea ice zone
MODIS	MODerate-resolution Imaging Spectroradiometer
MOSAiC	Multidisciplinary drifting Observatory for the Study of Arctic Climate
MOSAiC-ACA	Multidisciplinary Drifting Observatory for the Study of Arctic Climate - Airborne observations in the Central Arctic
MPC	mixed-phase cloud
MPH	mixed-phase haze
MPIC	Max-Planck-Institut für Chemie
NASA	National Aeronautics and Space Administration
OAP	Optical Array Probe
OLYMPEX	Olympic Mountain Experiment
OPC	optical particle counter
p-TOMCAT	parallelised-Tropospheric Offline Model of Chemistry and Transport
PADS	Particle Analysis and Display System
PANGAEA	Data Publisher for Earth & Environmental Science
PBP	particle by particle
PIN	positive-intrinsic-negative
PIP	Precipitation Imaging Probe
PMS	particle measurement system
PN	Polar Nephelometer
PSD	particle size distribution
radar	radio detection and ranging
SODA	Software for OAP Data Analysis
SPEC Inc.	Stratton Park Engineering Company
SSA	sea salt aerosol
STP	pressure-corrected to standard temperature and pressure
WAI	warm air intrusion
WBF	Wegener–Bergeron–Findeisen

List of Symbols

Symbol	*Description of Symbol (SI Unit)*
a	gain stage calibration value a (m^2)
a_{ij}	matrix element ( )
a'	Kelvin term of the Köhler equation (m)
α	parameter α for mass-dimension relationship ($kg\,m^{-b}$)
α'	resolution of the OAP (m)
A	set of 1 Hz cloud data ( )
adc_l	ADC lower threshold ( )
adc_u	ADC upper threshold ( )
ASC	angular scattering coefficient ( )
b'	Raoult term of the Köhler equation (m^3)
β	parameter β for mass-dimension relationship ( )
b	gain stage calibration value b (m^2)
B	set of 1 Hz cloud data ( )
Bin_k	bin of the size range k ( )
CWC	cloud water content ($kg\,m^{-3}$)
$\widetilde{CWC}$	median cloud water content ($kg\,m^{-3}$)
$\widetilde{CWC}_{<50\mu m}$	median cloud water content for particles smaller 50 µm ($kg\,m^{-3}$)
$\widetilde{CWC}_{>50\mu m}$	median cloud water content for particles larger 50 µm ($kg\,m^{-3}$)
$\overline{d_{cloud}}$	mean horizontal cloud extent (m)
D	cloud particle diameter (m)
$D_{Droplets}$	droplet diameter (m)
D_{eff}	effective diameter (m)
$\tilde{D}_{eff}$	median effective diameter (m)
$\tilde{D}_{eff<50\mu m}$	median effective diameter for particles smaller 50 µm (m)
$\tilde{D}_{eff>50\mu m}$	median effective diameter for particles larger 50 µm (m)
D_i	diameter corresponding to size bin i (m)
D_l	lower size bin (m)
D_{lt}	lower size detection threshold (m)
D_{max}	maximum diameter (m)
D_p	particle diameter (m)
D_u	upper size bin (m)
D_y	particle diameter in the direction of the array (m)
DOF	depth of field (m)
e_i	saturation vapour pressure over ice (Pa)
e_w	saturation vapour pressure over water (Pa)
e	mathematical constant Euler's number ( )

Ext. Coef.	extinction coefficient (m^{-1})
F	cumulative distribution function ( )
f_s	sampling frequency (s^{-1})
f	focal length (m)
g	asymmetry parameter ( )
g_e	hygroscopic growth factor ( )
γ	active time correction value ( )
i_v	van't Hoff factor ( )
I_0	laser light intensity level ($W\,m^{-2}$)
I	light intensity level ($W\,m^{-2}$)
IWC	ice water content ($kg\,m^{-3}$)
IWC_i	ice water content of the size bin i ($kg\,m^{-3}$)
IPT	inter-particle arrival time (s)
k	number of detector elements ( )
λ'	slope of the gamma function (m^{-1})
λ	wavelength (m)
LWC	liquid water content ($kg\,m^{-3}$)
LWC_i	liquid water content of the size bin i ($kg\,m^{-3}$)
m_i	ice mass in the size bin i (kg)
m_s	mass of solute (m)
M_S	molar mass of the solute ($kg\,mol^{-1}$)
M_V	molar mass of water ($kg\,mol^{-1}$)
μ	dispersion of the gamma function ( )
n	refractive index ( )
n_i	number of particles in the size bin i ( )
N	total number concentration (m^{-3})
$\tilde{N}$	median number concentration (m^{-3})
$\tilde{N}_{<50\mu m}$	median number concentration for particles smaller 50 µm (m^{-3})
$\tilde{N}_{>50\mu m}$	median number concentration for particles larger 50 µm (m^{-3})
N_0	intercept of the gamma function ($m^{-4-\mu}$)
N_{all}	number of particles counted in the 1 Hz file ( )
N_i	particle number concentration in size bin i (m^{-3})
N_{image}	number of particles counted in the image file ( )
p	probability value ( )
π	mathematical constant pi ( )
Q_e	extinction efficiency ( )
r	radius of a droplet or wet aerosol particle (m)
r_0	radius of a dry aerosol particle (m)
r_c	critical radius (m)

R	particle radius (m)
$\mathrm{RH_{ice}}$	relative humidity with respect to ice ( )
$\mathrm{RH_w}$	relative humidity with respect to water ( )
ρ_{ice}	density of ice ($\mathrm{kg\,m^{-3}}$)
ρ_{w}	density of water ($\mathrm{kg\,m^{-3}}$)
R_v	gas constant for water vapor ($\mathrm{J\,kg^{-1}\,K^{-1}}$)
S_{c}	critical saturation ratio ( )
S	saturation ratio ( )
SA	sample area ($\mathrm{m^2}$)
SV	sampling volume ($\mathrm{m^3}$)
$\mathrm{SV_i}$	sampling volume of the size bin i ($\mathrm{m^3}$)
SIC	sea ice concentration ( )
σ	surface tension ($\mathrm{J\,m^{-2}}$)
σ_{4-12°	scattering cross section from 4° to 12° ($\mathrm{m^2}$)
T	temperature (K)
T_{cloud}	cloud temperature (K)
t_{a}	active time (s)
$t_{\mathrm{a},\gamma}$	γ-corrected active time (s)
t_{d}	dead time (s)
t_{s}	sampling time (s)
TAS	true airspeed ($\mathrm{m\,s^{-1}}$)
w_{eff}	effective array width (m)
W	metric to calculate the Wasserstein distance ( )
z	altitude (m)
Z	distance to the object plane (m)
Z_{d}	diffraction image variable ( )
$Z_{\mathrm{d\,max}}$	diffraction image variable with an intensity threshold; DOF constant ( )

Bibliography

Bansemer, A. (2023). *System for OAP Data Analysis*. Zenodo. Version v2.23.0. DOI: 10.5281/zenodo.7803116.

Barrie, L. A., Bottenheim, J. W., Schnell, R. C., Crutzen, P. J., and Rasmussen, R. A. (1988). "Ozone destruction and photochemical reactions at polar sunrise in the lower Arctic atmosphere". In: *Nature* 334.6178, pp. 138–141. ISSN: 1476-4687. DOI: 10.1038/334138a0.

Baumgardner, D., Jonsson, H., Dawson, W., O'Connor, D., and Newton, R. (2001). "The Cloud, Aerosol and Precipitation Spectrometer: A New Instrument for Cloud Investigations". In: *Atmospheric Research*. 13th International Conference on Clouds and Precipitation 59–60, pp. 251–264. ISSN: 0169-8095. DOI: 10.1016/S0169-8095(01)00119-3.

Baumgardner, D., Brenguier, J., Bucholtz, A., Coe, H., DeMott, P., Garrett, T., Gayet, J.-F., Hermann, M., Heymsfield, A. J., Korolev, A., Krämer, M., Petzold, A., Strapp, W., Pilewskie, P., Taylor, J., Twohy, C., and Wendisch, M. (2011). "Airborne Instruments to Measure Atmospheric Aerosol Particles, Clouds and Radiation: A Cook's Tour of Mature and Emerging Technology". In: *Atmos. Res.* 102, pp. 10–29. DOI: 10.1016/j.atmosres.2011.06.021.

Baumgardner, D., Newton, R., Krämer, M., Meyer, J., Beyer, A., Wendisch, M., and Vochezer, P. (2014). "The Cloud Particle Spectrometer with Polarization Detection (CPSPD): A next generation open-path cloud probe for distinguishing liquid cloud droplets from ice crystals". In: *Atmospheric Research* 142, pp. 2–14. DOI: 10.1016/j.atmosres.2013.12.010.

Baumgardner, D., Abel, S. J., Axisa, D., Cotton, R., Crosier, J., Field, P., Gurganus, C., Heymsfield, A. J., Korolev, A., Krämer, M., Lawson, R. P., McFarquhar, G., Ulanowski, Z., and Um, J. (2017). "Cloud Ice Properties: In Situ Measurement Challenges". In: *Meteorological Monographs* 58, pp. 9.1–9.23. DOI: 10.1175/amsmonographs-d-16-0011.1.

Benmoshe, N. and Khain, A. P. (2014). "The effects of turbulence on the microphysics of mixed-phase deep convective clouds investigated with a 2-D cloud model with spectral bin microphysics". In: *Journal of Geophysical Research: Atmospheres* 119.1, pp. 207–221. DOI: 10.1002/2013jd020118.

Bergeron, T. (1935). "On the physics of clouds and precipitation." In: *International Union of Geodesy and Geophysics*.

Blanchard, D. C. (1989). "The Ejection of Drops from the Sea and Their Enrichment with Bacteria and Other Materials: A Review". In: *Estuaries* 12.3, p. 127. DOI: 10.2307/1351816.

Blanke, A., Heymsfield, A. J., Moser, M., and Trömel, S. (2023). "Evaluation of polarimetric ice microphysical retrievals with OLYMPEX campaign data". In: *Atmospheric Measurement Techniques* 16.8, pp. 2089–2106. DOI: 10.5194/amt-16-2089-2023.

Bock, L., Lauer, A., Schlund, M., Barreiro, M., Bellouin, N., Jones, C., Meehl, G. A., Predoi, V., Roberts, M. J., and Eyring, V. (2020). "Quantifying Progress Across Different CMIP Phases With the ESMValTool". In: *Journal of Geophysical Research: Atmospheres* 125.21. DOI: 10.1029/2019jd032321.

Bodas-Salcedo, A., Hill, P. G., Furtado, K., Williams, K. D., Field, P. R., Manners, J. C., Hyder, P., and Kato, S. (2016). "Large Contribution of Supercooled Liquid Clouds to the Solar Radiation Budget of the Southern Ocean". In: *Journal of Climate* 29.11, pp. 4213–4228. DOI: 10.1175/jcli-d-15-0564.1.

Boer, G. de, Morrison, H., Shupe, M. D., and Hildner, R. (2011). "Evidence of liquid dependent ice nucleation in high-latitude stratiform clouds from surface remote sensors: LIQUID INDUCED ICE NUCLEATION". In: *Geophysical Research Letters* 38.1. ISSN: 0094-8276. DOI: 10.1029/2010gl046016.

Brands, M., Kamphus, M., Böttger, T., Schneider, J., Drewnick, F., Roth, A., Curtius, J., Voigt, C., Borbon, A., Beekmann, M., Bourdon, A., Perrin, T., and Borrmann, S. (2011). "Characterization of a Newly Developed Aircraft-Based Laser Ablation Aerosol Mass Spectrometer (ALABAMA) and First Field Deployment in Urban Pollution Plumes over Paris During MEGAPOLI 2009". In: *Aerosol Science and Technology* 45.1, pp. 46–64. ISSN: 1521-7388. DOI: 10.1080/02786826.2010.517813.

Bräuer, T. (2022). "Flugzeuggetragene Messungen der Eigenschaften von Kondensstreifen aus Biotreibstoffgemischen". PhD thesis. Bundeswehr-Universität München. DOI: 10.57676/PQT5-Y634.

Brown, P. R. A. and Francis, P. N. (1995). "Improved Measurements of the Ice Water Content in Cirrus Using a Total-Water Probe". In: *Journal of Atmospheric and Oceanic Technology* 12.2, pp. 410–414. DOI: 10.1175/1520-0426(1995)012<0410:IMOTIW>2.0.CO;2.

Budyko, M. I. (1969). "The effect of solar radiation variations on the climate of the Earth". In: *Tellus* 21.5, pp. 611–619. ISSN: 2153-3490. DOI: 10.1111/j.2153-3490.1969.tb00466.x.

Caldwell, P. M., Zelinka, M. D., Taylor, K. E., and Marvel, K. (2016). "Quantifying the Sources of Intermodel Spread in Equilibrium Climate Sensitivity". In: *Journal of Climate* 29.2, pp. 513–524. DOI: 10.1175/jcli-d-15-0352.1.

Carlsen, T. and David, R. O. (2022). "Spaceborne Evidence That Ice-Nucleating Particles Influence High-Latitude Cloud Phase". In: *Geophysical Research Letters* 49.14. ISSN: 1944-8007. DOI: 10.1029/2022gl098041.

Carslaw, K. S. (2022). *Aerosols and climate*. Elsevier.

Ceppi, P., Brient, F., Zelinka, M. D., and Hartmann, D. L. (2017). "Cloud feedback mechanisms and their representation in global climate models". In: *WIREs Climate Change* 8.4. DOI: 10.1002/wcc.465.

Cohen, J., Zhang, X., Francis, J., Jung, T., Kwok, R., Overland, J., Ballinger, T. J., Bhatt, U. S., Chen, H. W., Coumou, D., Feldstein, S., Gu, H., Handorf, D., Henderson, G., Ionita, M., Kretschmer, M., Laliberte, F., Lee, S., Linderholm, H. W., Maslowski, W., Peings, Y., Pfeiffer, K., Rigor, I., Semmler, T., Stroeve, J., Taylor, P. C., Vavrus, S., Vihma, T., Wang, S., Wendisch, M., Wu, Y., and Yoon, J. (2019). "Divergent consensuses on Arctic amplification influence on midlatitude severe winter weather". In: *Nature Climate Change* 10.1, pp. 20–29. ISSN: 1758-6798. DOI: 10.1038/s41558-019-0662-y.

Costa, A., Meyer, J., Afchine, A., Luebke, A., Günther, G., Dorsey, J. R., Gallagher, M. W., Ehrlich, A., Wendisch, M., Baumgardner, D., Wex, H., and Krämer, M. (2017). "Classification of Arctic, midlatitude and tropical clouds in the mixed-phase temperature regime". In: *Atmospheric Chemistry and Physics* 17.19, pp. 12219–12238. DOI: 10.5194/acp-17-12219-2017.

Coumou, D., Capua, G. D., Vavrus, S., Wang, L., and Wang, S. (2018). "The influence of Arctic amplification on mid-latitude summer circulation". In: *Nature Communications* 9.1. DOI: 10.1038/s41467-018-05256-8.

Cronin, T. W. and Tziperman, E. (2015). "Low clouds suppress Arctic air formation and amplify high-latitude continental winter warming". In: *Proceedings of the National Academy of Sciences* 112.37, pp. 11490–11495. ISSN: 1091-6490. DOI: 10.1073/pnas.1510937112.

Curry, J. A., Schramm, J. L., Rossow, W. B., and Randall, D. (1996). "Overview of Arctic Cloud and Radiation Characteristics". In: *Journal of Climate* 9.8, pp. 1731–1764. DOI: 10.1175/1520-0442(1996)009<1731:OOACAR>2.0.CO;2.

D'Alessandro, J. J., Diao, M., Wu, C., Liu, X., Jensen, J. B., and Stephens, B. B. (2019). "Cloud Phase and Relative Humidity Distributions over the Southern Ocean in Austral Summer Based on In Situ Observations and CAM5 Simulations". In: *Journal of Climate* 32.10, pp. 2781–2805. ISSN: 1520-0442. DOI: 10.1175/jcli-d-18-0232.1.

Dahlke, S., Solbès, A., and Maturilli, M. (2022). "Cold Air Outbreaks in Fram Strait: Climatology, Trends, and Observations During an Extreme Season in 2020". In: *Journal of Geophysical Research: Atmospheres* 127.3. DOI: 10.1029/2021jd035741.

Dall´Osto, M., Beddows, D. C. S., Tunved, P., Krejci, R., Ström, J., Hansson, H.-C., Yoon, Y. J., Park, K.-T., Becagli, S., Udisti, R., Onasch, T., O´Dowd, C. D., Simó, R., and Harrison, R. M. (2017). "Arctic sea ice melt leads to atmospheric new particle formation". In: *Scientific Reports* 7.1. DOI: 10.1038/s41598-017-03328-1.

De La Torre Castro, E., Jurkat-Witschas, T., Afchine, A., Grewe, V., Hahn, V., Kirschler, S., Krämer, M., Lucke, J., Spelten, N., Wernli, H., Zöger, M., and Voigt, C. (2023). "Differences in microphysical properties of cirrus at high and mid-latitudes". In: *Atmospheric Chemistry and Physics* 23.20, pp. 13167–13189. ISSN: 1680-7324. DOI: 10.5194/acp-23-13167-2023.

Deike, L., Reichl, B. G., and Paulot, F. (2022). "A Mechanistic Sea Spray Generation Function Based on the Sea State and the Physics of Bubble Bursting". In: *AGU Advances* 3.6. DOI: 10.1029/2022av000750.

Dekoutsidis, G., Groß, S., Wirth, M., Krämer, M., and Rolf, C. (2023). "Characteristics of supersaturation in midlatitude cirrus clouds and their adjacent cloud-free air". In: *Atmospheric Chemistry and Physics* 23.5, pp. 3103–3117. DOI: 10.5194/acp-23-3103-2023.

Dong, X., Schwantes, A. C., Xi, B., and Wu, P. (2015). "Investigation of the marine boundary layer cloud and CCN properties under coupled and decoupled conditions over the Azores". In: *Journal of Geophysical Research: Atmospheres* 120.12, pp. 6179–6191. ISSN: 2169-8996. DOI: 10.1002/2014jd022939.

Droplet Measurement Technologies, I. (2017a). *Operator Manual, DOC-0012 Revision D: Spinning Disk Calibrator, For use with CIP, CCP, CAPS, MPS, PIP and OAP*. 2545 Central Avenue, Boulder, CO 80301-5727 USA.

Droplet Measurement Technologies, I. (2017b). *Operator Manual, DOC-0120 Rev K-1: Precipitation Imaging Probe*. 2545 Central Avenue, Boulder, CO 80301-5727 USA.

Druckenmiller, M. L., Thoman, R. L., and Moon, T. A. (2022). *NOAA Arctic Report Card 2022: Executive Summary*. NOAA technical report OAR ARC ; 22-01. DOI: 10.25923/YJX6-R184.

Dupuy, R., Gourbeyre, C., Mioche, G., and Jourdan, O. (2022a). *French Airborne Measurement Platform (PMA) cloud particle size distribution and volumic cloud particle diffusion properties dataset near Svalbard for AFLUX measurement campaign with POLAR 5 in 2019*. PANGAEA - Data Publisher for Earth & Environmental Science. DOI: 10.1594/PANGAEA.941498.

Dupuy, R., Gourbeyre, C., Mioche, G., Moser, M., and Jourdan, O. (2022b). *French Airborne Measurement Platform (PMA) cloud particle size distribution and volumic cloud particle diffusion properties dataset near Svalbard for MOSAIC-ACA measurement campaign in 2020*. PANGAEA - Data Publisher for Earth & Environmental Science. DOI: 10.1594/PANGAEA.941538.

Efron, B. and Tibshirani, R. (1994). *An Introduction to the Bootstrap*. Chapman and Hall/CRC. ISBN: 9780429246593. DOI: 10.1201/9780429246593.

Ehrlich, A., Wendisch, M., Lüpkes, C., Buschmann, M., Bozem, H., Chechin, D., Clemen, H.-C., Dupuy, R., Eppers, O., Hartmann, J., Herber, A., Jäkel, E., Järvinen, E., Jourdan, O., Kästner, U., Kliesch, L.-L., Köllner, F., Mech, M., Mertes, S., Neuber, R., Ruiz-Donoso, E., Schnaiter, M., Schneider, J., Stapf, J., and Zanatta, M. (2019). "A comprehensive in situ and remote sensing data set from the Arctic CLoud Observations Using airborne measurements during polar Day (ACLOUD) campaign". In: *Earth System Science Data* 11.4, pp. 1853–1881. ISSN: 1866-3516. DOI: 10.5194/essd-11-1853-2019.

Eirund, G. K., Possner, A., and Lohmann, U. (2020). "The Impact of Warm and Moist Airmass Perturbations on Arctic Mixed-Phase Stratocumulus". In: *Journal of Climate* 33.22, pp. 9615–9628. DOI: 10.1175/jcli-d-20-0163.1.

Elvidge, A. D., Renfrew, I. A., Brooks, I. M., Srivastava, P., Yelland, M. J., and Prytherch, J. (2021). "Surface Heat and Moisture Exchange in the Marginal Ice Zone: Observations and a New Parameterization Scheme for Weather and Climate Models". In: *Journal of Geophysical Research: Atmospheres* 126.17. DOI: 10.1029/2021jd034827.

Eppers, O., Clemen, H.-C., and Schneider, J. (2023a). *Airborne in-situ measurement of particle number concentration and size distribution using an optical particle counter during HALO-AC3*. data set. PANGAEA - Data Publisher for Earth & Environmental Science. DOI: 10.1594/PANGAEA.963284.

Eppers, O., Clemen, H.-C., and Schneider, J. (2023b). *Aircraft-based measurement of particle size and chemical composition for individual aerosol particles during the HALO-AC3 campaign 2022*. data set. PANGAEA - Data Publisher for Earth & Environmental Science. DOI: 10.1594/PANGAEA.963290.

Esposito, B. M., Bachalo, W. D., Leroy, D., Schwarzenboeck, A., Jurkat, T., Voigt, C., and Bansmer, S. (2019). "Wind Tunnel Measurements of Simulated Glaciated Cloud Conditions to Evaluate Newly Developed 2D Imaging Probes". In: *SAE Technical Paper Series*. ICE. SAE International. DOI: 10.4271/2019-01-1981.

Etheridge, D. M., Steele, L. P., Langenfelds, R. L., Francey, R. J., Barnola, J.-M., and Morgan, V. I. (1996). "Natural and anthropogenic changes in atmospheric CO_2 over the last 1000 years from air in Antarctic ice and firn". In: *Journal of Geophysical Research: Atmospheres* 101.D2, pp. 4115–4128. DOI: 10.1029/95jd03410.

Faber, S., French, J. R., and Jackson, R. (2018). "Laboratory and in-flight evaluation of measurement uncertainties from a commercial Cloud Droplet Probe (CDP)". In: *Atmospheric Measurement Techniques* 11.6, pp. 3645–3659. DOI: 10.5194/amt-11-3645-2018.

Field, P. R., Heymsfield, A. J., and Bansemer, A. (2006). "Shattering and Particle Interarrival Times Measured by Optical Array Probes in Ice Clouds". In: *Journal of Atmospheric and Oceanic Technology* 23.10, pp. 1357–1371. DOI: 10.1175/jtech1922.1.

Field, P. R., Lawson, R. P., Brown, P. R. A., Lloyd, G., Westbrook, C., Moisseev, D., Miltenberger, A., Nenes, A., Blyth, A., Choularton, T., Connolly, P., Buehl, J., Crosier, J.,

Cui, Z., Dearden, C., DeMott, P., Flossmann, A., Heymsfield, A., Huang, Y., Kalesse, H., Kanji, Z. A., Korolev, A., Kirchgaessner, A., Lasher-Trapp, S., Leisner, T., McFarquhar, G., Phillips, V., Stith, J., and Sullivan, S. (2016). "Chapter 7. Secondary Ice Production - current state of the science and recommendations for the future". In: *Meteorological Monographs*. ISSN: 0065-9401. DOI: 10.1175/amsmonographs-d-16-0014.1.

Findeisen, F. (1938). "Kolloid-meteorologische Vorgänge bei Niederschlagsbildung". In: *Meteor*.

Francis, J. A. and Vavrus, S. J. (2012). "Evidence linking Arctic amplification to extreme weather in mid-latitudes". In: *Geophysical Research Letters* 39.6. DOI: 10.1029/2012gl051000.

Francis, J. A. and Vavrus, S. J. (2015). "Evidence for a wavier jet stream in response to rapid Arctic warming". In: *Environmental Research Letters* 10.1, p. 014005. ISSN: 1748-9326. DOI: 10.1088/1748-9326/10/1/014005.

Friedlingstein, P., O'Sullivan, M., Jones, M. W., Andrew, R. M., Gregor, L., Hauck, J., Quéré, C. L., Luijkx, I. T., Olsen, A., Peters, G. P., Peters, W., Pongratz, J., Schwingshackl, C., Sitch, S., Canadell, J. G., Ciais, P., Jackson, R. B., Alin, S. R., Alkama, R., Arneth, A., Arora, V. K., Bates, N. R., Becker, M., Bellouin, N., Bittig, H. C., Bopp, L., Chevallier, F., Chini, L. P., Cronin, M., Evans, W., Falk, S., Feely, R. A., Gasser, T., Gehlen, M., Gkritzalis, T., Gloege, L., Grassi, G., Gruber, N., Gürses, Ö., Harris, I., Hefner, M., Houghton, R. A., Hurtt, G. C., Iida, Y., Ilyina, T., Jain, A. K., Jersild, A., Kadono, K., Kato, E., Kennedy, D., Goldewijk, K. K., Knauer, J., Korsbakken, J. I., Landschützer, P., Lefèvre, N., Lindsay, K., Liu, J., Liu, Z., Marland, G., Mayot, N., McGrath, M. J., Metzl, N., Monacci, N. M., Munro, D. R., Nakaoka, S.-I., Niwa, Y., O'Brien, K., Ono, T., Palmer, P. I., Pan, N., Pierrot, D., Pocock, K., Poulter, B., Resplandy, L., Robertson, E., Rödenbeck, C., Rodriguez, C., Rosan, T. M., Schwinger, J., Séférian, R., Shutler, J. D., Skjelvan, I., Steinhoff, T., Sun, Q., Sutton, A. J., Sweeney, C., Takao, S., Tanhua, T., Tans, P. P., Tian, X., Tian, H., Tilbrook, B., Tsujino, H., Tubiello, F., Werf, G. R. van der, Walker, A. P., Wanninkhof, R., Whitehead, C., Wranne, A. W., Wright, R., Yuan, W., Yue, C., Yue, X., Zaehle, S., Zeng, J., and Zheng, B. (2022). "Global Carbon Budget 2022". In: *Earth System Science Data* 14.11, pp. 4811–4900. DOI: 10.5194/essd-14-4811-2022.

Frieß, U., Kreher, K., Querel, R., Schmithüsen, H., Smale, D., Weller, R., and Platt, U. (2023). "Source mechanisms and transport patterns of tropospheric bromine monoxide: findings from long-term multi-axis differential optical absorption spectroscopy measurements at two Antarctic stations". In: *Atmospheric Chemistry and Physics* 23.5, pp. 3207–3232. ISSN: 1680-7324. DOI: 10.5194/acp-23-3207-2023.

Fruchterman, T. M. J. and Reingold, E. M. (1991). "Graph drawing by force-directed placement". In: *Software: Practice and Experience* 21.11, pp. 1129–1164. DOI: 10.1002/spe.4380211102.

Fugal, J. P., Shaw, R. A., Saw, E. W., and Sergeyev, A. V. (2004). "Airborne digital holographic system for cloud particle measurements". In: *Applied Optics* 43.32, p. 5987. ISSN: 1539-4522. DOI: 10.1364/ao.43.005987.

Gayet, J.-F., Crépel, O., Fournol, J. F., and Oshchepkov, S. (1997). "A new airborne polar Nephelometer for the measurements of optical and microphysical cloud properties. Part I: Theoretical design". In: *Annales Geophysicae* 15.4, pp. 451–459. DOI: 10.1007/s00585-997-0451-1.

Gayet, J.-F., Auriol, F., Minikin, A., Ström, J., Seifert, M., Krejci, R., Petzold, A., Febvre, G., and Schumann, U. (2002). "Quantitative Measurement of the Microphysical and Op-

tical Properties of Cirrus Clouds with Four Different in Situ Probes: Evidence of Small Ice Crystals". In: *Geophysical Research Letters* 29.24. ISSN: 1944-8007. DOI: 10.1029/2001GL014342.

Gayet, J.-F., Shcherbakov, V., Voigt, C., Schumann, U., Schäuble, D., Jessberger, P., Petzold, A., Minikin, A., Schlager, H., Dubovik, O., and Lapyonok, T. (2012). "The evolution of microphysical and optical properties of an A380 contrail in the vortex phase". In: *Atmospheric Chemistry and Physics* 12.14, pp. 6629–6643. DOI: 10.5194/acp-12-6629-2012.

Gerber, H., Takano, Y., Garrett, T. J., and Hobbs, P. V. (2000). "Nephelometer Measurements of the Asymmetry Parameter, Volume Extinction Coefficient, and Backscatter Ratio in Arctic Clouds". In: *Journal of the Atmospheric Sciences* 57.18, pp. 3021–3034. ISSN: 0022-4928, 1520-0469. DOI: 10.1175/1520-0469(2000)057<3021:NMOTAP>2.0.CO;2.

Gerber, H., Frick, G., Malinowski, S. P., Brenguier, J.-L., and Burnet, F. (2005). "Holes and Entrainment in Stratocumulus". In: *Journal of the Atmospheric Sciences* 62.2, pp. 443–459. DOI: 10.1175/jas-3399.1.

Gong, X., Zhang, J., Croft, B., Yang, X., Frey, M. M., Bergner, N., Chang, R. Y.-W., Creamean, J. M., Kuang, C., Martin, R. V., Ranjithkumar, A., Sedlacek, A. J., Uin, J., Willmes, S., Zawadowicz, M. A., Pierce, J. R., Shupe, M. D., Schmale, J., and Wang, J. (2023). "Arctic warming by abundant fine sea salt aerosols from blowing snow". In: *Nature Geoscience* 16.9, pp. 768–774. ISSN: 1752-0908. DOI: 10.1038/s41561-023-01254-8.

Guélis, T. V. de, Schwarzenböck, A., Shcherbakov, V., Gourbeyre, C., Laurent, B., Dupuy, R., Coutris, P., and Duroure, C. (2019). "Study of the diffraction pattern of cloud particles and the respective responses of optical array probes". In: *Atmospheric Measurement Techniques* 12.4, pp. 2513–2529. DOI: 10.5194/amt-12-2513-2019.

Gurganus, C. and Lawson, R. P. (2018). "Laboratory and Flight Tests of 2D Imaging Probes: Toward a Better Understanding of Instrument Performance and the Impact on Archived Data". In: *Journal of Atmospheric and Oceanic Technology* 35.7, pp. 1533–1553. DOI: 10.1175/jtech-d-17-0202.1.

Hartmann, M., Adachi, K., Eppers, O., Haas, C., Herber, A., Holzinger, R., Hünerbein, A., Jäkel, E., Jentzsch, C., Pinxteren, M., Wex, H., Willmes, S., and Stratmann, F. (2020). "Wintertime Airborne Measurements of Ice Nucleating Particles in the High Arctic: A Hint to a Marine, Biogenic Source for Ice Nucleating Particles". In: *Geophysical Research Letters* 47.13. DOI: 10.1029/2020gl087770.

Herber, A., Becker, S., Belter, H. J., Brauchle, J., Ehrlich, A., Klingebiel, M., Krumpen, T., Lüpkes, C., Mech, M., Moser, M., and Wendisch, M. (2021). "MOSAiC Expedition: Airborne Surveys with Research Aircraft POLAR 5 and POLAR 6 in 2020". In: *Berichte zur Polar- und Meeresforschung = Reports on polar and marine research* 754. DOI: 10.48433/BzPM_0754_2021.

Heukamp, F. O., Aue, L., Wang, Q., Ionita, M., Kanzow, T., Wekerle, C., and Rinke, A. (2023). "Cyclones modulate the control of the North Atlantic Oscillation on transports into the Barents Sea". In: *Communications Earth & Environment* 4.1. ISSN: 2662-4435. DOI: 10.1038/s43247-023-00985-1.

Heymsfield, A. J. and Parrish, J. L. (1978). "A Computational Technique for Increasing the Effective Sampling Volume of the PMS Two-Dimensional Particle Size Spectrometer". In: *Journal of Applied Meteorology* 17.10, pp. 1566–1572. ISSN: 0021-8952. DOI: 10.1175/1520-0450(1978)017<1566:actfit>2.0.co;2.

Heymsfield, A. J., Schmitt, C., Bansemer, A., and Twohy, C. H. (2010). "Improved Representation of Ice Particle Masses Based on Observations in Natural Clouds". In: *Journal of the Atmospheric Sciences* 67.10, pp. 3303–3318. DOI: 10.1175/2010jas3507.1.

Heymsfield, A. J., Bansemer, A., Heymsfield, G., Noone, D., Grecu, M., and Toohey, D. (2023). "Relationship of Multiwavelength Radar Measurements to Ice Microphysics from the IMPACTS Field Program". In: *Journal of Applied Meteorology and Climatology* 62.3, pp. 289–315. DOI: 10.1175/jamc-d-22-0057.1.

Hobbs, P. V. and Wallace, J. M. (2006). *Atmospheric Science: An Introductory Survey*. 2nd ed. International geophysics series. San Diego, CA: Academic Press.

Hogan, R. J., Tian, L., Brown, P. R. A., Westbrook, C. D., Heymsfield, A. J., and Eastment, J. D. (2012). "Radar Scattering from Ice Aggregates Using the Horizontally Aligned Oblate Spheroid Approximation". In: *Journal of Applied Meteorology and Climatology* 51.3, pp. 655–671. DOI: 10.1175/jamc-d-11-074.1.

Houze, R. A., McMurdie, L. A., Petersen, W. A., Schwaller, M. R., Baccus, W., Lundquist, J. D., Mass, C. F., Nijssen, B., Rutledge, S. A., Hudak, D. R., Tanelli, S., Mace, G. G., Poellot, M. R., Lettenmaier, D. P., Zagrodnik, J. P., Rowe, A. K., DeHart, J. C., Madaus, L. E., Barnes, H. C., and Chandrasekar, V. (2017). "The Olympic Mountains Experiment (OLYMPEX)". In: *Bulletin of the American Meteorological Society* 98.10, pp. 2167–2188. DOI: 10.1175/bams-d-16-0182.1.

Huang, J. and Jaeglé, L. (2017). "Wintertime enhancements of sea salt aerosol in polar regions consistent with a sea ice source from blowing snow". In: *Atmospheric Chemistry and Physics* 17.5, pp. 3699–3712. DOI: 10.5194/acp-17-3699-2017.

Huang, Y., Dong, X., Bailey, D. A., Holland, M. M., Xi, B., DuVivier, A. K., Kay, J. E., Landrum, L. L., and Deng, Y. (2019). "Thicker Clouds and Accelerated Arctic Sea Ice Decline: The Atmosphere-Sea Ice Interactions in Spring". In: *Geophysical Research Letters* 46.12, pp. 6980–6989. ISSN: 1944-8007. DOI: 10.1029/2019gl082791.

Intrieri, J. M. and Shupe, M. D. (2004). "Characteristics and Radiative Effects of Diamond Dust over the Western Arctic Ocean Region". In: *Journal of Climate* 17.15, pp. 2953–2960. ISSN: 1520-0442. DOI: 10.1175/1520-0442(2004)017<2953:careod>2.0.co;2.

IPCC (2013). *Climate Change 2013: The Physical Science Basis. Contribution of Working Group I to the Fifth Assessment Report of the Intergovernmental Panel on Climate Change*. Vol. In Press. Cambridge, United Kingdom and New York, NY, USA: Cambridge University Press.

IPCC (2021). *Climate Change 2021: The Physical Science Basis. Contribution of Working Group I to the Sixth Assessment Report of the Intergovernmental Panel on Climate Change*. Vol. In Press. Cambridge, United Kingdom and New York, NY, USA: Cambridge University Press. DOI: 10.1017/9781009157896.

Jaffeux, L., Schwarzenböck, A., Coutris, P., and Duroure, C. (2022). "Ice crystal images from optical array probes: classification with convolutional neural networks". In: *Atmospheric Measurement Techniques* 15.17, pp. 5141–5157. ISSN: 1867-8548. DOI: 10.5194/amt-15-5141-2022.

Jeffries, M. O., Overland, J. E., and Perovich, D. K. (2013). "The Arctic shifts to a new normal". In: *Physics Today* 66.10, pp. 35–40. DOI: 10.1063/pt.3.2147.

Jones, A. E., Anderson, P. S., Begoin, M., Brough, N., Hutterli, M. A., Marshall, G. J., Richter, A., Roscoe, H. K., and Wolff, E. W. (2009). "BrO, blizzards, and drivers of polar tropo-

spheric ozone depletion events". In: *Atmospheric Chemistry and Physics* 9.14, pp. 4639–4652. ISSN: 1680-7324. DOI: 10.5194/acp-9-4639-2009.

Jourdan, O., Oshchepkov, S., Shcherbakov, V., Gayet, J.-F., and Isaka, H. (2003). "Assessment of Cloud Optical Parameters in the Solar Region: Retrievals from Airborne Measurements of Scattering Phase Functions". In: *Journal of Geophysical Research: Atmospheres* 108.D18. ISSN: 2156-2202. DOI: 10.1029/2003JD003493.

Jourdan, O., Mioche, G., Garrett, T. J., Schwarzenböck, A., Vidot, J., Xie, Y., Shcherbakov, V., Yang, P., and Gayet, J.-F. (2010). "Coupling of the Microphysical and Optical Properties of an Arctic Nimbostratus Cloud during the ASTAR 2004 Experiment: Implications for Light-Scattering Modeling". In: *Journal of Geophysical Research* 115.D23. DOI: 10.1029/2010JD014016.

Kanji, Z. A., Ladino, L. A., Wex, H., Boose, Y., Burkert-Kohn, M., Cziczo, D. J., and Krämer, M. (2017). "Overview of Ice Nucleating Particles". In: *Meteorological Monographs* 58, pp. 1.1–1.33. ISSN: 0065-9401. DOI: 10.1175/amsmonographs-d-16-0006.1.

Kikuchi, K., Kameda, T., Higuchi, K., and Yamashita, A. (2013). "A global classification of snow crystals, ice crystals, and solid precipitation based on observations from middle latitudes to polar regions". In: *Atmospheric Research* 132–133, pp. 460–472. ISSN: 0169-8095. DOI: 10.1016/j.atmosres.2013.06.006.

Kirpes, R. M., Bondy, A. L., Bonanno, D., Moffet, R. C., Wang, B., Laskin, A., Ault, A. P., and Pratt, K. A. (2018). "Secondary sulfate is internally mixed with sea spray aerosol and organic aerosol in the winter Arctic". In: *Atmospheric Chemistry and Physics* 18.6, pp. 3937–3949. DOI: 10.5194/acp-18-3937-2018.

Kirschler, S., Voigt, C., Anderson, B., Campos Braga, R., Chen, G., Corral, A. F., Crosbie, E., Dadashazar, H., Ferrare, R. A., Hahn, V., Hendricks, J., Kaufmann, S., Moore, R., Pöhlker, M. L., Robinson, C., Scarino, A. J., Schollmayer, D., Shook, M. A., Thornhill, K. L., Winstead, E., Ziemba, L. D., and Sorooshian, A. (2022). "Seasonal updraft speeds change cloud droplet number concentrations in low-level clouds over the western North Atlantic". In: *Atmospheric Chemistry and Physics* 22.12, pp. 8299–8319. ISSN: 1680-7324. DOI: 10.5194/acp-22-8299-2022.

Kleine, J., Voigt, C., Sauer, D., Schlager, H., Scheibe, M., Jurkat-Witschas, T., Kaufmann, S., Kärcher, B., and Anderson, B. E. (2018). "In Situ Observations of Ice Particle Losses in a Young Persistent Contrail". In: *Geophysical Research Letters* 45.24. DOI: 10.1029/2018gl079390.

Kleine, J. (2019). "Flugzeuggetragene Messungen von Eis- und Rußpartikeln in Kondensstreifen bei Verwendung konventioneller und synthetischer Treibstoffe". PhD thesis. Johannes Gutenberg-Universität Mainz. DOI: 10.25358/OPENSCIENCE-3574.

Klingebiel, M., Lozar, A. de, Molleker, S., Weigel, R., Roth, A., Schmidt, L., Meyer, J., Ehrlich, A., Neuber, R., Wendisch, M., and Borrmann, S. (2015). "Arctic low-level boundary layer clouds: in situ measurements and simulations of mono- and bimodal supercooled droplet size distributions at the top layer of liquid phase clouds". In: *Atmospheric Chemistry and Physics* 15.2, pp. 617–631. DOI: 10.5194/acp-15-617-2015.

Klingebiel, M., Ghate, V. P., Naumann, A. K., Ditas, F., Pöhlker, M. L., Pöhlker, C., Kandler, K., Konow, H., and Stevens, B. (2019). "Remote Sensing of Sea Salt Aerosol below Trade Wind Clouds". In: *Journal of the Atmospheric Sciences* 76.5, pp. 1189–1202. DOI: 10.1175/jas-d-18-0139.1.

Knollenberg, R. G. (1970). “The Optical Array: An Alternative to Scattering or Extinction for Airborne Particle Size Determination”. In: *Journal of Applied Meteorology* 9.1, pp. 86–103. DOI: 10.1175/1520-0450(1970)009<0086:toaaat>2.0.co;2.

Knust, R. (2017). “Polar Research and Supply Vessel POLARSTERN operated by the Alfred-Wegener-Institute”. In: *Journal of large-scale research facilities JLSRF* 3. DOI: 10.17815/jlsrf-3-163.

Köllner, F., Schneider, J., Willis, M. D., Klimach, T., Helleis, F., Bozem, H., Kunkel, D., Hoor, P., Burkart, J., Leaitch, W. R., Aliabadi, A. A., Abbatt, J. P. D., Herber, A. B., and Borrmann, S. (2017). “Particulate trimethylamine in the summertime Canadian high Arctic lower troposphere”. In: *Atmospheric Chemistry and Physics* 17.22, pp. 13747–13766. ISSN: 1680-7324. DOI: 10.5194/acp-17-13747-2017.

Köllner, F., Schneider, J., Willis, M. D., Schulz, H., Kunkel, D., Bozem, H., Hoor, P., Klimach, T., Helleis, F., Burkart, J., Leaitch, W. R., Aliabadi, A. A., Abbatt, J. P. D., Herber, A. B., and Borrmann, S. (2021). “Chemical composition and source attribution of sub-micrometre aerosol particles in the summertime Arctic lower troposphere”. In: *Atmos. Chem. Phys.* 21.8, pp. 6509–6539.

Korolev, A., Strapp, J. W., and Isaac, G. A. (1998). “Evaluation of the Accuracy of PMS Optical Array Probes”. In: *Journal of Atmospheric and Oceanic Technology* 15.3, pp. 708–720. DOI: https://doi.org/10.1175/1520-0426(1998)015<0708:EOTAOP>2.0.CO;2.

Korolev, A. and Isaac, G. (2003). “Phase transformation of mixed-phase clouds”. In: *Quarterly Journal of the Royal Meteorological Society* 129.587, pp. 19–38. DOI: https://doi.org/10.1256/qj.01.203. eprint: https://rmets.onlinelibrary.wiley.com/doi/pdf/10.1256/qj.01.203.

Korolev, A. and Isaac, G. (2006). “Relative Humidity in Liquid, Mixed-Phase, and Ice Clouds”. In: *Journal of The Atmospheric Sciences - J ATMOS SCI* 63, pp. 2865–2880. DOI: 10.1175/JAS3784.1.

Korolev, A., Emery, E., and Creelman, K. (2013a). “Modification and Tests of Particle Probe Tips to Mitigate Effects of Ice Shattering”. In: *Journal of Atmospheric and Oceanic Technology* 30.4, pp. 690–708. DOI: 10.1175/jtech-d-12-00142.1.

Korolev, A., Emery, E. F., Strapp, J. W., Cober, S. G., and Isaac, G. A. (2013b). “Quantification of the Effects of Shattering on Airborne Ice Particle Measurements”. In: *Journal of Atmospheric and Oceanic Technology* 30.11, pp. 2527–2553. ISSN: 1520-0426. DOI: 10.1175/jtech-d-13-00115.1.

Korolev, A., McFarquhar, G., Field, P. R., Franklin, C., Lawson, R. P., Wang, Z., Williams, E., Abel, S. J., Axisa, D., Borrmann, S., Crosier, J., Fugal, J., Krämer, M., Lohmann, U., Schlenczek, O., Schnaiter, M., and Wendisch, M. (2017). “Mixed-Phase Clouds: Progress and Challenges”. In: *Meteorological Monographs* 58, pp. 5.1–5.50. DOI: 10.1175/amsmonographs-d-17-0001.1.

Krämer, M., Schiller, C., Afchine, A., Bauer, R., Gensch, I., Mangold, A., Schlicht, S., Spelten, N., Sitnikov, N., Borrmann, S., Reus, M. de, and Spichtinger, P. (2009). “Ice supersaturations and cirrus cloud crystal numbers”. In: *Atmospheric Chemistry and Physics* 9.11, pp. 3505–3522. DOI: 10.5194/acp-9-3505-2009.

Krautstrunk, M. and Giez, A. (2012). “The Transition From FALCON to HALO Era Airborne Atmospheric Research”. In: *Research Topics in Aerospace*. Springer Berlin Heidelberg, pp. 609–624. ISBN: 9783642301834. DOI: 10.1007/978-3-642-30183-4_37.

Kretschmer, M., Coumou, D., Agel, L., Barlow, M., Tziperman, E., and Cohen, J. (2018). "More-Persistent Weak Stratospheric Polar Vortex States Linked to Cold Extremes". In: *Bulletin of the American Meteorological Society* 99.1, pp. 49–60. DOI: 10.1175/bams-d-16-0259.1.

Kretzschmar, J., Stapf, J., Klocke, D., Wendisch, M., and Quaas, J. (2020). "Employing airborne radiation and cloud microphysics observations to improve cloud representation in ICON at kilometer-scale resolution in the Arctic". In: *Atmospheric Chemistry and Physics* 20.21, pp. 13145–13165. DOI: 10.5194/acp-20-13145-2020.

Lance, S., Brock, C. A., Rogers, D., and Gordon, J. A. (2010). "Water droplet calibration of the Cloud Droplet Probe (CDP) and in-flight performance in liquid, ice and mixed-phase clouds during ARCPAC". In: *Atmospheric Measurement Techniques* 3.6, pp. 1683–1706. DOI: 10.5194/amt-3-1683-2010.

Lawson, R. P., Baker, B. A., Schmitt, C. G., and Jensen, T. L. (2001). "An overview of microphysical properties of Arctic clouds observed in May and July 1998 during FIRE ACE". In: *Journal of Geophysical Research: Atmospheres* 106.D14, pp. 14989–15014. ISSN: 0148-0227. DOI: 10.1029/2000jd900789.

Lawson, R. P., O'Connor, D., Zmarzly, P., Weaver, K., Baker, B., Mo, Q., and Jonsson, H. (2006). "The 2D-S (Stereo) Probe: Design and Preliminary Tests of a New Airborne, High-Speed, High-Resolution Particle Imaging Probe". In: *Journal of Atmospheric and Oceanic Technology* 23.11, pp. 1462–1477. DOI: 10.1175/JTECH1927.1.

Lawson, R. P. and Zuidema, P. (2009). "Aircraft Microphysical and Surface-Based Radar Observations of Summertime Arctic Clouds". In: *Journal of the Atmospheric Sciences* 66.12, pp. 3505–3529. DOI: 10.1175/2009jas3177.1.

Lelli, L., Vountas, M., Khosravi, N., and Burrows, J. P. (2023). "Satellite remote sensing of regional and seasonal Arctic cooling showing a multi-decadal trend towards brighter and more liquid clouds". In: *Atmospheric Chemistry and Physics* 23.4, pp. 2579–2611. ISSN: 1680-7324. DOI: 10.5194/acp-23-2579-2023.

Leroy, D., Fontaine, E., Schwarzenboeck, A., Strapp, J. W., Korolev, A., McFarquhar, G., Dupuy, R., Gourbeyre, C., Lilie, L., Protat, A., Delanoe, J., Dezitter, F., and Grandin, A. (2017). "Ice Crystal Sizes in High Ice Water Content Clouds. Part II: Statistics of Mass Diameter Percentiles in Tropical Convection Observed during the HAIC/HIWC Project". In: *Journal of Atmospheric and Oceanic Technology* 34.1, pp. 117–136. ISSN: 0739-0572, 1520-0426. DOI: 10.1175/JTECH-D-15-0246.1.

Lewandowska, A. U. and Falkowska, L. M. (2013). "Sea salt in aerosols over the southern Baltic. Part 1. The generation and transportation of marine particles**Parts of this paper were originally published in Polish: Lewandowska A., 2011, Chemizm aerozoli w rejonie Zatoki Gdańskiej, Wyd. UG, Gdańsk, 184pp." In: *Oceanologia* 55.2, pp. 279–298. DOI: 10.5697/oc.55-2.279.

Li, H., Möhler, O., Petäjä, T., and Moisseev, D. (2021). "Two-year statistics of columnar-ice production in stratiform clouds over Hyytiälä, Finland: environmental conditions and the relevance to secondary ice production". In: *Atmospheric Chemistry and Physics* 21.19, pp. 14671–14686. ISSN: 1680-7324. DOI: 10.5194/acp-21-14671-2021.

Linke, O., Quaas, J., Baumer, F., Becker, S., Chylik, J., Dahlke, S., Ehrlich, A., Handorf, D., Jacobi, C., Kalesse-Los, H., Lelli, L., Mehrdad, S., Neggers, R. A. J., Riebold, J., Saavedra Garfias, P., Schnierstein, N., Shupe, M. D., Smith, C., Spreen, G., Verneuil, B., Vinjamuri, K. S., Vountas, M., and Wendisch, M. (2023). "Constraints on simulated past Arctic ampli-

fication and lapse rate feedback from observations". In: *Atmospheric Chemistry and Physics* 23.17, pp. 9963–9992. ISSN: 1680-7324. DOI: 10.5194/acp-23-9963-2023.

Liou, K. N. (2002). *An Introduction to Atmospheric Radiation*. 2nd. Vol. 84. International Geophysics Series. Academic Press. ISBN: 0-12-451451-0.

Lohmann, U., Lüönd, F., and Mahrt, F. (2016). *An Introduction to Clouds: From the Microscale to Climate*. Cambridge University Press. DOI: 10.1017/cbo9781139087513.

Lucke, J. (2024). "Detection and Differentiation of Supercooled Large Droplet Icing Conditions". PhD thesis. Delft University of Technology.

Lüpkes, C., Vihma, T., Birnbaum, G., Dierer, S., Garbrecht, T., Gryanik, V. M., Gryschka, M., Hartmann, J., Heinemann, G., Kaleschke, L., Raasch, S., Savijärvi, H., Schlünzen, K. H., and Wacker, U. (2011). "Mesoscale Modelling of the Arctic Atmospheric Boundary Layer and Its Interaction with Sea Ice". In: *Arctic Climate Change*. Springer Netherlands, pp. 279–324. DOI: 10.1007/978-94-007-2027-5_7.

Mann, M. E., Rahmstorf, S., Kornhuber, K., Steinman, B. A., Miller, S. K., and Coumou, D. (2017). "Influence of Anthropogenic Climate Change on Planetary Wave Resonance and Extreme Weather Events". In: *Scientific Reports* 7.1. DOI: 10.1038/srep45242.

McCoy, D. T., Tan, I., Hartmann, D. L., Zelinka, M. D., and Storelvmo, T. (2016). "On the relationships among cloud cover, mixed-phase partitioning, and planetary albedo in GCMs". In: *Journal of Advances in Modeling Earth Systems* 8.2, pp. 650–668. DOI: 10.1002/2015ms000589.

McFarquhar, G. M. and Heymsfield, A. J. (1996). "Microphysical Characteristics of Three Anvils Sampled during the Central Equatorial Pacific Experiment". In: *Journal of the Atmospheric Sciences* 53.17, pp. 2401–2423. DOI: 10.1175/1520-0469(1996)053<2401:mcotas>2.0.co;2.

McFarquhar, G. M. and Heymsfield, A. J. (1998). "The Definition and Significance of an Effective Radius for Ice Clouds". In: *Journal of the Atmospheric Sciences* 55.11, pp. 2039–2052. DOI: 10.1175/1520-0469(1998)055<2039:tdasoa>2.0.co;2.

McFarquhar, G. M., Zhang, G., Poellot, M. R., Kok, G. L., McCoy, R., Tooman, T., Fridlind, A., and Heymsfield, A. J. (2007a). "Ice properties of single-layer stratocumulus during the Mixed-Phase Arctic Cloud Experiment: 1. Observations". In: *Journal of Geophysical Research* 112.D24. DOI: 10.1029/2007jd008633.

McFarquhar, G. M., Um, J., Freer, M., Baumgardner, D., Kok, G. L., and Mace, G. (2007b). "Importance of small ice crystals to cirrus properties: Observations from the Tropical Warm Pool International Cloud Experiment (TWP-ICE)". In: *Geophysical Research Letters* 34.13. ISSN: 1944-8007. DOI: 10.1029/2007gl029865.

McFarquhar, G. M., Baumgardner, D., Bansemer, A., Abel, S. J., Crosier, J., French, J., Rosenberg, P., Korolev, A., Schwarzoenboeck, A., Leroy, D., Um, J., Wu, W., Heymsfield, A. J., Twohy, C., Detwiler, A., Field, P., Neumann, A., Cotton, R., Axisa, D., and Dong, J. (2017). "Processing of Ice Cloud In Situ Data Collected by Bulk Water, Scattering, and Imaging Probes: Fundamentals, Uncertainties, and Efforts toward Consistency". In: *Meteorological Monographs* 58, pp. 11.1–11.33. DOI: 10.1175/amsmonographs-d-16-0007.1.

Mech, M., Maahn, M., Kneifel, S., Ori, D., Orlandi, E., Kollias, P., Schemann, V., and Crewell, S. (2020). "PAMTRA 1.0: the Passive and Active Microwave radiative TRAnsfer tool for simulating radiometer and radar measurements of the cloudy atmosphere". In: *Geoscientific Model Development* 13.9, pp. 4229–4251. DOI: 10.5194/gmd-13-4229-2020.

Mech, M., Ehrlich, A., Herber, A., Lüpkes, C., Wendisch, M., Becker, S., Boose, Y., Chechin, D., Crewell, S., Dupuy, R., Gourbeyre, C., Hartmann, J., Jäkel, E., Jourdan, O., Kliesch, L.-L., Klingebiel, M., Kulla, B. S., Mioche, G., Moser, M., Risse, N., Ruiz-Donoso, E., Schäfer, M., Stapf, J., and Voigt, C. (2022). "MOSAiC-ACA and AFLUX - Arctic airborne campaigns characterizing the exit area of MOSAiC". In: *Scientific Data* 9.1. DOI: 10.1038/s41597-022-01900-7.

Meerkötter, R., Schumann, U., Doelling, D. R., Minnis, P., Nakajima, T., and Tsushima, Y. (1999). "Radiative forcing by contrails". In: *Annales Geophysicae* 17.8, pp. 1080–1094. ISSN: 1432-0576. DOI: 10.1007/s00585-999-1080-7.

Mertes, S. and Wetzel, B. (2023). *Airborne in-situ measurements of aerosol properties of cloud particle residuals / ambient particles and of the cloud water content / water vapor during the HALO-AC3 campaign in March and April 2022*. data set. PANGAEA - Data Publisher for Earth & Environmental Science. DOI: 10.1594/PANGAEA.963771.

Michaelis, J. and Lüpkes, C. (2022). "The Impact of Lead Patterns on Mean Profiles of Wind, Temperature, and Turbulent Fluxes in the Atmospheric Boundary Layer over Sea Ice". In: *Atmosphere* 13.1, p. 148. DOI: 10.3390/atmos13010148.

Mioche, G., Jourdan, O., Delanoë, J., Gourbeyre, C., Febvre, G., Dupuy, R., Monier, M., Szczap, F., Schwarzenboeck, A., and Gayet, J.-F. (2017). "Vertical distribution of microphysical properties of Arctic springtime low-level mixed-phase clouds over the Greenland and Norwegian seas". In: *Atmospheric Chemistry and Physics* 17.20, pp. 12845–12869. DOI: 10.5194/acp-17-12845-2017.

Morrison, H., Boer, G. de, Feingold, G., Harrington, J., Shupe, M. D., and Sulia, K. (2011). "Resilience of persistent Arctic mixed-phase clouds". In: *Nature Geoscience* 5.1, pp. 11–17. DOI: 10.1038/ngeo1332.

Moschos, V., Dzepina, K., Bhattu, D., Lamkaddam, H., Casotto, R., Daellenbach, K. R., Canonaco, F., Rai, P., Aas, W., Becagli, S., Calzolai, G., Eleftheriadis, K., Moffett, C. E., Schnelle-Kreis, J., Severi, M., Sharma, S., Skov, H., Vestenius, M., Zhang, W., Hakola, H., Hellén, H., Huang, L., Jaffrezo, J.-L., Massling, A., Nøjgaard, J. K., Petäjä, T., Popovicheva, O., Sheesley, R. J., Traversi, R., Yttri, K. E., Schmale, J., Prévôt, A. S. H., Baltensperger, U., and Haddad, I. E. (2022). "Equal abundance of summertime natural and wintertime anthropogenic Arctic organic aerosols". In: *Nature Geoscience* 15.3, pp. 196–202. DOI: 10.1038/s41561-021-00891-1.

Moser, M. (2018). "Characterization and calibration of an optical array probe and airborne in-situ measurements of mixed-phase clouds". Master's thesis. Friedrich-Alexander-Universität Erlangen-Nürnberg.

Moser, M., Voigt, C., Jurkat-Witschas, T., Hahn, V., Mioche, G., Jourdan, O., Dupuy, R., Gourbeyre, C., Schwarzenboeck, A., Lucke, J., Boose, Y., Mech, M., Borrmann, S., Ehrlich, A., Herber, A., Lüpkes, C., and Wendisch, M. (2023). "Microphysical and thermodynamic phase analyses of Arctic low-level clouds measured above the sea ice and the open ocean in spring and summer". In: *Atmospheric Chemistry and Physics* 23.13, pp. 7257–7280. DOI: 10.5194/acp-23-7257-2023.

Murray-Watson, R. J., Gryspeerdt, E., and Goren, T. (2023). "Investigating the development of clouds within marine cold-air outbreaks". In: *Atmospheric Chemistry and Physics* 23.16, pp. 9365–9383. ISSN: 1680-7324. DOI: 10.5194/acp-23-9365-2023.

Naud, C. M., Booth, J. F., and Genio, A. D. D. (2014). "Evaluation of ERA-Interim and MERRA Cloudiness in the Southern Ocean". In: *Journal of Climate* 27.5, pp. 2109–2124. DOI: 10.1175/jcli-d-13-00432.1.

O'Shea, S., Crosier, J., Dorsey, J., Gallagher, L., Schledewitz, W., Bower, K., Schlenczek, O., Borrmann, S., Cotton, R., Westbrook, C., and Ulanowski, Z. (2021). "Characterising optical array particle imaging probes: implications for small-ice-crystal observations". In: *Atmospheric Measurement Techniques* 14.3, pp. 1917–1939. DOI: 10.5194/amt-14-1917-2021.

Ovadnevaite, J., Ceburnis, D., Canagaratna, M., Berresheim, H., Bialek, J., Martucci, G., Worsnop, D. R., and O'Dowd, C. (2012). "On the effect of wind speed on submicron sea salt mass concentrations and source fluxes". In: *Journal of Geophysical Research: Atmospheres* 117.D16. DOI: 10.1029/2011jd017379.

Overland, J., Dunlea, E., Box, J. E., Corell, R., Forsius, M., Kattsov, V., Olsen, M. S., Pawlak, J., Reiersen, L.-O., and Wang, M. (2019). "The urgency of Arctic change". In: *Polar Science* 21, pp. 6–13. DOI: 10.1016/j.polar.2018.11.008.

Parol, F., Buriez, J. C., Brogniez, G., and Fouquart, Y. (1991). "Information Content of AVHRR Channels 4 and 5 with Respect to the Effective Radius of Cirrus Cloud Particles". In: *Journal of Applied Meteorology* 30.7, pp. 973–984. DOI: 10.1175/1520-0450-30.7.973.

Pasquier, J. T., Henneberger, J., Ramelli, F., Lauber, A., David, R. O., Wieder, J., Carlsen, T., Gierens, R., Maturilli, M., and Lohmann, U. (2022). "Conditions favorable for secondary ice production in Arctic mixed-phase clouds". In: *Atmospheric Chemistry and Physics* 22.23, pp. 15579–15601. ISSN: 1680-7324. DOI: 10.5194/acp-22-15579-2022.

Pinto, J. O. (1998). "Autumnal Mixed-Phase Cloudy Boundary Layers in the Arctic". In: *Journal of the Atmospheric Sciences* 55.11, pp. 2016–2038. ISSN: 1520-0469. DOI: 10.1175/1520-0469(1998)055<2016:ampcbl>2.0.co;2.

Pithan, F., Medeiros, B., and Mauritsen, T. (2013). "Mixed-phase clouds cause climate model biases in Arctic wintertime temperature inversions". In: *Climate Dynamics* 43.1–2, pp. 289–303. ISSN: 1432-0894. DOI: 10.1007/s00382-013-1964-9.

Pithan, F., Svensson, G., Caballero, R., Chechin, D., Cronin, T. W., Ekman, A. M. L., Neggers, R., Shupe, M. D., Solomon, A., Tjernström, M., and Wendisch, M. (2018). "Role of air-mass transformations in exchange between the Arctic and mid-latitudes". In: *Nature Geoscience* 11.11, pp. 805–812. ISSN: 1752-0908. DOI: 10.1038/s41561-018-0234-1.

Porter, G. C. E., Adams, M. P., Brooks, I. M., Ickes, L., Karlsson, L., Leck, C., Salter, M. E., Schmale, J., Siegel, K., Sikora, S. N. F., Tarn, M. D., Vüllers, J., Wernli, H., Zieger, P., Zinke, J., and Murray, B. J. (2022). "Highly Active Ice-Nucleating Particles at the Summer North Pole". In: *Journal of Geophysical Research: Atmospheres* 127.6. DOI: 10.1029/2021jd036059.

Pruppacher, H. and Klett, J. (2010). *Microphysics of Clouds and Precipitation*. Atmospheric and Oceanographic Sciences Library. Springer Netherlands. ISBN: 9780306481000. DOI: 10.1007/978-0-306-48100-0.

Quinn, P. K., Shaw, G., Andrews, E., Dutton, E. G., Ruoho-Airola, T., and Gong, S. L. (2007). "Arctic haze: current trends and knowledge gaps". In: *Tellus B* 59.1. ISSN: 0280-6509. DOI: 10.3402/tellusb.v59i1.16972.

Radke, L. F., Hobbs, P. V., and Bailey, I. H. (1984). "Airborne observations of Arctic aerosols. III: Origins and effects of airmasses". In: *Geophysical Research Letters* 11.5, pp. 401–404. ISSN: 1944-8007. DOI: 10.1029/gl011i005p00401.

Rahn, K. A., Borys, R. D., and Shaw, G. E. (1977). "The Asian source of Arctic haze bands". In: *Nature* 268.5622, pp. 713–715. ISSN: 1476-4687. DOI: 10.1038/268713a0.

Ramdas, A., Garcia, N., and Cuturi, M. (2015). "On Wasserstein Two Sample Testing and Related Families of Nonparametric Tests". In: *arXiv*. DOI: 10.48550/ARXIV.1509.02237.

Raschke, E., Kinne, S., Rossow, W. B., Stackhouse, P. W., and Wild, M. (2016). "Comparison of Radiative Energy Flows in Observational Datasets and Climate Modeling". In: *Journal of Applied Meteorology and Climatology* 55.1, pp. 93–117. DOI: 10.1175/jamc-d-14-0281.1.

Rollins, A. W., Thornberry, T. D., Gao, R. S., Woods, S., Lawson, R. P., Bui, T. P., Jensen, E. J., and Fahey, D. W. (2016). "Observational constraints on the efficiency of dehydration mechanisms in the tropical tropopause layer". In: *Geophysical Research Letters* 43.6, pp. 2912–2918. DOI: 10.1002/2016gl067972.

Rolph, G., Stein, A., and Stunder, B. (2017). "Real-time environmental applications and display sYstem: READY". In: *Environ. Model. Softw.* 95, pp. 210–228.

Rosenberg, P. D., Dean, A. R., Williams, P. I., Dorsey, J. R., Minikin, A., Pickering, M. A., and Petzold, A. (2012). "Particle sizing calibration with refractive index correction for light scattering optical particle counters and impacts upon PCASP and CDP data collected during the Fennec campaign". In: *Atmospheric Measurement Techniques* 5.5, pp. 1147–1163. DOI: 10.5194/amt-5-1147-2012.

Ruiz-Donoso, E., Ehrlich, A., Schäfer, M., Jäkel, E., Schemann, V., Crewell, S., Mech, M., Kulla, B. S., Kliesch, L.-L., Neuber, R., and Wendisch, M. (2020). "Small-scale structure of thermodynamic phase in Arctic mixed-phase clouds observed by airborne remote sensing during a cold air outbreak and a warm air advection event". In: *Atmospheric Chemistry and Physics* 20.9, pp. 5487–5511. DOI: 10.5194/acp-20-5487-2020.

Schirmacher, I., Kollias, P., Lamer, K., Mech, M., Pfitzenmaier, L., Wendisch, M., and Crewell, S. (2023). "Assessing Arctic low-level clouds and precipitation from above – a radar perspective". In: *Atmospheric Measurement Techniques* 16.17, pp. 4081–4100. ISSN: 1867-8548. DOI: 10.5194/amt-16-4081-2023.

Schmale, J., Zieger, P., and Ekman, A. M. L. (2021). "Aerosols in current and future Arctic climate". In: *Nature Climate Change* 11.2, pp. 95–105. DOI: 10.1038/s41558-020-00969-5.

Seguin, A. M., Norman, A.-L., and Barrie, L. (2014). "Evidence of sea ice source in aerosol sulfate loading and size distribution in the Canadian High Arctic from isotopic analysis". In: *Journal of Geophysical Research: Atmospheres* 119.2, pp. 1087–1096. DOI: 10.1002/2013jd020461.

Sellers, W. D. (1969). "A Global Climatic Model Based on the Energy Balance of the Earth-Atmosphere System". In: *Journal of Applied Meteorology* 8.3, pp. 392–400. ISSN: 0021-8952. DOI: 10.1175/1520-0450(1969)008<0392:agcmbo>2.0.co;2.

Serreze, M. C. and Francis, J. A. (2006). "The Arctic Amplification Debate". In: *Climatic Change* 76.3-4, pp. 241–264. DOI: 10.1007/s10584-005-9017-y.

Shcherbakov, V., Gayet, J.-F., Baker, B., and Lawson, R. P. (2006). "Light Scattering by Single Natural Ice Crystals". In: *Journal of the Atmospheric Sciences* 63.5, pp. 1513–1525. ISSN: 0022-4928, 1520-0469. DOI: 10.1175/JAS3690.1.

Shupe, M. D. and Intrieri, J. M. (2004). "Cloud Radiative Forcing of the Arctic Surface: The Influence of Cloud Properties, Surface Albedo, and Solar Zenith Angle". In: *Journal of Climate* 17.3, pp. 616–628. DOI: 10.1175/1520-0442(2004)017<0616:crfota>2.0.co;2.

Shupe, M. D., Matrosov, S. Y., and Uttal, T. (2006). "Arctic Mixed-Phase Cloud Properties Derived from Surface-Based Sensors at SHEBA". In: *Journal of the Atmospheric Sciences* 63.2, pp. 697–711. DOI: 10.1175/JAS3659.1.

Shupe, M. D., Persson, P. O. G., Brooks, I. M., Tjernström, M., Sedlar, J., Mauritsen, T., Sjogren, S., and Leck, C. (2013). "Cloud and boundary layer interactions over the Arctic sea ice in late summer". In: *Atmospheric Chemistry and Physics* 13.18, pp. 9379–9399. ISSN: 1680-7324. DOI: 10.5194/acp-13-9379-2013.

Shupe, M. D., Rex, M., Blomquist, B., Persson, P. O. G., Schmale, J., Uttal, T., Althausen, D., Angot, H., Archer, S., Bariteau, L., Beck, I., Bilberry, J., Bucci, S., Buck, C., Boyer, M., Brasseur, Z., Brooks, I. M., Calmer, R., Cassano, J., Castro, V., Chu, D., Costa, D., Cox, C. J., Creamean, J., Crewell, S., Dahlke, S., Damm, E., Boer, G. de, Deckelmann, H., Dethloff, K., Dütsch, M., Ebell, K., Ehrlich, A., Ellis, J., Engelmann, R., Fong, A. A., Frey, M. M., Gallagher, M. R., Ganzeveld, L., Gradinger, R., Graeser, J., Greenamyer, V., Griesche, H., Griffiths, S., Hamilton, J., Heinemann, G., Helmig, D., Herber, A., Heuzé, C., Hofer, J., Houchens, T., Howard, D., Inoue, J., Jacobi, H.-W., Jaiser, R., Jokinen, T., Jourdan, O., Jozef, G., King, W., Kirchgaessner, A., Klingebiel, M., Krassovski, M., Krumpen, T., Lampert, A., Landing, W., Laurila, T., Lawrence, D., Lonardi, M., Loose, B., Lüpkes, C., Maahn, M., Macke, A., Maslowski, W., Marsay, C., Maturilli, M., Mech, M., Morris, S., Moser, M., Nicolaus, M., Ortega, P., Osborn, J., Pätzold, F., Perovich, D. K., Petäjä, T., Pilz, C., Pirazzini, R., Posman, K., Powers, H., Pratt, K. A., Preußer, A., Quéléver, L., Radenz, M., Rabe, B., Rinke, A., Sachs, T., Schulz, A., Siebert, H., Silva, T., Solomon, A., Sommerfeld, A., Spreen, G., Stephens, M., Stohl, A., Svensson, G., Uin, J., Viegas, J., Voigt, C., Gathen, P. von der, Wehner, B., Welker, J. M., Wendisch, M., Werner, M., Xie, Z., and Yue, F. (2022). "Overview of the MOSAiC expedition—Atmosphere". In: *Elementa: Science of the Anthropocene* 10.1. DOI: 10.1525/elementa.2021.00060.

Smith, D. M., Screen, J. A., Deser, C., Cohen, J., Fyfe, J. C., García-Serrano, J., Jung, T., Kattsov, V., Matei, D., Msadek, R., Peings, Y., Sigmond, M., Ukita, J., Yoon, J.-H., and Zhang, X. (2019). "The Polar Amplification Model Intercomparison Project (PAMIP) contribution to CMIP6: investigating the causes and consequences of polar amplification". In: *Geoscientific Model Development* 12.3, pp. 1139–1164. DOI: 10.5194/gmd-12-1139-2019.

Solomon, A., Shupe, M. D., Persson, P. O. G., and Morrison, H. (2011). "Moisture and dynamical interactions maintaining decoupled Arctic mixed-phase stratocumulus in the presence of a humidity inversion". In: *Atmospheric Chemistry and Physics* 11.19, pp. 10127–10148. ISSN: 1680-7324. DOI: 10.5194/acp-11-10127-2011.

Spreen, G., Kaleschke, L., and Heygster, G. (2008). "Sea ice remote sensing using AMSR-E 89-GHz channels". In: *Journal of Geophysical Research* 113.C2. DOI: 10.1029/2005jc003384.

Stapf, J., Ehrlich, A., Jäkel, E., Lüpkes, C., and Wendisch, M. (2020). "Reassessment of shortwave surface cloud radiative forcing in the Arctic: consideration of surface-albedo–cloud interactions". In: *Atmospheric Chemistry and Physics* 20.16, pp. 9895–9914. DOI: 10.5194/acp-20-9895-2020.

Stein, A. F., Draxler, R. R., Rolph, G. D., Stunder, B. J. B., Cohen, M. D., and Ngan, F. (2015). "NOAA's HYSPLIT atmospheric transport and dispersion modeling system". In: *Bull. Am. Meteorol. Soc.* 96.12, pp. 2059–2077.

Stevens, B., Sherwood, S. C., Bony, S., and Webb, M. J. (2016). "Prospects for narrowing bounds on Earth's equilibrium climate sensitivity". In: *Earth's Future* 4.11, pp. 512–522. DOI: 10.1002/2016ef000376.

Storelvmo, T. and Tan, I. (2015). "The Wegener-Bergeron-Findeisen process – Its discovery and vital importance for weather and climate". In: *Meteorologische Zeitschrift* 24.4, pp. 455–461. ISSN: 0941-2948. DOI: 10.1127/metz/2015/0626.

Stull, R. (2017). *Practical Meteorology: An Algebra-based Survey of Atmospheric Science*. Vancouver: University of British Columbia, p. 940. ISBN: 978-0-88865-283-6.

Tan, I. and Storelvmo, T. (2019). "Evidence of Strong Contributions From Mixed-Phase Clouds to Arctic Climate Change". In: *Geophysical Research Letters* 46.5, pp. 2894–2902. ISSN: 1944-8007. DOI: 10.1029/2018gl081871.

Tan, I., Sotiropoulou, G., Taylor, P. C., Zamora, L., and Wendisch, M. (2023). "A Review of the Factors Influencing Arctic Mixed-Phase Clouds: Progress and Outlook". In: *Clouds and Their Climatic Impacts*. Geophysical Monograph Series. Wiley, pp. 103–132. ISBN: 9781119700357. DOI: 10.1002/9781119700357.ch5.

Tang, I. N., Tridico, A. C., and Fung, K. H. (1997). "Thermodynamic and optical properties of sea salt aerosols". In: *Journal of Geophysical Research: Atmospheres* 102.D19, pp. 23269–23275. ISSN: 0148-0227. DOI: 10.1029/97jd01806.

Vavrus, S. (2004). "The Impact of Cloud Feedbacks on Arctic Climate under Greenhouse Forcing". In: *Journal of Climate* 17.3, pp. 603–615. ISSN: 1520-0442. DOI: 10.1175/1520-0442(2004)017<0603:tiocfo>2.0.co;2.

Vihma, T., Pirazzini, R., Fer, I., Renfrew, I. A., Sedlar, J., Tjernström, M., Lüpkes, C., Nygård, T., Notz, D., Weiss, J., Marsan, D., Cheng, B., Birnbaum, G., Gerland, S., Chechin, D., and Gascard, J. C. (2014). "Advances in understanding and parameterization of small-scale physical processes in the marine Arctic climate system: a review". In: *Atmospheric Chemistry and Physics* 14.17, pp. 9403–9450. DOI: 10.5194/acp-14-9403-2014.

Voigt, C., Schumann, U., Minikin, A., Abdelmonem, A., Afchine, A., Borrmann, S., Boettcher, M., Buchholz, B., Bugliaro, L., Costa, A., Curtius, J., Dollner, M., Dörnbrack, A., Dreiling, V., Ebert, V., Ehrlich, A., Fix, A., Forster, L., Frank, F., Fütterer, D., Giez, A., Graf, K., Grooß, J.-U., Groß, S., Heimerl, K., Heinold, B., Hüneke, T., Järvinen, E., Jurkat, T., Kaufmann, S., Kenntner, M., Klingebiel, M., Klimach, T., Kohl, R., Krämer, M., Krisna, T. C., Luebke, A., Mayer, B., Mertes, S., Molleker, S., Petzold, A., Pfeilsticker, K., Port, M., Rapp, M., Reutter, P., Rolf, C., Rose, D., Sauer, D., Schäfler, A., Schlage, R., Schnaiter, M., Schneider, J., Spelten, N., Spichtinger, P., Stock, P., Walser, A., Weigel, R., Weinzierl, B., Wendisch, M., Werner, F., Wernli, H., Wirth, M., Zahn, A., Ziereis, H., and Zöger, M. (2017). "ML-CIRRUS: The Airborne Experiment on Natural Cirrus and Contrail Cirrus with the High-Altitude Long-Range Research Aircraft HALO". In: *Bulletin of the American Meteorological Society* 98.2, pp. 271–288. DOI: 10.1175/bams-d-15-00213.1.

Voigt, C., Kleine, J., Sauer, D., Moore, R. H., Bräuer, T., Clercq, P. L., Kaufmann, S., Scheibe, M., Jurkat-Witschas, T., Aigner, M., Bauder, U., Boose, Y., Borrmann, S., Crosbie, E., Diskin, G. S., DiGangi, J., Hahn, V., Heckl, C., Huber, F., Nowak, J. B., Rapp, M., Rauch, B., Robinson, C., Schripp, T., Shook, M., Winstead, E., Ziemba, L., Schlager, H., and Anderson, B. E. (2021). "Cleaner burning aviation fuels can reduce contrail cloudiness". In: *Communications Earth & Environment* 2.1. DOI: 10.1038/s43247-021-00174-y.

Walbröl, A., Michaelis, J., Becker, S., Dorff, H., Gorodetskaya, I., Kirbus, B., Lauer, M., Maherndl, N., Maturilli, M., Mayer, J., Müller, H., Neggers, R. A. J., Paulus, F. M., Röttenbacher, J., Rückert, J. E., Schirmacher, I., Slättberg, N., Ehrlich, A., Wendisch, M., and Crewell, S. (2023). "Environmental conditions in the North Atlantic sector of the Arctic during the HALO–(AC)³ campaign". In: *EGUsphere*. DOI: 10.5194/egusphere-2023-668.

Walser, A., Sauer, D., Spanu, A., Gasteiger, J., and Weinzierl, B. (2017). "On the parametrization of optical particle counter response including instrument-induced broadening of size spectra and a self-consistent evaluation of calibration measurements". In: *Atmospheric Measurement Techniques* 10.11, pp. 4341–4361. ISSN: 1867-8548. DOI: 10.5194/amt-10-4341-2017.

Wang, Y., Yang, P., Hioki, S., King, M. D., Baum, B. A., Di Girolamo, L., and Fu, D. (2019). "Ice Cloud Optical Thickness, Effective Radius, And Ice Water Path Inferred From Fused MISR and MODIS Measurements Based on a Pixel-Level Optimal Ice Particle Roughness Model". In: *Journal of Geophysical Research: Atmospheres* 124.22, pp. 12126–12140. ISSN: 2169-8996. DOI: 10.1029/2019jd030457.

Wegener, A. (1912). "Thermodynamik der Atmosphäre". In: *Nature* 90.2237, pp. 31–31. DOI: 10.1038/090031a0.

Wendisch, M., Keil, A., and Korolev, A. (1996). "FSSP Characterization with Monodisperse Water Droplets". In: *Journal of Atmospheric and Oceanic Technology* 13.6, pp. 1152–1165. DOI: 10.1175/1520-0426(1996)013<1152:fcwmwd>2.0.co;2.

Wendisch, M. and Brenguier, J. (2013). *Airborne Measurements for Environmental Research – Methods and Instruments*. Weinheim, Germany: Wiley–VCH Verlag GmbH & Co. KGaA, Weinheim, Germany.

Wendisch, M., Macke, A., Ehrlich, A., Lüpkes, C., Mech, M., Chechin, D., Dethloff, K., Velasco, C. B., Bozem, H., Brückner, M., Clemen, H.-C., Crewell, S., Donth, T., Dupuy, R., Ebell, K., Egerer, U., Engelmann, R., Engler, C., Eppers, O., Gehrmann, M., Gong, X., Gottschalk, M., Gourbeyre, C., Griesche, H., Hartmann, J., Hartmann, M., Heinold, B., Herber, A., Herrmann, H., Heygster, G., Hoor, P., Jafariserajehlou, S., Jäkel, E., Järvinen, E., Jourdan, O., Kästner, U., Kecorius, S., Knudsen, E. M., Köllner, F., Kretzschmar, J., Lelli, L., Leroy, D., Maturilli, M., Mei, L., Mertes, S., Mioche, G., Neuber, R., Nicolaus, M., Nomokonova, T., Notholt, J., Palm, M., Pinxteren, M. van, Quaas, J., Richter, P., Ruiz-Donoso, E., Schäfer, M., Schmieder, K., Schnaiter, M., Schneider, J., Schwarzenböck, A., Seifert, P., Shupe, M. D., Siebert, H., Spreen, G., Stapf, J., Stratmann, F., Vogl, T., Welti, A., Wex, H., Wiedensohler, A., Zanatta, M., and Zeppenfeld, S. (2019). "The Arctic Cloud Puzzle: Using ACLOUD/PASCAL Multiplatform Observations to Unravel the Role of Clouds and Aerosol Particles in Arctic Amplification". In: *Bulletin of the American Meteorological Society* 100.5, pp. 841–871. DOI: 10.1175/bams-d-18-0072.1.

Wendisch, M., Brückner, M., Crewell, S., Ehrlich, A., Notholt, J., Lüpkes, C., Macke, A., Burrows, J. P., Rinke, A., Quaas, J., Maturilli, M., Schemann, V., Shupe, M. D., Akansu, E. F., Barrientos-Velasco, C., Bärfuss, K., Blechschmidt, A.-M., Block, K., Bougoudis, I., Bozem, H., Böckmann, C., Bracher, A., Bresson, H., Bretschneider, L., Buschmann, M., Chechin, D. G., Chylik, J., Dahlke, S., Deneke, H., Dethloff, K., Donth, T., Dorn, W., Dupuy, R., Ebell, K., Egerer, U., Engelmann, R., Eppers, O., Gerdes, R., Gierens, R., Gorodetskaya, I. V., Gottschalk, M., Griesche, H., Gryanik, V. M., Handorf, D., Harm-Altstädter, B., Hartmann, J., Hartmann, M., Heinold, B., Herber, A., Herrmann, H., Heygster, G., Höschel, I., Hofmann, Z., Hölemann, J., Hünerbein, A., Jafariserajehlou, S., Jäkel, E., Jacobi, C., Janout, M., Jansen, F., Jourdan, O., Jurányi, Z., Kalesse-Los, H., Kanzow, T., Käthner, R., Kliesch, L. L., Klingebiel, M., Knudsen, E. M., Kovács, T., Körtke, W., Krampe, D., Kretzschmar, J., Kreyling, D., Kulla, B., Kunkel, D., Lampert, A., Lauer, M., Lelli, L., Lerber, A. von, Linke, O., Löhnert, U., Lonardi, M., Losa, S. N., Losch, M., Maahn, M., Mech, M., Mei, L., Mertes, S., Metzner, E., Mewes, D., Michaelis, J., Mioche, G., Moser, M., Nakoudi, K., Neggers, R., Neuber, R., Nomokonova, T., Oelker, J., Papakonstantinou-Presvelou, I.,

Pätzold, F., Pefanis, V., Pohl, C., Pinxteren, M. van, Radovan, A., Rhein, M., Rex, M., Richter, A., Risse, N., Ritter, C., Rostosky, P., Rozanov, V. V., Donoso, E. R., Saavedra-Garfias, P., Salzmann, M., Schacht, J., Schäfer, M., Schneider, J., Schnierstein, N., Seifert, P., Seo, S., Siebert, H., Soppa, M. A., Spreen, G., Stachlewska, I. S., Stapf, J., Stratmann, F., Tegen, I., Viceto, C., Voigt, C., Vountas, M., Walbröl, A., Walter, M., Wehner, B., Wex, H., Willmes, S., Zanatta, M., and Zeppenfeld, S. (2022). "Atmospheric and Surface Processes, and Feedback Mechanisms Determining Arctic Amplification: A Review of First Results and Prospects of the $(AC)^3$ Project". In: *Bulletin of the American Meteorological Society*. DOI: 10.1175/bams-d-21-0218.1.

Wesche, C., Steinhage, D., and Nixdorf, U. (2016). "Polar aircraft Polar5 and Polar6 operated by the Alfred Wegener Institute". In: *Journal of large-scale research facilities JLSRF* 2. DOI: 10.17815/jlsrf-2-153.

Westbrook, C. D. and Illingworth, A. J. (2013). "The formation of ice in a long-lived supercooled layer cloud". In: *Quarterly Journal of the Royal Meteorological Society* 139.677, pp. 2209–2221. ISSN: 1477-870X. DOI: 10.1002/qj.2096.

Willis, M. D., Leaitch, W. R., and Abbatt, J. P. (2018). "Processes Controlling the Composition and Abundance of Arctic Aerosol". In: *Reviews of Geophysics* 56.4, pp. 621–671. DOI: 10.1029/2018rg000602.

Wiscombe, W. J. (1980). "Improved Mie scattering algorithms". In: *Applied Optics* 19.9, p. 1505. DOI: 10.1364/ao.19.001505.

World Meteorological Organization (2012). *Guide to Meteorological Instruments and Methods of Observation, 2008 edition updated 2010.* WMO. DOI: 10.25607/OBP-1528.

Wu, W. and McFarquhar, G. M. (2016). "On the Impacts of Different Definitions of Maximum Dimension for Nonspherical Particles Recorded by 2D Imaging Probes". In: *Journal of Atmospheric and Oceanic Technology* 33.5, pp. 1057–1072. DOI: 10.1175/jtech-d-15-0177.1.

Xu, L., Russell, L. M., and Burrows, S. M. (2016). "Potential sea salt aerosol sources from frost flowers in the pan-Arctic region". In: *J. Geophys. Res.* 121.18, pp. 10, 840–10, 856.

Yang, X., Pyle, J. A., and Cox, R. A. (2008). "Sea salt aerosol production and bromine release: Role of snow on sea ice". In: *Geophysical Research Letters* 35.16. DOI: 10.1029/2008gl034536.

Yang, X., Frey, M. M., Rhodes, R. H., Norris, S. J., Brooks, I. M., Anderson, P. S., Nishimura, K., Jones, A. E., and Wolff, E. W. (2019). "Sea salt aerosol production via sublimating wind-blown saline snow particles over sea ice: parameterizations and relevant microphysical mechanisms". In: *Atmospheric Chemistry and Physics* 19.13, pp. 8407–8424. ISSN: 1680-7324. DOI: 10.5194/acp-19-8407-2019.

Yang, X., Blechschmidt, A.-M., Bognar, K., McClure-Begley, A., Morris, S., Petropavlovskikh, I., Richter, A., Skov, H., Strong, K., Tarasick, D. W., Uttal, T., Vestenius, M., and Zhao, X. (2020). "Pan-Arctic surface ozone: modelling vs. measurements". In: *Atmospheric Chemistry and Physics* 20.24, pp. 15937–15967. ISSN: 1680-7324. DOI: 10.5194/acp-20-15937-2020.

Yau, M. K. and Rogers, R. R. (1996). *A short course in cloud physics*. Elsevier.

Young, G., Jones, H. M., Choularton, T. W., Crosier, J., Bower, K. N., Gallagher, M. W., Davies, R. S., Renfrew, I. A., Elvidge, A. D., Darbyshire, E., Marenco, F., Brown, P. R. A., Ricketts, H. M. A., Connolly, P. J., Lloyd, G., Williams, P. I., Allan, J. D., Taylor, J. W., Liu, D., and

Flynn, M. J. (2016). “Observed microphysical changes in Arctic mixed-phase clouds when transitioning from sea ice to open ocean”. In: *Atmospheric Chemistry and Physics* 16.21, pp. 13945–13967. DOI: 10.5194/acp-16-13945-2016.

Zelinka, M. D., Klein, S. A., and Hartmann, D. L. (2012). “Computing and Partitioning Cloud Feedbacks Using Cloud Property Histograms. Part II: Attribution to Changes in Cloud Amount, Altitude, and Optical Depth”. In: *Journal of Climate* 25.11, pp. 3736–3754. DOI: 10.1175/jcli-d-11-00249.1.

Zieger, P., Väisänen, O., Corbin, J. C., Partridge, D. G., Bastelberger, S., Mousavi-Fard, M., Rosati, B., Gysel, M., Krieger, U. K., Leck, C., Nenes, A., Riipinen, I., Virtanen, A., and Salter, M. E. (2017). “Revising the hygroscopicity of inorganic sea salt particles”. In: *Nature Communications* 8.1. ISSN: 2041-1723. DOI: 10.1038/ncomms15883.

Appendix

A Discussion of shattering for the scattering cloud probes

Figure 64 shows inter-particle arrival time (IPT) histograms from the particle by particle (PBP) files for different cloud situations. The histograms (a), (b), and (c) were measured with the Cloud Aerosol Spectrometer (CAS), while the others were carried out with the Cloud Droplet Probe (CDP). The cloud conditions were identified according to the cloud classification from Chapter 4.6. An additional small distribution mode besides the main mode, which is located at IPTs smaller than 0.1 ms, can be observed in plots (a), (b), and (c). This smaller mode may indicate shattering events, but its fraction is well below 5% in all situations and can therefore be neglected. The IPT mode around 0.005 ms in the CAS data could also be caused by artifacts in the PBP file. Artifacts are most likely the reason for this mode since no ice crystals are present in the pure aerosol measurements in case (a), and therefore, no shattering can occur.
The IPT histograms in Fig. 64 emphasize that shattering events in aerosol and in mixed-phase haze conditions do not play a significant role, and no correction is required. In pure liquid clouds and mixed-phase clouds, the IPT histogram is dominated by droplets. A smaller shattering mode would be expected in the same IPT regime as the liquid droplets and therefore remains undetectable. The number concentration caused by possible shattering events is negligible compared to the total number concentration of liquid particles and thus has little influence on the derived microphysical parameters. Different absolute values of the IPT from the CAS and CDP measurements in similar cloud situations can be caused by the different operating principles of the two instruments, such as different sampling areas, different gain stages with overlaps for the CAS, or different sensitivities for certain particle sizes. The result that no shattering correction in mixed-phase clouds and mixed-phase haze is needed is consistent with Costa et al. (2017), where similar cloud situations were analyzed and shattered particles were found to be negligible.

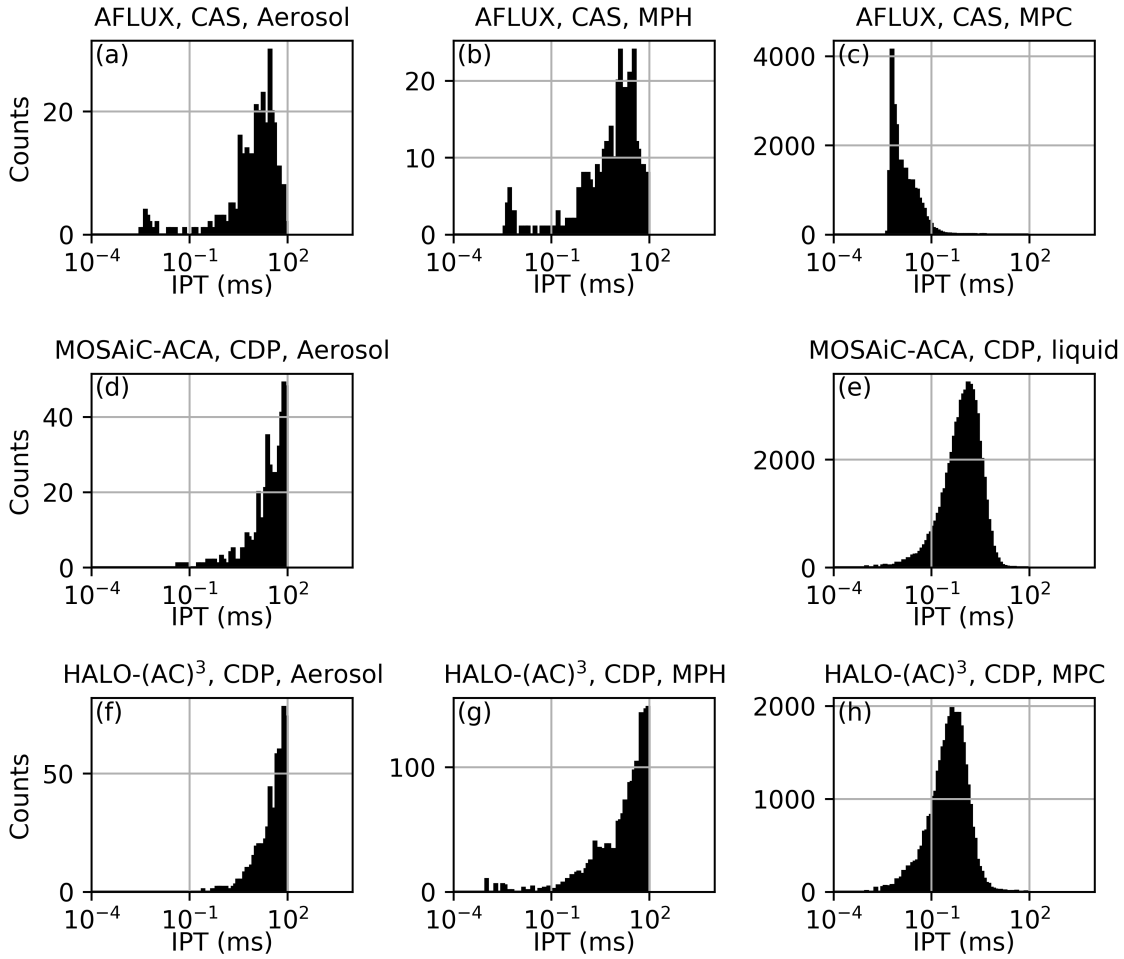

Figure 64 Inter-particle arrival time (IPT) histograms from the particle by particle (PBP) file of the CAS for the AFLUX campaign and the CDP for the MOSAiC-ACA and HALO-(AC)^3 campaign. (a, d, f) show histograms for measurements classified as aerosol, (b, g) for measurements classified as a mixed-phase haze condition, (c, h) for measurements classified as mixed-phase clouds, and (e) for measurements in liquid clouds.

B Bin settings for the processing of the scattering cloud probes

Index	$\mathrm{Bin_k}$	$\mathrm{adc_l}$	$\mathrm{adc_u}$	D_l	D_u
1	-	-	190	-	0.61
2	1	191	265	0.61	0.67
3	2	266	381	0.67	0.75
4	3	382	547	0.75	0.81
5	4	548	773	0.81	0.88
6	5	774	1071	0.88	0.95
7	6	1072	1441	0.95	1.02
8	7	1442	1890	1.02	1.10
9	8	1891	2412	1.10	1.17
10	9	2413	3072	1.17	1.27
11	-	3073	3209	-	-
12	10	3210	3544	1.27	2.69
13	11	3545	3716	2.69	2.73
14	11	3717	3887	2.73	2.79
15	12	3888	4555	2.79	3.02
16	12	4556	5224	3.02	4.95
17	13	5225	5475	4.95	5.05
18	13	5476	5727	5.05	5.25
19	13	5728	5935	5.25	7.67
20	14	5936	6144	7.67	7.83
21	-	6145	6238	-	-
22	14	6239	6277	7.83	9.98
23	15	6278	6427	9.98	13.70
24	16	6428	6571	13.70	18.61
25	17	6572	6797	18.61	22.76
26	18	6798	7020	22.76	27.45
27	19	7021	7319	27.45	31.50
28	20	7320	7651	31.50	36.52
29	21	7652	8191	36.52	43.63
30	22	8192	9216	43.63	54.00

Table 11 Final bin setting used for the CAS data processing for the AFLUX field campaign assuming liquid spheres. $\mathrm{Bin_k}$ is the bin number, $\mathrm{adc_l}$ ($\mathrm{adc_u}$) is the lower (upper) bin limit of the scattering cross section and D_l (D_u) is the lower (upper) bin limit of the particle diameter. Bins with index 11 and 21 are the gain stage bins of the CAS.

Index	$\mathrm{Bin_k}$	$\mathrm{adc_l}$	$\mathrm{adc_u}$	D_l	D_u
1	-	-	101	-	2.8
2	1	102	176	2.8	4.8
3	2	177	262	4.8	7.6
4	3	263	350	7.6	10.1
5	4	351	414	10.1	11.7
6	5	415	498	11.7	13.6
7	6	499	619	13.6	16.0
8	7	620	691	16.0	17.3
9	8	692	775	17.3	18.7
10	9	776	905	18.7	20.7
11	10	906	1063	20.7	22.9
12	11	1064	1196	22.9	24.6
13	12	1197	1450	24.6	27.6
14	13	1451	1643	27.6	29.7
15	14	1665	1851	30.0	32.0
16	15	1852	2016	32.0	34.0
17	16	2017	2230	34.0	36.0
18	17	2231	2513	36.0	38.0
19	18	2514	2771	38.0	40.0
20	19	2772	3003	40.0	42.0
21	20	3004	3220	42.0	44.0
22	21	3221	3424	44.0	46.0
23	22	3424	3660	46.0	48.0
24	23	3661	4095	48.0	50.0

Table 12 Final bin setting used for the CDP data processing for the MOSAiC-ACA field campaign assuming liquid spheres. $\mathrm{Bin_k}$ is the bin number, $\mathrm{adc_l}$ ($\mathrm{adc_u}$) is the lower (upper) bin limit of the scattering cross section and D_l (D_u) is the lower (upper) bin limit of the particle diameter. For particle sizing the PBP file is used from $\mathrm{Bin_k}$=1 to $\mathrm{Bin_k}$=13, and the bulk file starting from $\mathrm{Bin_k}$=14.

Index	$\mathrm{Bin_k}$	$\mathrm{adc_l}$	$\mathrm{adc_u}$	D_l	D_u
1	-	-	97	-	3.0
2	1	98	147	3.0	4.8
3	2	148	234	4.8	7.6
4	3	235	323	7.6	10.1
5	4	324	387	10.1	11.7
6	5	388	472	11.7	13.6
7	6	473	594	13.6	16.0
8	7	595	667	16.0	17.3
9	8	668	752	17.3	18.7
10	9	753	884	18.7	20.7
11	10	885	1044	20.7	22.9
12	11	1045	1177	22.9	24.6
13	12	1178	1311	24.6	26.2
14	13	1312	1434	26.2	27.6
15	14	1435	1629	27.6	29.7
16	15	1630	1815	29.7	31.6
17	16	1816	2010	31.6	33.5
18	17	2011	2148	33.5	34.8
19	18	2149	2312	34.8	36.3
20	19	2313	2619	36.3	39.0
21	20	2620	2797	39.0	40.5
22	21	2798	3031	40.5	42.4
23	22	3032	3146	42.4	43.3
24	23	3147	3357	43.3	44.9
25	24	3358	3494	44.9	45.9
26	25	3495	3739	45.9	47.6
27	26	3740	4018	47.6	49.4
28	27	4019	4084	49.4	49.8
29	27	4085	4100	49.8	49.9
30	27	4101	4116	49.9	50.0

Table 13 Final bin setting used for the CDP data processing for the HALO-(AC)^3 field campaign assuming liquid spheres. $\mathrm{Bin_k}$ is the bin number, $\mathrm{adc_l}$ ($\mathrm{adc_u}$) is the lower (upper) bin limit of the scattering cross section and D_l (D_u) is the lower (upper) bin limit of the particle diameter.

C Additional information to the active time correction in Sect. 3.3.1

For the processing of the OAP data of the CIP and PIP a new active time correction was introduced. However these analyses are based on CIP and 2D-S data during AFLUX only, but results from Sect. 3.3.1.2 are applied to all DMT cloud probe measurements within this thesis. In the mean time 2D-S data for the MOSAiC-ACA campaign were published as well and discussed regarding correlation with the CIP data set. Figures 65 and 66 are reproduced similar to the analyses in Sect. 3.3.1.2 but based on MOSAiC-ACA data. Only data from horizontal flight legs are taken into account. Due to the different settings in the PADS for the CIP during AFLUX, a slightly lower γ-value than 0.6 was expected. However results show, that an optimized correlation would have been achieved with $\gamma = 0.85$. When examining the values which are rejected in Fig. 65 (b) due to $t_a < 0.1$, it is evident that significantly fewer measurements (about 3%) are discarded compared to the CIP data from AFLUX (about 50%). This suggests that the CIP used during MOSAiC-ACA performed better compared to the CIP which was installed on the aircraft during AFLUX. This can have several reasons. Firstly, the electronics of the two CIPs may be different, and secondly, the environmental conditions in which the measurements were taken may have an effect on the performance of the instruments. During MOSAiC-ACA, the observed liquid particles are relatively small, which results in fewer image data that need to be recorded compared to the larger ice crystals that exist in the mixed-phase clouds often measured during AFLUX. Such large particles require a lot of image storage in a short amount of time, leading to overload conditions in the electronics of the CIP. Although the used γ value for the DMT data processing differs from the optimal value found afterwards, the hybrid solution using Eq. 3.14 with $\gamma = 0.5$ is still reasonable. Firstly the previous rejected 3% data are no longer discarded, and the values of r and m show only minor differences at $\gamma = 0.5$ and the optimal value of $\gamma = 0.85$.

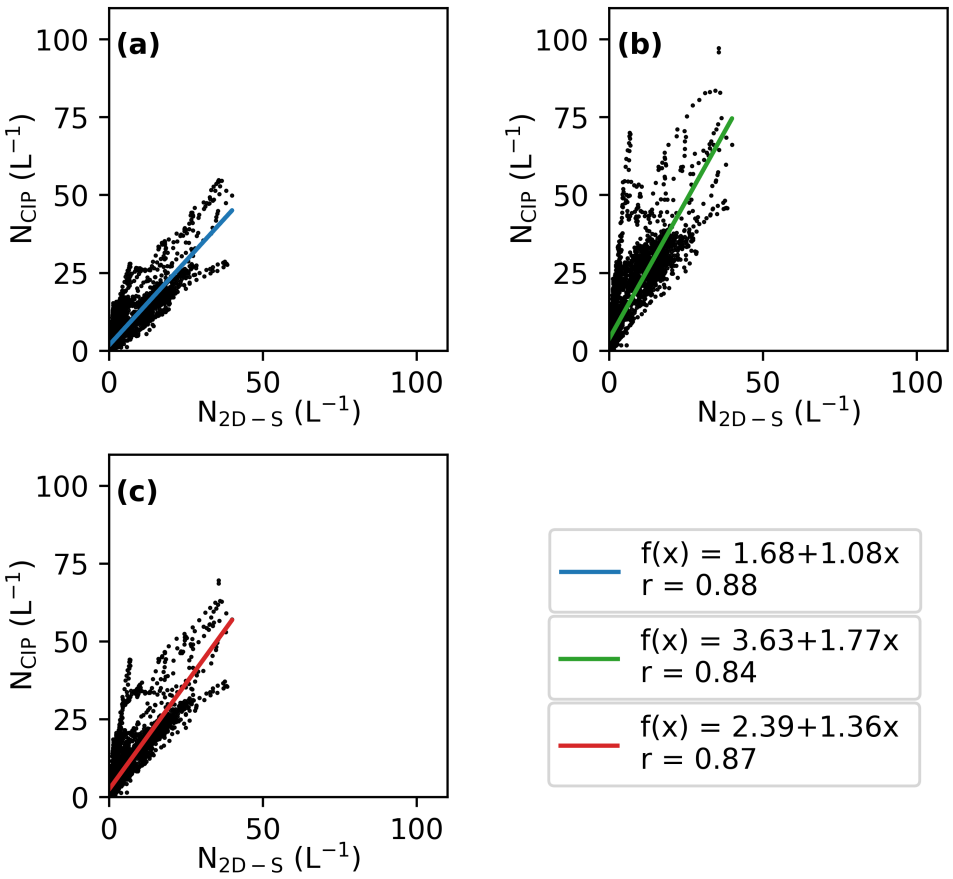

Figure 65 Similar to Fig. 26: Correlation of N for particles between 100 - 500 µm measured by the 2D-S and the CIP during the MOSAiC-ACA campaing. In a) no dead time is assumed for the CIP, b) CIP's active time is corrected following Gurganus and Lawson (2018), and c) a new hybrid version of (a) and (b) with γ - correction followed by Eq. 3.14 is applied to the CIP's active time (here $\gamma = 0.5$).

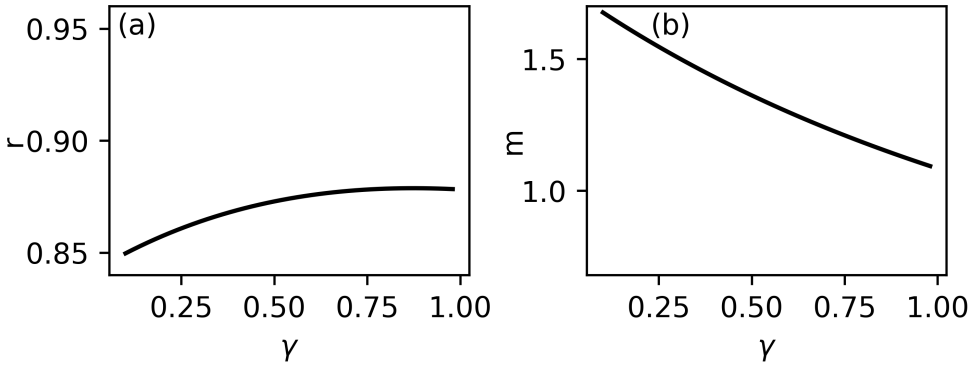

Figure 66 Similar to Fig. 27: Optimization of the γ value for the new active time correction based on the 2D-S and the CIP data from the MOSAiC-ACA campaing: a) gives the slope m of a linear fit on the correlation of 2D-S data and the new active time corrected CIP data with different γ values, and b) the Pearson correlation coefficient r of this correlation.

D Overview: Aircraft field campaigns

Date	Flight objective	Minutes in clouds		Air mass origin		T_{cloud}
dd.mm.yyyy		Total	Over sea ice/ over ocean	24h	Long range	Max/min (°C)
21.03.2019	In-situ measurement and remote sensing of clouds	25.4	24.9/0.0	Ocean	South	-5.8/-16.7
23.03.2019	Studying the evolution of a CAO from the sea ice to the ocean	68.4	44.3/0.0	Sea ice	Central Arctic	-13.1/-23.3
24.03.2019	In-situ measurement and remote sensing of clouds during a CAO	62.7	33.1/25.1	Sea ice	Siberia	-10.9/-27.0
25.03.2019	In-situ measurement and remote sensing of clouds during a CAO	61.3	50.1/7.2	Sea ice	Siberia	-10.2/-28.3
30.03.2019	In-situ measurement and remote sensing of clouds	49.5	19.6/0.0	Sea ice	Central Arctic	-21.3/-25.9
31.03.2019	In-situ measurement and remote sensing of clouds during a strong CAO	54.2	11.7/33.6	Sea ice	Greenland	-13.8/-26.4
01.04.2019	Validation of A-Train satellites observations	35.9	0.0/21.6	Sea ice	Greenland	-13.5/-24.4
03.04.2019	In-situ measurement and remote sensing of clouds	32.0	24.3/3.5	Sea ice	Siberia	-13.7/-21.8
04.04.2019	In-situ measurement and remote sensing of clouds ahead of a warm front over sea ice	14.7	0.1/13.6	Ocean	Greenland	-5.5/-14.7
06.04.2019	In-situ measurement and remote sensing of clouds during a CAO	127.8	48.0/42.5	Sea ice	Siberia	-12.5/-19.1
07.04.2019	Validation of A-Train satellites observations	48.7	1.1/5.5	Sea ice	Central Arctic	-13.9/-17.8
08.04.2019	In-situ measurement and remote sensing of clouds	23.4	14.3/8.5	Sea ice	Greenland	-9.1/-19.4
11.04.2019	In-situ measurement and remote sensing of clouds	52.8	52.5/0.1	Sea ice	Greenland	-1.8/-19.0

Table 14 Flight table for the AFLUX field campaign including the objective of the research flights, the time of low-level in-situ cloud measurements (< 500 m), a classification of the air mass origin and the temperature of the sampled clouds. Note that minutes in clouds over the sea ice and over the ocean do not add up to total, as for total all surface conditions are considered, for condition sea ice SIC > 80 % and condition ocean SIC < 20 % only.

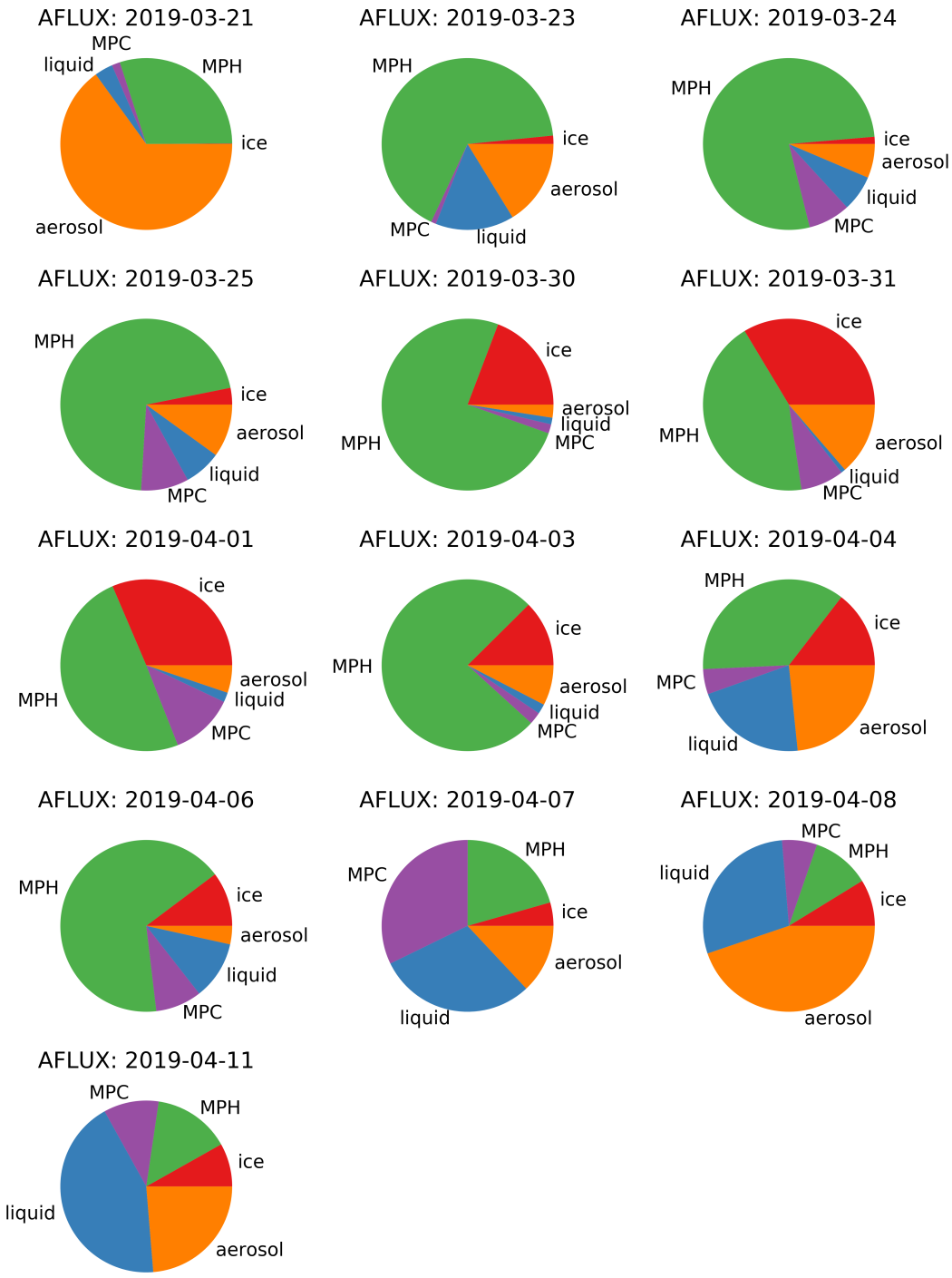

Figure 67 Thermodynamic phase distribution for each flight day during AFLUX. The data include all particle measurements below 1000 m, and the phase distribution is based on the method described in Sect. 4.6. Ice: Regimes 1a, 1b; Mixed-phase haze (MPH): Regimes 2a, 2b; Mixed-phase cloud (MPC): Regime 2c; Liquid: Regime 3; Aerosol: Regime 4.

Date	Flight objective	Minutes in clouds		Air mass origin		T_{cloud}
dd.mm.yyyy		Total	Over sea ice/ over ocean	24h	Long range	Max/min (°C)
02.09.2020	Validation of A-Train satellites observations	1.5	0.0/1.5	Sea ice	South	-1.0/-1.7
04.09.2020	In-situ measurement and remote sensing of clouds during a WAI	41.1	0.0/41.1	Ocean	South	13.6/4.7
07.09.2020	Remote sensing of clouds	0.0	0.0/0.0	Ocean	Central Arctic	-
08.09.2020	In-situ measurement and remote sensing of clouds	20.9	4.1/11.2	Ocean	Central Arctic	-1.4/-4.0
10.09.2020	In-situ measurement and remote sensing of clouds	36.0	12.8/21.2	Ocean	South	2.6/0.1
11.09.2020	In-situ measurement and remote sensing of multi-layer clouds	18.4	3.9/7.6	Ocean	South	0.2/-3.1
13.09.2020	In-situ measurement and remote sensing of clouds	36.4	8.0/27.7	Sea ice	Central Arctic	-3.2/-6.8

Table 15 List of research flights conducted during the MOSAiC-ACA field campaign. Same columns as in Table 14.

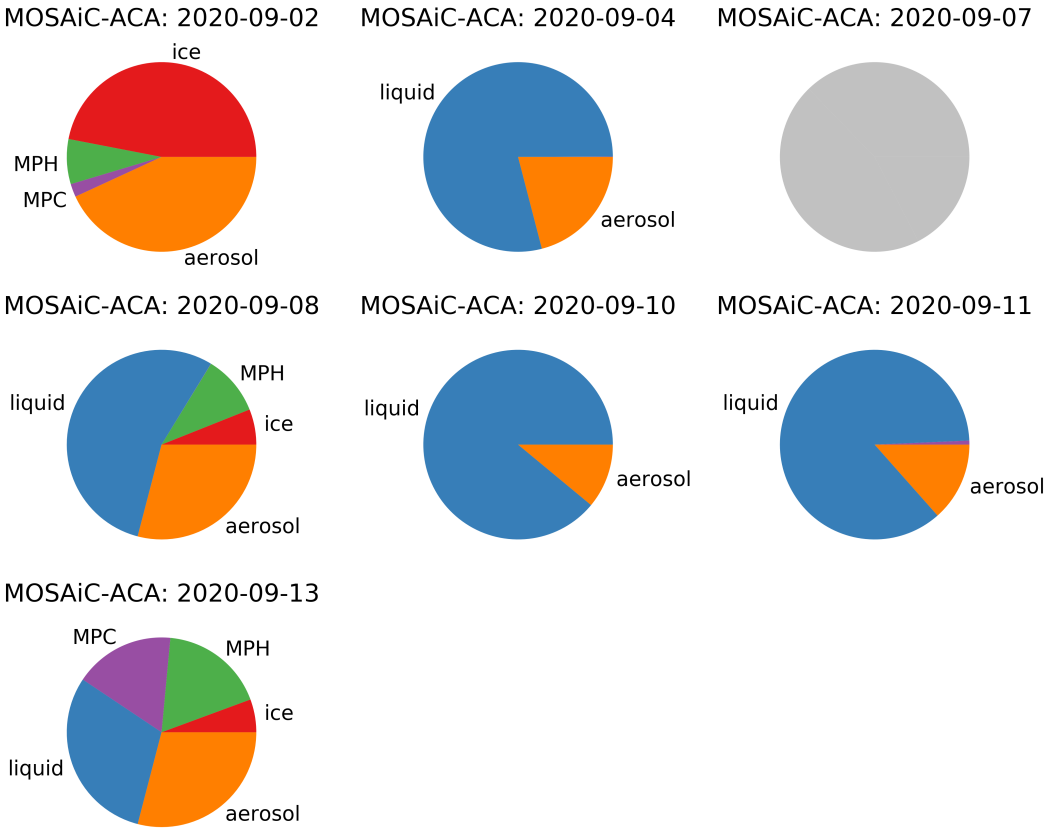

Figure 68 Thermodynamic phase distribution for each flight day during MOSAiC-ACA. The data include all particle measurements below 1000 m, and the phase distribution is based on the method described in Sect. 4.6. Ice: Regimes 1a, 1b; Mixed-phase haze (MPH): Regimes 2a, 2b; Mixed-phase cloud (MPC): Regime 2c; Liquid: Regime 3; Aerosol: Regime 4. No cloud particles in low-level altitudes were measured on 7 September 2020, as the research flight was planned for remote sensing only.

Date	Flight objective	Minutes in clouds		Air mass origin		T_{cloud}
dd.mm.yyyy		Total	Over sea ice/ over ocean	24h	Long range	Max/min (°C)
20.03.2022	In-situ cloud and aerosol measurements	24.4	0.9/23.4	Sea ice	Greenland	-9.3/-19.0
22.03.2022	In-situ cloud and aerosol measurements	86.0	29.6/36.4	Sea ice	Greenland	-13.7/-25.9
24.03.2022	In-situ cloud and aerosol measurements	54.3	3.5/49.7	Sea ice	Greenland	-13.5/-23.5
26.03.2022	Low-level cloud measurements during a CAO	53.7	3.2/26.2	Sea ice	Central Arctic	-10.4/-22.2
28.03.2022	Moderate CAO and cloud streets West of Svalbard	15.8	0.0/15.8	Land/ ocean	Siberia	no data
29.03.2022	In-situ cloud and aerosol measurements	59.8	0.0/59.7	Sea ice	Central Arctic	-8.9/-21.3
30.03.2022	In-situ cloud and aerosol measurements in the vicinity of the HALO flight track	5.2	0.7/4.3	Sea ice	Central Arctic	-6.3/-21.1
01.04.2022	Collocated measurements with HALO and Polar 5	72.4	15.4/56.9	Sea ice	Siberia	-12.7/-25.0
04.04.2022	Collocated measurements with HALO and Polar 5	47.8	0.7/45.9	Sea ice	Central Arctic	-6.2/-18.4
05.04.2022	Collocated measurements with Polar 5	37.4	18.7/18.6	Land/ ocean	Siberia	-6.2/-15.9
08.04.2022	Low-level cloud measurements in the vicinity of a polar low	25.5	15.2/0.0	Sea ice	Siberia	-15.8/-21.9
09.04.2022	Boundary layer measurements over ice and water	8.4	0.5/7.8	Land/ ocean	Siberia	-2.4/-13.9
10.04.2022	Collocated measurements with Polar 5	19.4	11.7/7.7	Land/ ocean/ sea ice*	Siberia	-1.8/-17.0

Table 16 List of research flights conducted during the HALO-(AC)^3 field campaign. Same columns as in Table 14. *From 10:40 - 11:40 UTC 24h air mass origin is from the sea ice, else from land/ocean.

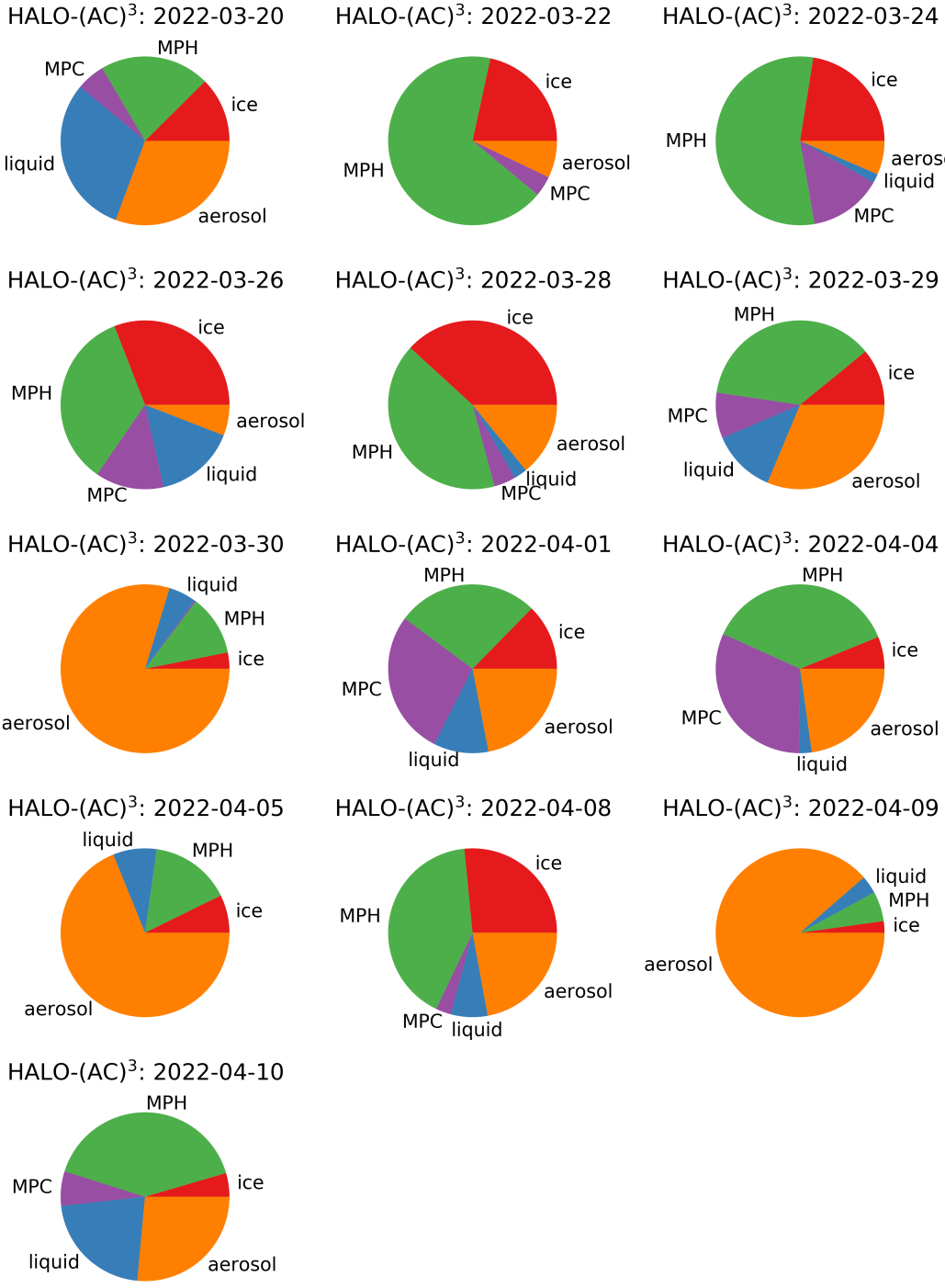

Figure 69 Thermodynamic phase distribution for each flight day during HALO-(AC)^3. The data include all particle measurements below 1000 m, and the phase distribution is based on the method described in Sect. 4.6. Ice: Regimes 1a, 1b; Mixed-phase haze (MPH): Regimes 2a, 2b; Mixed-phase cloud (MPC): Regime 2c; Liquid: Regime 3; Aerosol: Regime 4.

E Supplementary to Sect. 4.4: Microphysical properties separated by the thermodynamic phase

In this supplement, the microphysical cloud properties from Sect. 4.4 are presented separately for the ice, mixed-phase, liquid and aerosol regimes. The figures and tables in this appendix are published in Moser et al. (2023).

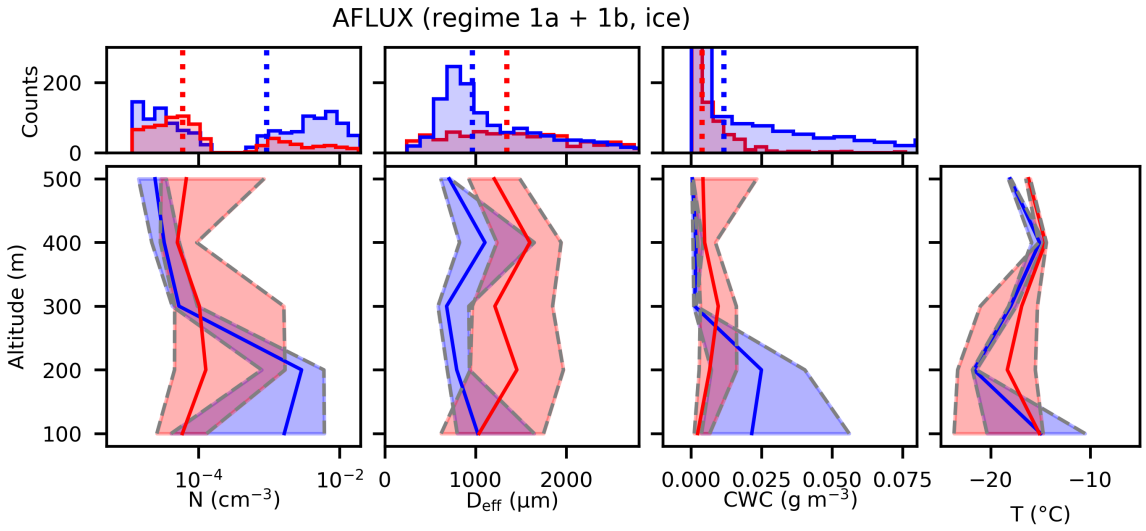

Figure 70 Same presentation of height resolved microphysical properties in Fig. 46, but for cloud data from regimes 1a and 1b, classified as ice phase. Hardly any ice phase was measured during MOSAiC-ACA. Corresponding median values are given in Table 17.

	AFLUX (spring)	
	sea ice	ocean
$\tilde{N}$ (cm^{-3})	(0.06 [0.03 / 0.82])×10^{-3}	(0.84 [0.03 / 4.87])×10^{-3}
$\tilde{D}_{\text{eff}}$ (µm)	1339 [829 / 1875]	956 [732 / 1545]
$\widetilde{\text{CWC}}$ (g m^{-3})	(3.9 [1.7 / 8.8])×10^{-3}	(10.8 [1.6 / 44.4])×10^{-3}

Table 17 Similar to Table 8 but with cloud data from regimes 1a and 1b, classified as ice phase.

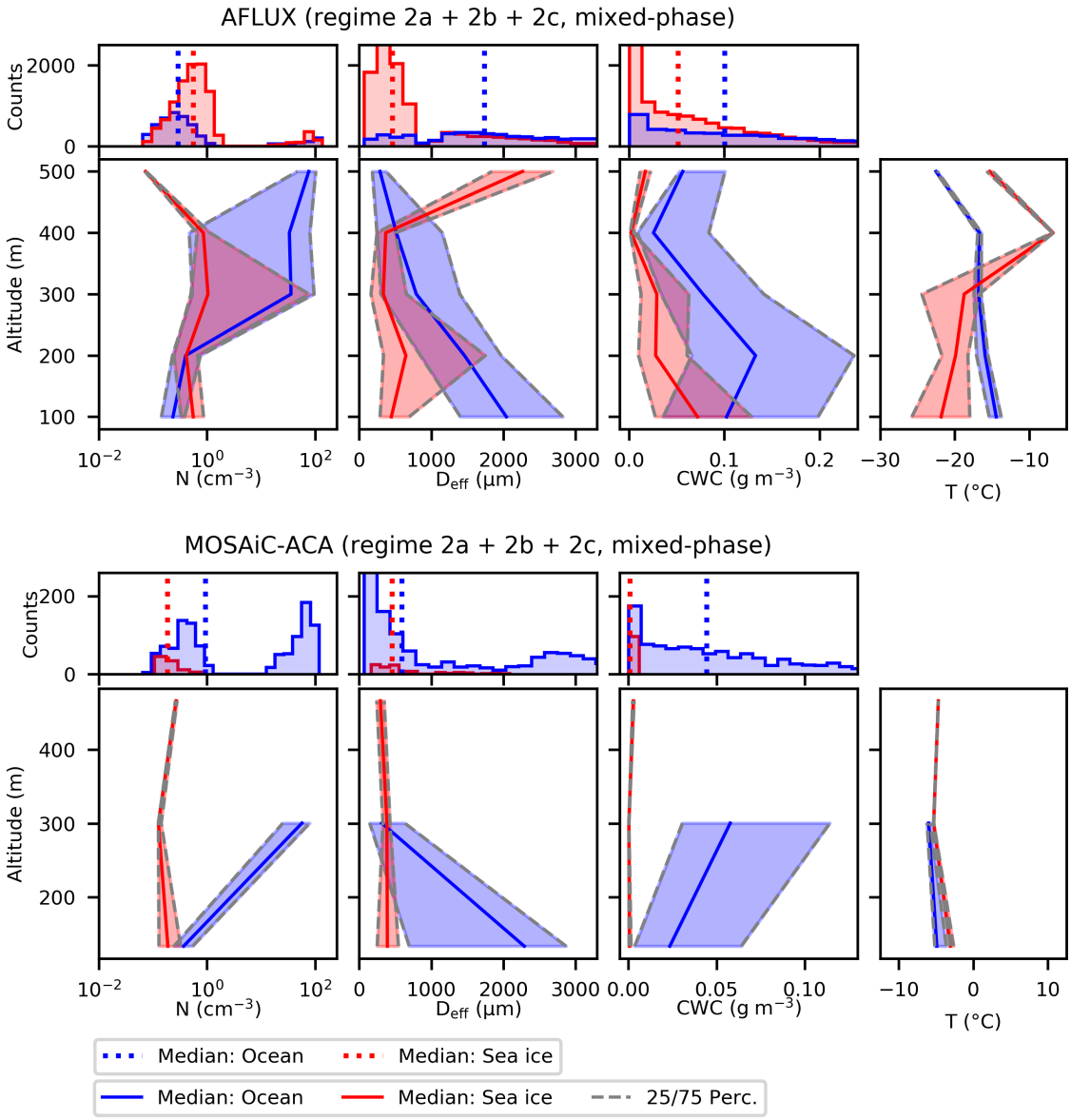

Figure 71 Same presentation of height resolved microphysical properties in Fig. 46, but for cloud data from regimes 2a, 2b and 2c, classified as mixed-phase. Corresponding median values are given in Table 18.

	AFLUX (spring)		MOSAiC-ACA (summer)	
	sea ice	ocean	sea ice	ocean
$\tilde{N}$ (cm^{-3})	0.56 [0.32 / 0.90]	0.29 [0.17 / 0.53]	0.15 [0.13 / 0.24]	0.93 [0.36 / 62.03]
$\tilde{D}_{\text{eff}}$ (µm)	455 [282 / 762]	1730 [1120 / 2546]	384 [249 / 576]	584 [227 / 2459]
$\widetilde{\text{CWC}}$ (g m^{-3})	(50.7 [12.9 / 107.2])×10^{-3}	(99.4 [35.7 / 194.4])×10^{-3}	(0.6 [0.2 / 1.4])×10^{-3}	(44.3 [16.4 / 88.6])×10^{-3}

Table 18 Similar to Table 8 but with cloud data from regimes 2a, 2b and 2c, classified as mixed-phase. Differences within one column were tested for significance with method used in Sect. 4.4.

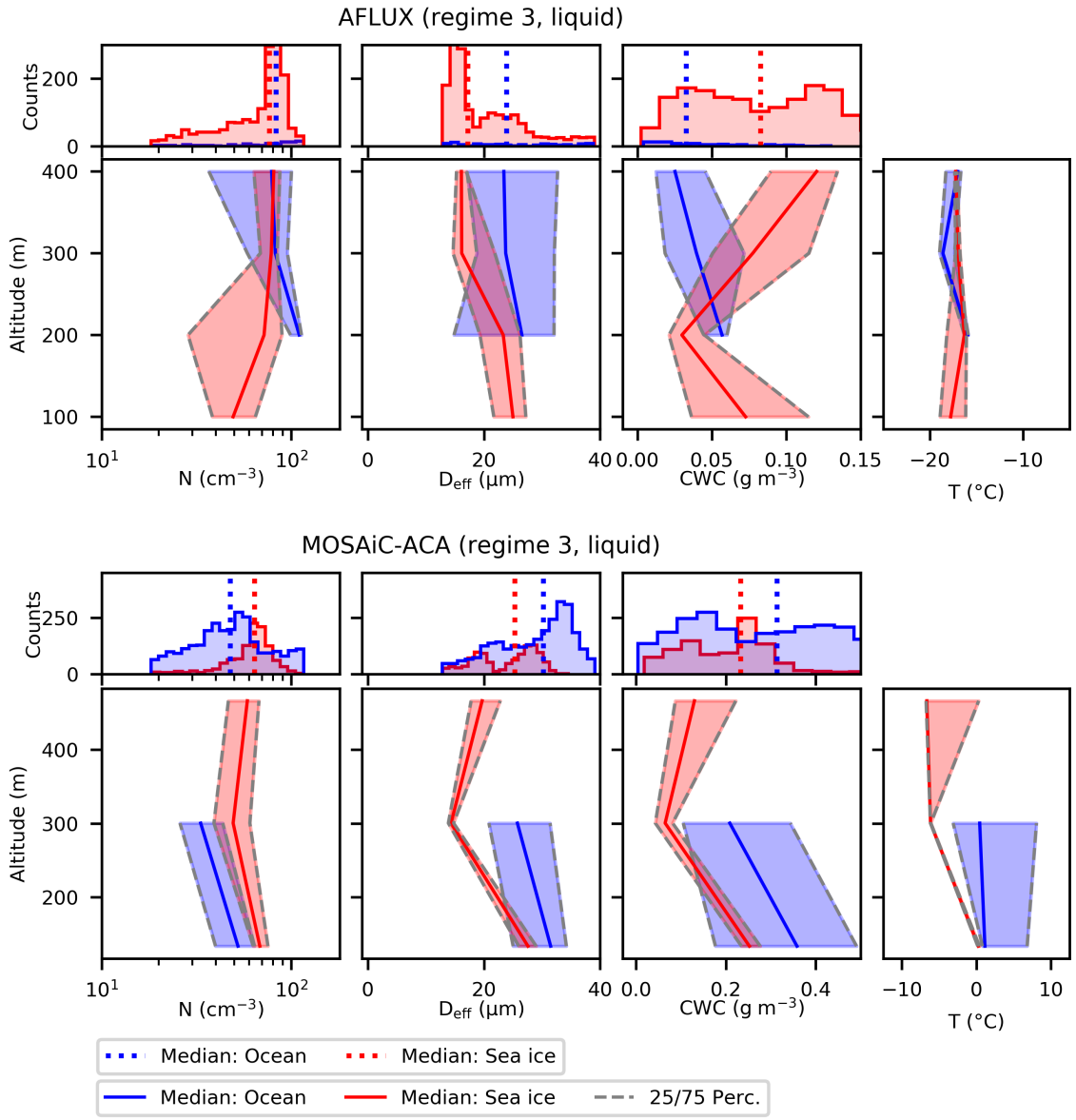

Figure 72 Same presentation of height resolved microphysical properties in Fig. 46, but for cloud data from regimes 3, classified as liquid phase. Corresponding median values are given in Table 19.

	AFLUX (spring)		MOSAiC-ACA (summer)	
	sea ice	ocean	sea ice	ocean
$\tilde{N}$ (cm^{-3})	76.77 [52.11 / 85.53]	83.27 [52.41 / 99.85]	64.13 [54.82 / 71.84]	47.68 [34.66 / 61.80]
$\tilde{D}_{\text{eff}}$ (µm)	17 [15 / 24]	24 [18 / 32]	25 [19 / 28]	30 [23 / 34]
$\widetilde{\text{CWC}}$ (g m^{-3})	0.08 [0.04 / 0.12]	0.03 [0.02 / 0.06]	0.23 [0.13 / 0.28]	0.31 [0.15 / 0.46]

Table 19 Similar to Table 8 but with cloud data from regime 3, classified as liquid phase. Differences within one column were tested for significance with method used in Sect. 4.4.

	AFLUX (spring)		MOSAiC-ACA (summer)	
	sea ice	ocean	sea ice	ocean
$\tilde{N}$ (cm^{-3})*	0.38 [0.21 / 0.56]	0.21 [0.12 / 0.31]	0.13 [0.12 / 0.22]	0.13 [0.12 / 0.25]

Table 20 Similar to Table 8 but with data from regime 4, classified as aerosol particles ($>2.8\,\mu m$). The asterisk indicates that one combination of two values within the column is not significantly different: im-om.

F Supplementary to Sect. 4.5: Gamma function parameters

Table 21 Fitted parameters for the gamma functions in Fig. 48 for the size range of the CDP/CAS, CIP and PIP. The index CAS represents both instruments, CAS and CDP. Table is from Moser et al. (2023).

regime	campain	$N_{0,\mathrm{CAS}}$ $(m^{-4-\mu})$	μ_{CAS} ()	λ'_{CAS} (m^{-1})	$N_{0,\mathrm{CIP}}$ $(m^{-4-\mu})$	μ_{CIP} ()	λ'_{CIP} (m^{-1})	$N_{0,\mathrm{PIP}}$ $(m^{-4-\mu})$	μ_{PIP} ()	λ'_{PIP} (m^{-1})
1a	AFLUX	-	-	-	-	-	-	2.42×10^{7}	0.77	1559.47
1a	MOSAiC	-	-	-	-	-	-	2.03×10^{5}	0.20	706.94
1b	AFLUX	-	-	-	1.48×10^{23}	3.79	2.24×10^{4}	9.50×10^{12}	1.86	3581.95
1b	MOSAiC	-	-	-	-	-	-	-	-	-
2a	AFLUX	3.94×10^{10}	0.18	1.11×10^{4}	2.32×10^{22}	3.11	3.06×10^{4}	5.15×10^{08}	0.41	3912.93
2a	MOSAiC	1.61×10^{13}	0.30	4.21×10^{5}	4.28×10^{19}	2.27	1.39×10^{5}	2.74×10^{14}	2.56	5774.83
2b	AFLUX	2.11×10^{12}	0.62	2.19×10^{4}	5.07×10^{13}	1.33	1.67×10^{4}	5.28×10^{11}	1.62	2395.79
2b	MOSAiC	9.71×10^{15}	0.75	5.22×10^{5}	3.60×10^{23}	2.93	1.70×10^{5}	2.41×10^{5}	0.03	642.56
2c	AFLUX	6.59×10^{8}	-0.84	1.48×10^{5}	4.88×10^{24}	4.11	2.50×10^{4}	4.79×10^{13}	2.07	3671.13
2c	MOSAiC	2.09×10^{81}	12.69	1.17×10^{6}	1.98×10^{51}	10.64	6.26×10^{4}	9.58×10^{35}	10.64	3635.66
3	AFLUX	2.85×10^{39}	5.08	4.31×10^{5}	541.68	-1.26	1.56×10^{4}	4.90×10^{10}	1.60	3585.70
3	MOSAiC	1.97×10^{20}	1.43	1.54×10^{5}	2.65×10^{20}	1.76	1.06×10^{5}	2231.82	-0.10	2206.11

G Supplementary to the analysis of mixed-phase haze and mixed-phase clouds

	AFLUX (spring)		HALO-(AC)^3 (summer)	
	sea ice	ocean	sea ice	ocean
$\tilde{N}_{\text{MPH}}$ (cm^{-3})	0.52 [0.30 / 0.80]	0.25 [0.15 / 0.41]	0.14 [0.07 / 0.30]	0.13 [0.07 / 0.21]
$\tilde{D}_{\text{eff, MPH}}$ (µm)	473 [299 / 1090]	1914 [1374 / 2680]	373 [272 / 546]	1266 [612 / 1721]
$\widetilde{\text{CWC}}_{\text{MPH}}$ (g m^{-3})	(50.4 [11.3 / 108.7])$\times 10^{-3}$	(104.4 [33.9 / 201.4])$\times 10^{-3}$	(12.6 [2.4 / 30.1])$\times 10^{-3}$	(37.5 [6.0 / 163.7])$\times 10^{-3}$
$\tilde{N}_{\text{MPC}}$ (cm^{-3})*	78.21 [50.88 / 89.60]	66.84 [35.39 / 106.21]	-	105.53 [51.36 / 145.95]
$\tilde{D}_{\text{eff, MPC}}$ (µm)	181 [112 / 365]	441 [227 / 695]	-	203 [121 / 400]
$\widetilde{\text{CWC}}_{\text{MPC}}$ (g m^{-3})	(51.8 [30.6 / 81.7])$\times 10^{-3}$	(85.5 [44.2 / 148.7])$\times 10^{-3}$	-	(132.0 [72.2 / 211.5])$\times 10^{-3}$

Table 22 Microphysical properties of Arctic low-level mixed-phase haze (MPH) and mixed-phase clouds (MPC) during AFLUX and HALO-(AC)^3 for surface condition sea ice or ocean: Median number concentration $\tilde{N}$, median effective diameter $\tilde{D}_{\text{eff}}$, and median cloud water content $\widetilde{\text{CWC}}$. Only data in the ABL is considered here (< 500 m). The values in the square brackets give the 25th and 75th percentile respectively. There is not enough data for the microphysical properties of MPC for the HALO-(AC)^3 campaign over the sea ice. The asterisk indicates that one combination of two values within the column is not significantly different. $\tilde{N}_{\text{MPC}}$: ia-oa.

Contributions to this study

Parts of this study were supported by the valuable contributions of colleagues, who are acknowledged here.

Christiane Voigt supervised the thesis and provided intensive feedback.
Yvonne Boose[now at 1], Valerian Hahn[2,3], Johannes Lucke[3,4], Johanna Mayer[3], Elena De La Torre Castro[2,3,4], Christiane Voigt, Guillaume Mioche[5], Olivier Jourdan[5], Régis Dupuy[5], Christophe Gourbeyre[5], Alfons Schwarzenboeck[5] and Stephan Borrmann[2,6] were co-responsible for the in-situ cloud instruments, provided support in the integration of the instruments on the research aircraft, and helped carrying out the in-situ cloud measurements. The sampling areas of the CDP and the CAS introduced in Sect. 3.2 have been determined in previous laboratory work carried out by Jonas Kleine[former at 2,3] and Marcus Klingebiel[7]. The bin setting of the CDP was determined with the help of Johannes Lucke. Régis Dupuy processed the data recorded by the Polar Nephelometer and the 2D-S probe. Olivier Jourdan and Guillaume Mioche analyzed the Polar Nephelometer data in Sect. 4.3.1 and Sect. 4.5. The laboratory work to trace the origin of the overestimation of the particle counter in the OAPs in Sect. 3.3.1.2 has been carried out in a joint project with Elena De La Torre Castro. Mario Mech[8], André Ehrlich[7], Andreas Herber[9], Christof Lüpkes[9], Susanne Crewell[8] and Manfred Wendisch[7] conceived the flight experiments. The analysis of the aerosol particle composition in the atmospheric boundary layer in Sect. 5.1 was performed by Oliver Eppers[6].

Parts of this work have been published in the peer-reviewed articles Mech et al. (2022) and Moser et al. (2023). This is clearly indicated in the respective sections.

1 Google, Tel Aviv, Israel
2 Institut für Physik der Atmosphäre, Johannes Gutenberg-Universität, Mainz, Germany
3 Institut für Physik der Atmosphäre, Deutsches Zentrum für Luft- und Raumfahrt, Weßling, Germany
4 Faculty of Aerospace Engineering, Delft University of Technology, Delft, the Netherlands
5 Laboratoire de Météorologie Physique, Université Clermont Auvergne, Clermont-Ferrand, France
6 Particle Chemistry Department, Max Planck Institute for Chemistry, Mainz, Germany
7 Leipziger Institut für Meteorologie, Universität Leipzig, Leipzig, Germany
8 Institut für Geophysik und Meteorologie, Universität zu Köln, Cologne, Germany
9 Alfred-Wegener-Institut, Helmholtz-Zentrum für Polar- und Meeresforschung, Bremerhaven, Germany

Acknowledgements

Acknowledgements are not included in the electronic version.

Curriculum Vitae

The curriculum vitae is not included in the electronic version.